

**DEVELOPMENT OF COMPONENT AND SYSTEM LEVEL TEST
METHODS TO CHARACTERIZE MANUAL WHEELCHAIR
PROPULSION COST**

A Dissertation
Presented to
The Academic Faculty

by

Morris Huang

In Partial Fulfillment
of the Requirements for the Degree
Doctor of Philosophy (Bioengineering) in the
George W. Woodruff School of Mechanical Engineering

Georgia Institute of Technology
December 2017

COPYRIGHT © 2017 BY MORRIS HUANG

**DEVELOPMENT OF COMPONENT AND SYSTEM LEVEL TEST
METHODS TO CHARACTERIZE MANUAL WHEELCHAIR
PROPULSION COST**

Approved by:

Dr. Stephen Sprigle, Advisor
School of Mechanical Engineering
Georgia Institute of Technology

Dr. Maysam Ghovanloo
School of Electrical and Computer
Engineering
Georgia Institute of Technology

Dr. Aldo Ferri
School of Mechanical Engineering
Georgia Institute of Technology

Dr. Young-Hui Chang
School of Biological Sciences
Georgia Institute of Technology

Dr. Jun Ueda
School of Mechanical Engineering
Georgia Institute of Technology

Mark Greig
Vice President of Research
Sunrise Medical LLC

Date Approved: November 8, 2017

ACKNOWLEDGEMENTS

I would like to thank Dr. Stephen Sprigle for his guidance and endless patience over the past four years as my dissertation adviser and mentor. I would like to thank my current colleagues of the Rehabilitation Engineering and Applied Research (REAR) lab, particularly Jacob Misch, Mark McJunkin, and Steven Pubilliones, which without them the myriad component tests could not have been done. I would like to acknowledge my past colleagues of the REAR lab, particularly Howard Liles, who really helped me revive and get the AMPS to a functional state. I would also like to acknowledge Jui-Te Lin, another past colleague who helped me fill the gaps on manual wheelchair performance from the human perspective with his parallel research. I would like to thank Dr. Teresa Snow for her assistance in the empirical modeling process. I would like to thank my committee for their involvement my work, particularly Mark Greig for providing the wheelchair components used in this dissertation work, and Dr. Aldo Ferri for offering many insights on the modeling of manual wheelchair dynamics. I would like to thank the Georgia Institute of Technology as a whole, whose facilities and resources across several departments were used. I would like to thank the National Institute on Disability, Independent Living, and Rehabilitation Research, whose foundation grant supported this research in part. Finally, I would like to thank my family and friends, whose emotional support was essential towards the completion of this dissertation. I couldn't have done it without you.

TABLE OF CONTENTS

| | |
|--|------------|
| ACKNOWLEDGEMENTS | iii |
| LIST OF TABLES | vi |
| LIST OF FIGURES | vii |
| SUMMARY | x |
| CHAPTER 1. | |
| Introduction | 1 |
| 1.1 Significance and Objectives | 1 |
| 1.2 Background | 1 |
| 1.3 Research Aims | 4 |
| CHAPTER 2. | |
| Component-level test methods | 7 |
| 2.1 Component Diversity | 8 |
| 2.2 Predicate Work (Trifilar Pendulum) | 14 |
| 2.3 Development of Coast-down Method | 17 |
| 2.3.1 System Design and Rationale | 18 |
| 2.3.2 System Validation | 29 |
| 2.4 Development of Wheel Scrub Method | 32 |
| 2.4.1 System Design | 34 |
| 2.4.2 System Validation | 44 |
| 2.5 Component Test Results and Discussion | 49 |
| 2.5.1 Component Mass and Moment of Inertia | 49 |
| 2.5.2 Rolling Resistance | 52 |
| 2.5.3 Scrub Torque | 59 |
| 2.5.4 Combined Analysis | 66 |
| CHAPTER 3. | |
| Anatomical model propulsion system | 70 |
| 3.1 System Design and Rationale | 71 |
| 3.1.1 Anthropomorphic Design | 71 |
| 3.1.2 Propulsion Control | 73 |
| 3.1.3 Data Acquisition | 78 |
| 3.2 Calibration and Validation | 79 |
| 3.2.1 Calibrating Motor Current Sensors | 80 |
| 3.2.2 System-level Validation | 83 |
| CHAPTER 4. | |
| System-level test methods | 86 |
| 4.1 Predicate Work (The iMachine) | 86 |
| 4.2 Defining Canonical Maneuvers | 93 |

| | | |
|-------------------|---|------------|
| 4.3 | Defining a Performance Metric | 107 |
| 4.4 | System-Level Study Designs | 109 |
| 4.4.1 | Impact of Mass and Weight Distribution on Propulsion Torque | 110 |
| 4.4.2 | Impact of Casters and Drive Wheels on Propulsion Cost | 111 |
| 4.5 | System-Level Experimental Results and Discussion | 115 |
| 4.5.1 | Impact of Mass and Weight Distribution on Propulsion Torque | 115 |
| 4.5.2 | Impact of Casters and Drive Wheels on Propulsion Cost | 125 |
| CHAPTER 5. | | |
| | Empirical modeling | 153 |
| 5.1 | Model Definitions | 153 |
| 5.2 | Modeling Methods | 156 |
| 5.3 | Model Results | 157 |
| CHAPTER 6. | | |
| | Conclusions and future work | 165 |
| 6.1 | Conclusions | 165 |
| 6.2 | Future Work | 168 |
| | References | 171 |

LIST OF TABLES

| | |
|--|-----|
| Table 1. Caster Wheel Properties..... | 9 |
| Table 2. Drive Wheel Properties..... | 11 |
| Table 3. Summary of Component Properties..... | 12 |
| Table 4. Component Loadings by Representative System Weight-Distribution..... | 13 |
| Table 5. Cart Weight-distribution Configuration Loads..... | 28 |
| Table 6. Wheel Scrub Test Configuration Loadings | 42 |
| Table 7. Caster Scrub Test Rig Normal Load Variability | 45 |
| Table 8. Drive Wheel Scrub Test Rig Normal Load Variability | 46 |
| Table 9. Drive Wheel Scrub Test Rig (with cross-brace) Normal Load Variability | 48 |
| Table 10. Caster Inertial Measurements | 50 |
| Table 11. Drive Wheel Inertial Measurements | 51 |
| Table 12. Caster and Drive Wheel Rolling Resistance Force on Tile | 52 |
| Table 13. Caster and Drive Wheel Rolling Resistance Forces on Carpet | 56 |
| Table 14. Caster and Drive Wheel Scrub Torque on Tile..... | 60 |
| Table 15. Caster and Drive Wheel Scrub Torque on Carpet | 63 |
| Table 16. AMPS Body Segment Parameters | 71 |
| Table 17. AMPS Propulsion Torque Repeatability | 84 |
| Table 18. System Resistance Models Nomenclature..... | 103 |
| Table 19. Test Wheelchair Configurations | 115 |
| Table 20. Propulsion Torques During Maneuvers on Tile | 116 |
| Table 21. Propulsion Torques During Maneuvers on Carpet | 117 |
| Table 22. AMPS Weight-Distribution Configurations and System Yaw Inertia..... | 125 |
| Table 23. AMPS Propulsion Cost for Straight Maneuvers on Tile | 126 |
| Table 24. AMPS Propulsion Cost for Straight Maneuvers on Carpet | 126 |
| Table 25. AMPS Propulsion Cost for Fixed Wheel Turn Maneuvers on Tile..... | 126 |
| Table 26. AMPS Propulsion Cost for Fixed Wheel Turn Maneuvers on Carpet | 127 |
| Table 27. AMPS Propulsion Cost for Zero Radius Turns Maneuvers on Tile..... | 127 |
| Table 28. AMPS Propulsion Cost for Zero Radius Turns Maneuvers on Carpet..... | 127 |
| Table 29. ANOVA of Straight Maneuvers on Tile..... | 128 |
| Table 30. ANOVA of Straight Maneuvers on Carpet..... | 129 |
| Table 31. ANOVA of Fixed Wheel Turn Maneuvers on Tile | 129 |
| Table 32. ANOVA of Fixed Wheel Turn Maneuvers on Carpet..... | 129 |
| Table 33. ANOVA of Zero Radius Turns Maneuvers on Tile | 130 |
| Table 34. ANOVA of Zero Radius Turns Maneuvers on Carpet | 130 |
| Table 35. Straight (Tile) Propulsion Cost % Differences and Effect Sizes | 133 |
| Table 36. Straight (Carpet) Propulsion Cost % Differences and Effect Sizes..... | 135 |
| Table 37. Fixed Wheel Turn (Tile) Propulsion Cost % Differences and Effect Sizes ... | 138 |
| Table 38. Fixed Wheel Turn (Carpet) Propulsion Cost % Difference and Effect Size .. | 141 |
| Table 39. Zero Radius Turns (Tile) Propulsion Cost % Differences and Effect Sizes... | 144 |
| Table 40. Zero Radius Turns (Carpet) Propulsion Cost % Difference and Effect Size.. | 146 |
| Table 41. Linear Regression Modeling Results | 157 |

LIST OF FIGURES

| | |
|--|----|
| Figure 1. Durometer measurement of tire hardness..... | 8 |
| Figure 2. Component Tire Profile Outlines | 12 |
| Figure 3. Samples of Test Surfaces..... | 14 |
| Figure 4. Drive Wheel Rotational Inertia Measurement by Trifilar Pendulum..... | 15 |
| Figure 5. Screenshot of Frame Counting for Cycle Period..... | 16 |
| Figure 6. Caster Rotational Inertia and Caster-and-Fork Yaw Inertia Measurement..... | 17 |
| Figure 7. Coast-down Cart Frame Design | 19 |
| Figure 8. Accelerometer Mounted on "Control" Wheel | 20 |
| Figure 9. Accelerometer Sample Data | 21 |
| Figure 10. Coast-down Cart Dimensional Variables | 22 |
| Figure 11. Velocity Profile of Single Coast-down..... | 23 |
| Figure 12. Coast-down Cart on iMachine..... | 24 |
| Figure 13. Cart Free-body Diagram..... | 25 |
| Figure 14. Measurement of "Control" Wheel Loaded Radius | 26 |
| Figure 15. Cart 60%WD Configurations for Caster and Drive Wheels | 27 |
| Figure 16. Tile and Carpet Test Tracks | 28 |
| Figure 17. Accelerometer Mounted on Digital Encoder for Validation Testing | 30 |
| Figure 18. Accelerometer versus Encoder Velocity Measurements | 31 |
| Figure 19. Coast-down Data Selection Criteria | 32 |
| Figure 20. Predicate Measurement Method of Caster Wheel Scrub Torque | 33 |
| Figure 21. Caster Wheel Scrub Torque Test Rig..... | 34 |
| Figure 22. Drive Wheel Scrub Torque Test Rig..... | 35 |
| Figure 23. Pull Force Actuator/Sensor..... | 35 |
| Figure 24. Caster Wheel Mounting Structure | 36 |
| Figure 25. Drive Wheel Mounting Structure | 37 |
| Figure 26. Surface Loading Post..... | 37 |
| Figure 27. Drive Wheel Contact Patch on Surface Mounting Plate | 38 |
| Figure 28. Pull Cable Alignment | 39 |
| Figure 29. Centering Test Surface Rotation in Caster | 40 |
| Figure 30. Caster Scrub Test Pull Force Data..... | 41 |
| Figure 31. Tile and Carpet Scrub Torque Test Surfaces..... | 43 |
| Figure 32. Carpet Test Surface Before and After Scrub Test Trial Set | 43 |
| Figure 33. Validating Normal Loading for Caster and Drive Wheel Scrub Test Rigs..... | 44 |
| Figure 34. Force Gauge Force Measurement Plot | 45 |
| Figure 35. Drive Wheel Test Rig Cross-Brace | 47 |
| Figure 36. Impact of Scrub Test Trial Order | 49 |
| Figure 37. Caster Rolling Resistance on Tile | 53 |
| Figure 38. Drive Wheel Rolling Resistance on Tile | 54 |
| Figure 39. Caster Rolling Resistance on Carpet | 57 |
| Figure 40. Drive Wheel Rolling Resistance on Carpet..... | 58 |
| Figure 41. Caster Scrub Torque on Tile..... | 61 |
| Figure 42. Drive Wheel Scrub Torque on Tile | 62 |

| | |
|---|-----|
| Figure 43. Caster Scrub Torque on Carpet | 64 |
| Figure 44. Drive Wheel Scrub Torque on Carpet | 65 |
| Figure 45. Caster Rolling Resistance versus Scrub Torque on Tile | 66 |
| Figure 46. Caster Rolling Resistance versus Scrub Torque on Tile | 67 |
| Figure 47. Drive Wheel Rolling Resistance versus Scrub Torque on Tile..... | 68 |
| Figure 48. Drive Wheel Rolling Resistance versus Scrub Torque on Carpet..... | 68 |
| Figure 49. The Anatomical Model Propulsion System (AMPS) | 70 |
| Figure 50. AMPS Leg and Torso Segments | 72 |
| Figure 51. Gear and sprocket interface between motor and pushrim | 74 |
| Figure 52. AMPS Control Diagram | 76 |
| Figure 53. AMPS VI Manual Trajectory Entry | 77 |
| Figure 54. AMPS VI Pre-defined Trajectory..... | 77 |
| Figure 55. Comparison of Current (Torque) and Force Data | 80 |
| Figure 56. Motor Current-Torque Relationship..... | 81 |
| Figure 57. AMPS Left Motor Calibration..... | 82 |
| Figure 58. AMPS Right Motor Calibration | 82 |
| Figure 59. Angular velocity profile of drive wheels at 2.33-rad/sec (0.7 m/s)..... | 85 |
| Figure 60. iMachine Schematic Diagram and Top View | 87 |
| Figure 61. iMachine with a Manual Wheelchair Loaded on the Platform..... | 88 |
| Figure 62. Free-body Diagram of Occupied Manual Wheelchair Normal Forces | 89 |
| Figure 63. iMachine VI During Load Centering (black rectangles)..... | 91 |
| Figure 64. iMachine Perturbation Triangle..... | 92 |
| Figure 65. iMachine VI During Measurement of System Yaw Inertia..... | 93 |
| Figure 66. Schematic of wheelchair for use in deriving wheelchair kinematics during over-ground motion | 94 |
| Figure 67. AMPS Straight Maneuver with Drive Wheel Velocity Profile | 96 |
| Figure 68. AMPS Fixed-Wheel Turn Maneuver with Drive Wheel Velocity Profile | 97 |
| Figure 69. AMPS Zero-Radius Turns Maneuver with Drive Wheel Velocity Profile (Carpet) | 98 |
| Figure 70. AMPS Zero-Radius Turns Maneuver Drive Wheel Velocity Profile (Tile) ... | 99 |
| Figure 71. System Kinetic Energies of the Straight Maneuver | 100 |
| Figure 72. System Kinetic Energies of the Fixed Wheel Turn Maneuver..... | 100 |
| Figure 73. System Kinetic Energies of the Zero Radius Turns Maneuver | 101 |
| Figure 74. System Resistances During Straight Maneuver | 104 |
| Figure 75. System Resistances During Fixed Wheel Turn Maneuver..... | 104 |
| Figure 76. System Resistances During Zero Radius Turns Maneuver | 106 |
| Figure 77. AMPS Drive Wheel Velocity and Torque Profiles | 108 |
| Figure 78. AMPS Loaded at the 70% WD Configuration | 112 |
| Figure 79. Propulsion torque across configurations for acceleration phase of straight maneuver..... | 118 |
| Figure 80. Propulsion torque across configurations for steady-state phase of straight maneuver..... | 119 |
| Figure 81. Propulsion torque across configurations for acceleration phase of turning maneuver..... | 120 |
| Figure 82. Propulsion torque across configurations for steady-state phase of turning maneuver..... | 121 |

| | |
|--|-----|
| Figure 83. Propulsion Cost of Drive Wheel Configurations for Straight Maneuvers on Tile | 133 |
| Figure 84. Propulsion Cost of Caster Configurations for Straight Maneuvers on Tile .. | 134 |
| Figure 85. Propulsion Cost of Drive Wheel Configurations for Straight Maneuvers on Carpet..... | 137 |
| Figure 86. Propulsion Cost of Caster Configurations for Straight Maneuvers on Carpet | 137 |
| Figure 87. Propulsion Cost of Drive Wheel Configurations for Fixed Wheel Turn Maneuvers on Tile | 138 |
| Figure 88. Propulsion Cost of Drive Wheel Configurations for Fixed Wheel Turn Maneuvers on Tile (Steady-State Phase) | 139 |
| Figure 89. Propulsion Cost of Caster Configurations for Fixed Wheel Turn Maneuvers on Tile | 140 |
| Figure 90. Propulsion Cost of Drive Wheel Configurations for Fixed Wheel Turn Maneuvers on Carpet | 142 |
| Figure 91. Propulsion Cost of Caster Configurations for Fixed Wheel Turn Maneuvers on Carpet..... | 143 |
| Figure 93. Propulsion Cost of Caster Configurations for Zero Radius Turns Maneuvers on Tile | 145 |
| Figure 92. Propulsion Cost of Drive Wheel Configurations for Zero Radius Turns Maneuvers on Tile | 145 |
| Figure 94. Propulsion Cost of Caster Configurations for Zero Radius Turns Maneuvers on Carpet..... | 147 |
| Figure 95. Propulsion Cost of Drive Wheel Configurations for Zero Radius Turns Maneuvers on Carpet | 148 |
| Figure 96. Straight versus Turning Propulsion Cost for DW Configurations on Tile | 149 |
| Figure 97. Straight versus Turning Propulsion Cost for DW Configurations on Carpet | 150 |
| Figure 98. Straight versus Turning Propulsion Cost for Caster Configurations on Tile | 151 |
| Figure 99. Straight versus Turning Propulsion Cost for Caster Configurations on Carpet | 152 |
| Figure 100. Straight Maneuver Linear Regression Model..... | 159 |
| Figure 101. Zero Radius Turns Maneuver Linear Regression Model | 160 |
| Figure 102. Fixed Wheel Turn Maneuver Linear Regression Model | 161 |
| Figure 103. Fixed Wheel Turn Maneuver Linear Regression Model..... | 162 |
| Figure 104. Fixed Wheel Turn Maneuver Linear Regression Model (System Resistance Minus Drive Wheel Scrub) | 163 |

SUMMARY

The current approach to manual wheelchair design lacks a sound and objective connection to metrics for manual wheelchair (MWC) performance. Wheelchair performance directly impacts propulsion effort, which is a strong determinant of user health and mobility. To date, medical reimbursement for MWCs is coded heavily around a 6-lb difference between standard (low-end) and ultra-lightweight (high-end) wheelchairs, with three other weight-based wheelchair categories falling within this small weight range. This further reflects the pervasive lack of a suitable metric for characterizing wheelchair performance. Studies to date have attempted to distinguish performance between different manual wheelchairs, but have lacked the repeatability or external validity necessary. Human subject tests are mostly non-representative of everyday MWC mobility and have demonstrated a low sensitivity to performance differences. Studies of MWC mechanical design, while more sensitive, are almost exclusively based on passive measurements not involving active propulsion of the MWC.

The objective of this dissertation research was to develop capabilities to characterize and predict manual wheelchair performance, with three specific research aims:

1. Develop component-level test methods to evaluate the inertial and resistive properties of manual wheelchair components.
2. Develop a system-level test method to distinguish the mechanical performance of various manual wheelchair configurations across maneuvers representative of everyday wheelchair mobility.

3. Develop empirical models to relate component-level measures to system-level results.

The first research aim was accomplished through designed methodologies that characterized the rotational inertia, rolling resistance, and scrub torque of caster and drive wheels. Three new measurement devices were fabricated to this end: the coast-down cart, the caster scrub test rig, and the drive wheel scrub test rig. A diverse set of 4 drive wheels and 8 casters were evaluated for tile and carpet surfaces with these instruments. These tests demonstrated the variance in the resistive properties of wheelchair components, as well as illustrated different optimal components for different surfaces.

The second research aim was accomplished by methodologies that quantified the propulsion torque and propulsion cost of various MWC configurations on tile and carpet. To this end, a wheelchair-propelling robot, AMPS, was developed. Three canonical maneuvers for AMPS were defined, based on their external validity and balanced collective representation of different kinetic energies and resistive losses. These maneuvers were applied towards investigating the impact of mass and weight-distribution on propulsion torque, as well as the impact of 4 casters and 3 drive wheels on propulsion cost. The first study identified weight-distribution as having a larger impact on propulsion torque in turning than in straight maneuvers. The second study identified the tradeoffs of wheelchairs configured with different components, with drive wheel differences exerting a greater performance impact across all maneuvers.

The research aim of predicting system-level MWC performance was accomplished by applying linear regression modeling. System-level propulsion costs from the second

aim were used as outcome variables, and component measures of resistive loss from the first aim were used to calculate system resistance predictor variables. The system resistance definitions were based on the resistive loss models developed as part of the second aim. System yaw inertia and weight-distribution were also entered as predictor variables. Two of the empirical models (straight and zero-radius turns) demonstrated strong predictive capabilities that linking system propulsion cost to component resistive properties.

The outcomes of this research empower clinicians and users to make a more informed choice in wheelchair selection by means of a standard, scientifically-motivated performance metric. Furthermore, the empirical models offer manufacturers a basis by which to optimize their future wheelchair designs, thus motivating a better product for all wheelchair stakeholders.

CHAPTER 1. INTRODUCTION

1.1 Significance and Objectives

The current approach to manual wheelchair design lacks a sound and objective connection to metrics for wheelchair performance. Wheelchair performance directly impacts propulsion effort, which is a strong determinant of user health and mobility (Bohannon, 2007; Levy et al., 2010; Oyster et al., 2011; Sonenblum SE, Sprigle S, & Lopez RA, 2012b). Certain wheelchair designs and configurations require more effort to propel because of their inertial and frictional parameters. Given the breadth of wheelchair options, users, clinicians and manufacturers need information about how these options impact the effort required to propel wheelchairs. Most directly, wheelchair manufacturers can use information about the influences of configuration on propulsion effort to optimize designs and improve their development cycles. **The objective of this research is to empirically characterize the inertial and resistive properties of different wheelchair components and configurations, and develop empirical models for wheelchair manufacturers that define the impact of these properties on system-level wheelchair performance.**

1.2 Background

For the 1.6 million wheelchair users who live in the United States (Kaye, Kang, & LaPlante, 2000), the wheelchair forms the foundation for all of their academic, vocational, and societal activities (Bohannon, 2007; Levy et al., 2010; Oyster et al., 2011; Sonenblum SE et al., 2012b). Amongst these users, 94% own manual wheelchairs (MWCs), a mobility device that relies on the occupant for propulsive force (Kaye et al., 2000). The inefficient

nature of wheelchair propulsion (van der Woude LHV, Veeger HEJ, Rozendal RH, & et al, 1988; van der Woude LHV, 1988) often has a detrimental effect on the user well-being. Wheelchair users move about in short bouts of activity (Sonenblum SE et al., 2012b) where the higher inertia and greater energy loss translates into the need for users to perform more propulsion work during wheelchair maneuvers. Furthermore, less mechanically efficient wheelchairs require the user to exert greater instantaneous force and total effort for accomplishing desired travel. Greater propulsion effort can lead to difficulty in achieving desired speeds, a higher probability of fatigue over long bouts of mobility, and difficulty negotiating inclines. The accumulation of this greater effort can also increase the potential for injury in the upper extremities (Boninger et al., 2003; van der Woude LHV, Dallmeijer AJ, Janssen TWJ, & Veeger D, 2001). Regretfully, despite the risks associated with low performance wheelchairs, modern wheelchair design is hinged upon meeting unempirical weight cutoffs defined by Medicare for varying amounts of financial coverage.

The need to improve manual wheelchair mobility has motivated a substantial body of research targeting wheelchair propulsion effort. The effort required to propel manual wheelchairs is a reflection of two sets of variables: the **mechanics of the wheelchair** and the **biomechanics of the human propulsion**. This project focuses on the wheelchair as a mechanical system which, to date, has not received much attention from the research community. The existing studies of mechanical systems target improved design and configuration and have largely focused on frictional energy loss. In 2003, van der Woude evaluated a rolling-resistance measurement technique that measured the force required to push (via handlebars) different wheelchairs at various constant speeds over multiple surface types (Thacker & Foraiati, 1991; van der Woude, Geurts, Winkelman, & Veeger,

2003). Alternatively, Frank and Abel investigated the impact of caster size and shape on caster rolling resistance (Frank & Abel, 1989). Within the same study, they also measured the scrub resistance of different casters by loading individual casters on a turntable and measuring the requisite torque to rotate the platform. In a 1989 study by Gordon, multiple performance characteristics of different wheelchair drive wheels were assessed, including rolling resistance, static friction, and spring rate (Gordon, Kauzlarich, & Thacker, 1989). In 2002, roll-down tests by Sawatzky compared the rolling resistance of a lightweight manual wheelchair when fitted with five different sets of drive wheels (Sawatzky, Denison, & Kim, 2002). While the findings of these studies do further the base of knowledge for wheelchair resistive losses, they do not fully translate to clinically-useful knowledge because they are largely limited to component-level tests and omit the complex interactions that take place between wheelchair components at a systems level during active propulsion.

System-level dynamic wheelchair models would offer the ability to analytically investigate how different components and designs influence performance. The prevalence of dynamic models for mechanical systems is a testament to their value as analytical tools. In the automotive industry, vehicle dynamics are modeled in order to optimize suspension systems, chassis form, and various other design factors that determine performance (Ellis, 1969). Bicycle models have also been implemented for design optimization, as well as to investigate lateral stability (Franke, Suhr, & Rieß, 1990). Similar models have been developed by the wheelchair community, but these are either limited or lack sufficient empirical validation. Multiple models for characterizing the rolling resistance of drive wheels have been developed, with Kauzlarich presenting the hysteresis loss model for solid-filled tires (J. J. Kauzlarich & J. Thacker, 1985) and Sauret defining a simplified

model where only system mass, wheel mass, wheel radius, and the fore-aft distance between the theoretical and actual tire centers of pressure are required (Sauret et al., 2012). System-level wheelchair models have been developed in two separate studies by Cooper and Chenier, but the former is a model limited to straight motion (Cooper, 1990), while the latter lacks accurate modeling of kinetics by assuming all system rolling resistance is attributed to the caster wheels (Chénier, Bigras, & Aissaoui, 2011). In 1985, Johnson and Aylor did develop a substantial dynamic model for controlling an electric wheelchair that was mechanically similar to modern manual wheelchairs, encompassing the power transmission dynamics from the motor to the drive wheels and all of the potential resistive forces that may act at the wheel-surface interfaces (Johnson & Aylor, 1985). However, the resistive forces included in this model were largely estimated without empirical measurements, and model validation was only conducted for straight maneuvers with the casters angled at different initial headings. The lack of model validation for the Johnson and Aylor study was likely a result of limited system controllability and repeatability, indicating the need for a controllable precision propulsion system that could drive the wheelchair through a wide range of maneuvers to validate the wheelchair dynamic model.

1.3 Research Aims

Based on the reviewed literature, we can conclude that manual wheelchair research can greatly benefit from the two following advancements: 1) a standardized and higher resolution benchmark for wheelchair performance, and 2) models based on empirical testing that inform manufacturers how to optimize the design of MWC components. For this purpose, a wheelchair-propelling robot (Liles, Huang, Caspall, & Sprigle, 2014) has been developed to permit highly repeatable measurements and a larger volume of collected

trials than possible with human subjects. While the use of this robot excludes the human biomechanics from wheelchair propulsion, it is not different from modern test methods that characterize the *mechanical* performance of a system independent of the user. Coupling this system-level testbed with empirical models further represent a novel and synergistic approach to the study of MWC performance. The basis of these models are centered on the energy conservation equation defining MWC propulsion work (**Equation 1**), assuming it is traveling over a level surface.

$$W_{in} = \Delta KE + E_{loss} \quad (1)$$

In this equation, W_{in} is the input propulsion work, KE is the system kinetic energy, and E_{loss} is the resistive energy loss. The stored energy represented by KE is a function of the inertial properties of the wheelchair components, while the dissipated work, E_{loss} , is dependent on the resistive/frictional forces associated with each component. Furthermore, both types of work are dependent on the motion of each wheelchair component. This relationship illustrates that propulsion work is a function of the wheelchair's inertial and frictional parameters, as well as the type of maneuver performed.

The work of this dissertation can be summarized into the three following research aims.

1. **Develop component-level test methods to evaluate the inertial and resistive properties of manual wheelchair components.**

Under this aim, we seek to design component-level test methods with motivation from theoretical models of MWC kinetic energy and resistive energy loss. For the test methods that show precedent in the current literature, we will attempt to simplify and refine

the existing methods. Fulfilling this aim will offer manufacturers a series of tools for comparing the ex-situ energy consumption of various wheelchair components.

2. Develop a system-level test method to distinguish the mechanical performance of various manual wheelchair configurations across maneuvers representative of everyday wheelchair mobility.

Prior human-based approaches have demonstrated their lack of measurement resolution when attempting to distinguish MWC configurations. Furthermore, the maneuvers are largely constrained to linear motion, effectively neglecting the impact of turning on everyday MWC mobility. Previous mechanical system-level experiments are also largely constrained to linear motion, and their measurements of passive motion may not translate accurately to active propulsion. Fulfilling this aim would offer a reliable method and metric by which clinicians and manufacturers can define mechanical MWC performance.

3. Develop empirical models to relate component-level measures to system-level results.

The system-level test method, while a better measure of in-situ performance, is likely to be much more instrumentation-intensive than the component-level test methods. Thus, fulfilling this third aim will create an opportunity for manufacturers to key off of the simpler component-level tests to estimate the system-level MWC performance. By improving accessibility to this information, manufacturers will be empowered to better optimize their MWC designs.

CHAPTER 2. COMPONENT-LEVEL TEST METHODS

Like with any other mechanical system, the components that a MWC is comprised of determine its mechanical performance. The composite mass and inertia of the components dictate the difficulty with which the MWC system can accelerate, and resistive losses due to frame flexion and vibrations can lead to increased propulsion effort during the non-braking phase of maneuvers. For this study, the components that were selected for characterizing their inertial and resistive properties are the MWC drive wheels (rear wheels) and casters (front wheels). This decision was motivated by the general notion that the tires in most wheel-based system are usually the strongest determinants of that system's performance, and MWC especially so. Unlike automobiles, the typical MWC relies solely on human-applied forces to navigate, thus rendering propulsion efficiency a predominantly biomechanics-dependent variable. When compared to other human-propelled vehicles such as the bicycle, the MWC is distinct in its significantly lower range of operating velocities (Sonnenblum SE et al., 2012b), which diminish its sensitivity to vibrational loss and air drag. Experimental and modeling wheelchair literature lend support that drag and bearing loss contributions can be considered negligible (Hofstad & Patterson, 1994), which leaves casters and drive wheels as the predominant sources of loss for MWCs. The component-level tests for the drive wheels and casters will be divided into the assessment of their properties of inertia and resistive loss. Furthermore, the inertial properties will be divided into measurement of component mass and moment of inertia, while the resistive loss properties will be divided into rolling resistance force and scrub torque.

2.1 Component Diversity

A diverse set of casters and drive wheels were selected for component testing. This wide variety enabled us to capture a better representation of the variance in commercial wheelchair components. Additionally, being able to test components of various size and shape demonstrates the robust capabilities of the developed measurement methods. This will describe the dimensions, shape, and tire hardness of the selected casters and drive wheels, as well as the different loading conditions and surface types they were tested across for evaluating their resistive loss properties.




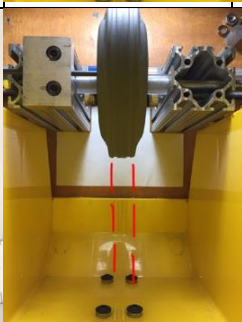




Figure 1. Durometer measurement of tire hardness

Each wheelchair caster and drive wheel were acquired brand new for the purpose of component testing, and were assumed to be a representative sample for that entire component type. The unloaded diameter of each caster and drive wheel were measured via ruler and their tire thicknesses were measured via caliper. A digital scale was used to measure the mass of each drive wheel and caster. In lieu of tire stiffness, tire hardness was measured using a Type A durometer as demonstrated in **Figure 1**. To mitigate the impact of tire surface non-homogeneity, three hardness readings were taken for each wheel, and


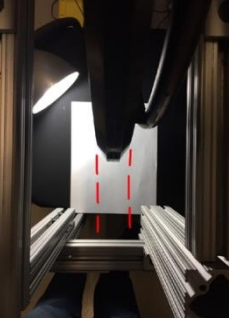



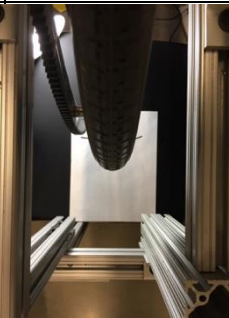

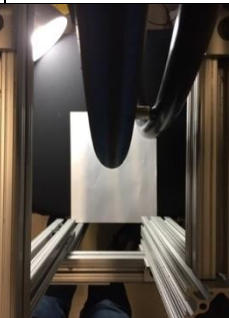
the resultant average recorded as the representative tire hardness. All measurements of pneumatic casters and wheels were taken with their inner tubes inflated to the recommended pressure. The comprehensive properties of each caster and drive wheel are described in **Table 1** and **Table 2**, respectively.

Table 1. Caster Wheel Properties

| Caster Wheel (Hub View) | Caster Wheel (Profile View) | Name | Diameter [cm] | Tire width [cm] | Mass [kg] | Tire Hardness |
|---|---|--|---------------|-----------------|-----------|---------------|
|  |  | 4 x 1.5" Frog Legs Soft Roll (FLSR) | 10.6 | 3.60 | 0.22 | 76 |
|  |  | 5 x 1.5" Primo Soft Roll (SR) | 12.6 | 2.18 | 0.39 | 65 |
|  |  | 5 x 1" Primo | 12.4 | 2.43 | 0.22 | 85 |

| | | | | | | |
|---|---|---|------|------|------|----|
|  |  | 6 x 1" Primo Pneumatic (35 psi inflation) | 15.1 | 2.79 | 0.26 | 60 |
|  |  | 6 x 1.5" Primo | 14.7 | 3.69 | 0.33 | 89 |
|  |  | 6 x 1" Primo | 14.4 | 2.58 | 0.30 | 89 |
|  |  | 3 x 1" Frog Legs Narrow Court (FLNC) | 7.6 | 2.45 | 0.12 | 88 |
|  |  | 6 x 1" Frog Legs Narrow Court (FLNC) | 15.2 | 2.45 | 0.31 | 89 |

Table 2. Drive Wheel Properties

| Drive Wheel (Hub View) | Drive Wheel (Profile View) | Name | Diameter [cm] | Tire width [cm] | Mass [kg] | Tire Hardness |
|---|---|--|------------------|--------------------|--------------|------------------|
|  |  | 24 x 1'' Solid Mag | 62 | 2.75 | 2.07 | 82 |
|  |  | 24 x 1'' Spinerdy (100 psi inflation) | 60 | 2.65 | 1.71 | 49 |
|  |  | 24 x 1-3/8'' Primo Orion Stock Pneumatic (75 psi inflation) | 62 | 3.28 | 1.86 | 67 |
|  |  | 24 x 1'' Schwalbe Right Run (100 psi inflation) | 60 | 2.85 | 1.82 | N/A |

The ranges and medians of each wheel property, separated by casters and drive wheels, is given in **Table 3**. Based on the statistics, the casters are quite diverse in their diameter and mass, while their tire width tends towards the lower end of the range and their hardness

tends towards the higher end of the range. The drive wheels do not appear to vary much in both diameter and mass, but present a moderate diversity in both tire width and hardness, with the tire width tending towards the lower end of the range. The wheel profile outlines in **Figure 2** further serve to illustrate the diversity of the shapes and sizes of the tested components.

Table 3. Summary of Component Properties

| Wheel Property | <i>Casters (8 total)</i> | | <i>Drive Wheels (4 total)</i> | |
|-----------------|--------------------------|--------|-------------------------------|--------|
| | Range | Median | Range | Median |
| Diameter [cm] | 7.6 – 15.2 | 13.5 | 60 – 62 | 60 |
| Tire Width [cm] | 2.18 – 3.69 | 2.52 | 2.65 – 3.28 | 2.85 |
| Mass [kg] | 0.12 – 0.39 | 0.28 | 1.71 – 1.86 | 1.82 |
| Hardness | 60 – 89 | 86.5 | 49 – 67 | 58 |

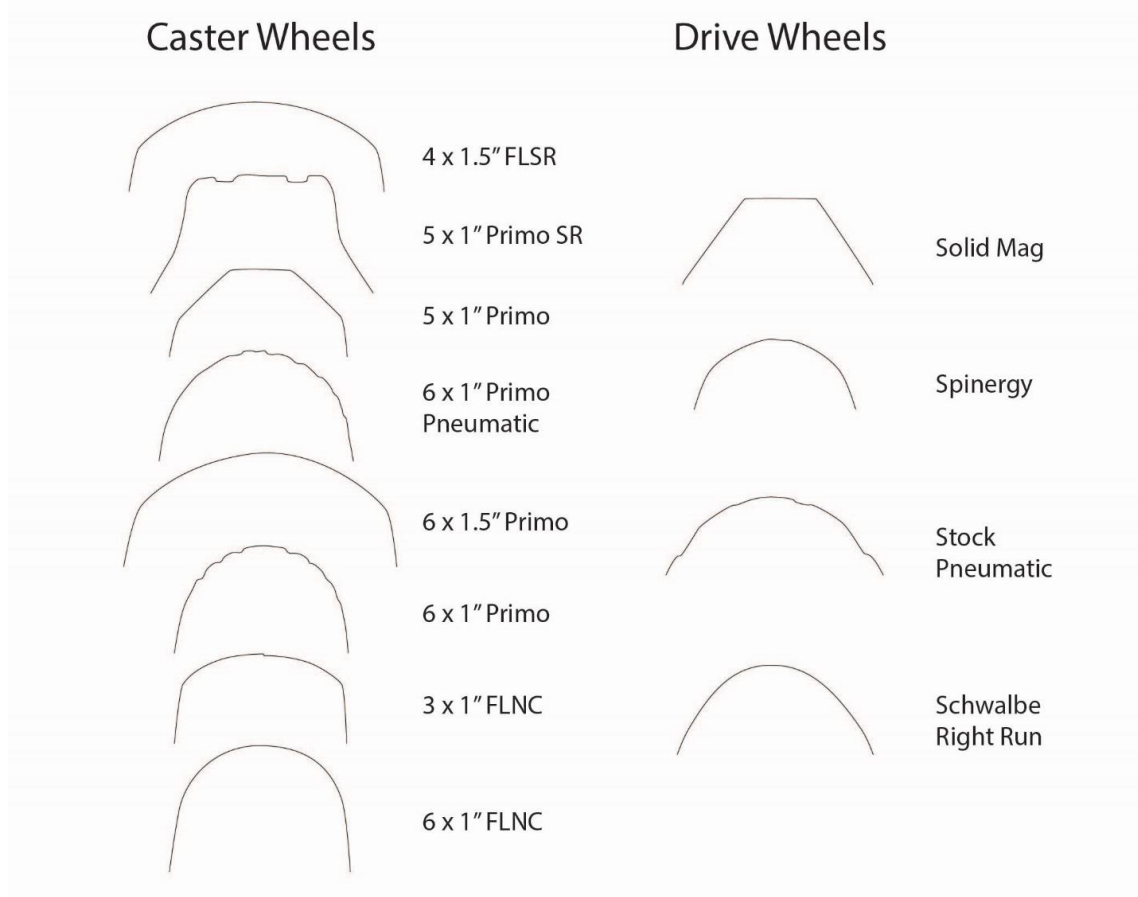


Figure 2. Component Tire Profile Outlines

The loading conditions applied to the casters and drive wheels for measurements of rolling resistance force and scrub torque were based on the framework of an idealized MWC at three distinct weight distributions. The total mass of the loaded MWC was defined as 100 kg and configuration weight distributions were identified as 60%, 70%, and 80% load on the drive (rear) wheels. Thus, this equated to the casters and drive wheels each being loaded at their three representative configuration loads during the resistive loss component tests. **Table 4** defines these loading values and their corresponding wheels and configurations.

Table 4. Component Loadings by Representative System Weight-Distribution

| Percent Load on Drive Wheels (Total Load = 100 kg) | Normal Load on Each Caster | Normal Load on Each Drive Wheel |
|---|-----------------------------------|--|
| 60% | 20 kg | 30 kg |
| 70% | 15 kg | 35 kg |
| 80% | 10 kg | 40 kg |

The surfaces types on which the component resistive losses were measured are linoleum tile and low-pile carpet. Since test surfaces have to accommodate both extractable samples and sufficient space for corresponding systems-level MWC testing, the tile material was sourced from the old Rehabilitation Engineering and Applied Research lab space, which was assessed to have sufficient room to accommodate a systems-level MWC test track. Given its comparative ease of installation and removal, the carpet was sourced from Home Depot in a large enough roll to provide a systems-level MWC test track. **Figure 3** depicts a sample of each surface type.

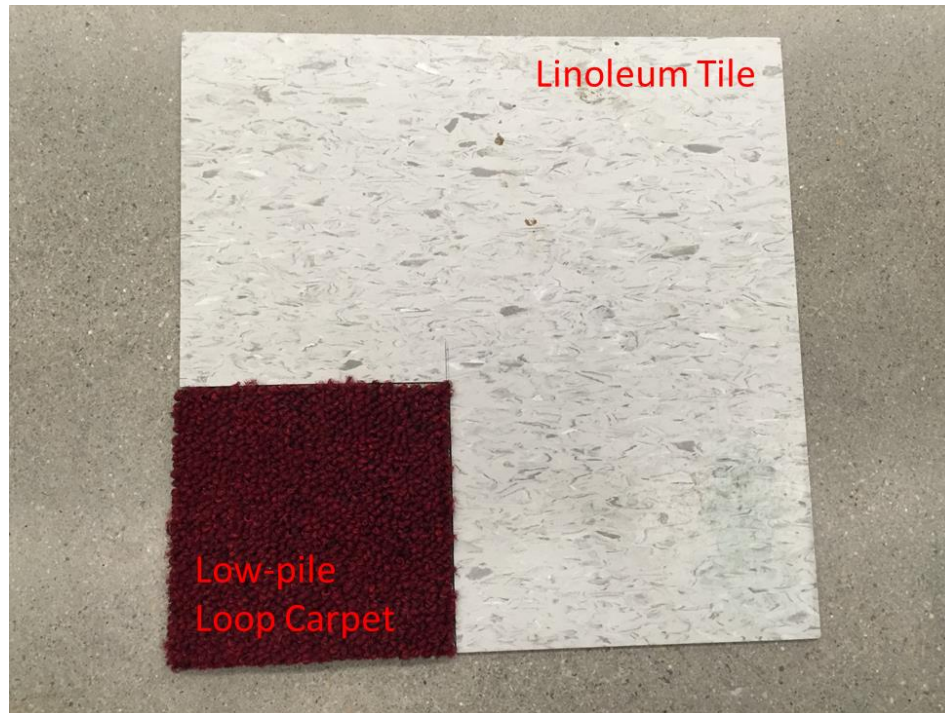


Figure 3. Samples of Test Surfaces

2.2 Predicate Work (Trifilar Pendulum)

The inertia and mass of the wheelchair system's components contribute to the total propulsion work that is stored as mechanical energy. While the mass of these components can be easily evaluated, the rotational inertias are not. Due to the irregular shape and non-homogenous density of the wheelchair system components, it is necessary to empirically measure the wheelchair constants mass and moment of inertia. An instrument well-documented in literature, the trifilar pendulum (Du Bois JL, Lieven NA, & Adhikari S, 2009; Hou ZC, Lu Y, Lao Y, & Liu D, 2009; Ringegni, Actis, & Patanella, 2001), was employed to measure the moment of inertias of the various drive wheels and casters used within this study. The trifilar pendulum is comprised of two equilateral Dibond triangles connected by their corners via steel wires. One of the triangles are fixed to the ceiling,

leaving the second one to be suspended in the air via the aforementioned steel wires, with both triangles adjusted to be perpendicular to gravity via a level. When the bottom triangle is perturbed such that it oscillates about its yaw axis without translation, it presents the behavior of a simple damped harmonic system. The operating principal of this device is that the moment of inertia of the bottom triangle is a function of its mass and period of rotation, specifically described as

$$I = \frac{mgR^2T^2}{4\pi^2L} \quad (2)$$

where I is the moment of inertia of the bottom triangle, m is the mass of the bottom triangle, g is gravitational acceleration, R is the distance from the triangle center to a triangle corner, L is the wire length connecting the two triangles, and T is the period of yaw rotation. This relationship remains true when a wheelchair component such as a drive wheel (**Figure 4**) is placed atop the bottom triangle, except now m and I represent the combined component and platform mass and moment of the inertia, respectively. Note that the component being



Figure 4. Drive Wheel Rotational Inertia Measurement by Trifilar Pendulum

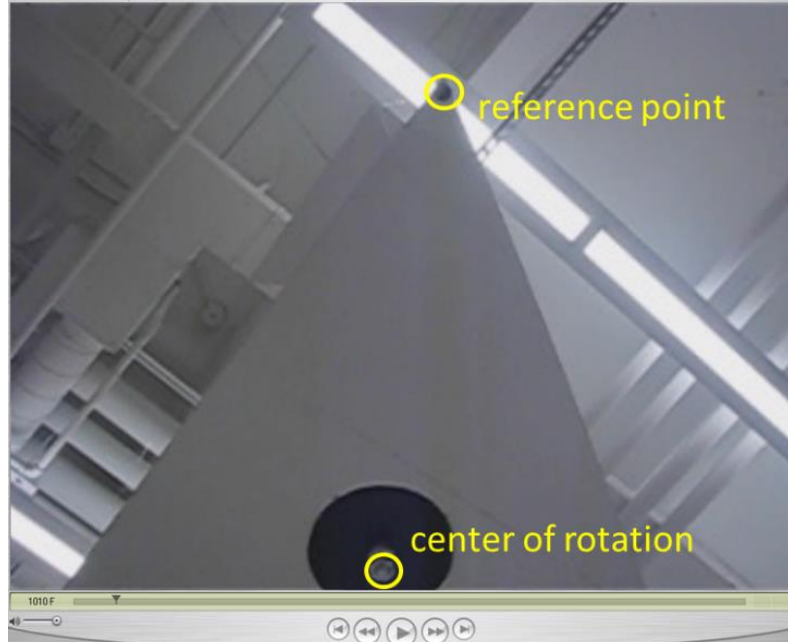


Figure 5. Screenshot of Frame Counting for Cycle Period

tested must be centered on its rotational/yaw axis, and cannot be allowed to rotate as the platform oscillates. The mass of the component is measured via a digital scale and the length dimensions are measured with a ruler and tape measure. The period of oscillation is derived from a video recording of the bottom of the platform (**Figure 5**) using a camera of known frame rate (60 fps). By tracking one of the triangle corners as a reference point, it is possible to manually count the number of frames (in QuickTime Player) it takes for the reference point to oscillate 50 cycles; converting these frames to time and dividing by the number of cycles results in the period, T . Using this method also allows the experimenter to confirm that there is minimal translational motion of the platform's center of rotation.

In addition to the drive wheels (**Figure 5**) and casters (**Figure 6**) rotational inertias being assessed on the trifilar pendulum, the yaw inertias of the casters-and-fork assemblies (**Figure 6**) were characterized to account for the swivel kinematics presented in wheelchair

maneuvers. These methods were adopted for this study to characterize the moment of inertias of 8 casters and 6 drive wheels, which will be detailed in the results section of this chapter.

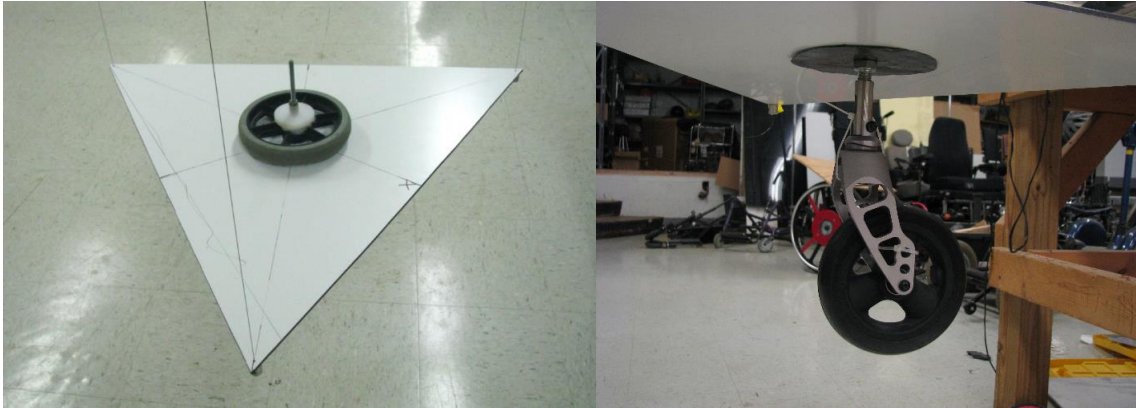


Figure 6. Caster Rotational Inertia and Caster-and-Fork Yaw Inertia Measurement

2.3 Development of Coast-down Method

The rolling resistance of the caster and drive wheels were assessed utilizing a coast-down cart method. Prior approaches documented in literature include the “rolling” of a two-wheel cart over a treadmill/roller while forces are measured on the un-wheeled end (Frank & Abel, 1989). This methodology minimizes the need for four identical wheels and measures the rolling resistance forces directly. Utilizing this method, however, greatly limits the surfaces that can be evaluated given the constraints of what can be applied to a treadmill/roller surface. Over-ground methods, on the other hand, rely on measuring or inferring the deceleration rate of a rolling, four-wheel cart on the surface of interest. Conventionally, this is approached in one of two ways: 1) controlling the release velocity and measuring the cart travel distance, or 2) measuring the change in velocity during a

distance/period of the cart's travel. The former approach usually requires a curved ramp that allows the cart to be released with a fixed potential energy and a smooth ramp-to-surface transition, as well as needing a sufficiently large space for the cart to complete its travel (Frank & Abel, 1989). The second approach is much less constrained by space, but typically requires a series of break-beam sensors to evaluate a series of discrete time-position data points for the cart (Hoffman, Millet, Hoch, & Candau, 2003). An instrumented drive wheel (SmartWheel) popularly used in studies of wheelchair propulsion biomechanics (Cowan, Boninger, Sawatzky, Mazoyer, & Cooper, 2008; Hurd, Morrow, Kaufman, & An, 2009) could potentially be used to measure the cart deceleration as a function of wheel rotation rate. However, the use of an instrumented wheel is not only expensive, but also bases all rolling resistance measures on the properties of that particular drive wheel. In most of these existing over-ground rolling resistance measurement methods, the manual wheelchair itself has been used as the "cart", which means these system-level rolling resistances do not allow for the impact of casters and drive wheels to be differentiated.

2.3.1 System Design and Rationale

The coast-down cart method devised in this study improves upon all facets of the existing rolling resistance measurement methods: 1) the cart is adaptable use for both casters and drives wheels, 2) the instrumentation does not impact the component inertias and resistive forces, 3) the cart can be used on any surface, 4) there are comparatively minimal space requirements, and 5) only two "test" wheels are needed. These enhancements are a result of three particular design features in the coast-down cart methodology: multi-axle mounts, wheel "encoders", and "control" cart wheels.

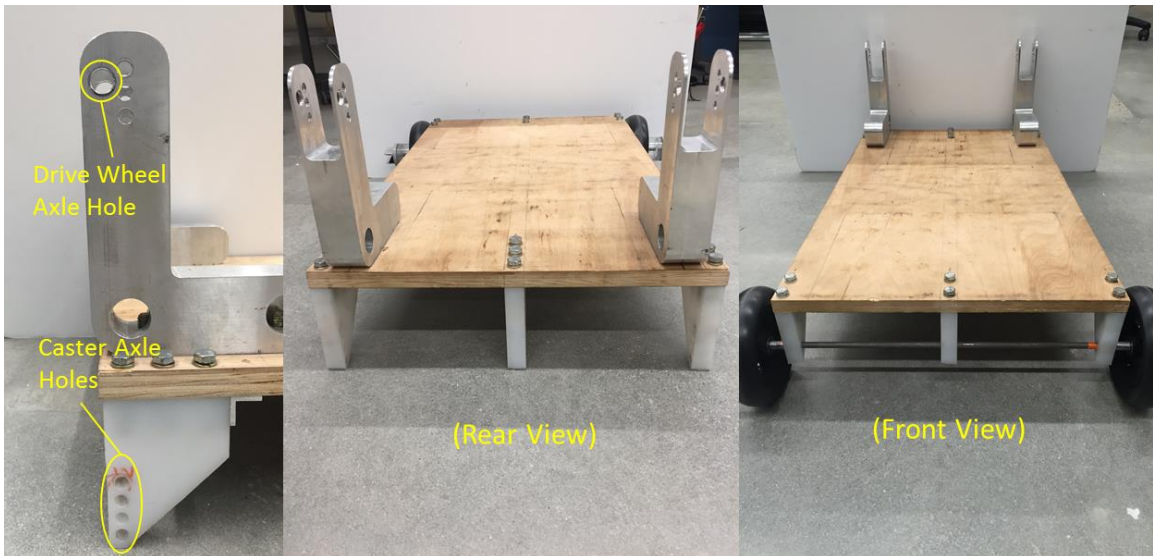


Figure 7. Coast-down Cart Frame Design

The body of the coast-down cart was constructed with a 41 cm x 71 cm sheet of plywood, with a 3/4" thickness to support loads upwards of 100 kg. The front axle mounts were designed to only accommodate the “control” wheels (6"x 1.5" Primo casters), and thus required a single mounting hole. These wheels are always mounted to the cart for reasons that will be described later in this section. The rear axle mounts however, were designed for mounting the “test” wheels, and thus meant to accommodate both drive wheels and various sizes of casters. The height of these axle holes were cut such that when a set of “test” wheels were mounted, the angle of cart surface formed with the floor surface never exceeded 2 degrees, meaning that the intended normal loads on the cart were impacted by less than 0.1%. The drive wheel axle hole was designed for nominal 24"-diameter drive wheels, while the caster axle holes could fit casters with diameters of 3", 4", 5", or 6". Furthermore, the hole and axle sizes were selected based on the common bearing diameter of the drive wheels (1/2") and casters (5/16") used in this experiment.

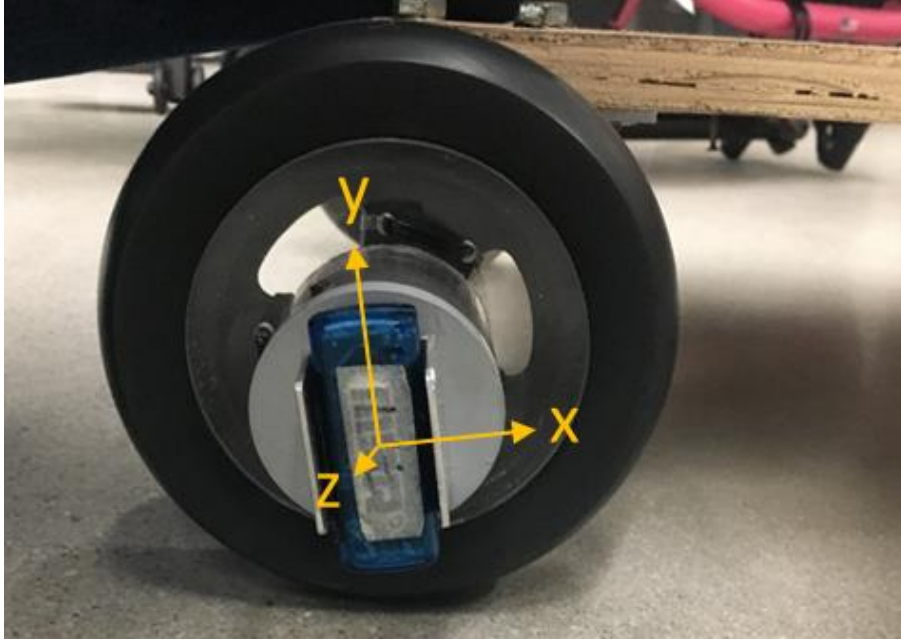


Figure 8. Accelerometer Mounted on "Control" Wheel

The “encoders” used on the coast-down cart are simply a pair of time-synchronized 3-axis accelerometers (MSR Electronics) that are mounted to the face of the “control” wheels. Each accelerometer is set to sample at the maximum rate of 51.2 Hz. Given that the coast-down decelerations are significantly smaller than that of gravitational acceleration (5% or less), the accelerometers can be used reliably as angular encoders by tracking the angle their intrinsic coordinate axes form with the direction of gravitational acceleration. More specifically, the equation describing this can be written as:

$$= \begin{cases} 2\arctan\left(\frac{a_y}{\sqrt{a_x^2 + a_y^2} + a_x}\right) & \text{if } a_x > 0 \text{ or } a_y \neq 0, \\ \pi & \text{if } a_x < 0 \text{ and } a_y = 0, \\ \text{undefined} & \text{if } a_x = 0 \text{ and } a_y = 0. \end{cases} \quad (3)$$

where ϕ is the angle the accelerometer x-axis forms with the direction of gravity, a_x is the acceleration measured along the accelerometer x-axis, and a_y is the acceleration measured

along the accelerometer y-axis. This calculation is employed in a MATLAB script as the “atan2” function, which calculates this four-quadrant inverse tangent. Taking the time-derivative of ϕ results in that “control” wheel’s angular velocity.

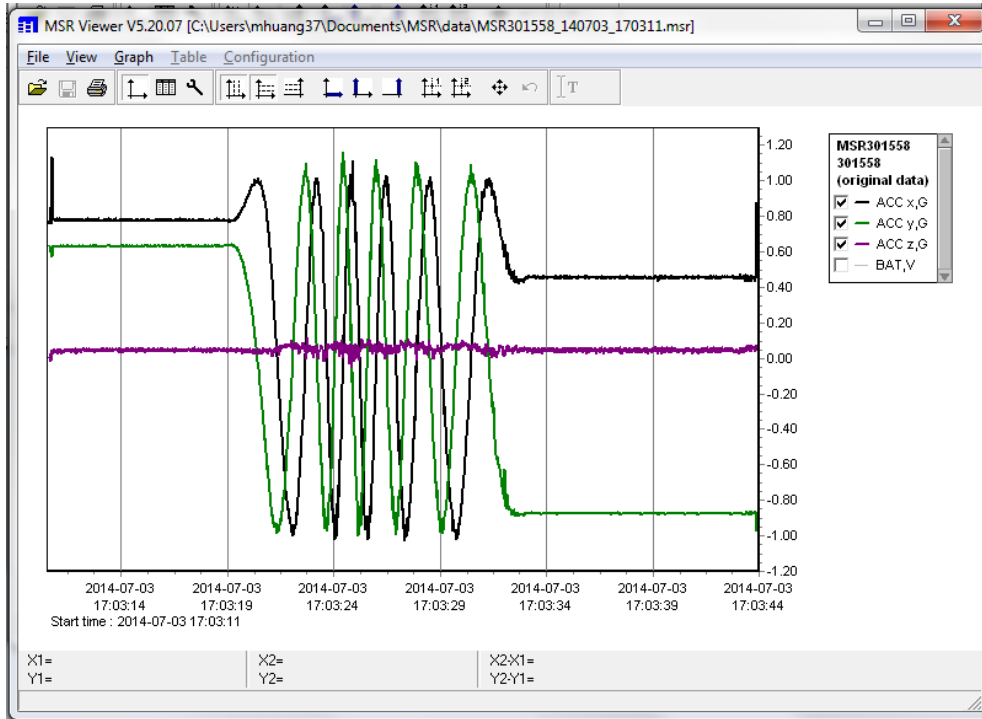


Figure 9. Accelerometer Sample Data

The **Figure 8** depicts how the accelerometer is mounted onto the “control” wheel and **Figure 9** shows a sample reading of one of the sensors following a few revolutions of the “control” wheel. Using this measurement method, one can see that a higher frequency measurement equates to higher rotational velocities. The wheel angular velocity derived from these accelerometers are then coupled with dimensional measurements of the cart and “control” wheels to determine the velocity of the center of mass. **Figure 10** illustrates the dimensions for **Equations 4 - 6** that define the velocity of the cart at the center of the front axle, the cart yaw rate, and the velocity of the cart at the center of mass, respectively.

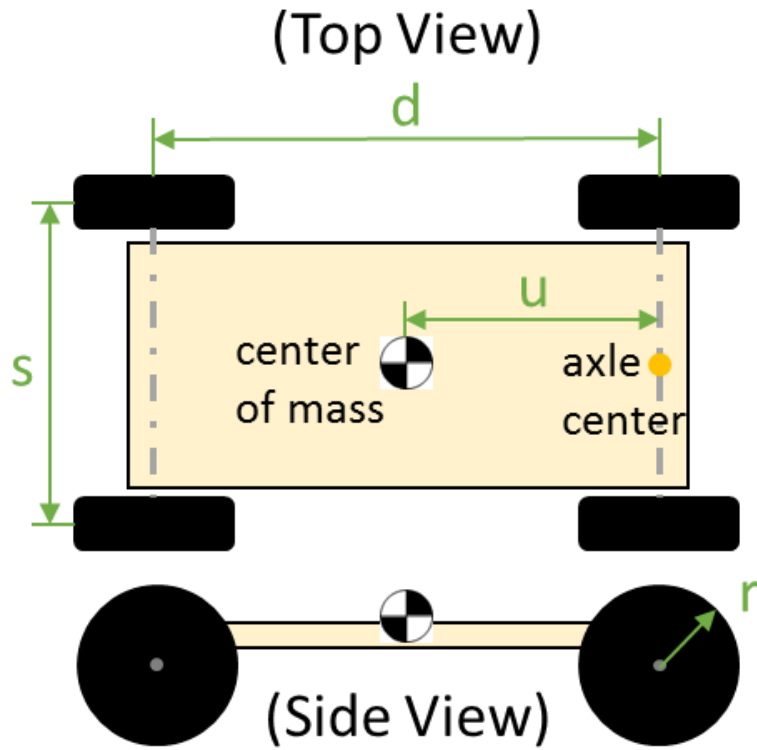


Figure 10. Coast-down Cart Dimensional Variables

$$v_{AC} = r \left(\frac{\dot{\phi}_L + \dot{\phi}_R}{2} \right) \quad (4)$$

$$\dot{\psi} = r \left(\frac{\dot{\phi}_R - \dot{\phi}_L}{s} \right) \quad (5)$$

$$v_{COM} = \sqrt{v_{AC}^2 + (u\dot{\psi})^2} \quad (6)$$

The v_{AC} is the cart front axle center velocity, $\dot{\psi}$ is the cart yaw (turning) rate, v_{COM} is the cart center of mass velocity, r is the “control” (front) wheel radii, s is the lateral

wheel base of the “control” wheels, $\dot{\phi}_L$ and $\dot{\phi}_R$ are the left and right “control” wheel angular velocities, and u is the distance from the front axle to the center of mass.

Utilizing a MATLAB code to implement **Equations 4 - 6**, both v_{AC} and v_{COM} are calculated. A velocity window of 0.95 m/s to 0.65 m/s – defined based on wheelchair user propulsion speeds (Sonenblum SE et al., 2012b) – is applied to parse out a segment of the coast-down velocity, as shown in **Figure 11** (0.95 m/s green line; 0.65 m/s red line). A linear regression is fit to this segment and the slope of the line is taken as the average deceleration rate. For a typical coast-down test, the manually pushed release speed (peak velocity) is controlled to be within the ranges of 1.0-1.2 m/s, all while maintaining the same point of release. While it has been previously established that wheelchair deceleration rate is not a function of velocity (Bascou, Sauret, Villa, Lavaste, & Pillet, 2015; Lin, Huang, & Sprigle, 2015), we have secondary reasons for controlling the release velocity. The minimum bound of this release speed ensured the desired window of analysis was captured. The maximum bound was enforced for spatial constraints, as well as to ensure the coast-

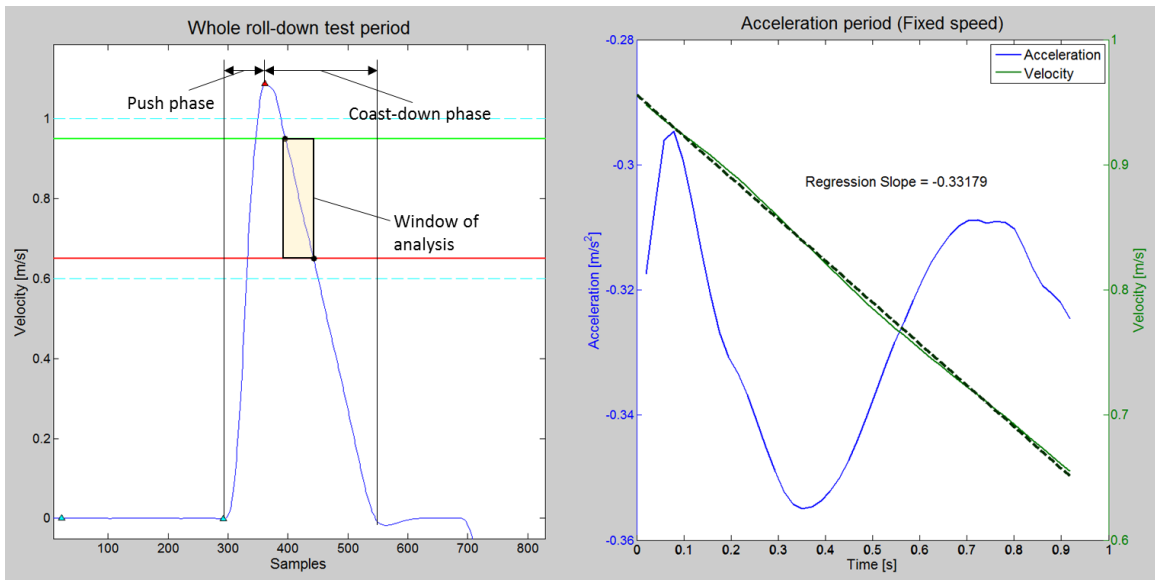


Figure 11. Velocity Profile of Single Coast-down

down phase took place over a consistent stretch of surface, diminishing the impact of surface irregularities.

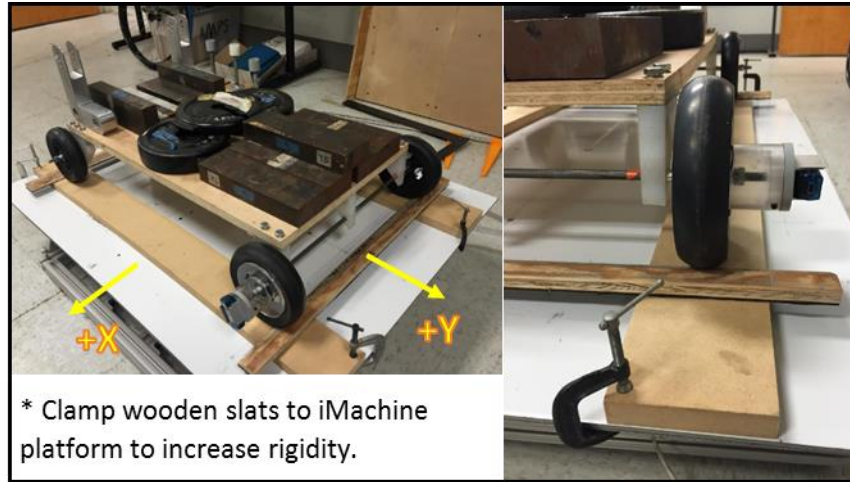


Figure 12. Coast-down Cart on iMachine

Taking a step back, we should note that v_{COM} is a function of u (distance from front axle to center of mass), which, unlike the wheelbase, is not a fixed physical dimension of the cart that can be directly measured. To evaluate the COM position, we placed the cart on the iMachine (Eicholtz, Caspall, Dao, Sprigle, & Ferri, 2012), an in-house device that can measure the mass and horizontal center of gravity of large bodies, as shown in **Figure 12**. As per iMachine protocol, the cart was adjusted via feedback from the iMachine’s visual interface until the cart COM coincided with the origin of the platform coordinates. Measuring the front axle position along the y -axis in this configuration yields u . It is important to point out here that r , the “control” wheel radius, is a function of u . This arises from the fact that u can be used to calculate the fore-aft weight distribution of the cart, which impacts the load on the “control” wheels, and thus the wheel radius. To calculate the fore-aft weight distribution, we refer to the free body diagram in **Figure 13** and take moments about A, the point of contact between the “control” (front) wheels and the surface.

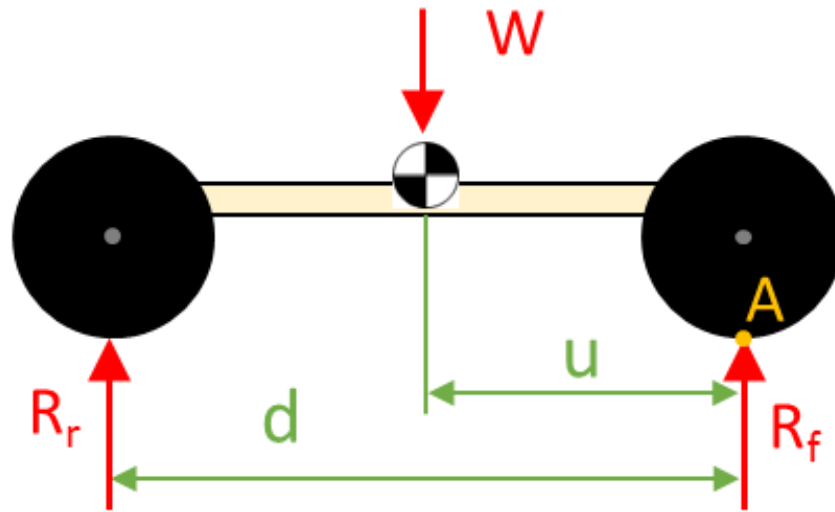


Figure 13. Cart Free-body Diagram

Combining like terms yields **Equation 7**,

$$R_r = W \left(\frac{u}{d} \right) \quad (7)$$

where R_r is the reaction force of the “test” (rear) wheels, W is the total load (including cart weight), u is the horizontal distance from the front axle to the center of mass, and d is the horizontal distance from the front axle to rear axle. Since the total reaction forces equate to the total load, the load on the front wheels can be defined by **Equation 8** as

$$R_f = W \left(1 - \frac{u}{d} \right) \quad (8)$$

Once the load on the “control” (front) wheels have been established, one can measure its corresponding loaded radius. This measurement is taken via a standing caliper that measures the height of the cart top (**Figure 14**). Subtracting this height by the fixed vertical

distance from the cart top to the axle center yields the loaded “control” wheel radius. This loaded radius estimates the active radius of the “control” wheels during coast-downs.



Figure 14. Measurement of "Control" Wheel Loaded Radius

Having described all of the parameters and methods necessary to evaluate the cart’s coast-down deceleration, the final step is to translate this deceleration rate into rolling resistance force. The utility of the “control” wheels allows for the rolling resistance forces of the “test” wheels to be isolated. By loading a cart fitted with four identical “control” wheels such that there is 50-50 fore-aft weight distribution and lateral load symmetry, the rolling resistance force of a single “control” wheel can be described by **Equation 9**

$$(F_{RR})_c = \frac{Ma_{COM}}{4} \quad (9)$$

where $(F_{RR})_c$ is the rolling resistance force of a single “control” wheel, M is the total mass of the loaded cart system, and a_{COM} is the deceleration of the cart center of mass as

measured by coast-down. By pairing this rolling resistance force with cart configurations that have the same $\frac{M}{4}$ load on each “control” (front) wheel, the equation for the rolling resistance force on the “test” (rear) wheels can be defined by **Equation 10**

$$(F_{RR})_t = \frac{Ma_{COM} - 2(F_{RR})_c}{2} \quad (10)$$

where $(F_{RR})_t$ is the rolling resistance force of a single “test” wheel.

To apply the previously designated configuration loads to each caster and drive wheel, a total of six cart configurations were defined, three for casters and three for drive wheels. Two cart configurations, both corresponding to the 60% weight distribution on drive wheels for a 100 kg MWC, are depicted in **Figure 15**. **Table 5** further defines each configuration’s cart load, combined “control” wheel load, and combined “test” wheel load.



Figure 15. Cart 60%WD Configurations for Caster and Drive Wheels

Table 5. Cart Weight-distribution Configuration Loads

| Configuration | Cart Total Mass | Combined “Control” Wheel Load | Combined “Test” Wheel Load |
|-----------------------------------|------------------------|--------------------------------------|-----------------------------------|
| 60% Load on DWs (Testing Casters) | 80 kg | 40 kg | 40 kg |
| 60% Load on DWs (Testing Casters) | 60 kg | 30 kg | 30 kg |
| 60% Load on DWs (Testing Casters) | 40 kg | 20 kg | 20 kg |
| 60% Load on DWs (Testing DWs) | 100 kg | 40 kg | 60 kg |
| 60% Load on DWs (Testing DWs) | 100 kg | 30 kg | 70 kg |
| 60% Load on DWs (Testing DWs) | 100 kg | 20 kg | 80 kg |

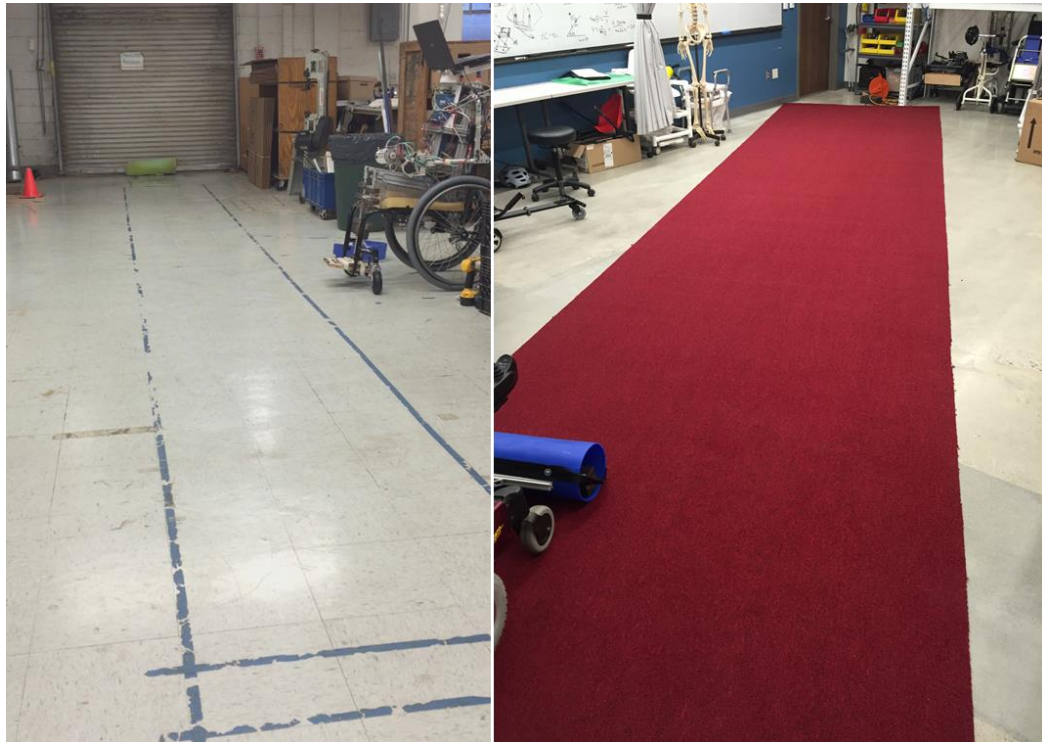


Figure 16. Tile and Carpet Test Tracks

For the specific tile and carpet surfaces utilized in our study, cleaning procedures were followed to ensure a consistent surface condition across all trials. The tile surface

was wiped down with a light cleaner after each set of coast-downs, while the carpet was vacuumed with the same frequency. Since the carpet test surface would normally be stored as a roll between uses, a power wheelchair was used to drive over the carpet after it was initially laid out in order to help the carpet settle into a flat shape. **Figure 16** shows what both test tracks looked like.

2.3.2 *System Validation*

The coast-down cart methodology was validated in both measurement accuracy and test repeatability. The accuracy of the accelerometer-based angular velocity was validated against the angular velocity measured by a digital encoder (US Digital), a device designed for accurate measurement of rotational motion. The impact of cart turning and surface bias on COM deceleration accuracy was investigated, leading to the development of countermeasures. Test repeatability was considered achieved based on the benchmark of a CV (coefficient of variation) $< 10\%$ for deceleration rates measured across 10 repeated trials. CV is simply sample standard deviation divided by sample average. A manual wheelchair was used in a series of nine straight motion coast-down maneuvers to compare the angular velocity data collected via accelerometer and digital encoder. The manual wheelchair data was used because the digital encoders could not be easily retro-fit to the coast-down cart. The setup for the accelerometer versus digital encoder measurement method is shown in **Figure 17**, with the accelerometer mounted on the in-house casing built for the encoder. While it would have been more desirable to mount the accelerometer to the flat face of the encoder to minimize translational accelerations and more closely emulate the setup of the coast-down cart, the encoder signal cable obstructed the rotation of the accelerometer. **Figure 18** illustrates the angular velocity time series as measured by



Figure 17. Accelerometer Mounted on Digital Encoder for Validation Testing

the encoder and accelerometer (MSR). Solely from visual assessment, we can see that the two data sets are very close, with the MSR data presenting a slight negative offset from the encoder data at the peaks. An analytical comparison of data sets' coast-down decelerations resulted in the accelerometer data having an average absolute error of 1.76% with respect to the encoder data; the maximum error observed was 3.75%. These values indicate that the accelerometer measurement error of coast-down deceleration is sufficiently small to be considered an accurate substitute for the digital encoder. Furthermore, the positioning the accelerometers on the coast-down cart is conducive to reducing the errors that arise from translational acceleration due to the off-axis accelerometer positioning during the validation MWC coast-downs.

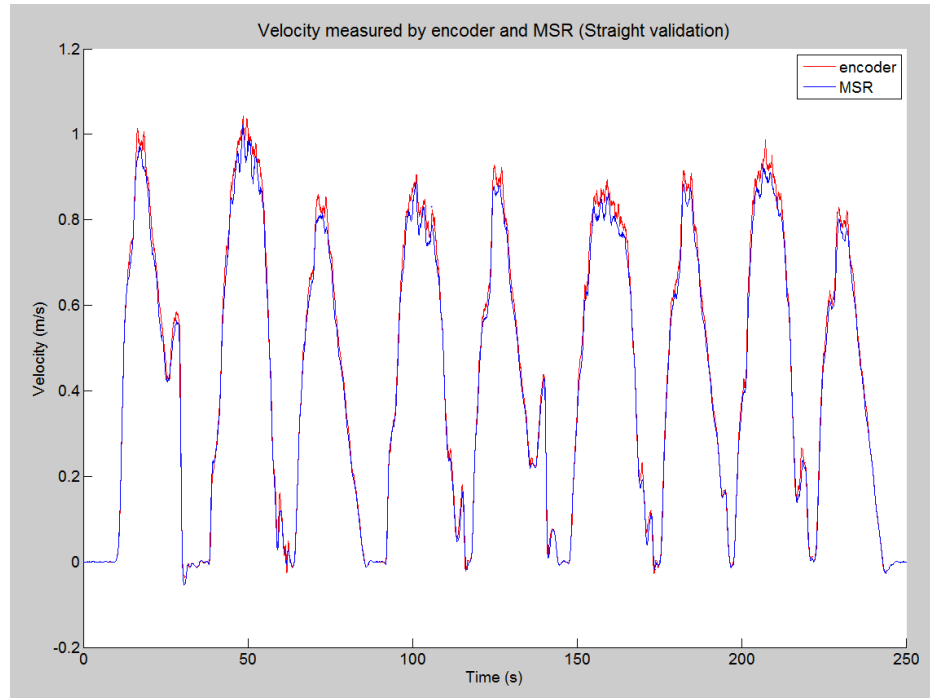


Figure 18. Accelerometer versus Encoder Velocity Measurements

During pilot cart coast-down tests, it was observed that small heading changes of ~ 10 degrees took place from start to stop of rolling. Seeing as the window of analysis (0.95 m/s to 0.65 m/s) only accounts for about 30% of the total displacement, the heading change during the analyzed period would be ~ 3 degrees. To ensure that this did not adversely affect the coast-down analysis, a_{COM} (the cart's COM deceleration) was compared to a_{AC} (the cart's front axle-center deceleration) in every trial for data quality control. All coast-downs were controlled such that the percent difference of a_{COM} with respect to a_{AC} never exceeded 1%. Furthermore, it was noted that coast-downs in two opposing direction would typically result in a difference of 10% or more in the deceleration values. Thus, to capture an accurate representation of rolling resistance over level ground, a designated track space was defined and tests were conducted in both the "forward" and "backward" directions along this track. The resulting deceleration values of the two directions were averaged and used to calculate rolling resistance force.

Test repeatability was characterized for every trial set of coast-downs. For each unique combination of cart load, “test” wheel, surface, and track direction, a series of 15 repeated coast-down trials were performed. From this series, a trial set of 10 were selected based whether their release velocities fell within the 1.0 – 1.2 m/s range, as well as if their linear regressions were good fits to the coast-down velocity curve. Initially, the R^2 value was used to assess the latter, but given that practically all the $R^2 > 0.99$, we opted to use a visual assessment of the plotted data. **Figure 19** illustrates an unacceptable and acceptable coast-down velocity curve. As long as the regression $R^2 > 0.99$ and the velocity regression line is shown to closely hug the velocity data (green), it is classified as an acceptable trial.

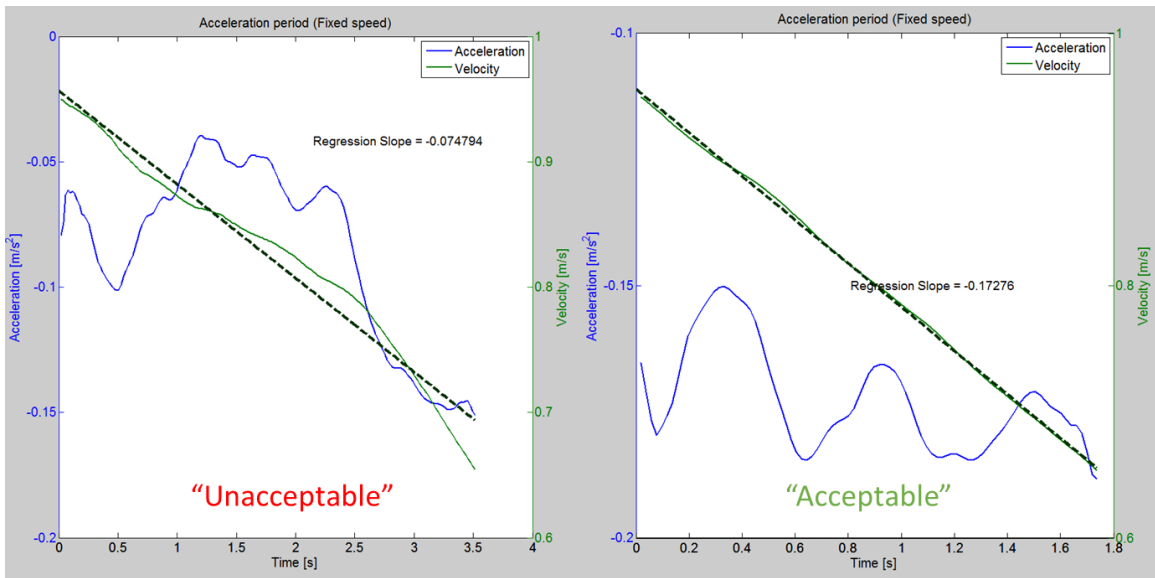


Figure 19. Coast-down Data Selection Criteria

2.4 Development of Wheel Scrub Method

Characterizing the rolling resistance of casters and drive wheels illustrates the resistive losses this components impart on the MWC during purely rectilinear motion. However, this is not reflective of everyday wheelchair mobility where turning maneuvers are ever-present (Sonnenblum SE et al., 2012b). Few studies have ventured to characterize

the turning resistances of maneuver wheelchairs as a system (Bascou et al., 2014; Bascou et al., 2015), and even less have examined the resistive losses of individual MWC components. Frank and Abel examined the resistive losses of casters in terms of their scrub torque, which is the resistance experienced by the wheel when pivoted without rolling (Frank & Abel, 1989). This torque can be likened to the resistance experienced when one dry steers in an automobile. However, as seen in **Figure 20**, the use of manual force via a handle to elicit wheel scrub may produce misleading results due to uncontrolled pulley rotation rates.

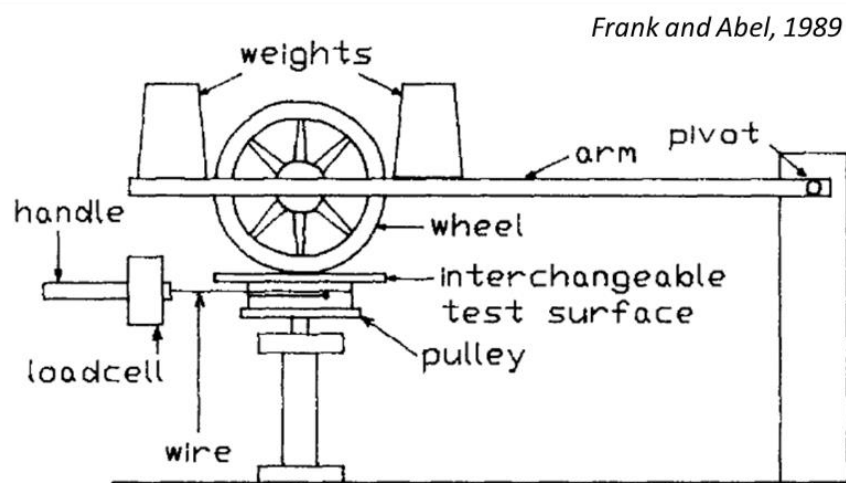


Figure 20. Predicate Measurement Method of Caster Wheel Scrub Torque

A more recent study (Silva, Corrêa, Eckert, Santiciolli, & Dedini, 2017) has taken steps to empirically measure the cornering force present in MWC drive wheels, a resistive force that manifests itself when the MWC undergoes any turns with a non-zero radius of curvature. Usually this involves the wheels simultaneously rolling and turning. For this study, we elected to characterize the scrub torque of the casters and drive wheels instead of their corner force. While measuring cornering forces would better represent curvilinear MWC maneuvers, there was a two-fold rationale for our choice: 1) the scrub torque

represents an upper bound on the turning resistance a component would experience at a given load, and 2) the scrub torque measurement methodology was significantly more simplistic, which is an important factor in the primary goal of making these component tests extendable to industry application.

2.4.1 System Design

The scrub measurement methodology in this study improves upon the existing Frank and Abel approach by defining and controlling consistent scrub (turning) rates representative of everyday wheelchair mobility, as well as implementing a modular design that allows for both casters and drive wheels to be tested on the same platform.

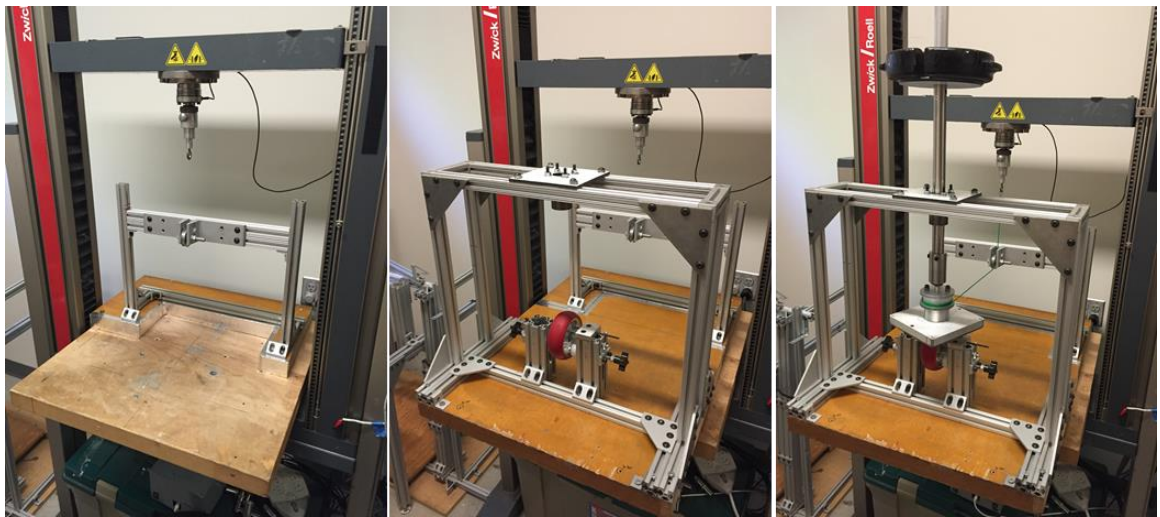


Figure 21. Caster Wheel Scrub Torque Test Rig

The wheel scrub torque measurement test rig operates by applying a normal load to a surface-wheel interface, and then applying pull forces that generate a constant rotation rate of the surface via an attached spool. The relative motion between the test surface and wheel emulates the wheel scrubbing (pivoting) on the test surface. The overall apparatus can be divided into three modular parts: 1) the pull force actuator/sensor, 2) the wheel

mounting structure, and 3) the surface loading post. As seen in **Figure 21**, these three modules are introduced incrementally from left to right. Note that the middle and right image depict the wheel mounting structure used for casters. In **Figure 22**, the wheel mounting structure used for drive wheels is incorporated instead.

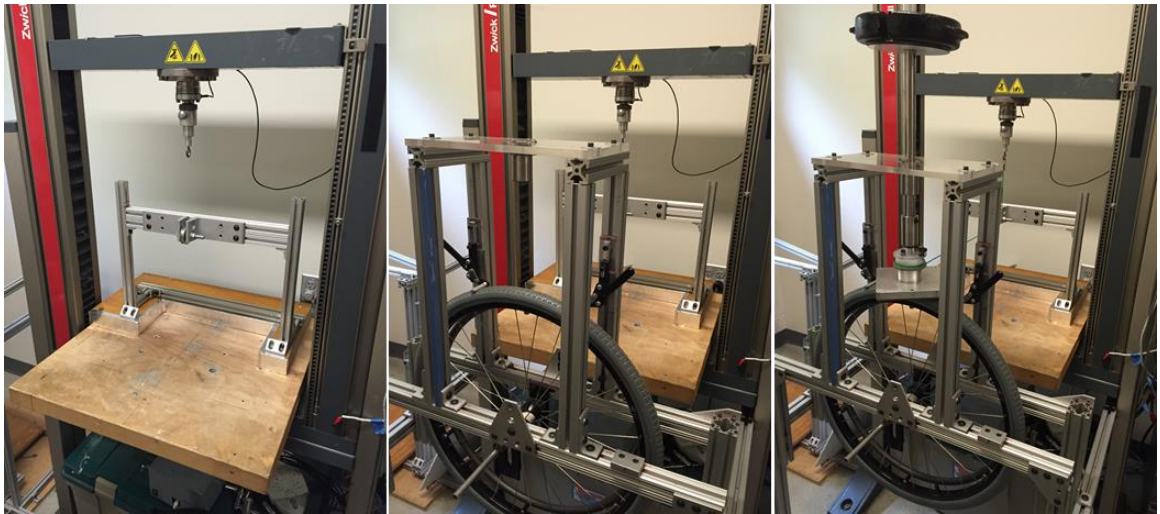


Figure 22. Drive Wheel Scrub Torque Test Rig

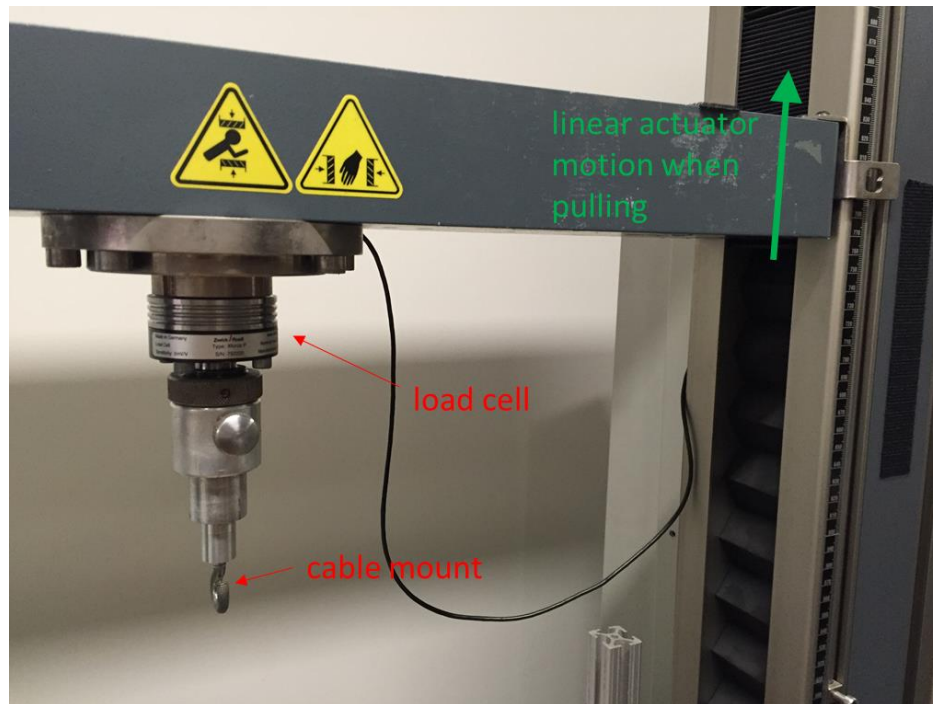


Figure 23. Pull Force Actuator/Sensor

The pull force actuator module incorporates a materials testing system (Zwick) to make use of its linear actuator, load cell, and data acquisition software (testXpert II). The load cell and actuator are pictured in **Figure 23**. A pulley attachment is also part of this module, and is responsible for translating the vertical pull force into a horizontal pull force via a cable.

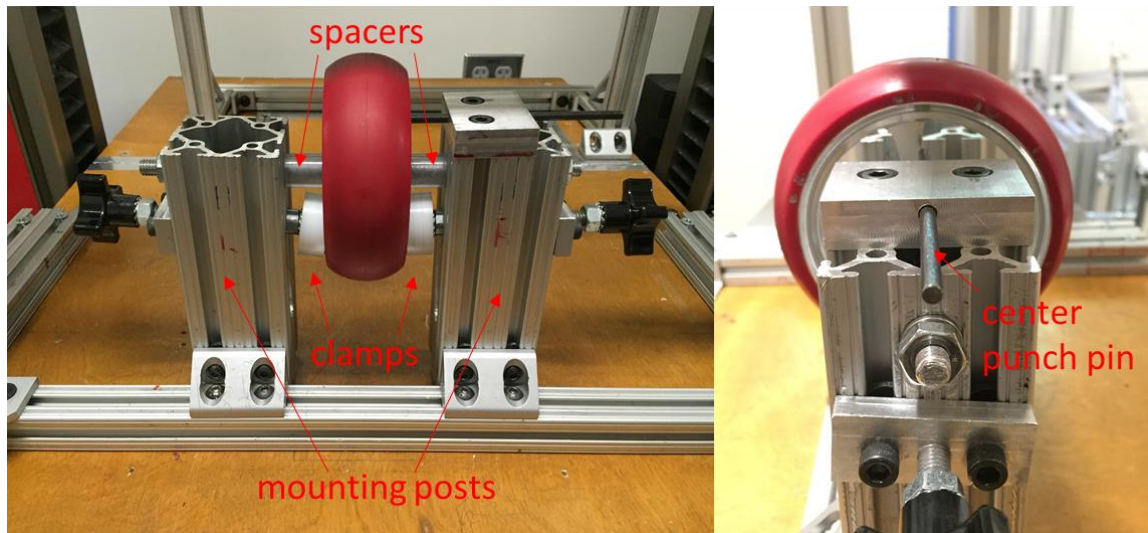


Figure 24. Caster Wheel Mounting Structure

The caster mounting structure (**Figure 24**) suspends the caster between a set of mounting posts via a threaded axle through its bearing. Properly sized spacers prevent lateral motion of the caster, and a set of plungers clamp the caster to prevent caster rotation when scrub torque is applied. While casters are not constrained in rotation during in-situ scrubbing, this constraint is enforced to remove the impact of caster rotation variance. To control and document the caster scrub test patches, a 5/32" centering punch pin mounted perpendicular to the caster hub face is used to align the caster angular position based on marked reference points on the caster rim. This module also includes the frame and vertical linear bearing used to house the surface loading post. The drive wheel mounting structure shares all of the same characteristics at the caster mounting structure, except the drive

wheel orientation is rotated by 90 degrees and wheelchair brakes are used to lock drive wheel rotation (**Figure 25**).

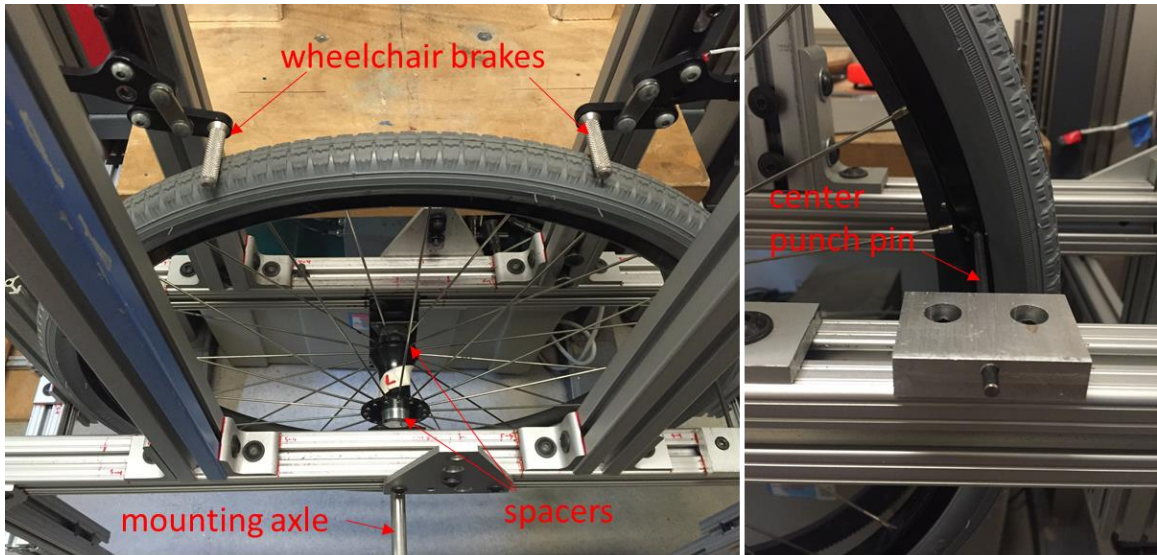


Figure 25. Drive Wheel Mounting Structure

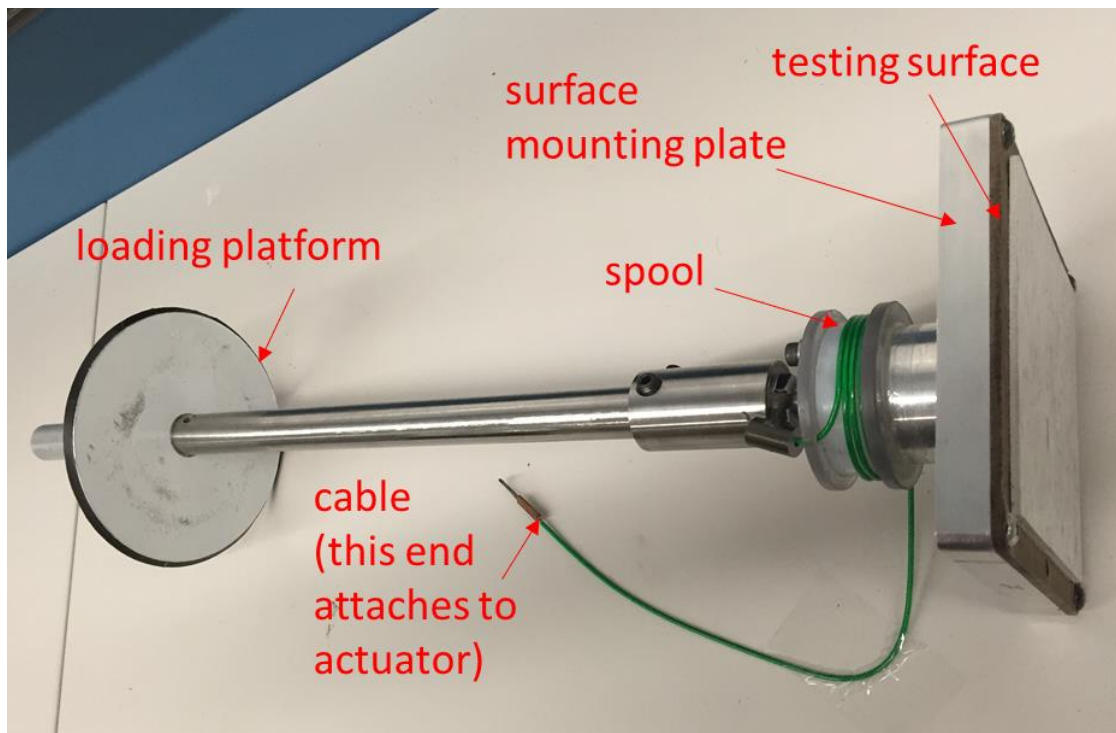


Figure 26. Surface Loading Post

The surface loading post is comprised of a loading platform, cable spool, and surface mounting plate (**Figure 26**). The loading platform is a circular Dibond disk designed to support multiple standard plate weights. A length of 1/2" steel rod connects the loading platform to the cable spool, although their rotational motion is disconnected due to a bearing internal to the spool. The spool holds the wound cable that connects to the Zwick linear actuator and is bolted to the surface mounting plate. Thus, when a pulling motion is applied to the cable, the spool and surface mounting plate rotate to scrub the wheel while the loading plate remains stationary. The test surfaces attach to the surface mounting plate via four attachment screws in each corner. The 5" x 5" size of these test surfaces were designed to accommodate the largest contact patch size of the drive wheels when loaded at 40-kg, as shown in (**Figure 27**).



Figure 27. Drive Wheel Contact Patch on Surface Mounting Plate

In order to accurately apply and measure scrub torque, the cabling is visually assessed to ensure proper alignment is maintained. As shown in **Figure 28**, the tangent of the spool should be aligned with the pulley and cable mount of the Zwick. Once aligned, the lateral position of the pulley and spool do not require any adjustments across any caster scrub tests. The vertical height of the pulley, however, is adjusted with every different wheel tested in order to maintain a horizontal cable from the spool to pulley. This alignment is necessary as any vertical component of the pull force would result in not only any inaccurate scrub torque reading, but also potentially alter the normal load on the wheel. Visual assessment of cable alignment is able to achieve alignment errors less than 5 degrees as verified with angle gauges. The impact of this error was demonstrated through small sample testing to change the scrub measurement by less than 0.2%

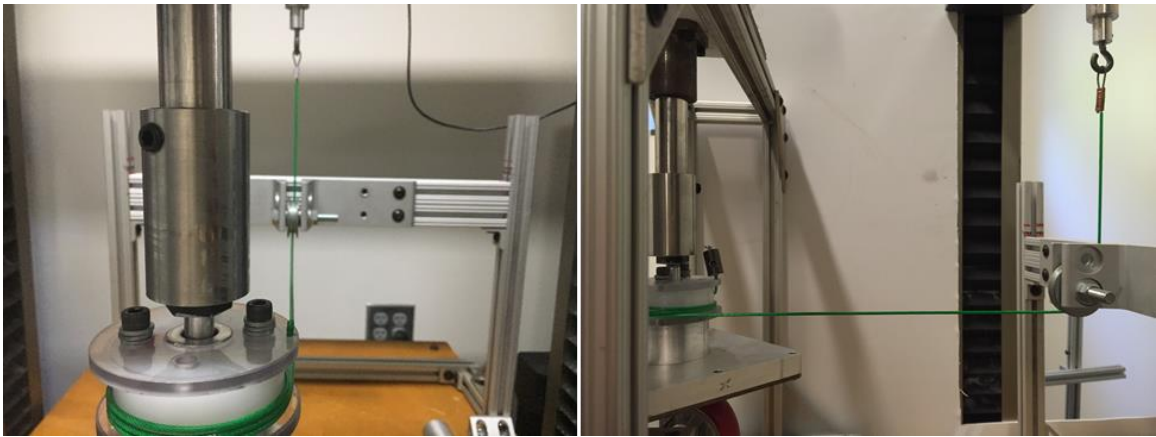


Figure 28. Pull Cable Alignment

In order to achieve pure scrub without sliding on the caster, the test surface's axis of rotation must align accurately with the center of the contact patch between the wheel and test surface. A pin-mounted centering bar is used to project the position of the axis onto a machined centering tip, which is then used as a point of reference to adjust the

position of the mounted wheel. An example of how a centered caster would look relative to the centering tip is displayed in **Figure 29**.



Figure 29. Centering Test Surface Rotation in Caster

For each scrub test, the pull rate of the linear actuator is 5 cm/s for a total pull length of 38 cm. Since the spool diameter is 6.41 cm, the linear motion equates to a rotational rate of 1.56 rad/s (a quarter revolution per second) and a total rotation of 11.85 radians (or 1.89 revolutions) for the test surface. This rotational rate was selected based on previously observed rates of MWC turning (Sonenblum SE et al., 2012b), while the rotational displacement was selected to capture at least one revolution of steady-state scrub torque.

The collected load cell pull force data and the corresponding actuator linear displacement were collected at a sample rate of 100 Hz by the data acquisition software and output for post-processing in MATLAB. The selected window of analysis was from 150 mm to 351 mm of the linear actuator displacement (also termed as standard travel). The lower limit of the window was selected to allow the linear actuator time to take up the slack in the cable, as well as for the caster-surface scrub interaction to enter a steady-state.

The 351 mm upper limit was selected based on its 201 mm difference with the 150 mm lower limit, which can be converted to a rotational displacement of exactly one full revolution. **Figure 30** illustrates this window by the shaded region in the MATLAB post-processing graph. The force data within this window was averaged and multiplied by the

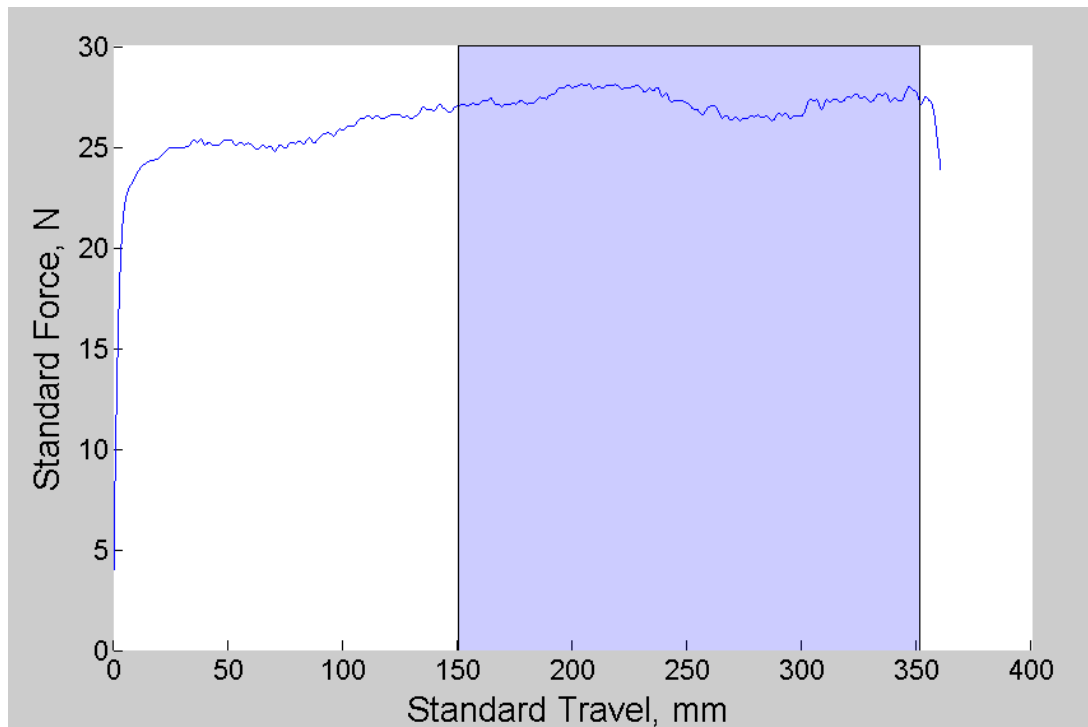


Figure 30. Caster Scrub Test Pull Force Data

spool diameter (6.41 cm) to yield the scrub torque for that trial. To catch instances of bad trials where the pull force data was too noisy, a criteria of $CV < 10\%$ was enforced for each trial's analyzed force data. Trials that did not meet this requirement were re-measured.

In characterizing the scrub torque of a caster for a single load on a single surface, a set of 5 repeated trials are performed on one pre-defined patch on the caster surface. This trial set is preceded by surface cleaning and a single surface conditioning trial, which brings the total number of trials per caster tire patch to 6. The scrub torques of the 5 trial set are averaged to give the representative value for that caster under that load and surface

configuration. The same protocol is followed for drive wheels, except that each configuration is tested on two tire patches instead of one, and the average scrub torque of the two patches is taken as the representative scrub torque. The test of two patches on drive wheels is intended to reduce the impact of greater tire non-homogeneity due to increased tire surface area.

To apply the previously designated configuration loads to each caster and drive wheel, a total of six disk weight combinations were defined, three for casters and three for drive wheels. **Table 6** defines each applied load, including the surface loading post mass.

Table 6. Wheel Scrub Test Configuration Loadings

| Percent Load on Drive Wheels (Total Load = 100 kg) | Load on Caster (with surface loading post) | Load on Drive Wheel (with surface loading post) |
|---|---|--|
| 60% | 20 kg | 30 kg |
| 70% | 15 kg | 35 kg |
| 80% | 10 kg | 40 kg |

For the specific tile and carpet test surfaces utilized in our study, cleaning and conditioning procedures were followed to ensure a consistent surface condition across all trials. A single tile test surface was used across all trials conducted in this study, while a new carpet test surface was used with every distinct tire patch. The reason for replacing the carpet test surface after each set of trials was to remove testing order bias as the carpet material experienced substantial wear with each repeated trial. **Figure 31** illustrates the two types of surface test patches, and **Figure 32** demonstrates the degree of carpet wear after a trial set of 5 trials and 1 pre-conditioning trial.



Figure 31. Tile and Carpet Scrub Torque Test Surfaces

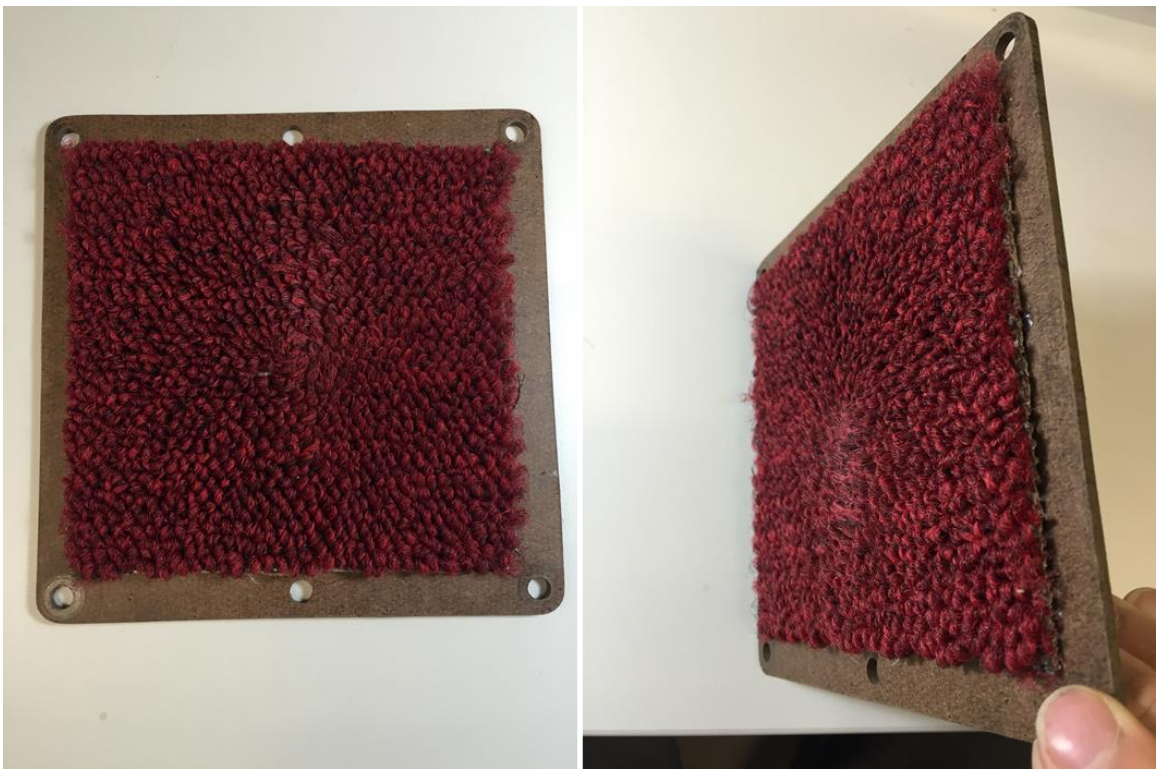


Figure 32. Carpet Test Surface Before and After Scrub Test Trial Set

2.4.2 System Validation

The wheel scrub measurement methodology was validated in both measurement accuracy and test repeatability. The measurement accuracy was not based on the Zwick load cell given its well-documented accuracy and periodic maintenance calibrations. Instead, the accuracy and variance of the applied normal load was assessed during scrub torque tests. Pilot testing indicated that pull forces on the caster test rig could reach 90 N and pull forces on the drive wheel test rig could be upwards of 250 N. These large lateral loads had the potential to misalign the surface loading post and cause binding in the steel post's linear bearing, thus impacting the applied normal load. To assess the consistency of the applied normal load, a digital force gauge (Shimpo Instruments) was retrofitted to the caster and drive wheel mounting structures. A rubber bumper was placed atop the force gauge to emulate the contact patch of the caster/drive wheel, as shown in **Figure 33**.

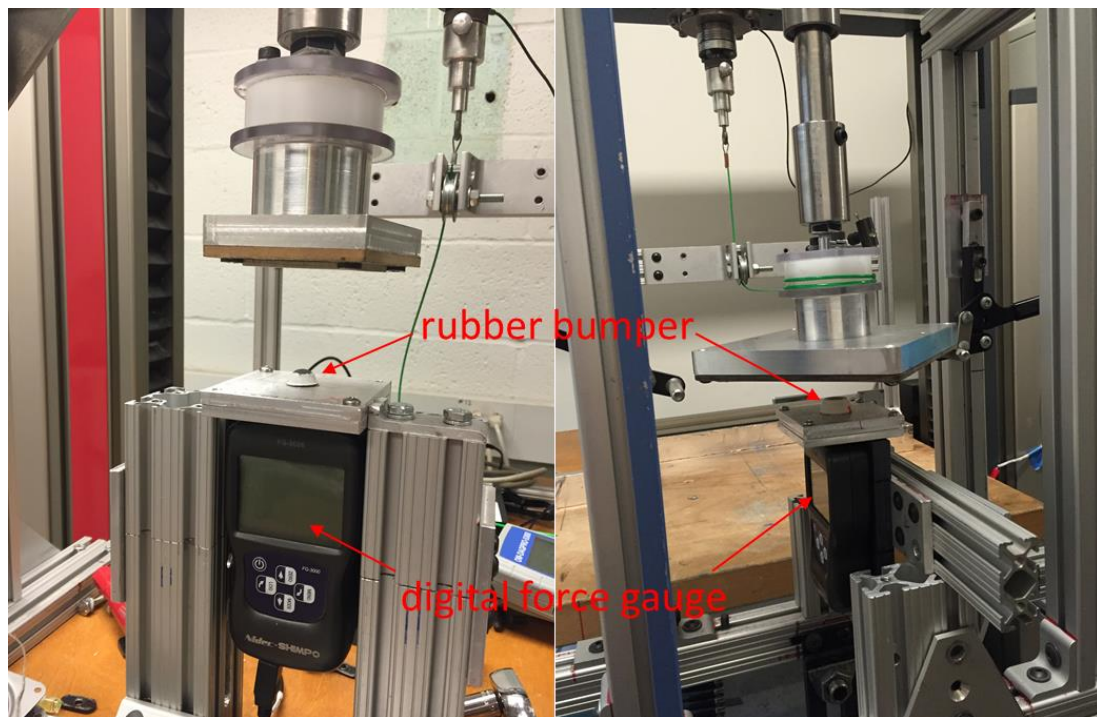


Figure 33. Validating Normal Loading for Caster and Drive Wheel Scrub Test

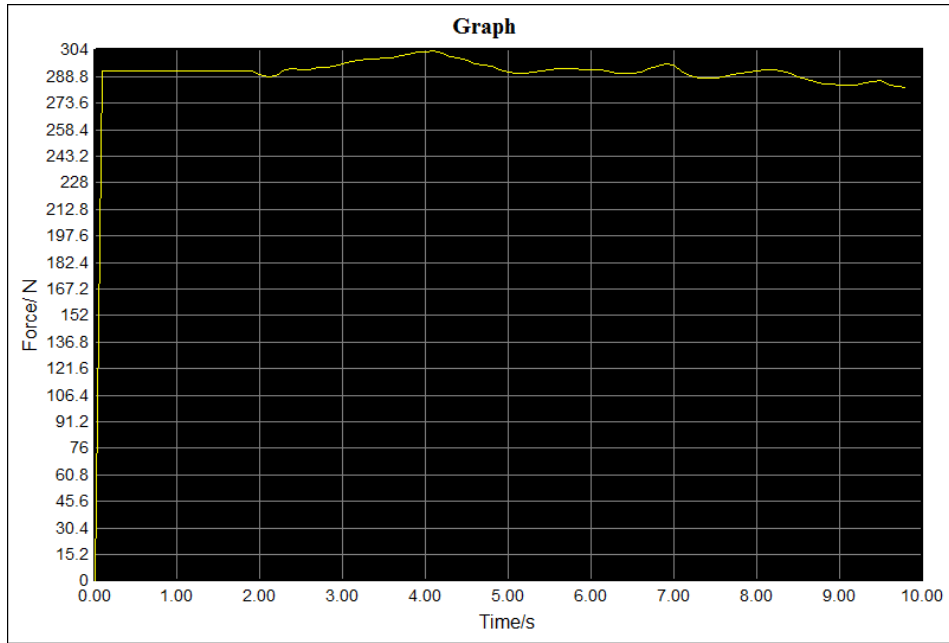


Figure 34. Force Gauge Force Measurement Plot

Normal force data was collected at a sample rate of 10 Hz over the course of each scrub test and transmitted in real-time to the force gauge software. **Figure 34** depicts the graphical output of the measured normal load for the drive wheel test rig loaded with 30 kg (60% WD configuration) on a tile test surface.

Table 7. Caster Scrub Test Rig Normal Load Variability

| Trial Name | <i>Mean Load [N]</i> | <i>StDev Load [N]</i> | <i>CV</i> | <i>Start Load [N]</i> | <i>Max Load Decr. [N]</i> | <i>Max Load Incr. [N]</i> | <i>Max Load Decr. [% Start Load]</i> | <i>Max Load Incr. [% Start Load]</i> | <i>Mean Load Diff. [% Start Load]</i> |
|-------------------|----------------------|-----------------------|-----------|-----------------------|---------------------------|---------------------------|--------------------------------------|--------------------------------------|---------------------------------------|
| (10kg) 1 | 97.2 | 0.5 | 0.01 | 97.4 | -1.4 | 0.6 | -1.44% | 0.62% | -0.21% |
| (10kg) 2 | 97.5 | 0.8 | 0.01 | 97.3 | -1.1 | 1.5 | -1.13% | 1.54% | 0.24% |
| (10kg) 3 | 97.7 | 0.6 | 0.01 | 97.4 | -1.0 | 1.3 | -1.03% | 1.33% | 0.30% |
| (15kg) 1 | 146.8 | 0.7 | 0.00 | 146.5 | -1.0 | 1.4 | -0.68% | 0.96% | 0.19% |
| (15kg) 2 | 146.4 | 0.8 | 0.01 | 146.4 | -1.6 | 1.2 | -1.09% | 0.82% | -0.02% |
| (15kg) 3 | 146.0 | 0.7 | 0.00 | 146.4 | -1.9 | 0.6 | -1.30% | 0.41% | -0.29% |
| (20kg) 1 | 195.2 | 0.5 | 0.00 | 195.6 | -1.5 | 0.2 | -0.77% | 0.10% | -0.22% |
| (20kg) 2 | 194.6 | 0.9 | 0.00 | 194.9 | -1.8 | 1.5 | -0.92% | 0.77% | -0.15% |
| (20kg) 3 | 195.4 | 0.8 | 0.00 | 195.6 | -1.6 | 1.0 | -0.82% | 0.51% | -0.10% |

Table 8. Drive Wheel Scrub Test Rig Normal Load Variability

| Trial Name | <i>Mean Load [N]</i> | <i>StDev Load [N]</i> | <i>CV</i> | <i>Start Load [N]</i> | <i>Max Load Decr. [N]</i> | <i>Max Load Incr. [N]</i> | <i>Max Load Decr. [% Start Load]</i> | <i>Max Load Incr. [% Start Load]</i> | <i>Mean Load Diff. [% Start Load]</i> |
|-------------------|----------------------|-----------------------|-----------|-----------------------|---------------------------|---------------------------|--------------------------------------|--------------------------------------|---------------------------------------|
| (30kg) 1 | 289.5 | 2.6 | 0.01 | 293.8 | -8.6 | 0.0 | -2.93% | 0.00% | -1.46% |
| (30kg) 2 | 297.8 | 3.8 | 0.01 | 294.4 | -1.8 | 10.5 | -0.61% | 3.57% | 1.15% |
| (30kg) 3 | 292.7 | 2.6 | 0.01 | 294.5 | -6.3 | 2.7 | -2.14% | 0.92% | -0.62% |
| (35kg) 1 | 347.1 | 4.3 | 0.01 | 343.9 | -3.5 | 11.2 | -1.02% | 3.26% | 0.93% |
| (35kg) 2 | 340.8 | 2.8 | 0.01 | 343.6 | -7.9 | 2.1 | -2.30% | 0.61% | -0.81% |
| (35kg) 3 | 342.2 | 3.6 | 0.01 | 342.4 | -6.5 | 6.6 | -1.90% | 1.93% | -0.07% |
| (40kg) 1 | 392.1 | 7.2 | 0.02 | 393.6 | -11.6 | 12.4 | -2.95% | 3.15% | -0.37% |
| (40kg) 2 | 386.9 | 4.9 | 0.01 | 393.3 | -13.4 | 2.6 | -3.41% | 0.66% | -1.62% |
| (40kg) 3 | 388.7 | 5.7 | 0.01 | 393.1 | -12.2 | 6.2 | -3.10% | 1.58% | -1.13% |

Validation tests were conducted on the tile test surface for both the caster and drive wheel test rigs. The caster test rig was tested at 10, 15, and 20 kg loads; the drive wheel test rig was tested at 30, 35, and 40 kg loads. Each load condition involved three repeated scrub test trials. The results of these trials are summarized in **Table 7** and **Table 8**. The results of the normal load validation experiment indicate that the caster test rig is capable of applying a consistent normal load, with maximum load deviations of less than 2 N and at most 1.54% of the starting load. The largest percent difference between the starting load and average applied load over the course of the scrubbing action is only 0.30%. This outcome is predictable given the lower pull forces that are being imparted to the caster test rig as a result of its lower configuration loadings.

The drive wheel test rig also exhibited the capacity to apply relatively consistent normal loads. However, maximum load deviations of 13 N and 3.57% of the starting load were considered marginally too high. Coupled with video observations of the surface loading post flexing during the 40 kg load trials, an additional structural support was introduced to the drive wheel test rig. **Figure 35** shows the removal cross brace used to constrain the surface loading post from flexing in the direction of the pull force. Adjustable standoffs prevent the cross brace from being too tight against the steel post. A ball bearing in the center of the brace allows the steel post to move vertically with minimal friction and normal loads to be transferred completely when in contact with the brace. Under these improved structural conditions, the normal load validation trials for the drive wheel were re-conducted to evaluate whether load consistency improved. **Table 9** summarizes the findings for the drive wheel test rig with the added cross brace.

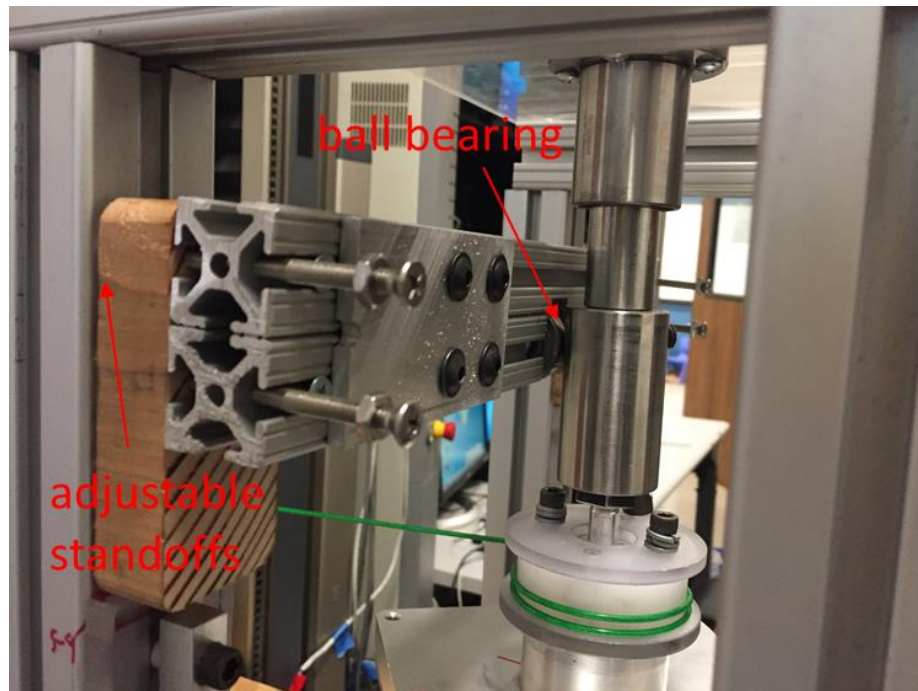


Figure 35. Drive Wheel Test Rig Cross-Brace

Table 9. Drive Wheel Scrub Test Rig (with cross-brace) Normal Load Variability

| Test Name | <i>Mean Load [N]</i> | <i>StDev Load [N]</i> | <i>CV</i> | <i>Start Load [N]</i> | <i>Max Load Decr. [N]</i> | <i>Max Load Incr. [N]</i> | <i>Max Load Decr. [% Start Load]</i> | <i>Max Load Incr. [% Start Load]</i> | <i>Mean Load Diff. [% Start Load]</i> |
|------------------|----------------------|-----------------------|-----------|-----------------------|---------------------------|---------------------------|--------------------------------------|--------------------------------------|---------------------------------------|
| (30kg) 1 | 293.7 | 2.9 | 0.01 | 293.8 | -5.8 | 4.1 | -1.97% | 1.40% | -0.03% |
| (30kg) 2 | 295.9 | 4.1 | 0.01 | 292.9 | -4.6 | 7.9 | -1.57% | 2.70% | 1.04% |
| (30kg) 3 | 296.8 | 3.6 | 0.01 | 293.9 | -4.0 | 7.9 | -1.36% | 2.69% | 0.99% |
| (35kg) 1 | 342.2 | 3.3 | 0.01 | 343.9 | -6.0 | 5.9 | -1.74% | 1.72% | -0.49% |
| (35kg) 2 | 340.9 | 1.0 | 0.00 | 343.5 | -3.8 | 0.0 | -1.11% | 0.00% | -0.74% |
| (35kg) 3 | 341.8 | 3.5 | 0.01 | 342.6 | -5.2 | 6.5 | -1.52% | 1.90% | -0.24% |
| (40kg) 1 | 388.5 | 3.0 | 0.01 | 391.8 | -7.5 | 2.1 | -1.91% | 0.54% | -0.85% |
| (40kg) 2 | 389.1 | 2.2 | 0.01 | 389.4 | -4.6 | 3.7 | -1.18% | 0.95% | -0.07% |
| (40kg) 3 | 389.3 | 3.5 | 0.01 | 392.1 | -7.3 | 3.8 | -1.86% | 0.97% | -0.72% |

The results of **Table 9** indicate that the additional cross brace provided the anticipated improvement to the normal load consistency during drive wheel scrub tests. The maximum load deviation was reduced by almost half to 7.9 N, while the maximum percent deviation was reduced by almost 1% to 2.70%. The largest percent difference between the trial average load from the trial start load was also lowered by 0.6% to 1.0%. Video observation of the scrub tests also affirmed that the cross brace was fulfilling its role by keeping the surface loading post vertical during scrub trials.

The repeatability of the scrub test rigs were assessed with the benchmark of $CV < 10\%$ for a trial set of 5 repeated trials. In conducting a few of these experiments, it was observed that the caster and drive wheel scrub torques underwent an incremental increase with each consecutive test, as illustrated by **Figure 36**. It is hypothesized that this increase was due to the abrasion of the caster surface caused by each test, which altered the patch material friction and increased contact area. The large rise in scrub torque between the

first and second trial can be explained by the removal of any cleaning residue during the abrasions caused by the first trial. The presence of this incremental increase prevented the test repeatability criteria from being achieved. Keying off of the repeatability assessment results, we noted that the incremental increase with each trial diminished significantly by the third or fourth trial. Thus, two complete trial sets were collected for each wheel surface patch, with the second trial set being used for analysis. This equated to the 5 trials of interest being preceded by two surface cleaning procedures and 7 conditioning trials (recall that a single trial set consists of 1 trial to pre-condition the surface after cleaning and 5 trials for the data). This conditioning methodology shares consistency with ASTM standards (D1349-14, 2014; E1337-90, 2012) for measuring auto tire braking resistance and evaluating rubber material friction. Analysis of this second, conditioned trial set allowed for the test repeatability benchmark of $CV < 10\%$ to be achieved across scrub torque measurements of both casters and drive wheels.

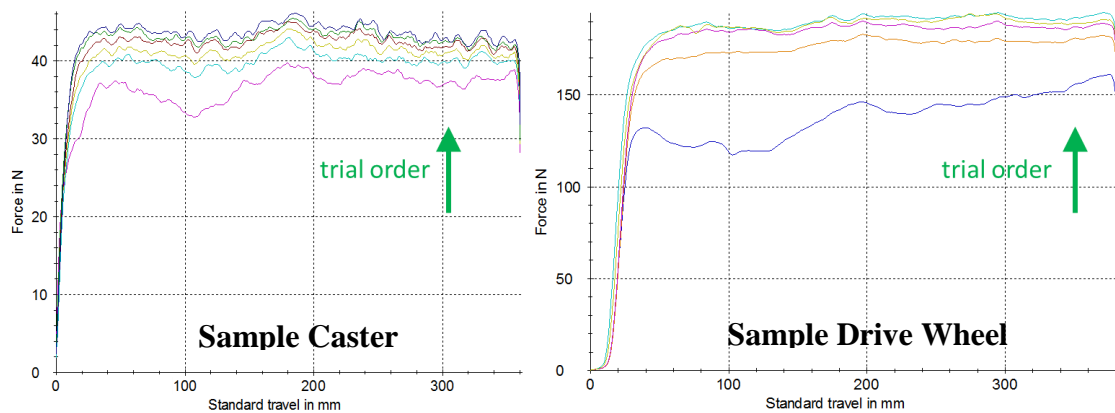


Figure 36. Impact of Scrub Test Trial Order

2.5 Component Test Results and Discussion

2.5.1 Component Mass and Moment of Inertia

The mass of the various casters were smaller than the mass of the drive wheels by about an order of magnitude, with casters ranging between 0.12 – 0.39 kg and drive wheels ranging between 1.71 – 2.07 kg (**Table 10** and **Table 11**). Within casters, the heaviest 5 x 1.5” Primo SR was 0.27 kg, or 225% greater in mass than the lightest 3 x 1” FLNC. Within drive wheels, the heaviest Solid Mag was 0.36 kg (21%) greater in mass than the lightest Spinergy. However, when comparing these components to the overall mass of the MWC system (approximated as 100 kg), the drive wheels and casters each only account at most for 4% and 0.8% of the system mass, indicating that the benefits gained from a lighter caster or drive wheel are minute. Let’s put this in the context of kinetic energy (KE), or the amount of mechanical energy that needs to be stored for a MWC system to reach a particular speed. The translational KE of a 100 kg MWC system traveling at 1 m/s² would be 100 J. If the described system was initially using Solid Mag drive wheels and switched to Spinergy drive wheels, the translational KE under the same conditions would only be reduced to 99.28 J, or by 0.72%. This percent reduction may indeed be greater in instances of turning maneuvers or lighter MWC loads, but in general will not exceed a few percent. Thus, the mass-based advantage of using different casters and drive wheels is very small.

Table 10. Caster Inertial Measurements

| Caster Wheel | Mass [kg] | Rotational Inertia [kg-m ²] | Yaw Inertia (with fork) [kg-m ²] |
|------------------------|-----------|---|--|
| 4 x 1.5” FLSR | 0.22 | 0.00050 | 0.00206 |
| 5 x 1.5” Primo SR | 0.39 | 0.00109 | 0.00204 |
| 5 x 1” Primo | 0.22 | 0.00076 | 0.00206 |
| 6 x 1” Primo Pneumatic | 0.26 | 0.00071 | 0.00209 |
| 6 x 1.5” Primo | 0.33 | 0.00116 | N/A |
| 6 x 1” Primo | 0.30 | 0.00097 | 0.00206 |
| 3 x 1” FLNC | 0.12 | 0.00042 | N/A |
| 6 x 1” FLNC | 0.31 | 0.00102 | N/A |

The caster-in-fork yaw inertias were very uniform and were twice in value compared to the greatest rotational inertia amongst the casters (**Table 10**). Despite this difference, it should be noted that the casters only undergo yaw angle displacement (swivel) during MWC direction changes, which are transient in nature. On the other hand, the rotation of the casters are ever-present in all instances of MWC motion. The rotational inertias of the various casters were smaller than the rotational inertias of the drive wheels by more than two orders of magnitude, with casters ranging between 0.00042 – 0.00116 kg-m² and drive wheels ranging between 0.1120 – 0.1242 kg-m². Within casters, the 6 x 1.5” Primo had the greatest rotational inertia and was 0.00074 kg-m², or 176% greater in rotational inertia than the 3 x 1” FLNC, which had the smallest rotational inertia.

Table 11. Drive Wheel Inertial Measurements

| Drive Wheel | Mass [kg] | Rotational Inertia [kg-m ²] |
|--------------------|-----------|---|
| Solid Mag | 2.07 | 0.1242 |
| Spinergy | 1.71 | 0.1120 |
| Stock Pneumatic | 1.86 | 0.1180 |
| Schwalbe Right Run | 1.82 | 0.1143 |

Within drive wheels (**Table 11**), the Solid Mag had the greatest rotational inertia and was 0.0122 kg-m² (11%) greater in rotational inertia than the Spinergy, which had the smallest rotational inertia. Again, we would like to understand whether these differences in component rotational inertia significantly impact the overall system KE. Assuming the MWC is traveling in a straight motion at 1 m/s, a drive wheel with an active radius of 30 cm would be rotating at a rate of 3.33 rad/s. Squaring this term and multiplying it with the drive wheel rotational inertia yields that component’s rotational KE. Thus, the rotational KE difference between using a Solid Mag and Spinergy drive wheel comes out to be 0.14

J. Doubling this value to account for there being two drive wheels, the system’s rotational KE changes from 2.76 J to 2.48 J. However, compared to the translational KE that dominates the system (100 J), this reduction accounts for less than 1% of the total system KE. Thus, the rotational-based advantages between using different casters and drive wheels is also very small.

2.5.2 Rolling Resistance

Table 12. Caster and Drive Wheel Rolling Resistance Force on Tile

| Rolling Resistance Force [N] | | | | | | |
|------------------------------|------------------|------|------|-------------------|----------|-----------|
| <i>Tile</i> | Caster Load (kg) | | | Linear Regression | | |
| Caster | 20 | 15 | 10 | Coefficient | Constant | R-squared |
| 6 x 1" Pneumatic | 3.59 | 2.58 | 1.47 | 0.212 | -0.635 | 0.999 |
| 5 x 1.5" Primo SR | 2.83 | 1.98 | 1.17 | 0.166 | -0.495 | 1 |
| 6 x 1.5" Primo | 2.63 | 1.82 | 1.09 | 0.154 | -0.462 | 0.999 |
| 3 x 1" FLNC | 2.44 | 1.67 | 0.92 | 0.152 | -0.598 | 1 |
| 5 x 1" Primo | 2.39 | 1.63 | 0.93 | 0.146 | -0.535 | 1 |
| 6 x 1" Primo | 2.06 | 1.52 | 0.96 | 0.11 | -0.134 | 1 |
| 6 x 1" FLNC | 1.7 | 1.21 | 0.7 | 0.1 | -0.294 | 1 |
| 4 x 1.5" FLSR | 1.69 | 1.14 | 0.64 | 0.106 | -0.426 | 0.999 |
| <i>Tile</i> | DW Load (kg) | | | Linear Regression | | |
| DW | 30 | 35 | 40 | Coefficient | Constant | R-squared |
| 24 x 1" Solid Mag | 3.61 | 4.51 | 5.48 | 0.187 | -2.029 | 1 |
| 24 x 1" Spinergy | 1.07 | 1.58 | 1.99 | 0.092 | -1.673 | 0.996 |
| 24 x 1" Schwalbe Right Run | 1.12 | 1.48 | 1.72 | 0.06 | -0.657 | 0.986 |
| 24 x 1-3/8" Stock Pneumatic | 0.53 | 1.12 | 1.37 | 0.084 | -1.919 | 0.946 |

In this section, the rolling resistances of casters and drive wheels under their configuration loads are tabulated, separated into tile and carpet results in **Table 12** and **Table 13**, respectively. Casters and drive wheels are separated in each table. Within each table section, the components are listed in descending order of average rolling resistance, which is the mean rolling resistance across all loads for a single component (not tabulated).

“Load” columns are ordered left to right to correspond to 60%, 70%, and 80% weight-distribution on drive wheels for a 100 kg wheelchair, respectively. Linear regressions of load versus rolling resistance were applied for each component, and their regression coefficient, constant, and R^2 are also included in the tables. Across all rolling resistance linear regressions, $R^2 > 0.94$, suggesting that it is suitable to use the regression slope as a metric of component sensitivity to load. The load versus rolling resistance regressions for casters on tile, drive wheels on tile, casters on carpet, and drive wheels on carpet are also plotted for illustrative purposes in **Figure 37**, **Figure 38**, **Figure 39**, and **Figure 40**, respectively.

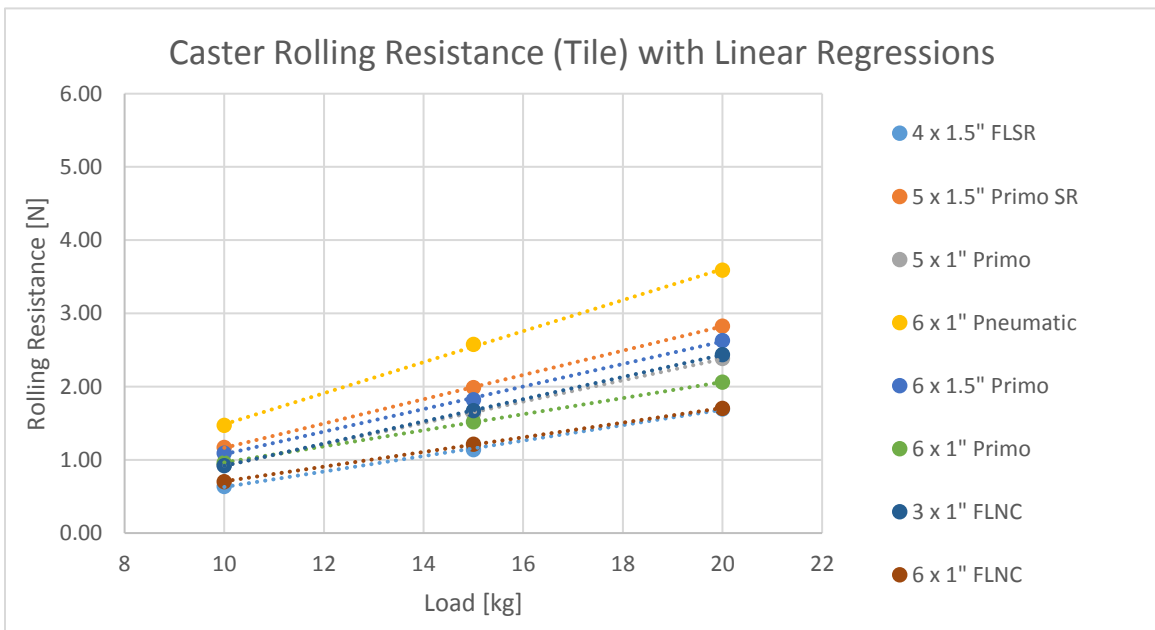


Figure 37. Caster Rolling Resistance on Tile

For casters on tile, the rolling resistance average across all three loads ranged from 1.16 – 2.55 N, with the lowest being the 4 x 1.5" FLSR and the highest being the 6 x 1" Pneumatic. Switching between these two casters equates to a 120% increase in average rolling resistance. For drive wheels on tile, the rolling resistance average across all three

loads ranged from 1.01 – 4.53 N, with the lowest being the Stock Pneumatic and the highest being the Solid Mag. Switching between these two drive wheels equates to a 349% increase in rolling resistance. These differences within casters and drive wheels are significant, especially since rolling resistance plays a dominant role in dissipating stored mechanical energy during any linear MWC motions.

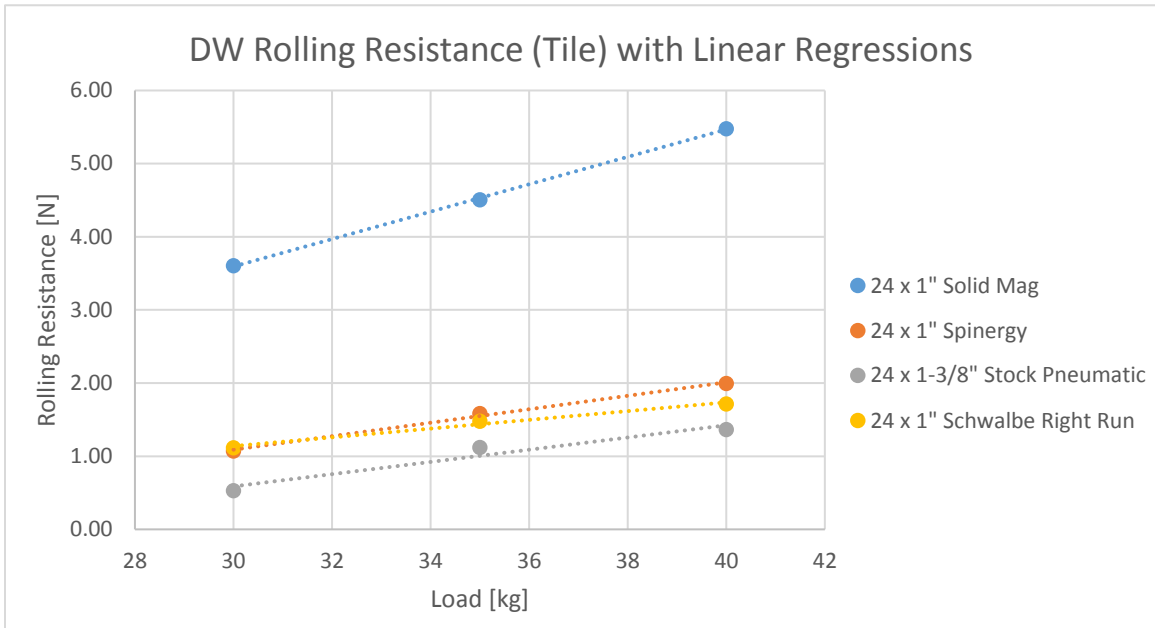


Figure 38. Drive Wheel Rolling Resistance on Tile

The casters rolling resistance data on tile present trends that both corroborate and conflict with the findings of a field assessment of manual wheelchair rolling resistance (Sauret et al., 2012). Rolling resistance forces fall within the same range found by the Sauret study, but casters do not seem to follow the trend of greater rolling resistance with decreasing diameter. This can be explained by our study’s much smaller sample size of components, where the variance of other caster properties prevent the impact of caster radius from being teased out. To investigate the impact of these other properties, we can compare three casters that are similar in dimensions and wheel profile, as depicted in **Table**

1 (pages 5-6): 6 x 1" Pneumatic, 6 x 1" Primo, and 6 x 1" FLNC. The 6 x 1" Pneumatic has the greatest rolling resistance and a tire hardness of 60, followed by the 6 x 1" Primo and 6 x 1" FLNC, which both share a tire hardness of 89. Conventional mechanics of deformable bodies indicate that rolling resistance is a function of wheel and surface stiffness, which could explain this separation. Wheel stiffness is impacted by not only the tire hardness, but also the rigidity of the wheel hub. This second concept may explain why the 6 x 1" Primo with a polymer hub had an average rolling resistance 26% greater than the 6 x 1" FLNC with an aluminum hub, despite registering the same tire hardness. This theory is consistent with drive wheels, where the Solid Mag, while having the greatest tire hardness, is the only drive wheel with polymer spokes instead of the more rigid tensioned metal spokes. **Figure 38** depicts the corresponding difference in rolling resistance, with the Solid Mag clearly a higher outlier to the remaining drive wheels. This results match well with the findings of a dynamometer-based rolling resistance study (Kwarciak AM, Yarossi M, Ramanujam A, Dyson-Hudson TA, & Sisto SA, 2009). Comparing three solid drive wheels to two pneumatic drive wheels, Kwarciak found – under the same load conditions as our study – that the solid tires presented rolling resistances of 4 – 9 N while pneumatic tires exhibited rolling resistances of 2 – 3 N. Specific value differences are likely due to their use of a dynamometer surface instead of a flat tile surface.

Examining caster sensitivity to load on tile, the magnitude of rolling resistance appears to correlate with the regression slope. This leads to a greater separation between casters at higher loads, with rolling resistances ranging from 1.69 – 3.59 N (1.9 N difference) at a 20 kg load, compared to rolling resistances of 0.64 – 1.47 N (0.83 N difference) at a 10 kg load. This suggests that when a MWC on tile is configured such that

the weight distribution on the casters are low (e.g. 100 kg @ 80% load on drive wheels), caster selection does not significantly impact rolling resistance. However, for weight distributions that equate to a caster load of 20 kg or more, the selection of casters can significantly affect the user effort. Drive wheel load sensitivity presents itself as quite uniform in **Figure 38**, with only the Solid Mag presenting a larger regression slope. Thus, amongst the metal spoked drive wheels, there is not weight-distribution based benefit to be gained relative to each other.

Table 13. Caster and Drive Wheel Rolling Resistance Forces on Carpet

| Rolling Resistance Force [N] | | | | | | |
|------------------------------|------------------|------|------|-------------------|----------|-----------|
| <i>Carpet</i> | Caster Load (kg) | | | Linear Regression | | |
| Caster | 20 | 15 | 10 | Coefficient | Constant | R-squared |
| 3 x 1" FLNC | 10.62 | 7.69 | 5.6 | 0.503 | 0.431 | 0.991 |
| 6 x 1" Primo | 8.35 | 6.68 | 4.5 | 0.385 | 0.738 | 0.994 |
| 6 x 1" FLNC | 7.92 | 5.89 | 4.34 | 0.358 | 0.686 | 0.994 |
| 6 x 1.5" Primo | 7.21 | 5.4 | 3.65 | 0.357 | 0.067 | 1 |
| 5 x 1.5" Primo SR | 7 | 5.01 | 3.52 | 0.348 | -0.044 | 0.993 |
| 5 x 1" Primo | 6.34 | 4.82 | 3.42 | 0.292 | 0.48 | 0.999 |
| 4 x 1.5" FLSR | 6.21 | 4.89 | 3.38 | 0.283 | 0.591 | 0.999 |
| 6 x 1" Pneumatic | 6.03 | 4.33 | 3.04 | 0.299 | -0.019 | 0.994 |
| <i>Carpet</i> | DW Load (kg) | | | Linear Regression | | |
| DW | 30 | 35 | 40 | Coefficient | Constant | R-squared |
| 24 x 1" Solid Mag | 5.25 | 7.25 | 8.54 | 0.329 | -4.505 | 0.985 |
| 24 x 1" Schwalbe Right Run | 3.44 | 4.41 | 5.13 | 0.168 | -1.563 | 0.993 |
| 24 x 1" Spinergy | 3.36 | 4.15 | 5.06 | 0.17 | -1.758 | 0.998 |
| 24 x 1-3/8" Stock Pneumatic | 2.34 | 3.24 | 4.27 | 0.193 | -3.467 | 0.998 |

Comparing the tile rolling resistances of casters and drive wheels, we see that all drive wheels besides the Solid Mag have lower rolling resistance values than the casters in the 60%WD load configuration (30 kg on DW, 20 kg on caster) despite their greater loading, and exhibit a greater load insensitivity compared to all casters. The Solid Mag, however, is similar in load sensitivity to the casters and exhibits larger rolling resistances

for its configuration loads. Based on these observations, the shifting of more load onto the metal spoke drive wheels is the most effective means of reducing rolling resistance on tile.

For casters on carpet, the rolling resistance average across all three loads ranged from 4.47 – 7.97 N, with the lowest being the 6 x 1" Pneumatic and the highest being the 3 x 1" FLNC. Switching between these two casters equates to a 78% increase in average rolling resistance. For drive wheels on tile, the rolling resistance average across all three loads ranged from 3.28 – 7.01 N, with the lowest being the Stock Pneumatic and the highest being the Solid Mag. Switching between these two drive wheels equates to a 114% increase in rolling resistance.

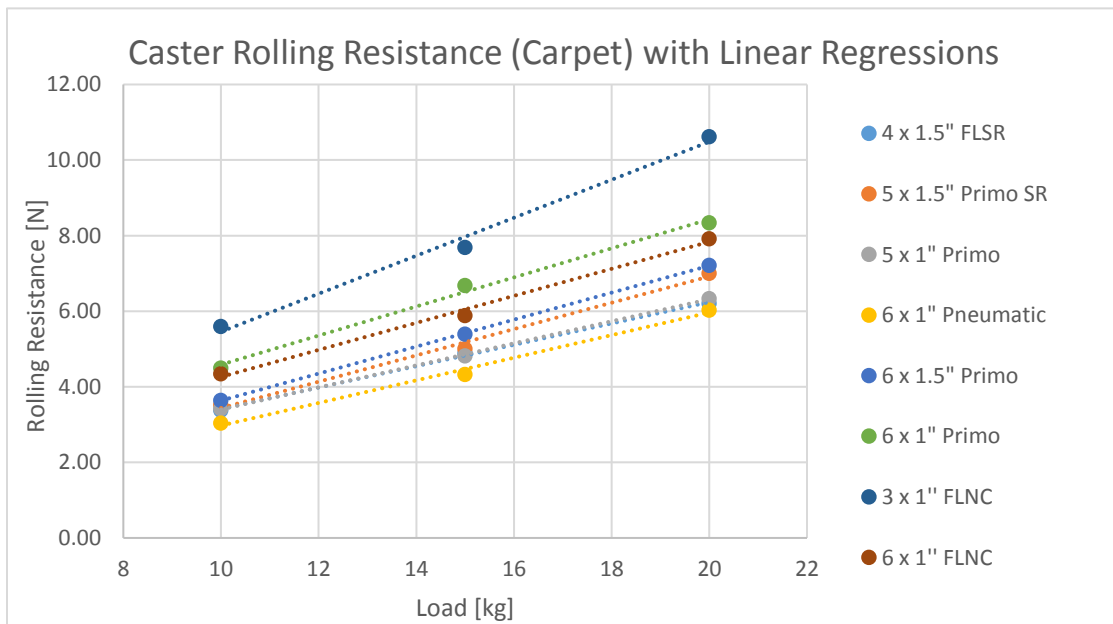


Figure 39. Caster Rolling Resistance on Carpet

The carpet rolling resistances increased by an average of 4 N compared to tile, while drive wheel rolling resistances increased by an average of 2.57 N compared to tile. The drive wheels' comparatively small change in rolling resistance may be attributed to its larger wheel radius, which has been shown to be inversely related with rolling resistance

(Sauret et al., 2012). Since rolling resistance is a function of surface deformation (Pacejka, 2005) as well, the flat wide profile of the Solid Mag and “buoyant” nature of the pneumatic drive wheels may have reduced the deformation of the softer carpet surface. These concepts can be extended to the casters which, unlike drive wheels, underwent a significant shift in the order of casters ranked by rolling resistance. The 6 x 1" Pneumatic went from having the greatest rolling resistance on tile to exhibiting the least rolling resistance on carpet. Simultaneously, the smallest 3 x 1" FLNC increased to having the greatest rolling resistance on carpet. This increase in rolling resistance with decreasing caster diameter is consistent with Sauret’s findings on carpet (Sauret et al., 2012). Casters with greater tire widths dropped in rank below narrower casters (except for the 5 x 1" Primo) which likely sank deeper into the carpet surface.

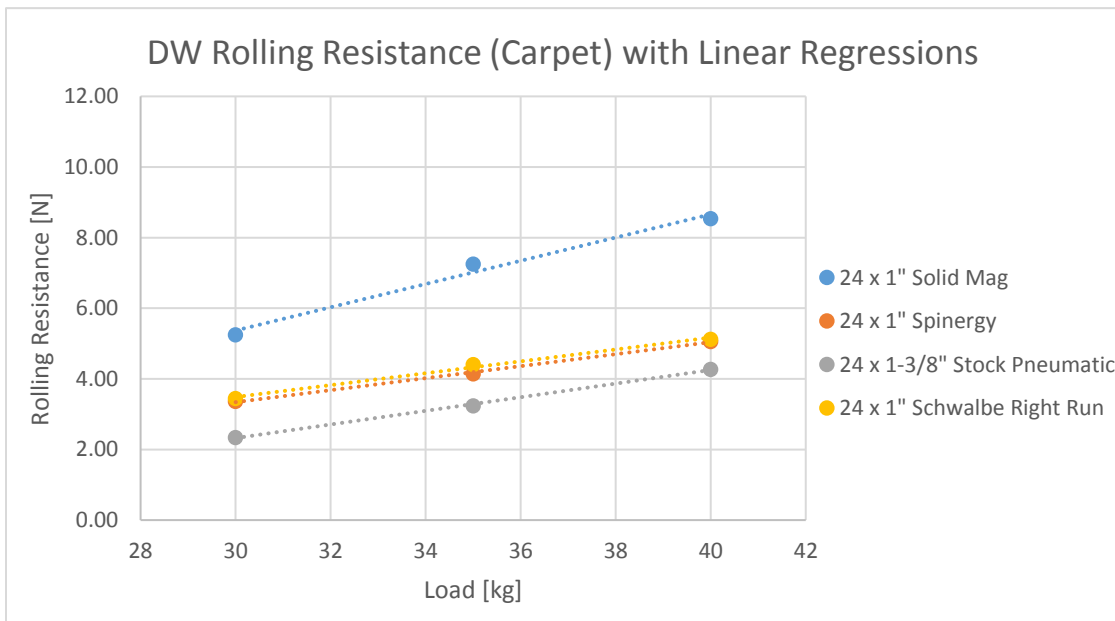


Figure 40. Drive Wheel Rolling Resistance on Carpet

Load sensitivity for both component types increased on carpet. Caster regression slopes increased by an average of 0.21 N/kg, while drive wheel regression slopes increased

by an average of 0.11 N/kg. Regression slopes for casters became more uniform, thus maintaining constant separation between casters across loads. However, the magnitude of the rolling resistance differences between casters is greater on carpet, indicating that across all weight distributions, casters selection is more impactful on carpet than tile.

Comparing the carpet rolling resistances of casters and drive wheels, we see that all drive wheels besides the Solid Mag have lower rolling resistance values than the casters in both the 60%WD and 70%WD load configurations despite their greater loading, and exhibit a greater load insensitivity compared to all casters. The Solid Mag, however, is similar in load sensitivity to the casters and exhibits larger rolling resistances for its configuration loads. Similar to the findings for rolling resistance on tile, the shifting of more load onto the metal spoke drive wheels is the most effective means of reducing rolling resistance on carpet. This approach should be even more effective than on tile, given the larger differences between drive wheel and caster rolling resistances on carpet.

2.5.3 Scrub Torque

In this section, the scrub torques of casters and drive wheels under their configuration loads are tabulated, separated into tile and carpet results in **Table 14** and **Table 15**, respectively. Casters and drive wheels are separated in each table. Within each table section, the components are listed in descending order of average scrub torque, which is the mean scrub torque across all loads for a single component (not tabulated). “Load” columns are ordered left to right to correspond to 60%, 70%, and 80% weight-distribution on drive wheels for a 100 kg wheelchair, respectively. Linear regressions of load versus rolling resistance were applied for each component, and their regression coefficient,

constant, and R^2 are also included in the tables. Across all rolling resistance linear regressions, $R^2 > 0.83$, suggesting that it is suitable to use the regression slope as a metric of component sensitivity to load. The load versus rolling resistance regressions for casters on tile, drive wheels on tile, casters on carpet, and drive wheels on carpet are also plotted for illustrative purposes in **Figure 41**, **Figure 42**, **Figure 43**, and **Figure 44**, respectively.

Table 14. Caster and Drive Wheel Scrub Torque on Tile

| Scrub Torque [Nm] | | | | | | |
|-----------------------------|------------------|------|------|-------------------|----------|-----------|
| <i>Tile</i> | Caster Load (kg) | | | Linear Regression | | |
| Caster | 20 | 15 | 10 | Coefficient | Constant | R-squared |
| 6 x 1" Pneumatic | 2.79 | 1.93 | 0.93 | 0.186 | -0.907 | 0.998 |
| 5 x 1.5" Primo SR | 1.76 | 1.33 | 0.91 | 0.085 | 0.064 | 1 |
| 4 x 1.5" FLSR | 1.74 | 1.23 | 0.74 | 0.1 | -0.262 | 1 |
| 6 x 1" Primo | 1.22 | 0.86 | 0.49 | 0.073 | -0.235 | 1 |
| 5 x 1" Primo | 1.03 | 0.67 | 0.42 | 0.061 | -0.211 | 0.99 |
| 6 x 1.5" Primo | 0.96 | 0.66 | 0.32 | 0.063 | -0.306 | 0.999 |
| 6 x 1" FLNC | 0.97 | 0.62 | 0.32 | 0.065 | -0.338 | 0.998 |
| 3 x 1" FLNC | 0.77 | 0.57 | 0.33 | 0.044 | -0.103 | 0.998 |
| <i>Tile</i> | DW Load (kg) | | | Linear Regression | | |
| DW | 30 | 35 | 40 | Coefficient | Constant | R-squared |
| 24 x 1-3/8" Stock Pneumatic | 5.72 | 6.97 | 8.18 | 0.246 | -1.658 | 1 |
| 24 x 1" Schwalbe Right Run | 4.83 | 4.99 | 6.19 | 0.136 | 0.576 | 0.837 |
| 24 x 1" Spinergy | 4.52 | 5.2 | 6.06 | 0.154 | -0.134 | 0.996 |
| 24 x 1" Solid Mag | 2.99 | 3.86 | 4.49 | 0.151 | -1.491 | 0.991 |

For casters on tile, the scrub torque average across all three loads ranged from 0.56 – 1.88 Nm, with the lowest being the 3 x 1" FLNC and the highest being the 6 x 1" Pneumatic. Switching between these two casters equates to a 236% increase in average rolling resistance. For drive wheels on tile, the scrub torque average across all three loads ranged from 3.78 – 6.96 Nm, with the lowest being the Solid Mag and the highest being the Stock Pneumatic. Switching between these two drive wheels equates to an 84% increase in rolling resistance. These differences within casters and drive wheels are of

particular significance as they are a strong determinant of the energy dissipated during any MWC motions involving direction change.

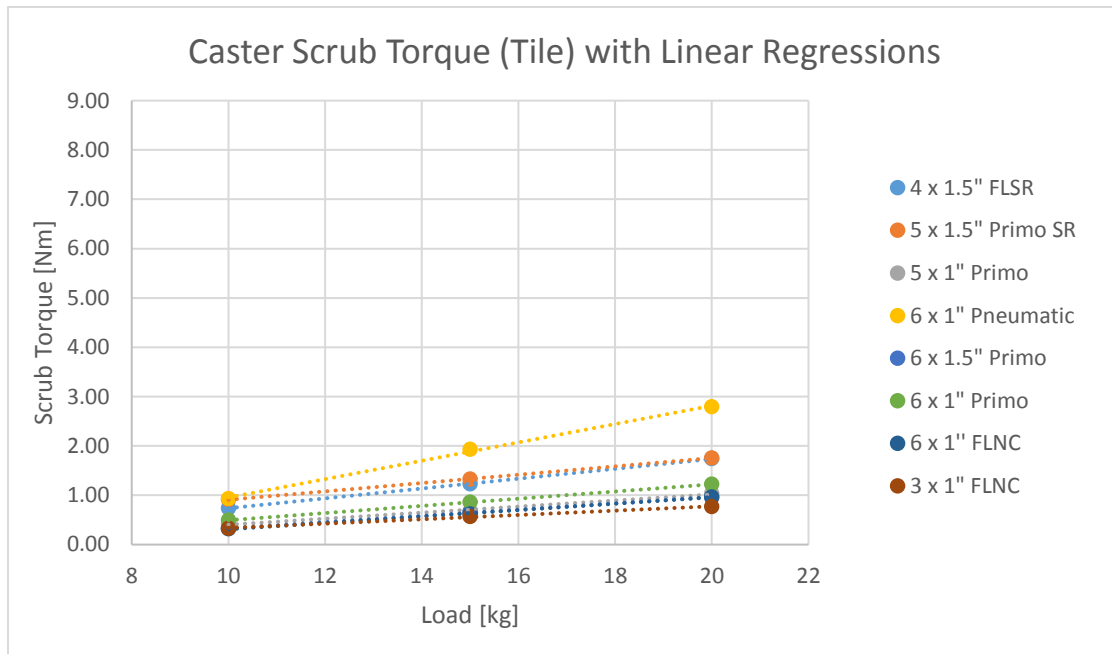


Figure 41. Caster Scrub Torque on Tile

Once again, we can compare three casters that are similar in dimensions and wheel profile, as depicted in **Table 1** (pages 5-6): 6 x 1" Pneumatic, 6 x 1" Primo, and 6 x 1" FLNC. The 6 x 1" Pneumatic has the greatest scrub torque and a tire hardness of 60, followed by the 6 x 1" Primo and 6 x 1" FLNC, which both share a tire hardness of 89. Since rotational friction is dependent upon the distribution of the contact area about the axis of rotation, it stands to reason that a more deformable tire such as the 6 x 1" Pneumatic would experience greater scrub torque than its similar counterparts. This idea is potentially reinforced by the fact that 5 x 1.5" Primo SR and 4 x 1.5" FLSR rank second and third in scrub torque on tile, respectively. In terms of tire hardness, they are only greater in value than the 6 x 1" Pneumatic, with hardnesses of 65 and 76, respectively. Furthermore, the greater tire width of these two casters may also contribute to the increased scrub torque,

although this theory is not entirely consistent with the 6 x 1.5" Primo. For drive wheels on tile (**Figure 42**), the Stock Pneumatic presents the largest tire width, which may be related to its particularly high scrub torque. The Solid Mag is the only tread-less drive wheel, which may link to its particularly low scrub torque.

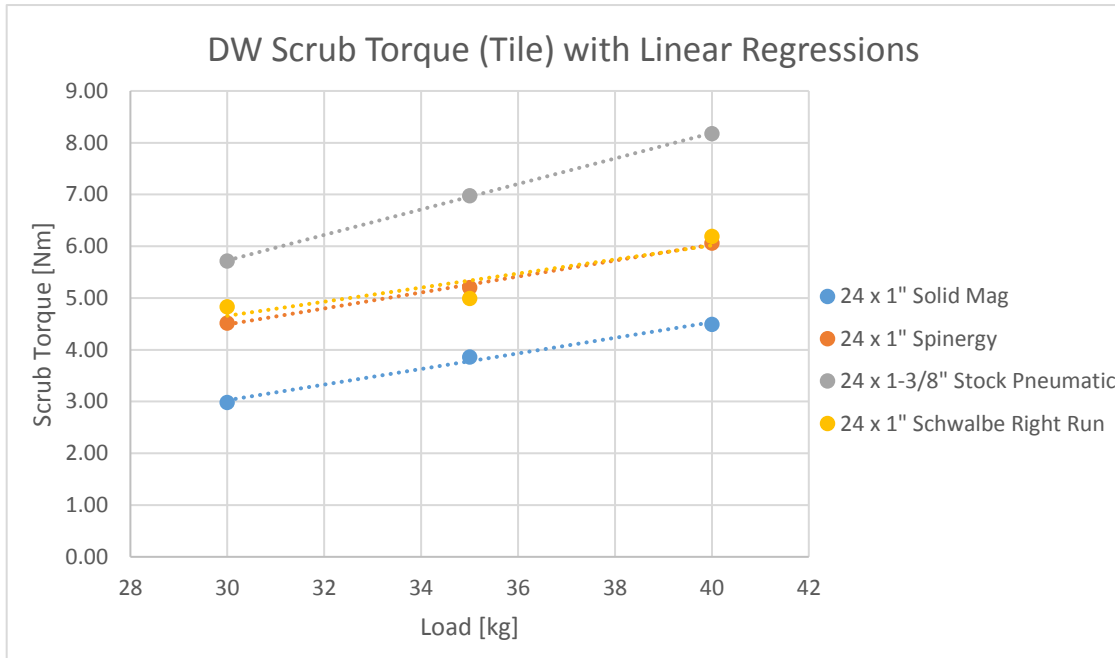


Figure 42. Drive Wheel Scrub Torque on Tile

With regards to component load sensitivity, the caster scrub torque on tile displays a behavior comparable to that of caster rolling resistance on tile. At the 80%WD configuration (10 kg) loading, the caster scrub torques only range from 0.33 – 0.93 Nm. However, due to casters with larger scrub torques exhibiting greater load sensitivity, caster scrub torques range from 0.77 – 2.79 Nm at the 60%WD configuration (20 kg) loading. The casters can be separated into three groups based on similar load sensitivities (regression slope), consisting of the 6 x 1" Pneumatic, the 5 x 1.5" Primo SR and 4 x 1.5" FLSR, and the remaining five casters. Thus, picking casters from between these three groups becomes impactful for a MWC (100 kg) in the 60%WD configuration in terms of

caster scrub torque. The drive wheels on average display a greater sensitivity to load than casters, with an average regression slope of 0.172 Nm/kg versus the casters' average regression slope of 0.085 Nm/kg. The Stock Pneumatic's load sensitivity is greater relative to the other drive wheels, leading to larger differences in drive wheel scrub torque in the 80% WD wheelchair configuration. Combined with the existing large separations between the drive wheels, these results suggest the impact of component selection on drive wheel scrub torque, and that this impact becomes more pronounced with increased drive wheel weight-distribution for the Stock Pneumatic.

Table 15. Caster and Drive Wheel Scrub Torque on Carpet

| Scrub Torque [Nm] | | | | | | |
|-----------------------------|------------------|------|------|-------------------|----------|-----------|
| <i>Carpet</i> | Caster Load (kg) | | | Linear Regression | | |
| Caster | 20 | 15 | 10 | Coefficient | Constant | R-squared |
| 6 x 1" Pneumatic | 2.53 | 1.75 | 1.19 | 0.133 | -0.177 | 0.991 |
| 5 x 1.5" Primo SR | 1.78 | 1.41 | 0.89 | 0.089 | 0.018 | 0.99 |
| 4 x 1.5" FLSR | 1.69 | 1.35 | 0.85 | 0.084 | 0.045 | 0.988 |
| 6 x 1" FLNC | 1.46 | 1.14 | 0.72 | 0.074 | 0 | 0.995 |
| 6 x 1.5" Primo | 1.55 | 1.05 | 0.63 | 0.092 | -0.302 | 0.997 |
| 6 x 1" Primo | 1.38 | 1.05 | 0.69 | 0.068 | 0.02 | 0.999 |
| 5 x 1" Primo | 1.41 | 1 | 0.66 | 0.075 | -0.103 | 0.998 |
| 3 x 1" FLNC | 1.21 | 0.93 | 0.53 | 0.068 | -0.13 | 0.988 |
| <i>Carpet</i> | DW Load (kg) | | | Linear Regression | | |
| DW | 30 | 35 | 40 | Coefficient | Constant | R-squared |
| 24 x 1" Spinergy | 6.41 | 7.24 | 8.32 | 0.191 | 0.626 | 0.994 |
| 24 x 1" Schwalbe Right Run | 5.9 | 6.87 | 8.15 | 0.224 | -0.874 | 0.994 |
| 24 x 1-3/8" Stock Pneumatic | 5.23 | 5.82 | 6.36 | 0.114 | 1.827 | 0.999 |
| 24 x 1" Solid Mag | 4.82 | 5.49 | 7.05 | 0.224 | -2.045 | 0.95 |

Comparing the tile scrub torques of casters and drive wheels, we see that all drive wheels present markedly greater scrub torques than the casters across all load configurations, and exhibit a greater load sensitivity compared to all casters except the 6 x 1" Pneumatic. Thus, contrary to rolling resistance, the shifting of more load onto the

casters is the most effective means of reducing the combined drive wheel and caster scrub torque. However, the instances of caster and drive wheel scrub may not be as coupled as the instances of caster and drive wheel rolling, suggesting that the effectiveness of this approach is more dependent on the type of curvilinear maneuvers executed.

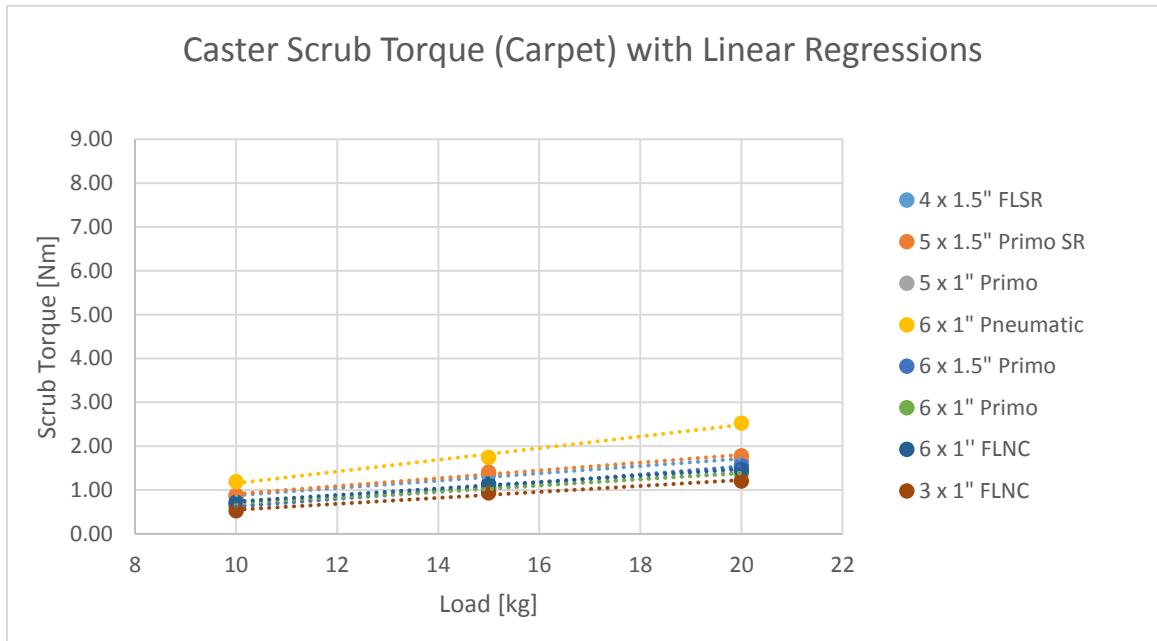


Figure 43. Caster Scrub Torque on Carpet

For casters on carpet, the scrub torque average across all three loads ranged from 0.89 – 1.82 Nm, with the lowest being the 3 x 1" FLNC and the highest being the 6 x 1" Pneumatic. Switching between these two casters equates to a 104% increase in average rolling resistance. For drive wheels on tile, the scrub torque average across all three loads ranged from 5.79 – 7.32 Nm, with the lowest being the Solid Mag and the highest being the Spinergy. Switching between these two drive wheels equates to an 84% increase in rolling resistance.

As a whole, the caster scrub torques changed very little between tile and carpet results, increasing only 0.22 Nm in scrub torque on average. In fact, the 5 x 1.5" Primo SR was entirely insensitive to the surface differences, while the 6 x 1" Pneumatic diminished slightly in both average scrub torque and load sensitivity, and almost all of the remaining casters increased marginally in both average scrub torque and load sensitivity. The ranking of casters by scrub torque underwent a single change, where the 5 x 1" Primo was reduced to the caster with the second lowest scrub torque on carpet. As a result of these changes, the differences between the caster scrub torques became more muted on carpet.

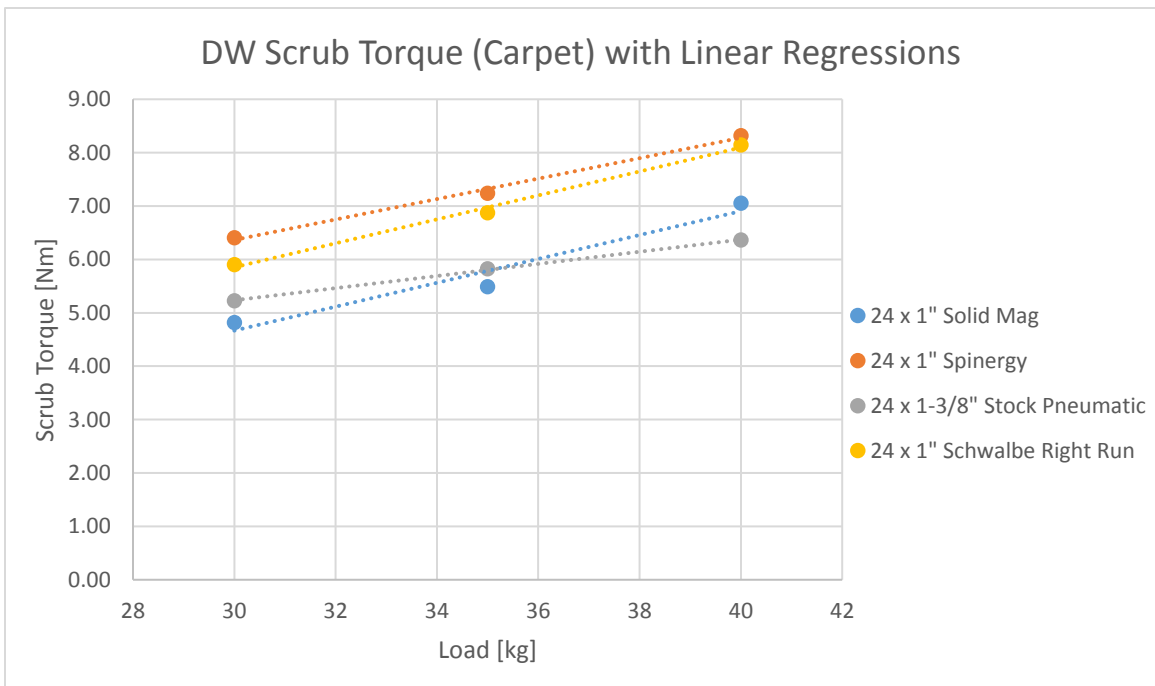


Figure 44. Drive Wheel Scrub Torque on Carpet

In transitioning from tile to carpet, the drive wheel scrub torques increased by 1.14 Nm in scrub torque on average. In **Figure 44**, however, we can see that the Stock Pneumatic's scrub torques decreased by an average of 1.15 Nm across all three loads, while the remaining drive wheels increased in scrub torque by an average of 1.90 Nm. Furthermore, while the load sensitivities of these three drive wheels did not vary much

from tile to carpet, the Stock Pneumatic's load sensitivity decreased from 0.246 Nm/kg to 0.114 Nm/kg. This ultimately results in the Stock Pneumatic having the least scrub torque on carpet at any weight distribution greater than 70%WD (35 kg on drive wheels). This difference between tile and carpet indicates that the utility of the Stock Pneumatic has become more advantageous on carpet in reducing drive wheel scrub torque.

2.5.4 Combined Analysis

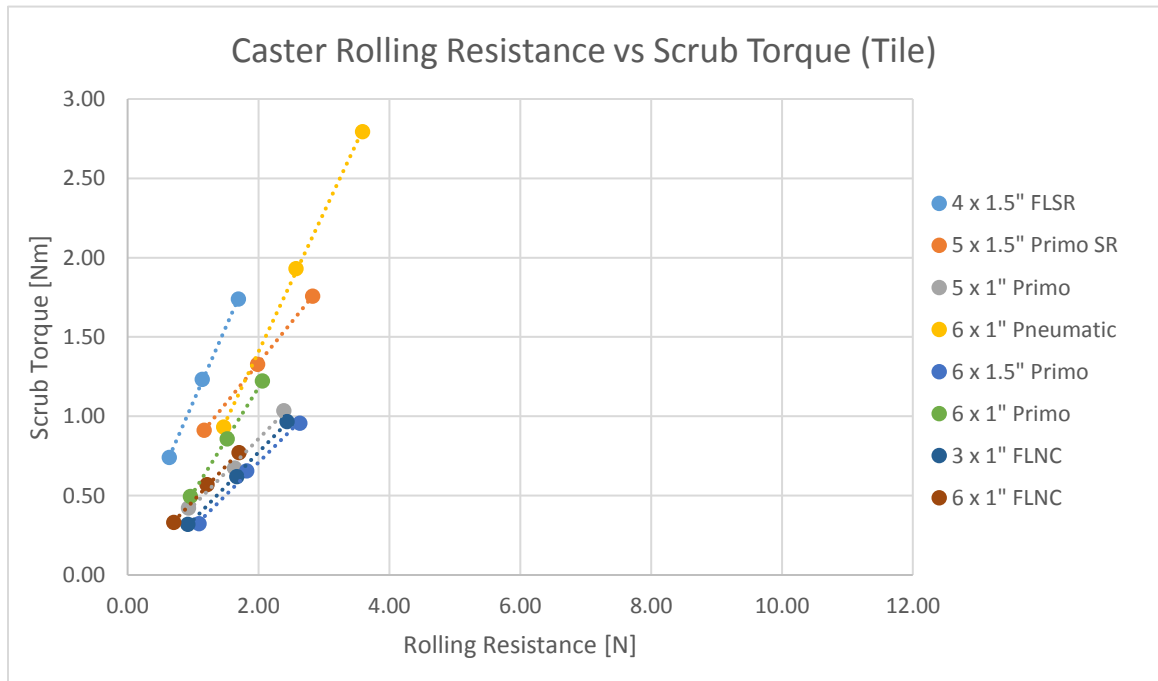


Figure 45. Caster Rolling Resistance versus Scrub Torque on Tile

To better visualize the combined resistive loss properties of components across surface types, **Figure 45**, **Figure 46**, **Figure 47**, and **Figure 48** plot rolling resistance versus scrub torque for casters and drive wheels on tile and carpet. Looking at **Figure 45**, we can see that the 4 x 1.5" FLSR experiences the lowest rolling resistance but has a moderate scrub torque. In contrast, the 3 x 1" FLNC experiences the lowest scrub torque but has a midrange rolling resistance. The 6 x 1" Pneumatic is high in both scrub torque and rolling resistance, and based on the spread of its points, is quite sensitive to load. In

contrast, the 6 x 1" FLNC is less sensitive to load, especially in terms of scrub torque, and represents one of the best balances in minimizing both types of resistive loss. However, depending on the nature of the usage, minimizing one type of resistive loss may take precedent over the other. For example, cases of heavy in-home MWC use may prioritize minimizing caster scrub due to the frequent direction changes, while long-distance outdoor usage would benefit more from a caster of lower rolling resistance.

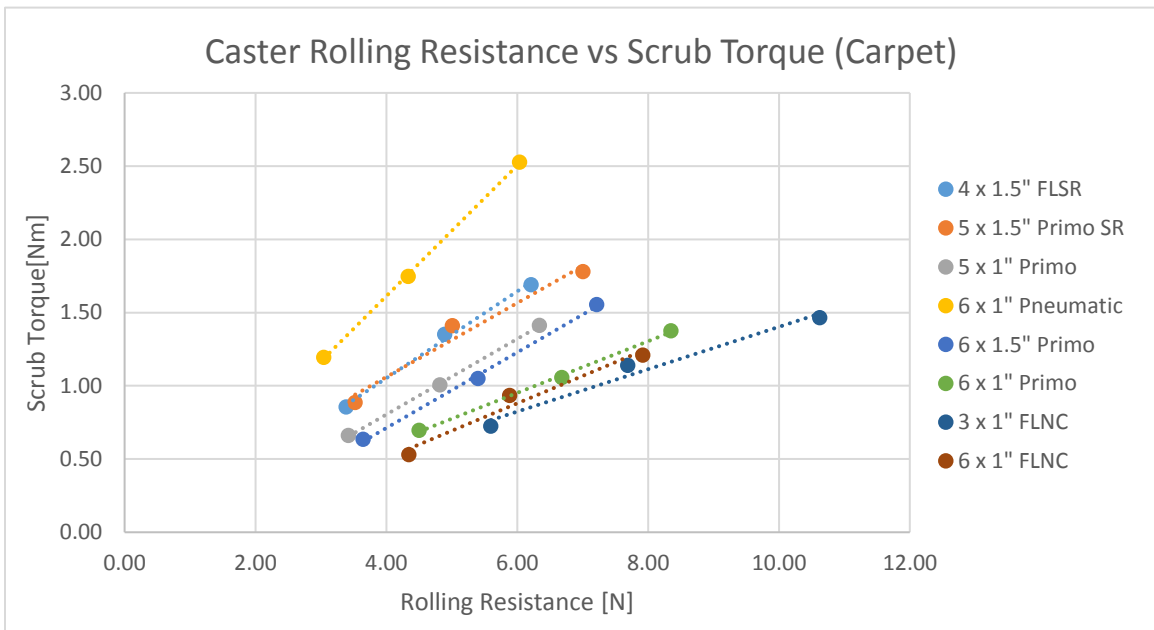


Figure 46. Caster Rolling Resistance versus Scrub Torque on Tile

In **Figure 46**, we observe that the 6 x 1" Pneumatic still experiences the greatest scrub torque on carpet, but has also shifted to exhibit the least rolling resistance on carpet. The 3 x 1" FLNC experiences increases in both resistive losses, with moderate scrub torque and the largest rolling resistance. On carpet, the 6 x 1" FLNC is no longer the most balanced caster due to its relative increase in rolling resistance. Instead, the 5 x 1" Primo offers a good compromise between scrub torque and rolling resistance on carpet.

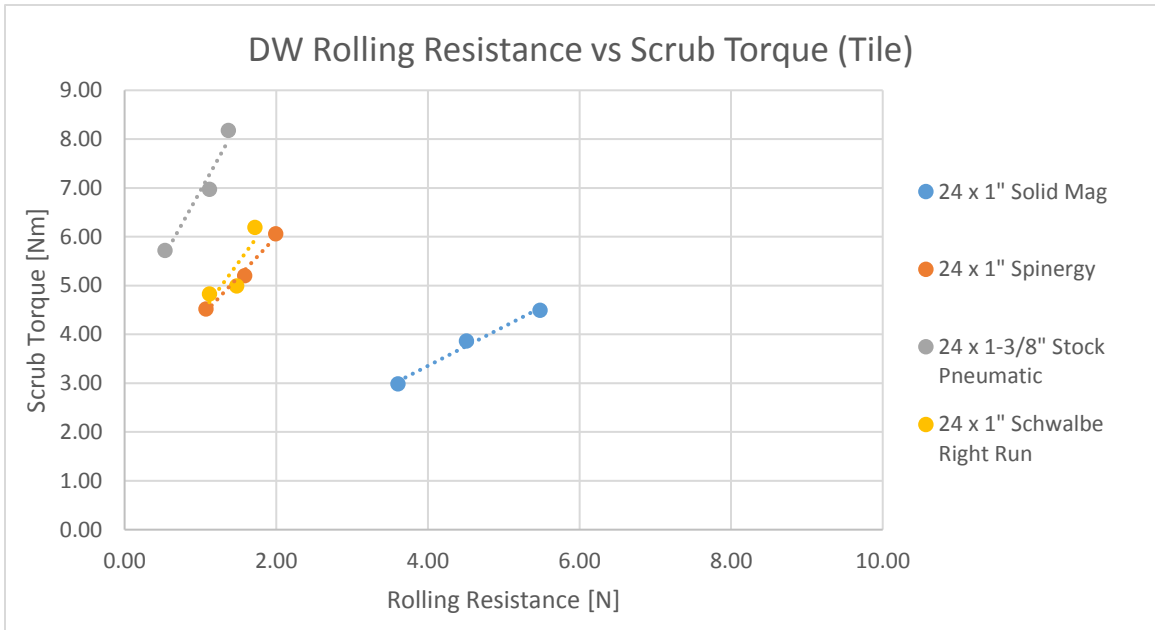


Figure 47. Drive Wheel Rolling Resistance versus Scrub Torque on Tile

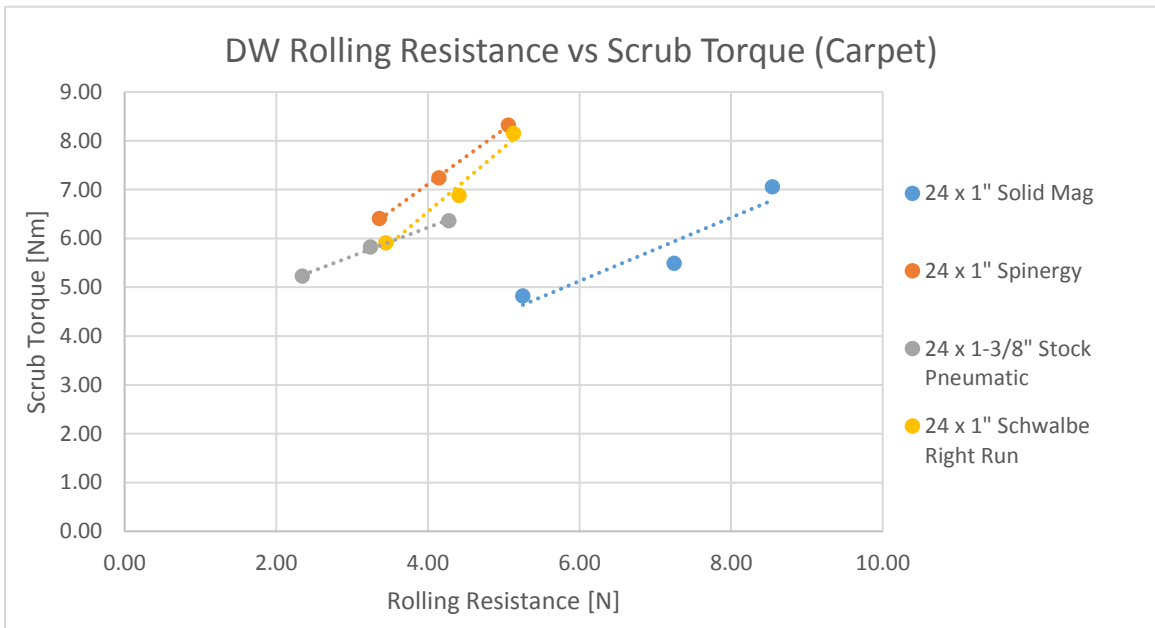


Figure 48. Drive Wheel Rolling Resistance versus Scrub Torque on Carpet

Figure 47 and **Figure 48** clearly illustrate the much larger differences in the resistive losses across drive wheels. On tile, the Solid Mag exhibits the lowest scrub torque, but is by far the greatest in rolling resistance. Its separation from the other drive

wheel rolling resistances is diminished on carpet, but at the cost of a reduced relative benefit in scrub torque. Amongst the four drive wheels, the Solid Mag's rolling resistance is the most sensitive to load. The Stock Pneumatic displays the least rolling resistance and both tile and carpet, and has the greatest scrub torque and load sensitivity to scrub torque on tile. The Spinergy and Schwalbe Right Run have very similar resistive losses across both surfaces. On tile, they are quite balanced with low rolling resistances and moderate scrub torques. On carpet, however, they both exhibit the highest scrub torques.

The collective results of the drive wheels demonstrate the tradeoffs between reducing rolling resistance and scrub torque. However, unlike casters, reducing drive wheel turning resistance beyond a threshold may negatively impact wheelchair traction and stability during turning. With this caveat in mind, we proceed to observe that the Solid Mag can be selected to minimize turning resistances at the expense of a greater rolling resistance, while the Stock Pneumatic has the least rolling resistance but is greatest in turning resistance on tile. On carpet, the differences in drive wheel scrub torque are diminished, and the Stock Pneumatic turning resistance is reduced relative to the Spinergy and Schwalbe Right Run. The Spinergy, sold commercially as high-cost, high-end drive wheels, do not seem to reflect a superior performance in either rolling resistance or scrub torque. While they can be said to be "balanced" on tile, their higher turning resistance and still greater rolling resistance than the Stock Pneumatic makes it difficult to warrant them as a performance improvement worth the cost.

CHAPTER 3. ANATOMICAL MODEL PROPULSION SYSTEM

The Anatomical Model Propulsion System (AMPS) is a robotic system designed to propel a MWC through maneuvers that reflect wheelchair usage in everyday life while measuring the applied propulsion forces and wheelchair kinematics (Liles et al., 2014). The AMPS is designed to autonomously navigate predefined maneuvers that, together, encompass all the important dynamic response characteristics of manual wheelchair propulsion. Derived results - obtained from the recorded wheel velocity and motor current data - are a set of torques and work energies corresponding to the various maneuvers, which collectively characterize the wheelchair as a mechanical system. The AMPS can be described via three primary subsystems: the anthropomorphic structure, the propulsion system, and the data acquisition system.

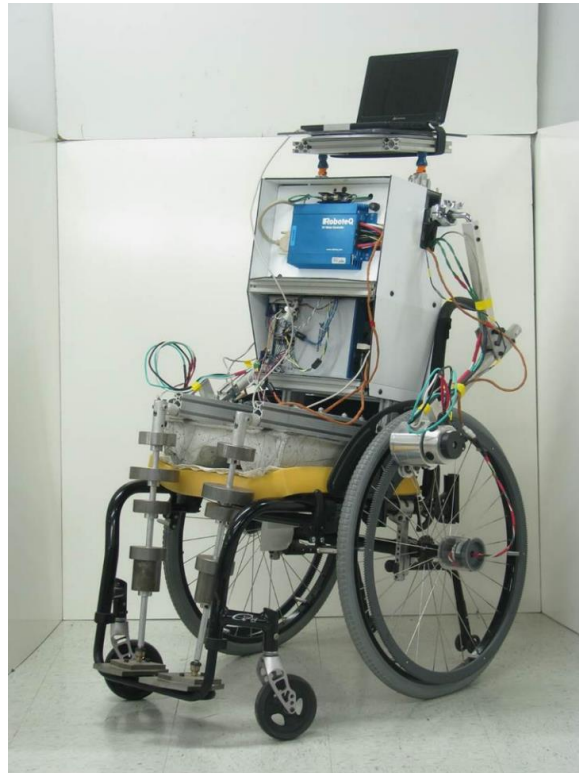


Figure 49. The Anatomical Model Propulsion System (AMPS)

3.1 System Design and Rationale

3.1.1 Anthropomorphic Design

The AMPS (**Figure 49**) represents a human operator in an abstract form, and was designed to be consistent with the wheelchair dummy used in standardized test methods defined in ISO 7176-11 (International Standards Organization, 2008). Using ISO 7176, the AMPS was designed with a mass of 100 kg to test typical adult size wheelchairs. Length parameters were defined by assessing the ISO 7176 dummy and relating its dimensions to the anthropometry of the Hybrid III ATD (Foster J, Kortge J, & Wolanin M, 1977) (**Table 16**). Overall, the AMPS reflects the body segment parameters of an American male at the 50th percentile in height and 95th percentile in mass.

Table 16. AMPS Body Segment Parameters

(Based on 100kg Wheelchair ISO Dummy and Hybrid III 50TH ATD)

| | Referenced metric | Referenced value | Reference |
|-----------------|--|------------------|--------------------------------------|
| Segment Mass | Torso (including head, arms, trunk) | 61±3 kg | ISO 7176-11 |
| | Upper Legs (including pelvis & thighs) | 31±3 kg | ISO 7176-11 |
| | Lower Legs | 7±1 kg | ISO 7176-11 |
| | Total | 100+5/-2 kg | ISO 7176-11 |
| Center of Mass* | Trunk (x-axis or fore-aft) | 68±10 mm | ISO 7176-11 |
| | Trunk (z-axis or vertical) | 298±10 mm | ISO 7176-11 |
| | Upper Legs (x-axis) | 203±10 mm | ISO 7176-11 |
| | Upper Legs (z-axis) | 67±10 mm | ISO 7176-11 |
| | Lower Legs (vertical from foot) | 235±3 mm | ISO 7176-11 |
| Segment lengths | Seated Shoulder Height (from seat surface) | 561 mm | Hybrid III 50 th Male ATD |
| | Shoulder Breadth | 455 mm | CAESAR Database |
| | Buttock to Knee Pivot | 550 mm | Hybrid III 50 th Male ATD |
| | Knee Pivot Height (from ground surface) | 498 mm | Hybrid III 50 th Male ATD |
| | Hip Breadth | 414 mm | CAESAR Database |

* Origin located at the midpoint of line formed by wheelchair seat and back planes intersecting.

The size and weight specifications are utilized to capture the inertia of an occupied wheelchair and the interaction between the occupant and the wheelchair. This interaction primarily consists of loadings on the frame joints, the casters and drive wheels, and their bearings. Matching the inertia and mass of the wheelchair user is vital, given that the user heavily influences the inertia and resistive losses within the wheelchair system.

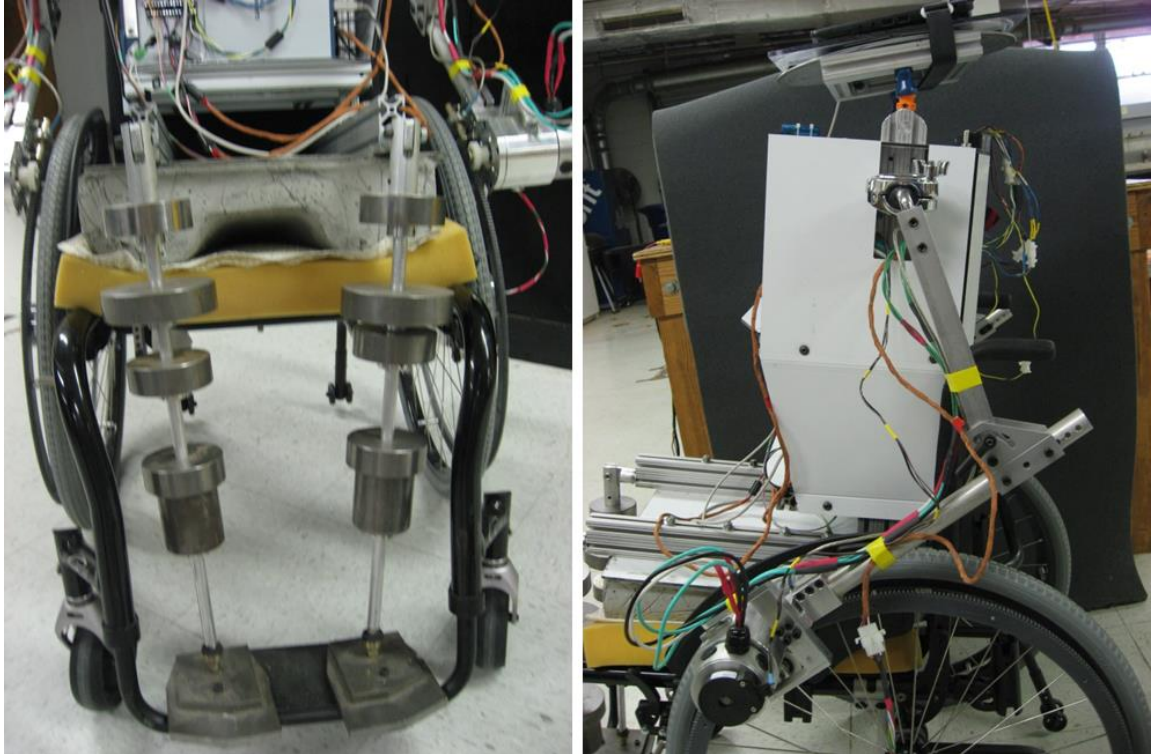


Figure 50. AMPS Leg and Torso Segments

The AMPS torso structure is composed of an aluminum frame that houses the batteries that power the AMPS, and together they approximate upper body mass. A concrete mold shaped to match the mass and profile of the human posterior supports the torso structure. This mold connects to two aluminum rods, which serve as the lower legs as shown in **Figure 50**. Weights are affixed along the length of these rods to mimic the mass distribution of the lower legs and feet. The arms are attached to the upper torso via a ball joint and are composed of aluminum tubing. The ball joints provide a significant range

of adjustability for the positioning of the arms on various manual wheelchairs. At the end of these adjustable arms, the motor housings are attached. Of note is the fact that this modular design offers the flexibility to alter the mass and mass distribution of the AMPS in order to model different types of wheelchair users.

3.1.2 Propulsion Control

The AMPS propulsion system was designed to emulate human propulsion forces by using tangential force drive, dedicated pushrim interfacing, and high-torque DC motors.

Manual wheelchairs are conventionally propelled by human users applying force to the pushrims. This applied force can be deconstructed to three force components: tangential, radial, and normal to the pushrim plane. In this case, only the tangential force performs work that contributes to propelling the wheelchair. However, humans are biomechanically constrained so that applying purely tangential force is impossible (Rozendaal LA, Veeger HE, & van der Woude LH, 2003). By applying purely tangential force to each pushrim, AMPS is able to isolate the efficiency of the mechanical design without the confounding inefficiencies associated with biomechanics. Additionally, the need to maneuver the wheelchair using differential drive led to the decision to use DC motors. Independent control of two DC motors enables turning and bidirectional motion, and the proximal motor mounting to the drive wheel offers a simple transmission. These motors contact the ring gears about 40 degrees forward of the top dead center of the drive wheel (**Figure 50**). This “hand” is positioned in the center of a wheelchair user’s contact with the pushrim during a propulsion stroke, making it coincident with where peak forces are applied in human kinetic studies (Robertson, Boninger, Cooper, & Shimada, 1996).

To accommodate the variety of manual wheelchair pushrim styles, two design alternatives were considered: 1) design a propulsion system that would be compatible with all pushrim sizes and cross-section shapes (van der Linden, Valent, Veeger, & van der Woude, 1996), or 2) design a dedicated pushrim that can be attached to all wheelchairs during testing. The latter approach was selected because it offered a standard interface that enabled consistent force input, a more robust gripping mechanism, and an overall simpler design. This dedicated handrim is a PVC ring gear interfaced with the motors via a pinion gear, as depicted in **Figure 51**. The ring gear has a mass of 0.75 pounds, which is within the range of commercial pushrims, whose weights vary between 0.7 and 1.5 pounds.

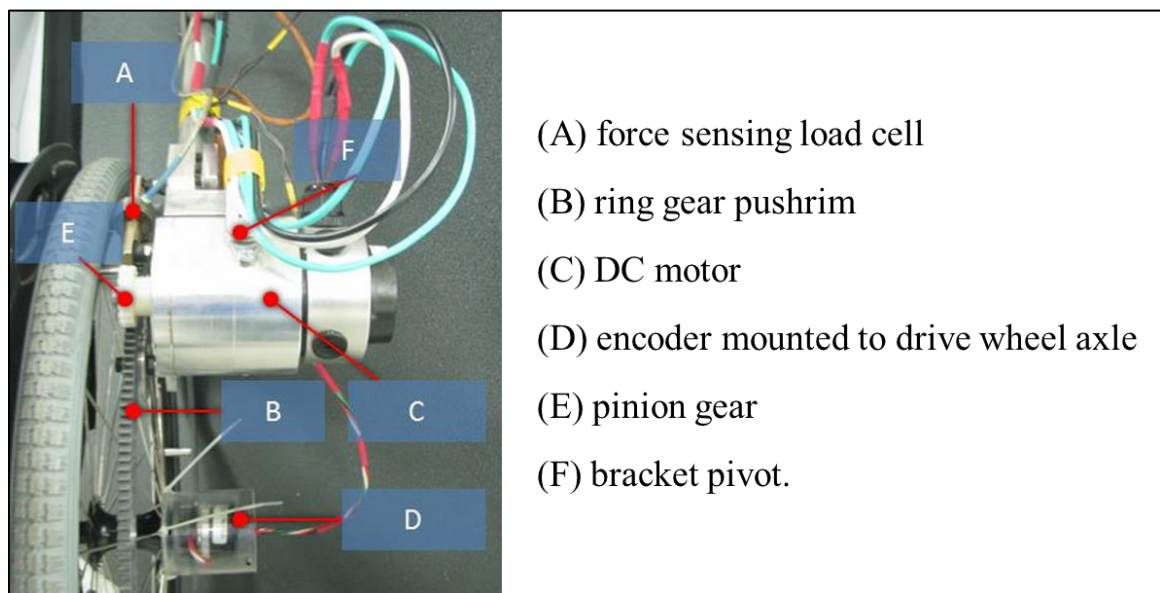


Figure 51. Gear and sprocket interface between motor and pushrim

DC motor specifications were based upon the torque demands required of over-ground motion. Literature sources indicate that the maximum tangential pushrim force applied during typical steady-state propulsion (~0.75 m/s) is less than 100N (22.5 lbf), and averages at 81N (18.2 lbf) (Robertson et al., 1996). Selection of an appropriate high-torque DC motor was based on matching the motor's peak efficiency torque to the nominal 81N,

while assuming a pinion gear pitch diameter of 1.25-in. An additional constraint required that the motor max RPM achieve a minimal 0.75 m/s tangential velocity on the pinion gear during peak motor efficiency.

Based on these specifications, a pair of A28-150 Ampflow motors was chosen to provide propulsion to the wheelchair, with one for each drive wheel. The motors selected for this design meet the torque and speed requirements of the system and are contained with a specialized housing fixture that enable them to appropriately interface with the load cell sensor bracket. This bracket contains two components – a force-sensing load cell and a pivot axis for the motor – which work in conjunction to enable direct measurement of the tangential force applied to the pushrim.

The motors are also directly attached to the AMPS arms so that the loading induced by action and reaction forces at the motor-pushrim interface will be translated to the upper torso via the shoulder joint in the same manner as would occur if the chair were being propelled by a human user. This enables the selected design to achieve realistic and representative loading on the MWC frame and upholstery. This configuration also enables widespread adaptability for a multitude of manual wheelchair designs and sizes. The propulsion of the AMPS is controlled by a Roboteq motor controller. This controller is supplied power by a set of four 12-volt batteries and serves as the interface through which the motors are powered. These internal batteries enable the AMPS to maneuver through a variety of environments without the need to connect to a local power source. This motor controller incorporates PID parameters and executes the closed loop velocity control of the motor system. While all desired trajectories are programmed via a NI data acquisition (DAQ) device, all real-time control of the motor is managed by the Roboteq controller.

Upon receiving the input command from the NI device, the controller performs the necessary real-time calculations to incorporate the feedback from the motor encoders, and continuously sends the appropriate commands to the motor. **Figure 52** depicts this control scheme, which is applied to the left and right motor separately.

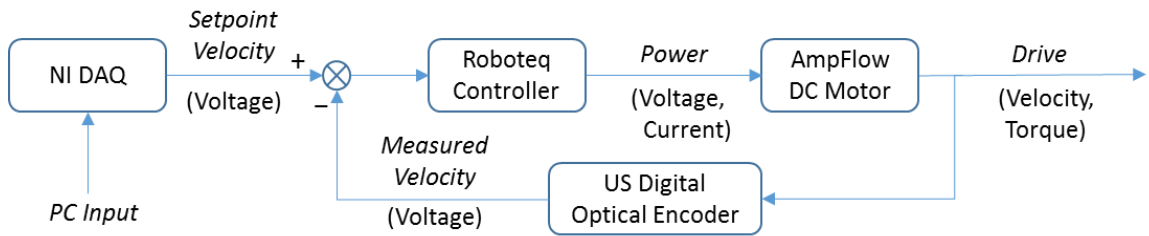


Figure 52. AMPS Control Diagram

The visual interface for the “PC Input” allows for maneuver kinematics to be defined by either manual entry or uploading predefined trajectory files. The manual entry is limited to defining a trapezoidal velocity profile for each drive wheel. The adjustable parameters using this method are wheel speed, ramp start time, ramp up duration, cruise duration, ramp down duration, coast duration, and wheel radius. By setting the wheel velocity and ramp times, it also become possible to dictate the acceleration and deceleration rate of the maneuver. Setting the velocity profiles for both wheels to be identical results in straight trajectories, whereas setting them differently results in various curvilinear paths. These parameters can be seen in the LabVIEW VI screenshot, **Figure 53**.

For maneuvers where the drive wheel(s) needs to accelerate or decelerate to multiple steady-state velocities, or for instances where the acceleration is non-constant, the use of a predefined trajectory file is required. These files are formatted as text files with two comma-separated columns, each representing the left and right wheel’s angular velocity, respectively. Since the NI DAQ is set to sample at 40 Hz, each row in the text

files are separated by 25 ms to match the real-time loop of the LabVIEW program. These text files are generated via a MATLAB code that takes a time vector, linear velocity vector, and wheel radius for each wheel. Figure 54 illustrates how the trajectory files are then selected for use in the LabVIEW program.

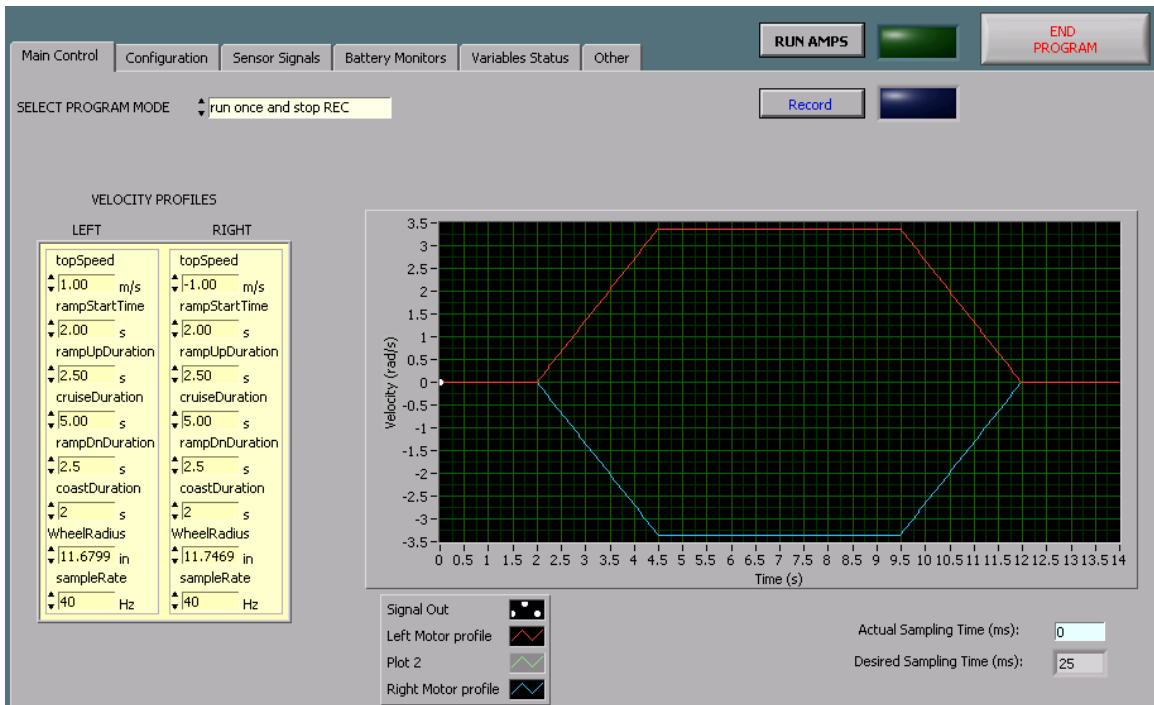


Figure 53. AMPS VI Manual Trajectory Entry

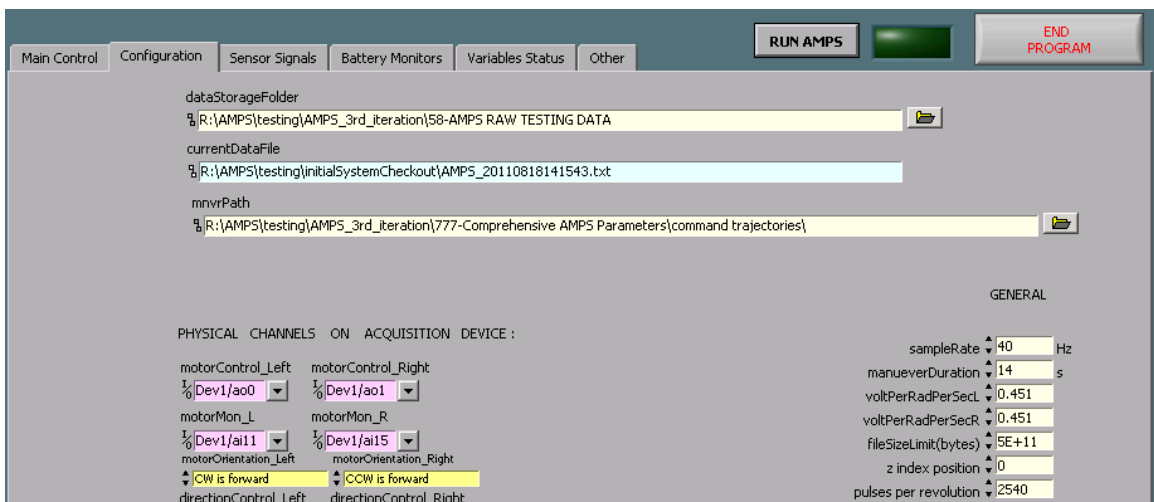


Figure 54. AMPS VI Pre-defined Trajectory

3.1.3 Data Acquisition

The requisite condition for calculating task propulsion work involves knowing the propulsion torque while monitoring system kinematics. Within the AMPS, this entails measuring the motor current, tangential pushrim force, and the rotational position of the drive wheels.

Measurement of the motor current is motivated by its proportionality with the motor torque. Two ACS758xCB current sensors are integrated into the circuit powering the drive motors by directly connecting to the motor power cables. Within this circuit, the sensors monitor the current flowing into the motors. The output reading is in the form of a voltage that is proportional to the current flowing through the sensors and is recorded by the DAQ. This data provides direct measurement of the energy that is input into the AMPS to execute the desired maneuvers.

Load cell measurement of the tangential pushrim force serves as a redundant system for determining the drive wheel torque. A pair of Omega LCFA-50 load cells are mounted onto a bracket connected to the motor housing unit. During propulsion, the reaction force of the gear teeth is tangential to the ring gear pushrim, requiring that the AMPS arm be positioned such that the load cell axis is parallel to the ring gear tangent. In this orientation, the propulsion force can be accurately measured by the load cell.

The AMPS incorporates a pair of M-260 Accu-Coder axle mounted encoders, each attached to the central axle of a drive wheel (as shown in **Figure 51**) via a custom housing connector. These 2540 count encoders provide angular position data to the AMPS system, enabling precise measurement of the drive wheel motion. Using the known motion of the

drive wheels with the predetermined geometry of the wheelchair, the system kinematics can be derived for kinetic energy calculations (Medola, Dao, Caspall, & Sprigle, 2013).

A NI USB-6341 data acquisition system is used to record data and serves as the primary system controller for the AMPS. This DAQ connects to a computer via USB, and a LabVIEW visual interface is used to communicate with the DAQ. The DAQ collects all the data from the AMPS drive wheel encoders, current sensors, and load cells. It also sends analog voltage signal commands to the Roboteq motor controller. The DAQ system is powered by a lithium-ion battery that is completely independent of the batteries supplying power to the AMPS propulsion subsystem.

In all data used for analysis, the measured raw force, current, and velocity are filtered in post-processing by passing them through a 3rd order Butterworth filter with a cutoff frequency of 0.15 Hz (MATLAB).

3.2 Calibration and Validation

Because the AMPS is a fundamentally new approach to measuring mechanical efficiency of wheelchairs, validating the hardware and measurement techniques was required. Specifically, the motor current sensors were calibrated, followed by system-level validation to investigate the repeatability of the commanded trajectory and measured propulsion torque during over-ground wheelchair maneuvers. The load cells were eliminated from use entirely due to their comparatively noisy data output during over ground maneuvers. **Figure 55** illustrates the qualitative difference between data collected via the current sensors and load cells. It was postulated that this noisier data was due the load cell detecting transient motions of the motor arm itself. Note that the large spikes

from the load cell data could have been (and were) dealt with via low-pass filtering in post-processing. However, the overall reduced quality of the force data combined with the load cell sensitivity to non-tangent alignment with the wheel rim led to their elimination as an unreliable measurement source.

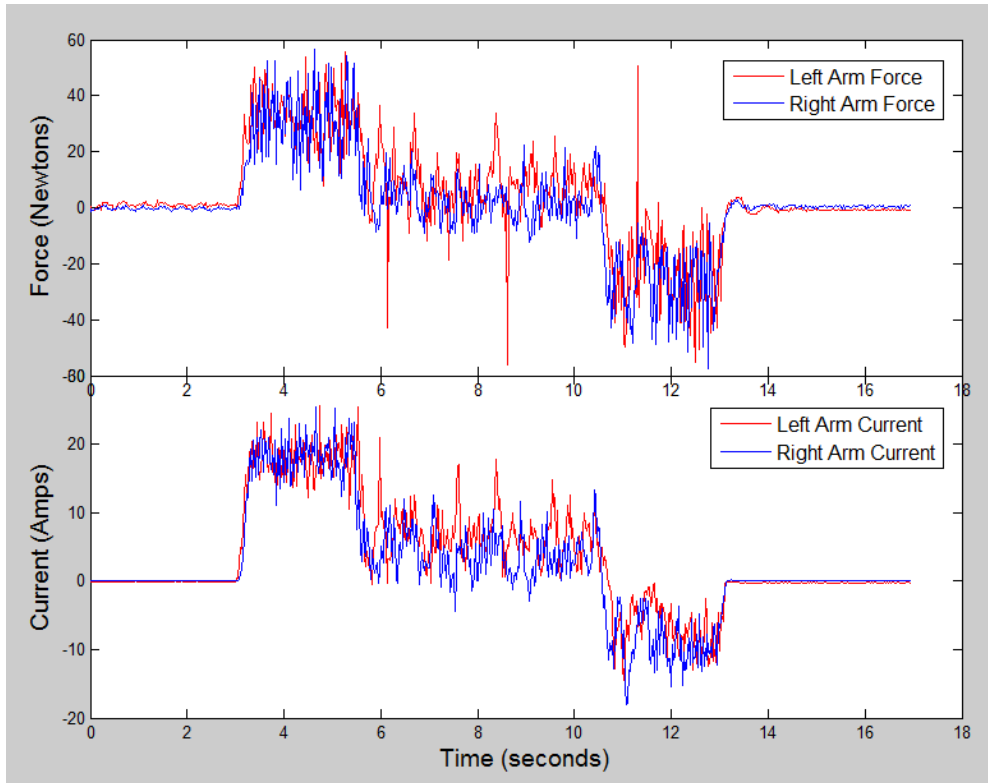


Figure 55. Comparison of Current (Torque) and Force Data

3.2.1 *Calibrating Motor Current Sensors*

To determine the relationship between current measured by the sensors and torque applied by the motors, some background on a motor’s current-torque curve is required. One of the properties of a DC motor is the proportional relationship between the current it draws and the torque it outputs. This is usually expressed as a “ K_t ” coefficient with units of torque per unit current (**Figure 56**). Furthermore, the current-torque curve is a piecewise function due the motor’s characteristic of no-load current.

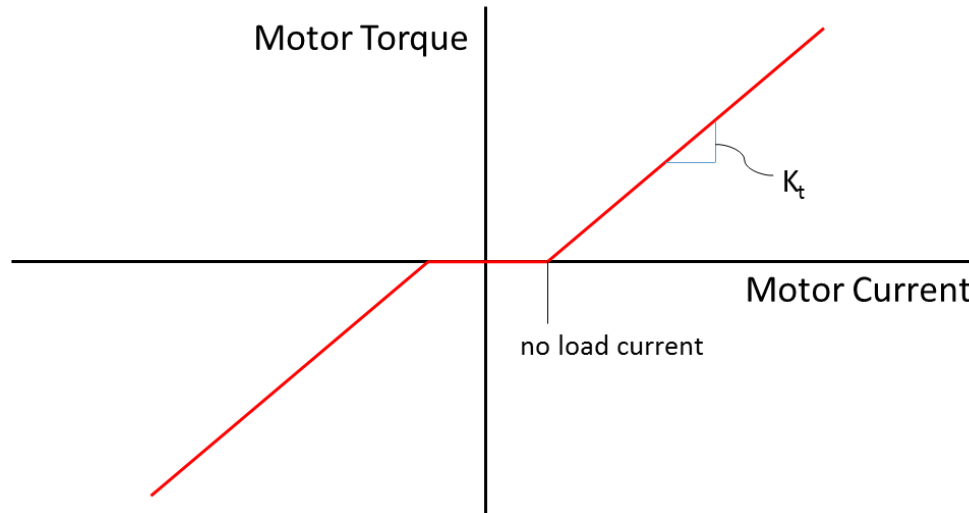


Figure 56. Motor Current-Torque Relationship

Therefore, to calculate these two defining properties, the motors were each loaded with a known torque by attaching a 3-inch diameter pulley to the motor shaft and using the motor as a winch to lift free-hanging weights of known mass. Simultaneously, the corresponding motor current for each applied torque was measured via the sensors and recorded. Several weights of varying mass were used to develop a calibration curve over a range of torques. The applied torques were determined by using mass of the weight, acceleration due to gravity and radius of the pulley. The measured current for each motor was then plotted against the applied torque, and a linear regression was fit to the data. **Figure 57** and **Figure 58** show the calibration curves for the two motors, both of which have an $R^2 > 0.99$. Based on the regression equation, the left motor was determined to have $K_t = 5.61$ oz-in. and no-load current = 1.96 A, while the right motor had $K_t = 5.73$ and no-load current = 1.60 A. These calibrated values are relatively close to the AmpFlow manufacturer-provided value of $K_t = 5.32$, but also distinct from their no-load current of 3.4 A. With the features of the current-torque curve for each motor defined, a simple step-wise function was then used to calculate the motor torque from the sensor-measured

current. It is important to note that in **Figure 57** and **Figure 58**, these torque values seem quite small because they represent the torque coming directly from the motor.

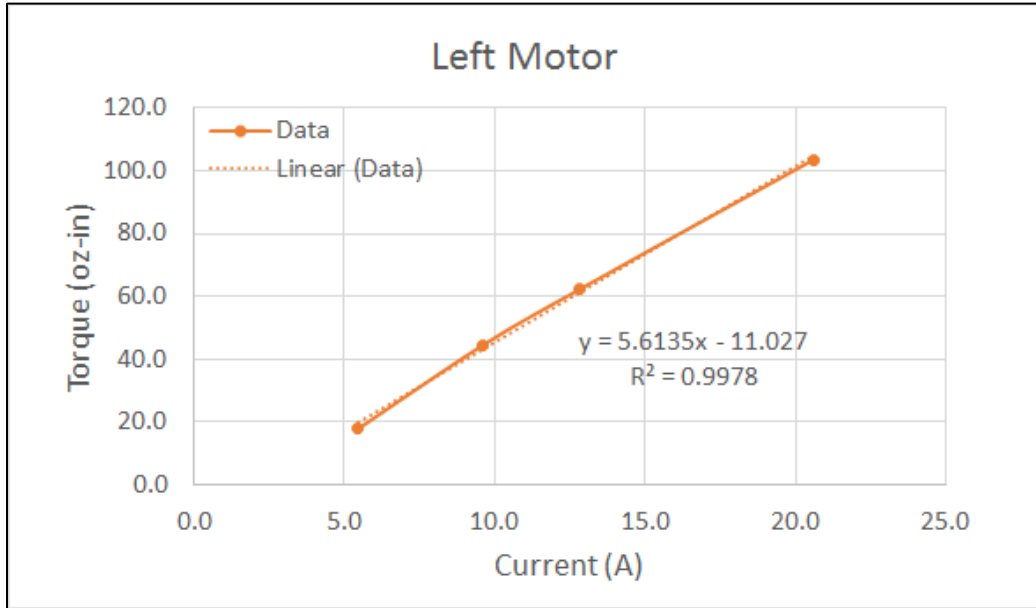


Figure 57. AMPS Left Motor Calibration

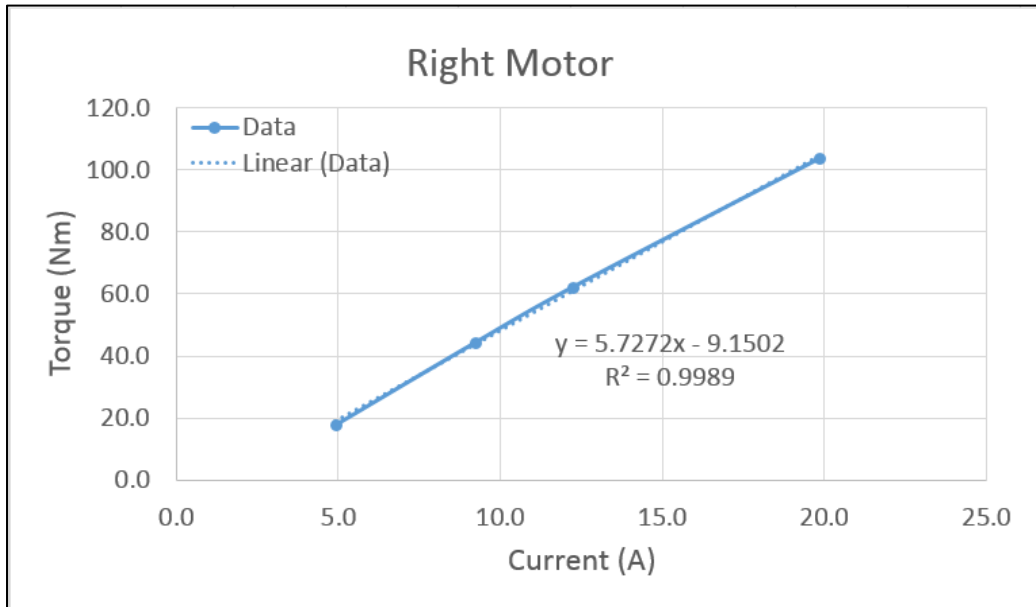


Figure 58. AMPS Right Motor Calibration

The torque of interest, or the drive wheel torque, is determined by the following equations (**Equations 11 and 12**).

$$\frac{\tau_{wheel}}{N_{ring\ gear}} = \frac{\tau_{motor}}{N_{pinion\ gear}} \quad (11)$$

$$\tau_{wheel} = \frac{N_{ring\ gear}}{N_{pinion\ gear}} \tau_{motor} \quad (12)$$

Note that τ_{wheel} and τ_{motor} are the torques on the drive wheel and motor shaft, and $N_{ring\ gear}$ and $N_{pinion\ gear}$ are the teeth count of the ring gear and pinion gear. Since the gear ratio between the ring gear and pinion gear is 17, the range of drive wheel torques the calibration procedure spans is about 2-Nm to 13-Nm, encompassing the bulk of torque values encountered during AMPS's over-ground maneuvers.

3.2.2 System-level Validation

The AMPS was also validated on a systems-level by performing maneuvers on a tile floor. The AMPS was loaded onto a Quickie GT manual wheelchair with 24" diameter, spoked, pneumatic tires. A straight maneuver was programmed, consisting of acceleration to a steady state speed over 2.5 seconds, maintaining this speed for 5 seconds, and then ramping down to a stop over 2.5 seconds. This maneuver was conducted at two speeds, 1.4 m/s and 0.7 m/s, and for a total of ten trials in each condition. These speeds represent greater than average velocities based upon measurements of wheelchair users during everyday mobility (Sonnenblum SE, Sprigle S, & Lopez RA, 2012a). The maneuver was conducted ten times at each speed while measuring wheel velocity, current, and force data.

**Table 17. AMPS Propulsion Torque Repeatability
(Derived from Motor Current)**

| | | Left Drive Wheel Torque (Nm) | | |
|------------|--------------------|--------------------------------------|------------|----------------------|
| speed | | peak accel | peak decel | steady-state average |
| 1.4 m/s | mean | 15.25 | 11.37 | 2.65 |
| | standard deviation | 0.66 | 0.60 | 0.07 |
| | CV (%) | 4.10 | 5.02 | 2.39 |
| | SEM | 0.21 | 0.19 | 0.02 |
| 0.7 m/s | mean | 9.29 | 4.95 | 2.23 |
| | standard deviation | 0.44 | 0.49 | 0.14 |
| | CV (%) | 4.46 | 9.40 | 6.11 |
| | SEM | 0.13 | 0.15 | 0.05 |
| | | Right Drive Wheel Torque (Nm) | | |
| speed | | peak accel | peak decel | steady-state average |
| 1.4 m/s | mean | 12.44 | 12.70 | 1.71 |
| | standard deviation | 0.56 | 0.55 | 0.04 |
| | CV (%) | 4.30 | 4.10 | 2.27 |
| | SEM | 0.18 | 0.17 | 0.01 |
| 0.7 m/s | mean | 6.80 | 5.95 | 0.94 |
| | standard deviation | 0.49 | 0.38 | 0.07 |
| | CV (%) | 6.83 | 6.11 | 7.18 |
| | SEM | 0.15 | 0.12 | 0.02 |

Control system accuracy was characterized by comparing the programmed velocity profile to the measured velocity profile and computing the error between the two waveforms (**Figure 59**) every 0.5 seconds. Furthermore, the repeatability of the profile was characterized by determining the coefficient of variation of the entire maneuver for both the left and right wheels at both speeds (Table 17). Velocity error was ≤ 0.1 m/s for both the left and right wheels across both speeds. Propulsion torque metrics included peak acceleration, peak deceleration and the average steady state torque. Repeatability of propulsion torque (Table III) was assessed for repeatability using the coefficient of variation (CV) and standard error of the mean (SEM). As indicated by the values in **Table**

17, the AMPS control scheme can deliver an accurate velocity profile and the system can reliably measure propulsion torque during over-ground maneuvers. The CVs of the current-based torque were <5% during acceleration, <10% during deceleration and <8% during steady state velocity.

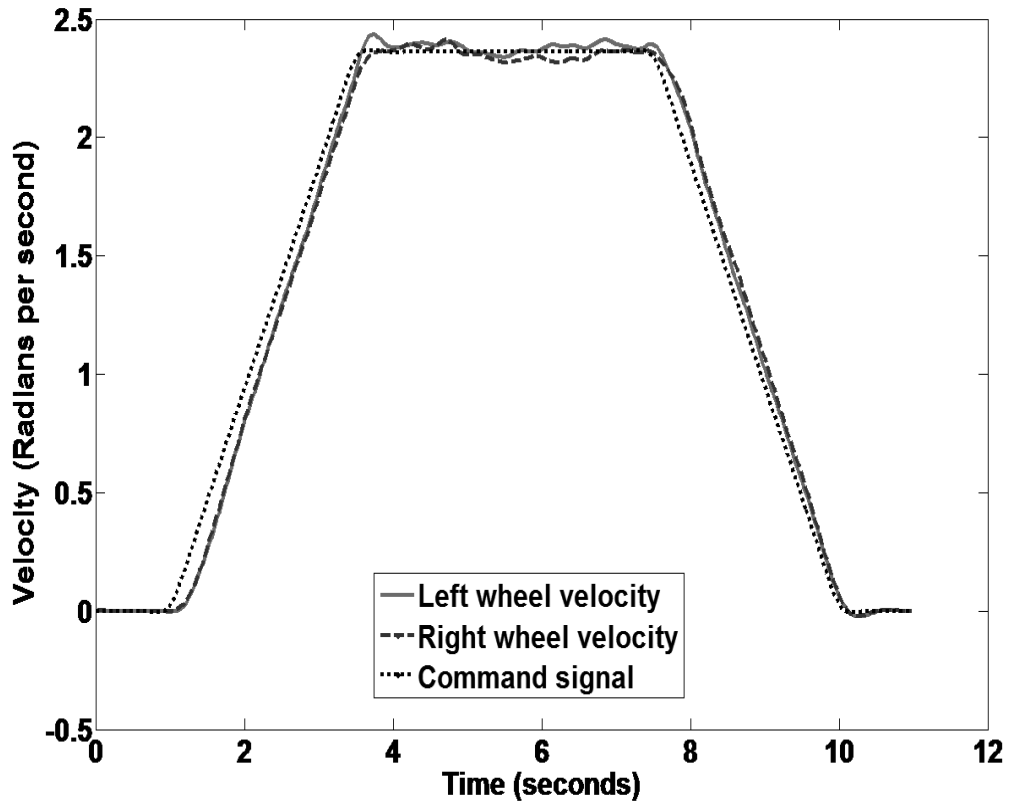


Figure 59. Angular velocity profile of drive wheels at 2.33-rad/sec (0.7 m/s)

CHAPTER 4. SYSTEM-LEVEL TEST METHODS

This chapter describes the system-level test methods that were developed to evaluate the mechanical performance of manual wheelchairs. Canonical maneuvers representative of everyday MWC mobility were defined and applied to the system-level tests. Models of MWC system-level kinetic energy and resistive energy loss were also used to generate additional rationale for the selection of canonical maneuvers. Clinically-relevant performance metrics were defined and applied towards two systems-level studies: 1) the impact of mass and weight distribution on propulsion torque, and 2) the impact of casters and drive wheels on propulsion cost.

4.1 Predicate Work (The iMachine)

In order to compare multiple different MWC configurations utilizing the AMPS, it is first necessary to characterize system-level properties of MWCs. According to literature (Brubaker, 1986; Caspall, Seligsohn, Dao, & Stephen Sprigle PhD, 2013), there are three particular attributes of MWC systems that can significantly influence propulsion effort: mass, yaw inertia, and weight distribution. Mass increases the rectilinear inertia of the system, thus requiring more force to propel the wheelchair in a straight motion. Yaw inertia is analogous to mass in turning motions, increasing the difficulty of changing direction quickly. Fore-aft weight distribution impacts not only the yaw inertia, but also the overall system resistances if the casters are more sensitive to loading than the drive wheels, and vice-versa.

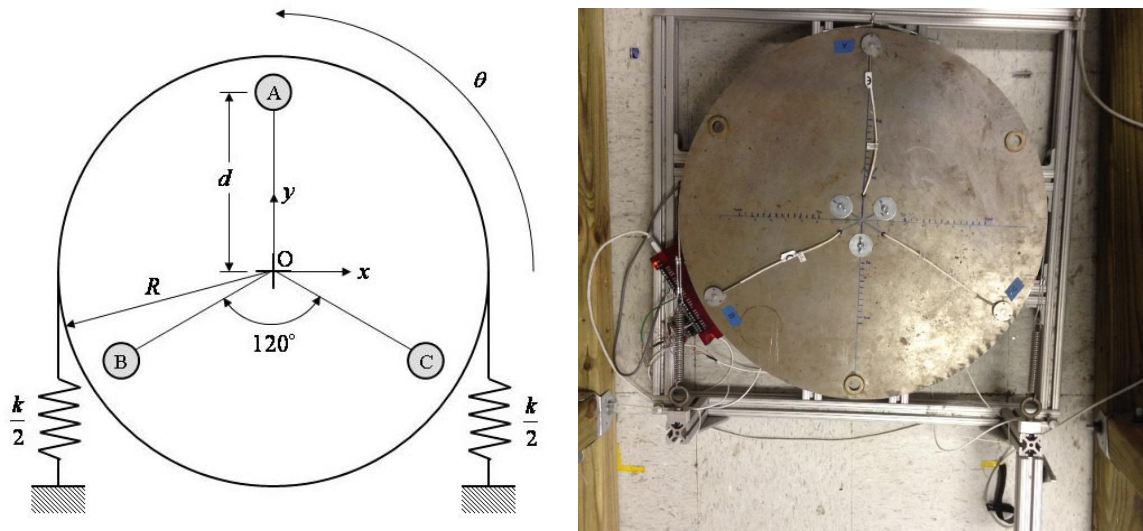


Figure 60. iMachine Schematic Diagram and Top View

The iMachine (Eicholtz et al., 2012) is a system-level measurement device that was designed precisely to characterize all three of the aforementioned system properties. The mechanical system is comprised of a turntable of circular steel mounted on a square frame of aluminum struts (80-20 Inc.). Two lengths of steel cable are anchored to one end of the turntable, and each run along the disc's circumference such that their other end attaches to a linear spring fixed to either the left or right vertical aluminum post (**Figure 60**). This effectively applies a torsional stiffness to the overall turntable. By applying a perturbation that induces a small angular displacement (~ 5 degrees), it is possible to determine the yaw (rotational) inertia of the disc and any mass placed atop it using the following equation,

$$I = \frac{K * R^2}{(w_n 2\pi)^2} \quad (13)$$

where I is the system yaw inertia, K is the combined spring stiffness, R is the disc radius, and w_n is the natural frequency of the disc rotation. Given that the spring stiffness and disc

radius are constant, the natural frequency is the only variable determined from instrumentation. This instrumentation comes in the form of a digital encoder (US Digital) that houses the stem of the turntable and tracks the relative angular position of the steel disc. However, it must be noted that in order to determine the yaw inertia of a MWC system (such as AMPS) placed atop the turntable, the MWC must be positioned with its center of mass over the axis of rotation. To accurately achieve this positioning, three button load cells (OMEGA Engineering) were fixed equidistance from the disc center and 120 degrees apart from each other.

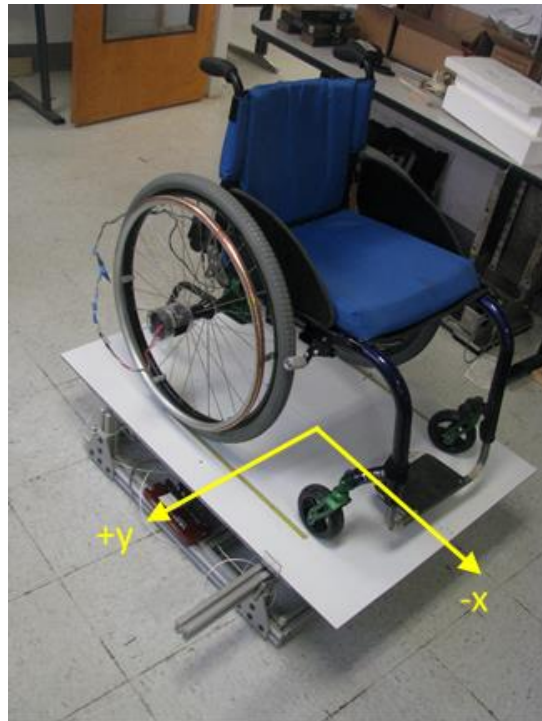


Figure 61. iMachine with a Manual Wheelchair Loaded on the Platform

A rectangular Dibond loading platform (**Figure 61**) reinforced with aluminum struts was then placed atop the disc such that the only three points of contact were the three load cells. Thus, by adjusting any MWC system placed on the loading platform until the load cells register a uniform reading, one can align the MWC center of mass with the axis

of rotation. As a helpful physical reference, the loading plate also has a coordinate system that corresponds to features on the disk. The origin is coincident with the center of rotation, the x-axis is parallel to the line connecting load cells B and C, and the y-axis intersects with load cell A. The remaining caveat to measuring MWC yaw inertia is that the yaw inertia of the unloaded disc and platform must first be measured (using the iMachine) so its value can be subtracted from the yaw inertia of loaded iMachine measurements.

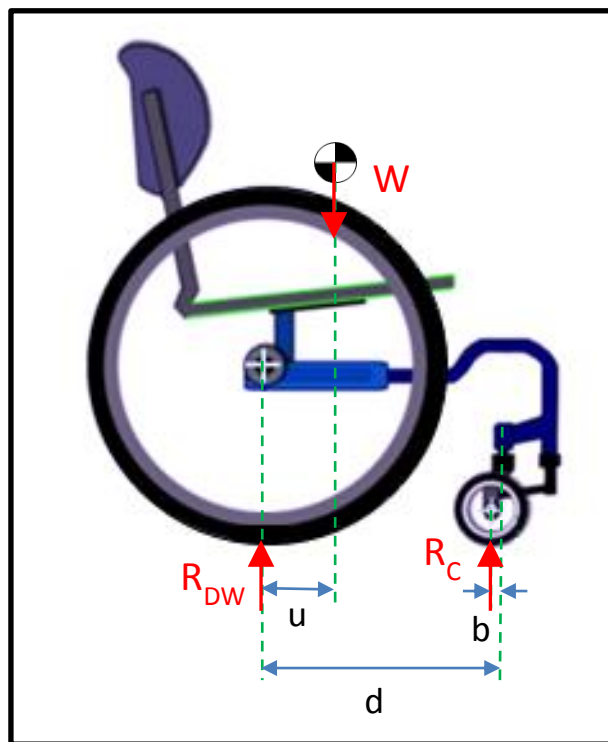


Figure 62. Free-body Diagram of Occupied Manual Wheelchair Normal Forces

Finding system mass using the existing iMachine instrumentation is a straightforward matter of summing the readings from all three load cells, given that the load cells have first zeroed out the mass of the loading platform. However, determining the MWC weight distribution requires additional information of the wheelchair dimensions. While the MWC is always adjusted to achieve lateral balance, the fore-aft weight distribution varies depending on the axle position relative to the center of mass

(COM) and front casters. Using the free-body diagram in **Figure 62**, we can take the sum of moments about the point the drive wheel ground reaction force (R_{DW}) is acting. Doing so, we find that

$$R_c = W \left(\frac{u}{d-b} \right) \quad (14)$$

where R_c is the caster ground reaction force, W is total load, u is the distance from the rear axle to the COM, d is the distance from the drive wheel axle to the caster fork stems, and b is the caster trail length. Normalizing this equation by the total load,

$$\% \text{ load on casters} = \left(\frac{u}{d-b} \right) \quad (15)$$

From this, we can also infer that

$$\% \text{ load on drive wheels} = 1 - \left(\frac{u}{d-b} \right) \quad (16)$$

For the scope of this research, **Equation 16** serves as the definition (termed %WD) for characterizing the fore-aft weight distribution of various MWC configurations due to its overlapping use in clinical settings. These dimensional parameters of the MWC system are determined via the use of a series of plumb lines and straight edges while the MWC is centered on the iMachine.

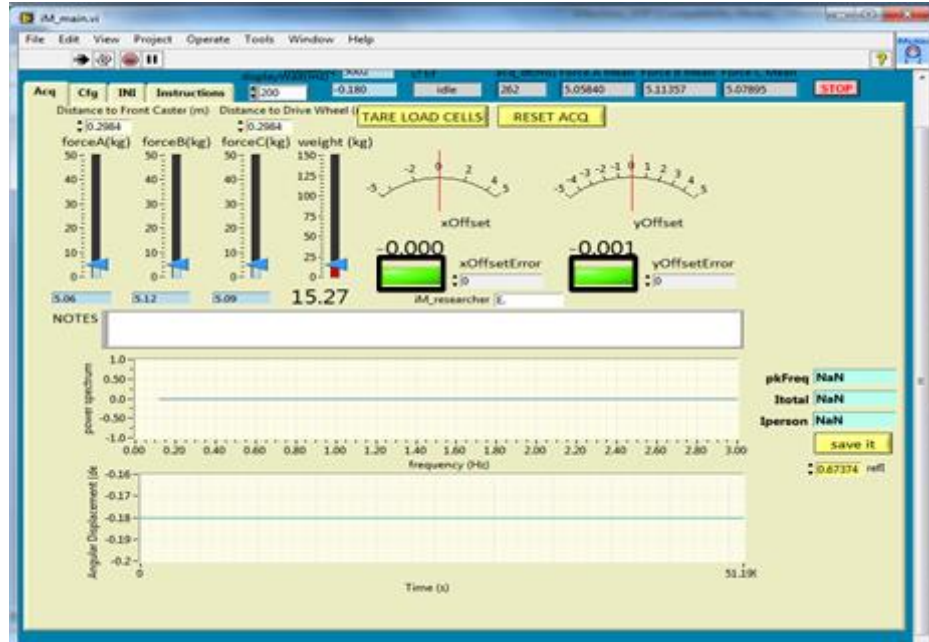


Figure 63. iMachine VI During Load Centering (black rectangles)

The iMachine data is collected in real-time via a LabVIEW program that runs off a LabJack DAQ. **Figure 63** displays the visual interface used to provide feedback on the MWC COM when loaded on the iMachine. As shown in the screenshot, the “xOffsetError” and “yOffsetError” denote (in meters) how far the MWC system’s COM is from the axis of rotation. As part of the protocol, all iMachine measurements were taken with offsets less than 5 mm. While all system yaw inertia measurements are corrected via the parallel axis theorem,

$$I_{sys} = (I_{measured} - I_{platform}) + M_{sys}(x_{offset}^2 + y_{offset}^2) \quad (17)$$

the tight alignment tolerance is enforced to avoid rotational imbalance that may skew measurements. After the MWC system is centered, the loading platform (and disc) is perturbed to rotate via the triangular arm shown in **Figure 64**.

The resultant periodic angular displacement measured by the encoder is sent to the LabJack and displayed on the VI as shown in **Figure 65**. The bottom display in the VI shows the window of angular displacement that is being used for yaw inertia calculation, and the top display is the fast-Fourier transform of the displacement data. The LabVIEW program extracts frequency of the dominant peak shown in this window uses it as the natural frequency for yaw inertia calculation in **Equation 13**.



Figure 64. iMachine Perturbation Triangle

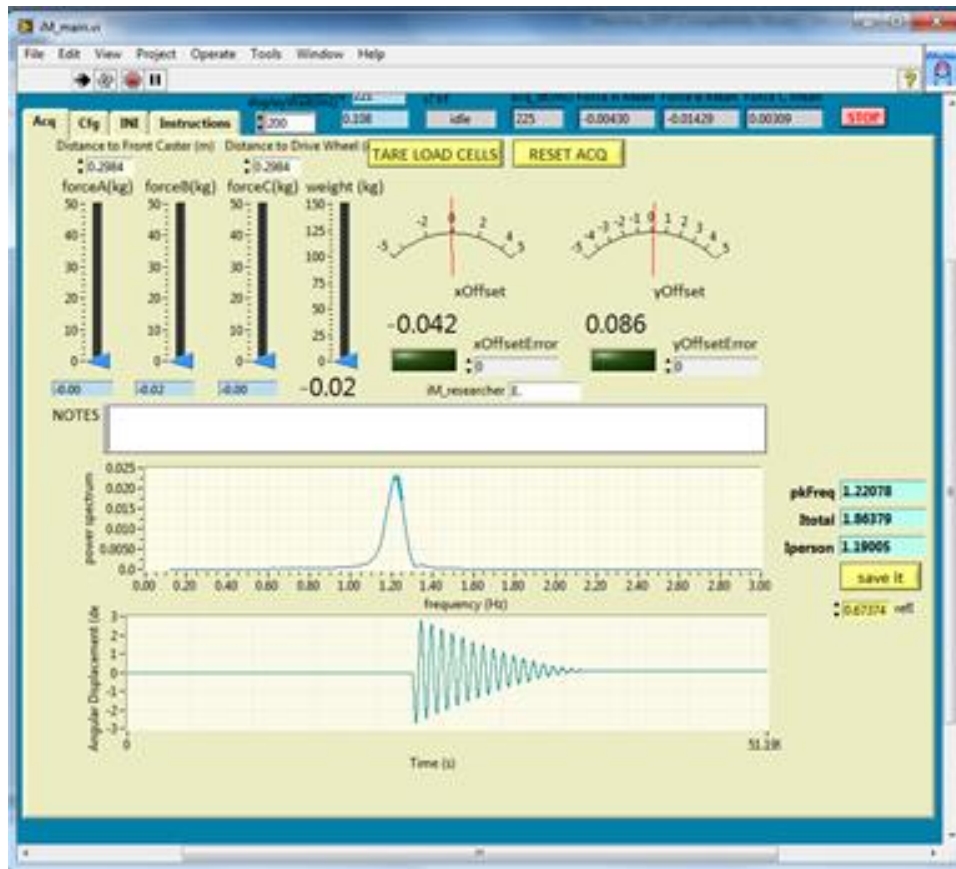


Figure 65. iMachine VI During Measurement of System Yaw Inertia

4.2 Defining Canonical Maneuvers

To fully characterize propulsion work, canonical maneuvers that represent typical MWC usage patterns were defined. These are relatively short maneuvers that collectively represent the complex maneuvers typical of everyday mobility. Predicate studies by researchers at the Rehabilitation Engineering and Applied Research lab have reported on how wheelchair users move about during everyday mobility (Sonnenblum SE et al., 2012b). Usage data show that most bouts of mobility are relatively short and low speed (<1 m/s), and are embodied by starting, stopping and turning. To be representative, the collection of canonical maneuvers must impart kinetic energy (KE) into the system and include the different types of resistive energy loss. Specifically,

the maneuvers should collectively impart all three types of KE – translational, turning (yaw), and rotational – and include rolling resistance and tire scrub of both the drive wheels and casters.

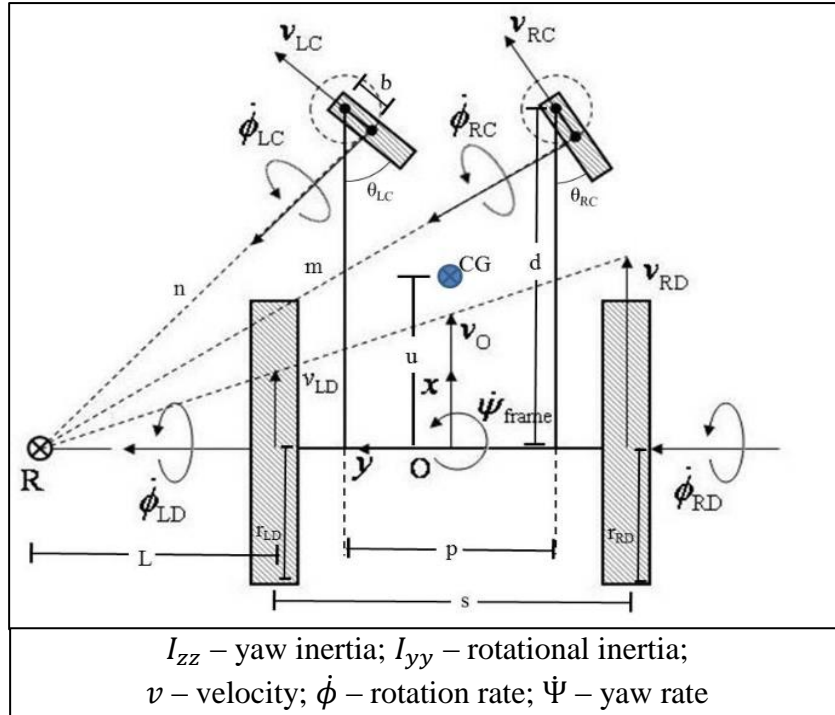


Figure 66. Schematic of wheelchair for use in deriving wheelchair kinematics during over-ground motion

In prior work, we described an approach for determining the kinematics and kinetic energy of a manual wheelchair (Medola et al., 2013). The wheelchair can be viewed as an assembly of 7 rigid bodies: frame, two drive wheels, two caster forks, and two caster wheels, as shown in **Figure 66**. Maneuvering the wheelchair over ground requires force input to both drive wheels. By measuring the drive wheels' rotation rates, one can determine via geometric constraints (wheelchair dimensions) the turning radius, velocity of the center of mass as well as the yaw rotation rate of the chair, and swivel and rotation rates of the caster wheel assemblies, assuming the wheelchair rolls without slipping.

Combining the inertias with kinematics, it becomes possible to calculate component kinetic energies. The summation of these individual energies can be used to define the kinetic energy of wheelchair motion on flat ground, as shown in **Equations 18-21**. (Nomenclature from **Figure 66**.) Translational KE is based solely on the system mass and COM velocity, while the turning (yaw) KE is based on the system and caster yaw inertias and their respective yaw rates. Rotational KE is based solely on the component properties and kinematics, defined as a function of caster and drive wheel rotational inertias and rotational speed. Combining these three categories of KE yields the total system KE.

$$KE_{translational} = \frac{1}{2} m_{sys} v_G^2 \quad (18)$$

$$KE_{turning} = \frac{1}{2} I_{ZZ,sys}^G \dot{\Psi}_{frame}^2 + \frac{1}{2} I_{ZZ,LFLC} \dot{\Psi}_{LC}^2 + \frac{1}{2} I_{ZZ,RFRC} \dot{\Psi}_{RC}^2 \quad (19)$$

$$KE_{rotational} = \frac{1}{2} I_{YY,LD} \dot{\Phi}_{LD}^2 + \frac{1}{2} I_{YY,RD} \dot{\Phi}_{RD}^2 + \frac{1}{2} I_{YY,LC} \dot{\Phi}_{LC}^2 + \frac{1}{2} I_{YY,RC} \dot{\Phi}_{RC}^2 \quad (20)$$

$$KE_{total} = KE_{translational} + KE_{turning} + KE_{rotational} \quad (21)$$

The variables described in **Equations 18 - 20** are all empirically determined via the component and system-level methods discussed thus far. By applying the AMPS as a test bed to perform the selected canonical maneuvers, the drive wheel rotational rates are measured via the system's wheel encoders, and the remaining system kinematics are inferred from the predicate kinematic model (Medola et al., 2013). The caster and drive wheel rotational inertias and caster-in-fork yaw inertias are derived from the trifilar pendulum measurements; the AMPS system yaw inertia is measured by the iMachine.

Keeping the kinetic energy model in mind, we move on to define the three canonical MWC maneuvers that the AMPS would perform to emulate the short bouts of everyday MWC mobility. Each maneuver description is accompanied by a figure of AMPS performing that maneuver, as well as a plot of pilot data illustrating the commanded, raw, and filtered AMPS wheel velocities for that maneuver.

- 1) Straight trajectory. Starting from rest, with casters aligned forward, accelerate to 1.0 m/s in 2.5 s, maintain this speed for 5 s and then decelerate to a stop in 2.5 s. Total linear distance traveled equates to 7.5 m.

Rationale: This maneuver highlights rectilinear inertia of the system, rotational inertia of the wheels, rolling resistance, and other resistive losses in the frame and bearings.

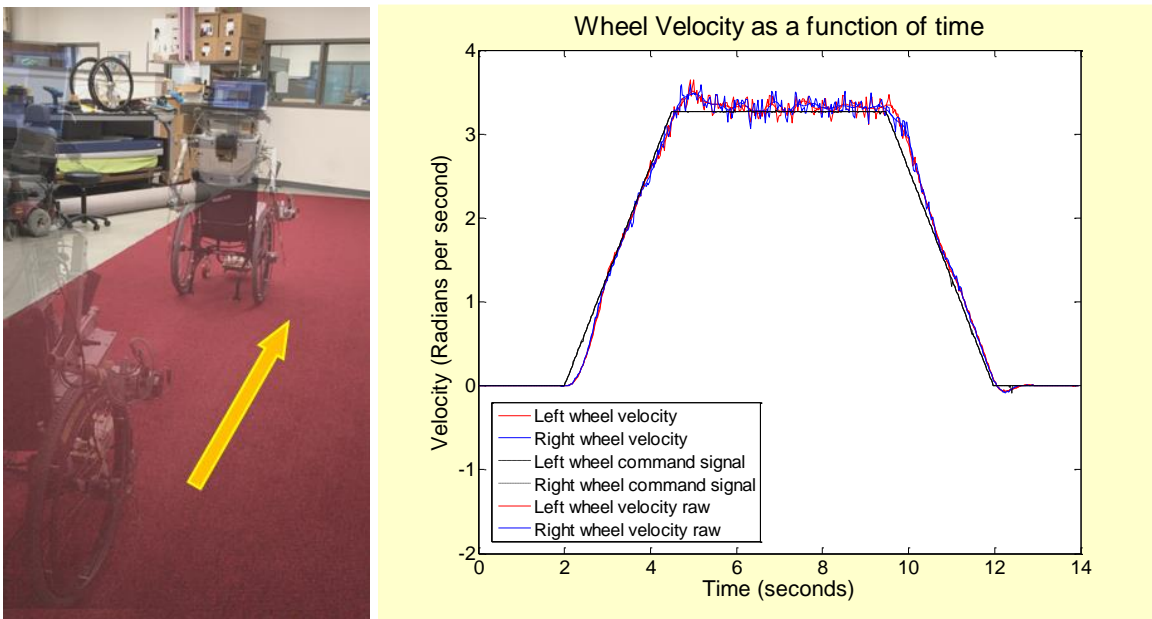


Figure 67. AMPS Straight Maneuver with Drive Wheel Velocity Profile

- 2) Fixed-wheel turn. Starting from a stop, with the casters aligned perpendicular to the center of the locked drive wheel, drive the unlocked drive wheel to accelerate the

system to a 1.56 rad/s (90 degree turn per second) yaw rate in 2.5 s. Maintain this yaw rate for 5 s, then decelerate to a stop in 2.5 s. Total system yaw displacement equates to 11.7 radians (a 675 degree turn).

Rationale: This maneuver highlights system yaw inertia, rotational wheel inertia, rolling resistance, caster and drive wheel scrub, and other resistive losses.

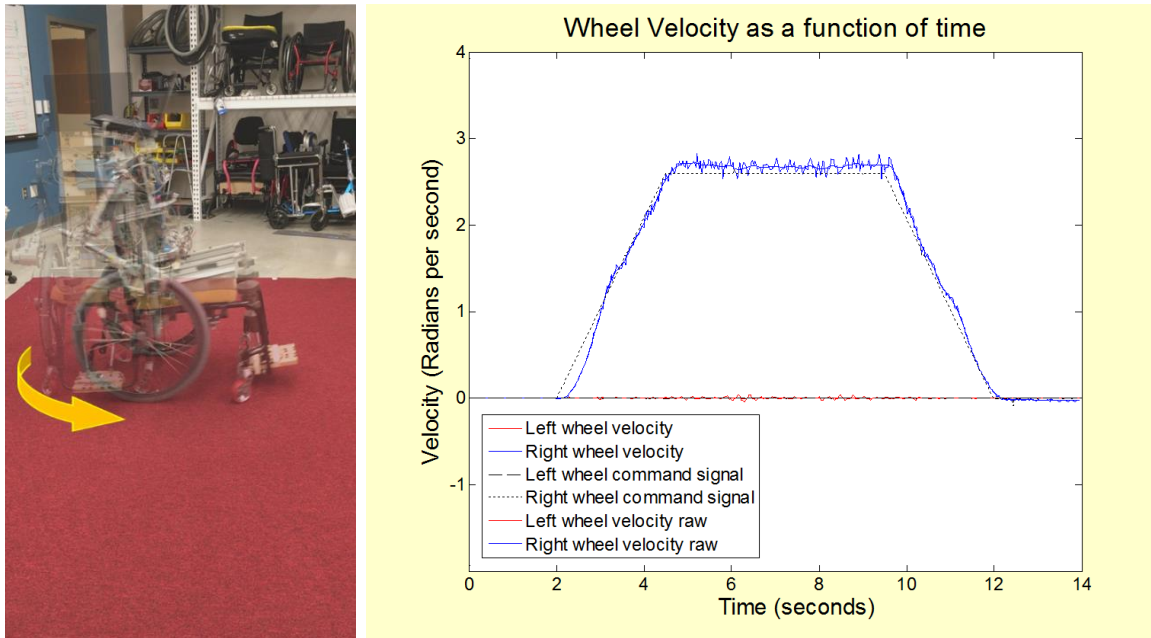


Figure 68. AMPS Fixed-Wheel Turn Maneuver with Drive Wheel Velocity Profile

- 3) Zero-radius turns. Due to unanticipated AMPS motor torque limits, this maneuver on carpet was reduced in velocity and acceleration, but the total yaw displacement was preserved.

On Tile. Starting from a stop, with casters aligned forward, counter-rotate drive wheels to reach a yaw rate of 1.56 rad/s (90 degree turn per second) in 1.0 s. Maintain this yaw rate for 1.0 s, then decelerate to a stop in 1.0 s. Pause for one second, then repeat the turn except with the drive wheels counter-rotating such that the MWC system turns

in the direction opposite to the preceding turn (e.g. a counter-clockwise turn would be preceded by clock-wise turn). Repeat until a total of six turns have been completed. System yaw displacement of a single turn equates to 3.14 radians (a 180 degree turn). Total system yaw displacement equates to 18.84 radians (a 1080 degree turn).

On Carpet. Same maneuver pattern, except the steady-state yaw rate is reduced to 1.17 rad/s (67.5 degree turn per second) and is maintained for 1.67 s.

Rationale: This maneuver includes direction changes that highlight caster swivel, system yaw inertia, rolling resistance, wheel and caster scrub and other resistive losses.

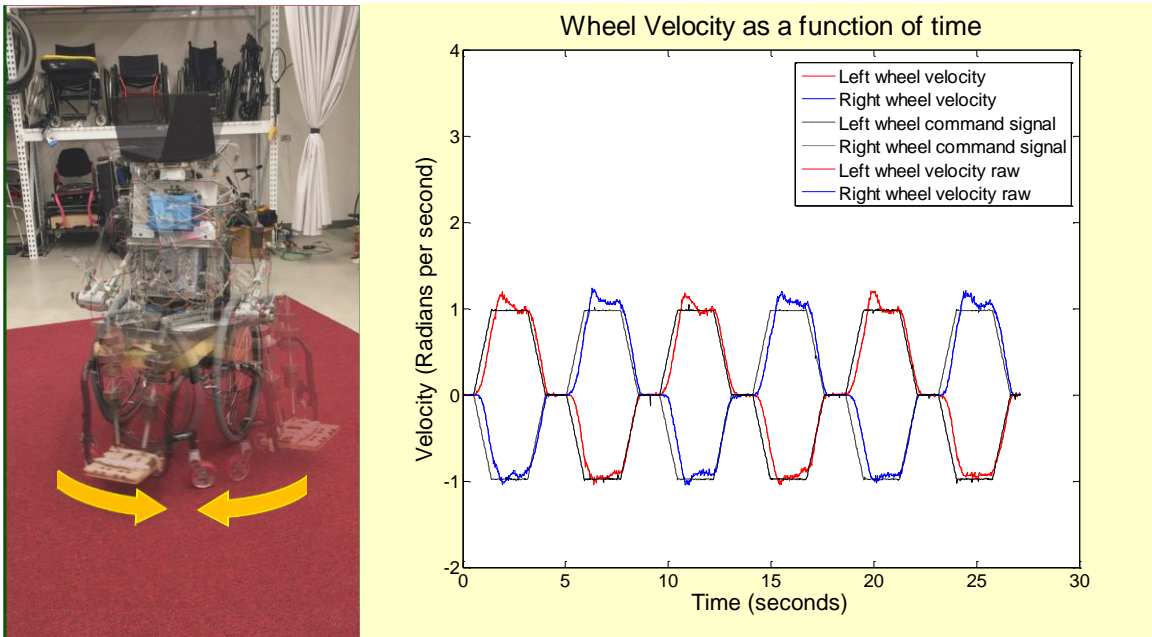


Figure 69. AMPS Zero-Radius Turns Maneuver with Drive Wheel Velocity Profile (Carpet)

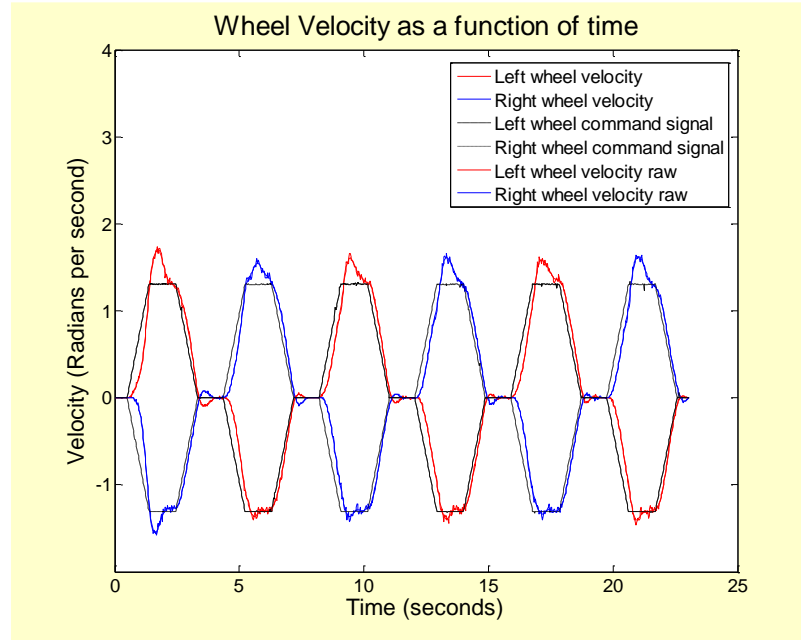


Figure 70. AMPS Zero-Radius Turns Maneuver Drive Wheel Velocity Profile (Tile)

Figure 71, **Figure 72**, and **Figure 73** illustrate how these selected canonical maneuvers collectively offer a balanced representation of all three types of kinetic energy. In **Figure 71**, we see that the KE of the straight maneuver is dominated by translational KE, with a very small stored as rotational KE and no presence of turning KE. This is an expected outcome given that the inertial contribution of the AMPS mass is several magnitudes greater than that of the rotational inertias of the casters and drive wheels. Additionally, the absence of directional changes in the straight maneuver support the lack of turning KE. In **Figure 72**, the system KE of the fixed wheel turn is close to evenly split between translational and turning KE, while rotational KE is comparatively very minimal. The presence of the translational KE arises from the velocity of the system COM, which is a function of the system yaw (turn) rate and the distance from the fixed wheel to the system COM, as shown in **Equation 22**.

$$v_G = \dot{\psi} \sqrt{\left(\frac{s}{2}\right)^2 + u^2} \quad (22)$$

In this equation, v_G is the COM velocity, $\dot{\psi}$ is the yaw rate of the system, $\frac{s}{2}$ is the distance from the fixed drive wheel to the axle center, and u is the distance from the axle center to the system COM.

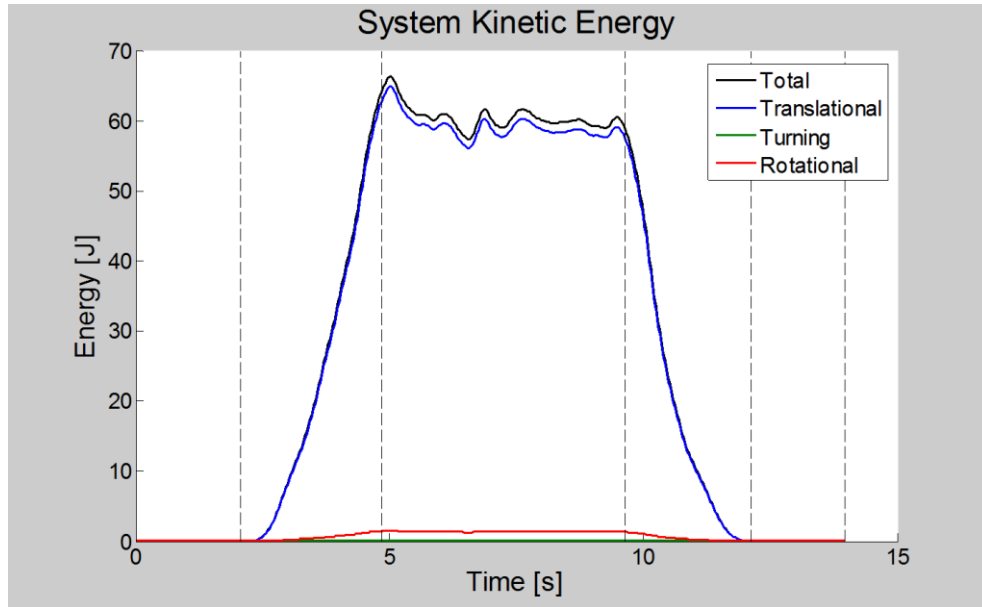


Figure 71. System Kinetic Energies of the Straight Maneuver

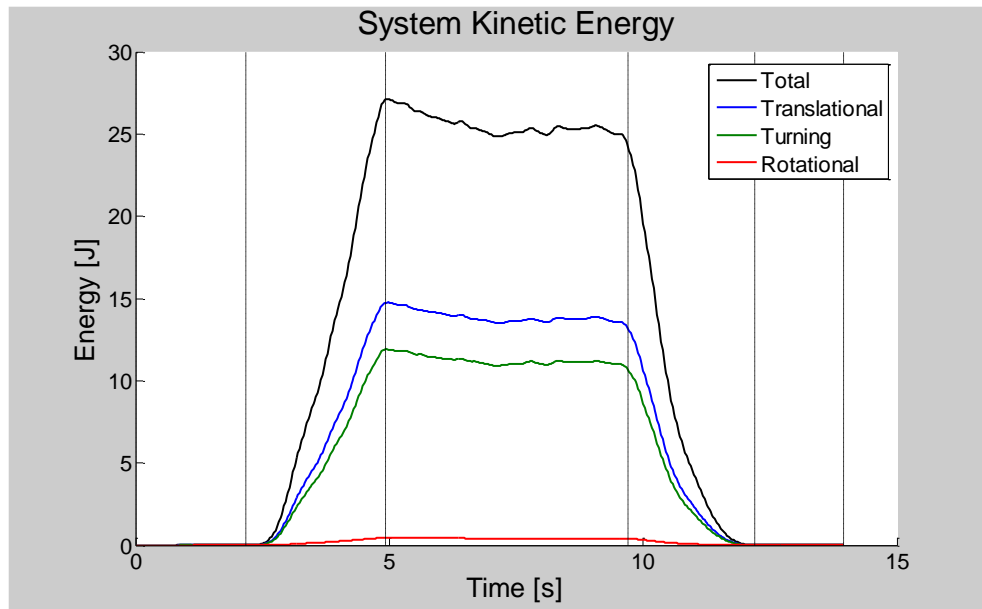


Figure 72. System Kinetic Energies of the Fixed Wheel Turn Maneuver

In **Figure 73**, the system KE of the zero radius turns is dominated by turning KE, and the remaining KE comprised of translational KE and a very small amount of rotational KE. Since the system turning occurs about the center of the axle, the presence of the translation KE arises from the COM velocity that is a function of system yaw rate and the COM-to-axle center distance. This is described by **Equation 23**.

$$v_G = \dot{\psi}u \quad (23)$$

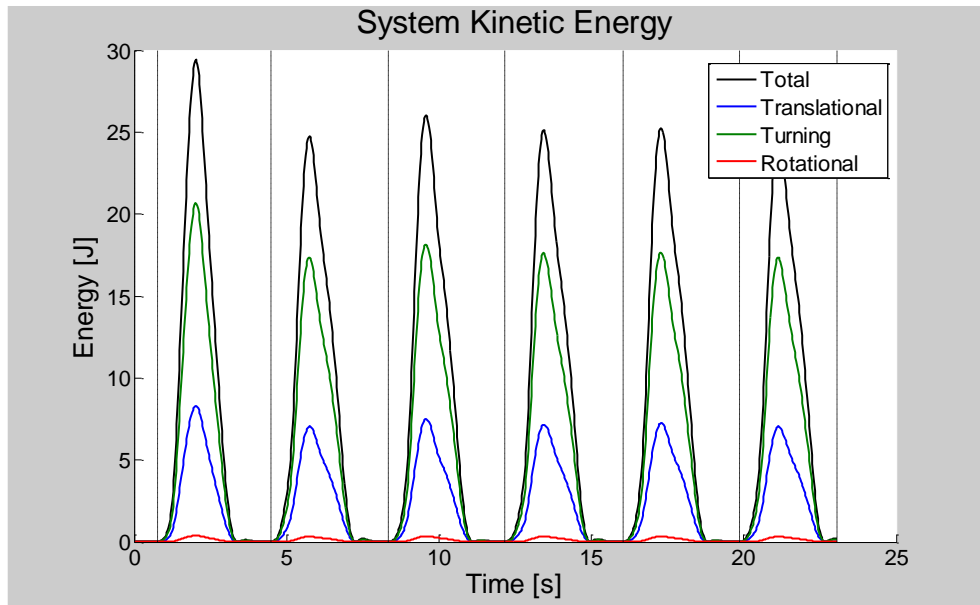


Figure 73. System Kinetic Energies of the Zero Radius Turns Maneuver

The v_G of the zero radius turns maneuver is much smaller than that of the fixed-wheel turn maneuver due to the reduced moment arm between the center of rotation and system COM. This reduction of v_G , and thus translational KE, was part of the designed rationale for using the zero radius turns maneuver. The goal of this maneuver is to investigate the impact of non-steady-state directional changes on propulsion effort. Alternative maneuvers that meet this goal were tested, including slalom or a series of chained, fixed-wheel left and right turns. However, these maneuvers all presented a dominant proportion of translational KE

that obscured the turning KE stored because of directional changes. Thus, the zero-radius turns maneuver was assessed to be most effective in pinpointing differences between different MWCs due to non-steady-state directional changes.

The resistive losses collectively experienced by the three canonical maneuvers also offer a balanced representation of the rolling resistances and scrub torques that were measured for casters and drive wheels in the component testing chapter. This parallel is critical for allowing us to link component resistive properties to the system-level performance of MWCs in the next chapter. The resistive forces acting on the MWC during each of the canonical maneuvers are illustrated in **Figure 74**, **Figure 75**, and **Figure 76**. Note that the propulsive forces are purposely excluded not only in the diagrams but also the equations of motion for this section. **Table 18** highlights the nomenclature used in these diagrams and equations of motion. Note that for instances where a wheel turned while rolling, the resultant resistive kinetics were broken up into the linear rolling resistance and a wheel scrub torque termed with a special subscript to denote its association with rolling. This additional term is meant to represent the increased rolling resistance that wheels experience from the cornering forces of turning.

Table 18. System Resistance Models Nomenclature

| Variable | Definition |
|-------------------|---|
| M_{sys} | Manual wheelchair system mass |
| I | Rotational inertia (note: I_G is system yaw inertia) |
| R | Wheel radius |
| $r_{X/Y}$ | Distance from point Y to point X (example) |
| θ | Angle between moment arm and force at a point |
| u | Distance from axle center to system center of mass |
| s | Distance between drive wheels |
| v_G | System center of mass velocity |
| a_G | System center of mass tangential acceleration |
| $\dot{\psi}$ | System yaw (turning) rate |
| F_{RR} | Rolling resistance force |
| τ_{ss} | Wheel scrub torque |
| Subscripts | Definition |
| A | Left caster (fork center) |
| B | Right caster (fork center) |
| C | Right drive wheel (tire center) |
| D | Left drive wheel (tire center) |
| O | Center of drive wheel axle |
| Caster | Used to denote caster forces/torques |
| DW | Used to denote drive wheel forces/torques |
| DW,RR | Special case used to denote drive wheel scrub torque with rolling |

For the straight maneuver (**Figure 74**), only rolling resistance forces act on the MWC system due to the lack of directional changings. This leads to the equation of motion in **Equation 24**, which is similarly derived in Sauret’s rolling resistance study (Sauret et al., 2012).

$$\left(M_{sys} + \frac{I_A}{R_A^2} + \frac{I_B}{R_B^2} + \frac{I_C}{R_C^2} + \frac{I_D}{R_D^2} \right) a_G = (F_{RR})_A + (F_{RR})_B + (F_{RR})_C + (F_{RR})_D \quad (24)$$

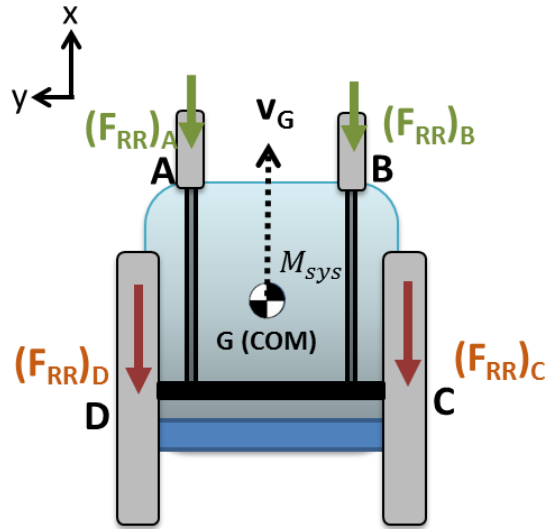


Figure 74. System Resistances During Straight Maneuver

From our results in Chapter 2, we know that the inertial contribution of the rotational inertias of the drive wheels and casters are very small relative to the system. Additionally, we can assume that A and B have the same caster rolling resistance, and C and D have the same drive wheel rolling resistance. Therefore, we can simplify **Equation 24** to the following.

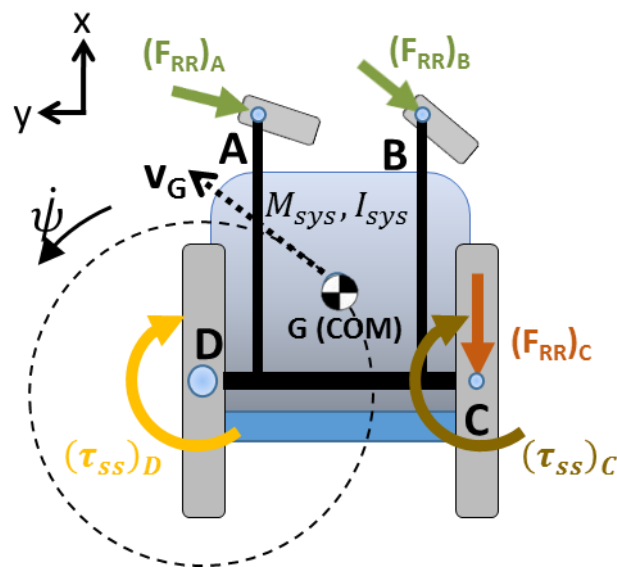


Figure 75. System Resistances During Fixed Wheel Turn Maneuver

$$M_{sys}a_G = 2(F_{RR})_{DW} + 2(F_{RR})_{Caster} \quad (25)$$

For the fixed-wheel turn maneuver, we can see than drive wheel scrub has been entered into the system because of the steady-state changes in heading. No significant scrub torque is experienced by the casters due to the lack of caster swivel. This leads to the equation of motion in **Equation 26**.

$$\begin{aligned} & \left[I_G + m \left(u^2 + \frac{1}{4} s^2 \right) + I_A \left(\frac{r_{A/D}}{R_A} \right)^2 \sin \theta_A + I_B \left(\frac{r_{B/D}}{R_B} \right)^2 \sin \theta_B \right. \\ & \quad \left. + I_C \left(\frac{r_{C/D}}{R_C} \right)^2 \right] \left(\frac{a_G}{r_{G/D}} \right) \\ & = (r_{A/D})(F_{RR})_A \sin \theta_A + (r_{B/D})(F_{RR})_B \sin \theta_B + (r_{C/D})(F_{RR})_C + (\tau_{ss})_C + (\tau_{ss})_D \end{aligned} \quad (26)$$

To simplify, we can assume the θ angles are very close to 90 degrees since based on typical wheelchair dimensions, θ is never less than 87 degrees in steady-state turning. Coupled with the previous assumptions, **Equation 26** becomes the following.

$$\begin{aligned} & \left[I_G + m \left(u^2 + \frac{1}{4} s^2 \right) \right] \left(\frac{a_G}{r_{G/D}} \right) \\ & = [(r_{A/D}) + (r_{B/D})](F_{RR})_{Caster} + (r_{C/D})(F_{RR})_{DW} + (\tau_{ss})_{DW, RR} + (\tau_{ss})_{DW} \end{aligned} \quad (27)$$

Note that the fixed-wheel turn equation of motion is structured to define the system yaw deceleration due to resistive losses. Therefore, the resistances are caster and drive wheel rolling resistance forces acting at different distances from the center of rotation, as well as drive wheel scrub torques. Of note is the rolling drive wheel's forces have been split into a pure rolling resistance force and rolling scrub torque in accordance with the previously described rationale.

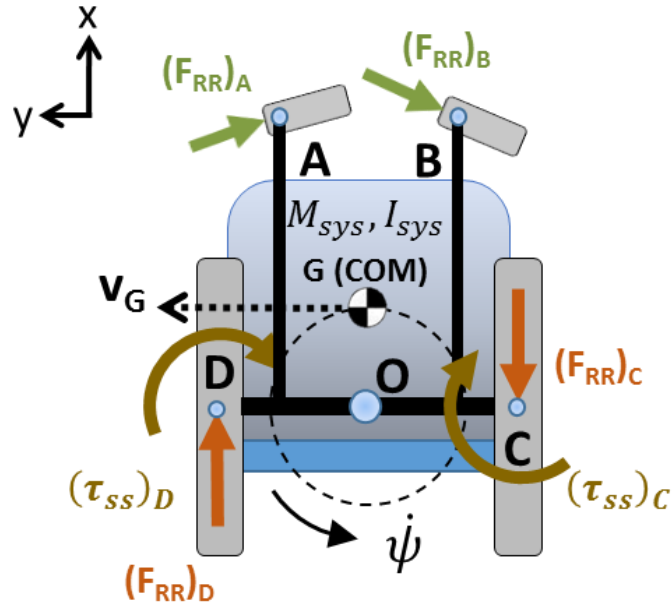


Figure 76. System Resistances During Zero Radius Turns Maneuver

The zero-radius turns maneuver incorporates the caster scrub torque that is absent from the straight and fixed-wheel turn maneuvers by changing directions between clockwise and counter-clockwise turning, causing the casters to swivel. **Figure 76** depicts the “steady-state” of the zero-radius turn where the casters have already aligned perpendicular to the center of rotation (Point O). The resistive loss term due to the transient caster swivel is added as the last term to **Equation 28** as a function of caster scrub torque.

$$\begin{aligned}
 & \left[I_G + mu^2 + I_A \left(\frac{r_{A/O}}{R_A} \right)^2 \sin \theta_A + I_B \left(\frac{r_{B/O}}{R_B} \right)^2 \sin \theta_B + I_C \left(\frac{r_{C/O}}{R_C} \right)^2 + I_D \left(\frac{r_{D/O}}{R_D} \right)^2 \right] \left(\frac{a_G}{r_{G/O}} \right) \\
 & = (r_{A/O})(F_{RR})_A \sin \theta_A + (r_{B/O})(F_{RR})_B \sin \theta_B + (r_{C/O})(F_{RR})_C + (r_{D/O})(F_{RR})_D \\
 & + (\tau_{SS})_C + (\tau_{SS})_D + f((\tau_{SS})_A, (\tau_{SS})_B)
 \end{aligned} \tag{28}$$

Applying the same simplifying assumptions that were used in the two previous equations, we get **Equation 29**.

$$[I_G + mu^2] \left(\frac{a_G}{r_{G/O}} \right) = (r_{A/O} + r_{B/O})(F_{RR})_{Caster} + (r_{C/O} + r_{D/O})(F_{RR})_{DW} + 2(\tau_{ss})_{DW, RR} + f((\tau_{ss})_A, (\tau_{ss})_B) \quad (29)$$

With these three maneuvers, the resistive losses of rolling resistance and scrub torque for both caster and drive wheels have been highlighted, each with considerable representation.

4.3 Defining a Performance Metric

Propulsion torque and propulsion cost are defined as the AMPS system-level performance metrics, and were inspired by their clinical relevance. Propulsion torque is directly measured by AMPS and describes the kinetics involved in driving the wheelchair. While the AMPS does not engage in cyclic propulsion like a human does, the propulsion torque of AMPS's continuous drive defines a lower bound for push forces a human user must apply to complete the same maneuver. An example of the velocity and torque profiles for a drive wheel is shown in **Figure 77**. The acceleration and steady-state phase propulsion torques (per drive wheel) are quantified by averaging the torque values bounded in their respective time spans, as denoted by regions A and B in **Figure 77**. These time spans key off of time versus torque plots, and are manually selected via the MATLAB function *ginput*. We define the phases based on an ideal torque and velocity profile, in which each velocity phase would have a constant torque associated with it. The transition phases of the torques are excluded since they do not reflect an accurate representation of

phase torque. The per drive wheel torques for phase are combined at the end to yield the system's phase propulsion torque.

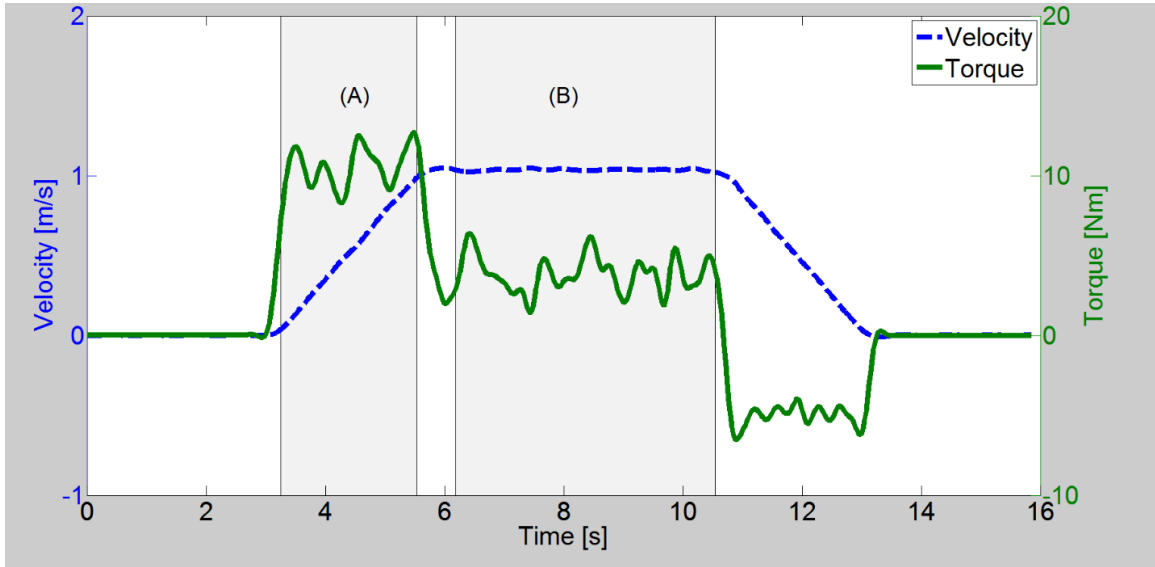


Figure 77. AMPS Drive Wheel Velocity and Torque Profiles

Propulsion cost keys off of the concept cost of transport, which quantifies the energy efficiency of transporting a human or vehicle from one place to another. Typically, it is defined as the transportation energy normalized against the transported weight and distance. In our application to the AMPS, we adopt the definition of propulsion work normalized against the displacement. Normalizing the AMPS propulsion work by each canonical maneuver's characteristic displacement minimizes the impact of path differences between each separate AMPS trial. For the straight maneuver, this definition becomes

$$Propulsion\ cost = \frac{W_{in}}{\Delta s} \quad (30)$$

where W_{in} is the propulsion work (units of joules) done by the AMPS motors and Δs is the length of the path traveled by the MWC system's COM (units of meters). For fixed-wheel turning and zero radius turns, the definition takes the form of

$$Propulsion\ cost = \frac{W_{in}}{\Delta\psi} \quad (31)$$

where $\Delta\psi$ is the total yaw angle traveled by the MWC system (units of radians). The propulsion work done by AMPS can be calculated as shown in **Equations 32** and **33**.

$$P_{in} = \tau\omega \quad (32)$$

$$W_{in} = \int_{t_i}^{t_f} [(P_{in})_L + (P_{in})_R]dt \quad (33)$$

In **Equation 32**, the AMPS propulsion power input for one motor is defined by the product of τ , the torque applied to the drive wheels, and ω , the angular velocity of the propelled drive wheel. Recall these are determined via measures of motor current sensors and digital encoders, respectively. In **Equation 33**, the left and right motor powers are combined and integrated over time to yield the propulsion work input.

4.4 System-Level Study Designs

The aforementioned canonical maneuvers were applied towards two studies which are detailed separately below. The first is a standalone study, whereas the second was used to model the relationship between component properties and propulsion cost (which will be detailed in the next chapter).

4.4.1 Impact of Mass and Weight Distribution on Propulsion Torque

Configurations

A TiLite Aero Z wheelchair was configured in four different manners to reflect different masses and weight distributions. The wheelchair had Primo 5 x 1.5” front casters and 24 x 1-3/8” stock pneumatic drive wheels. In its regular configuration, the wheelchair had a 12.1 kg mass and an axle position resulting in 70% weight distribution on drive wheels when occupied by the AMPS. The second configuration was based upon measurements of a standard folding frame wheelchair which had a mass of 17.6 kg and 55% of weight upon the drive wheels. These two configurations defined the mass and weight distributions to be tested. Specifically, the wheelchair was tested in four configurations defined by two masses (12.1 and 17.6 kg) and two weight distributions (70% and 55% weight over the drive wheels). The 5.6 kg additional mass was added at the center of mass of the standard TiLite configuration to minimize the impact on yaw inertia. Axle position was adjusted to achieve the different weight distributions. Occupied system mass and yaw inertia were measured using the iMachine.

Maneuvers

The straight and fixed-wheel turn canonical maneuvers were applied to this study. The fixed-wheel turn was programmed with a steady-state yaw rate of 1.9 rad/s instead of the previously defined 1.56 rad/s. Both fixed-wheel left and right turns were performed. Maneuvers were performed on tile and low pile carpet surfaces. Each configuration was tested 10 times for each maneuver and surface type, resulting in 240 total AMPS trials.

Analysis

The propulsion torque performance metric was applied to this study for the acceleration and steady-state phases of each maneuver. Analysis was performed on each configuration and surface combination for both straight and turning maneuvers. For each set of ten repeated trials, the propulsion torque mean and standard deviation for both the acceleration and steady-state phases were calculated. Left and right fixed-wheel turns were averaged together to yield a single propulsion torque value. The percent differences and effect sizes relative to the torque of the 12.1 kg chair with a 70% weight distribution were calculated. This reference configuration reflects that of an ULW wheelchair. Effect size, also termed Cohen's d (Cohen, 1988), can be interpreted as the average percentile standing of the tested configuration relative to the reference configuration. This data provides the most direct evaluation of differences with the ability to judge meaningfulness. In a strict sense, testing multiple wheelchair configurations over multiple trials does not permit use of ANOVA to infer differences due to the violation of the assumption of independence. However, in deference to convention, simple univariate ANOVA results are reported for the straight and turning maneuvers during the acceleration and steady-state phases.

4.4.2 Impact of Casters and Drive Wheels on Propulsion Cost

Configurations

A Quickie GT wheelchair was outfitted with combinations of three different types of drive wheels and four different types of casters, resulting in twelve MWC configurations with distinct component pairings. The casters used were the 4 x 1.5" FLSR, 5 x 1.5" Primo SR, 5 x 1" Primo, and 6 x 1" Pneumatic. The drive wheels used were the Solid Mag, Spinergy, and Stock Pneumatic. Each of these component pairings were adjusted to have

60%, 70%, and 80% load on drive wheels. These different weight distributions were achieved by shifting the weights inside the AMPS “buttocks”, whose original cement build had been replaced with a Dibond reinforced hollow acrylic mold to house removable weights. Including these different weight distributions, the total number of distinct MWC configurations used in this study was 36. The total mass (~113 kg) for all MWC configurations did not vary beyond the differences caused by switching components, which were < 1.5 kg across the board. The constant system mass helps frame the outcome of this study as the impact of casters and drive wheels for a single MWC user. Occupied system mass and yaw inertia were measured using the iMachine for all configurations.

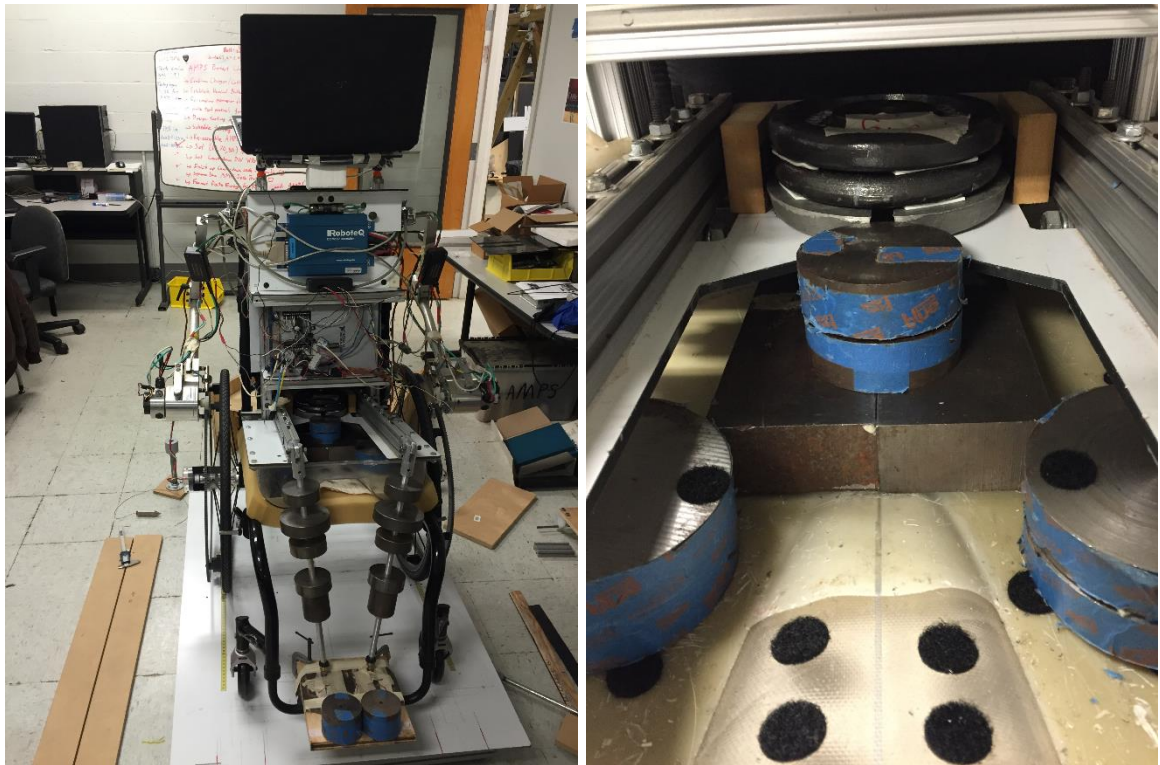


Figure 78. AMPS Loaded at the 70%WD Configuration

Maneuvers

The straight, fixed-wheel turn, and zero-radius turns canonical maneuvers were all applied to every configuration in this study. To minimize the impact of surface bias, two sets of trials were conducted for each canonical maneuver. For straight, a “forward” direction was defined by the first set of trials, and then trials were conducted at a 180 degree heading from this direction, termed the “backward” direction. Both left and right fixed-wheel turns were conducted, and zero-radius turns consisted of two trial sets that started with either clockwise (CW) yaw rotation or counter-clockwise (CCW) yaw rotation. All tests were conducted on both tile and carpet, with the zero-radius turns maneuver being reduced in steady-state speed on carpet due to motor torque constraints (detailed in Section 4.2). Each trial set consisted of 5 repeated trials, resulting in 2160 total AMPS trials.

Analysis

The propulsion cost performance metric was applied to this study. For AMPS trials of both straight and fixed-wheel turn maneuvers, the propulsion cost across the acceleration and steady-state phases was used for analysis (MATLAB). The deceleration or braking phase is intentionally omitted as the goal is to highlight energy expended for task propulsion. For AMPS trials of the zero-radius turns maneuver, the propulsion cost across the last four of the six total turns in each trial was used for analysis. The first two turns were omitted due to their propulsion instabilities from misaligned casters. The propulsion cost of each turn’s braking phase is included out of necessity, as the zero-radius turns do not exhibit as distinct and consistent of a propulsion phase as the straight and fixed-wheel turn maneuvers. Statistical analysis of each canonical maneuver and surface combination is handled separately. Within each canonical maneuver and surface combination, two sets

of trial averages were formed, one by collapsing data across casters to form drive wheel averages and one by collapsing data across drive wheels to form caster averages. Each drive wheel average consisted of 40 trials, while each caster average consisted of 30 trials. The standard deviation of the trials for each average was also calculated. For collapsed drive wheels, the percent differences and effect sizes relative to the 5 x 1" Primo caster within each weight-distribution was calculated. The percent differences and effect sizes relative to the 80%WD for each caster was also calculated. For collapsed casters, the percent differences and effect sizes relative to the Stock Pneumatic within each weight-distribution was calculated. Again, the percent differences and effect sizes relative to the 80%WD for each drive wheel was also calculated. The reference caster and drive wheels reflect the stock components used on ULW wheelchairs, while the reference weight-distribution is the clinically-recommended configuration for a ULW wheelchair. Effect size, also termed Cohen's *d* (Cohen, 1988), can be interpreted as the average percentile standing of the tested configuration relative to the reference configuration. This data provides the most direct evaluation of differences with the ability to judge meaningfulness. In a strict sense, testing multiple wheelchair configurations over multiple trials does not permit use of ANOVA to infer differences due of the violation of the assumption of independence. However, in deference to convention, a 3-way ANOVA was run to identify the wheelchair configuration factors that influence measures of propulsion cost for each task and surface. The 3 drive wheels, 4 casters and 3 weight distributions were entered into the analysis. In addition to main effects, second level interaction with weight distribution was included. All p-values are reported, and data significance is discussed at levels of $p \leq 0.05$.

4.5 System-Level Experimental Results and Discussion

4.5.1 Impact of Mass and Weight Distribution on Propulsion Torque

The mass, yaw inertias, and weight distributions of each configuration are shown in **Table 19**. The 5.5 kg mass represented a 45% increase in wheelchair mass, but when loaded with the AMPS, this increase was only 5%. Yaw inertia was increased by 33% when the mass was redistributed from 70% to 55% on the drive wheels. Acceleration and steady-state phase propulsion torque values of each wheelchair configuration are tabulated in **Table 20** and **Table 21** and plotted in **Figure 79** – **Figure 82** for both straight and fixed-wheel turning trajectories on tile and carpet.

Table 19. Test Wheelchair Configurations

| Configuration | Wheelchair Mass [kg] | Yaw Inertia [kg-m ²] | % weight on drive wheels |
|---------------|----------------------|----------------------------------|--------------------------|
| 12kg&70% | 12.1 | 7.82 | 71.6 |
| 17.6kg&70% | 17.6 | 7.89 | 72.1 |
| 12kg&55% | 12.2 | 10.21 | 58.1 |
| 17.6kg&55% | 17.7 | 10.68 | 56.5 |

The torques required to propel the four configurations differed during both straight and turning trajectories on both tile and carpet ($p < 0.0001$). The torques imparted during straight and turning trajectories were greater during acceleration than during steady-state speed ($p < 0.0001$).

On both surfaces, the lowest torques was recorded on the 12 kg wheelchair configured with 70% of its weight on the drive wheels (12kg&70% configuration). The relative differences between this torque and the other configurations varied across the different maneuvers and phases on the tile and carpet surfaces (**Table 20** and **Table 21**).

The effect sizes were very large in all cases, except during the steady-state straight trajectory (0.47) on carpet when comparing the 2 masses with a 70% weight distribution.

All other effect sizes exceeded 1.4.

Table 20. Propulsion Torques During Maneuvers on Tile

| Maneuver/Phase Torques | Configuration | Mean (Nm) | Stand. Dev. (Nm) | % change | Cohen's d |
|------------------------|---------------|-----------|------------------|----------|-----------|
| straight acceleration | 12kg&70% | 18.0 | 0.281 | | |
| | 17.6kg&70% | 19.1 | 0.427 | 6.1% | 3.04 |
| | 12kg&55% | 18.4 | 0.217 | 2.1% | 1.59 |
| | 17.6kg&55% | 20.0 | 0.648 | 10.9% | 4 |
| straight steady-state | 12kg&70% | 4.1 | 0.060 | | |
| | 17.6kg&70% | 4.2 | 0.078 | 2.5% | 1.43 |
| | 12kg&55% | 4.3 | 0.086 | 6.9% | 2.7 |
| | 17.6kg&55% | 5.0 | 0.144 | 23.1% | 8.15 |
| turning acceleration | 12kg&70% | 11.7 | 0.467 | | |
| | 17.6kg&70% | 12.3 | 0.312 | 4.7% | 1.38 |
| | 12kg&55% | 13.5 | 0.368 | 14.6% | 4.09 |
| | 17.6kg&55% | 14.5 | 0.503 | 23.9% | 5.77 |
| turning steady-state | 12kg&70% | 5.6 | 0.171 | | |
| | 17.6kg&70% | 5.7 | 0.157 | 2.3% | 0.791 |
| | 12kg&55% | 8.9 | 0.421 | 59.9% | 10.36 |
| | 17.6kg&55% | 10.6 | 0.274 | 90.0% | 21.89 |

Table 21. Propulsion Torques During Maneuvers on Carpet

| Maneuver/Phase Torques | Configuration | Mean (Nm) | Stand. Dev. (Nm) | % change | Cohen's d |
|---------------------------|---------------|--------------|---------------------|----------|--------------|
| straight acceleration | 12kg&70% | 21.9 | 0.477 | | |
| | 17.6kg&70% | 23.5 | 0.361 | 7.2% | 3.78 |
| | 12kg&55% | 22.6 | 0.354 | 3.2% | 1.67 |
| | 17.6kg&55% | 23.6 | 0.561 | 7.8% | 3.26 |
| straight steady-state | 12kg&70% | 7.0 | 0.129 | | |
| | 17.6kg&70% | 7.1 | 0.266 | 1.5% | 0.478 |
| | 12kg&55% | 7.7 | 0.131 | 9.3% | 5.38 |
| | 17.6kg&55% | 8.2 | 0.326 | 16.0% | 4.84 |
| turning acceleration | 12kg&70% | 19.4 | 0.567 | | |
| | 17.6kg&70% | 20.6 | 0.657 | 6.4% | 2.19 |
| | 12kg&55% | 20.7 | 0.523 | 6.6% | 2.36 |
| | 17.6kg&55% | 21.0 | 0.760 | 8.1% | 2.34 |
| turning steady-state | 12kg&70% | 11.4 | 0.211 | | |
| | 17.6kg&70% | 12.0 | 0.182 | 5.4% | 3.09 |
| | 12kg&55% | 12.0 | 0.157 | 5.6% | 3.39 |
| | 17.6kg&55% | 12.5 | 0.205 | 10.1% | 5.53 |

For the categories of straight steady-state, turning steady-state, and turning acceleration, the configurations with 55% weight distribution accounted for the highest propulsion torques. In distinction, the highest torques during straight acceleration were recorded for the chair configurations with a 17.6 kg mass. Torques on carpet were less different across configurations compared to torques measured on tile during both trajectories and phases. The greatest torque differences existed during the steady-state phases of both trajectories.

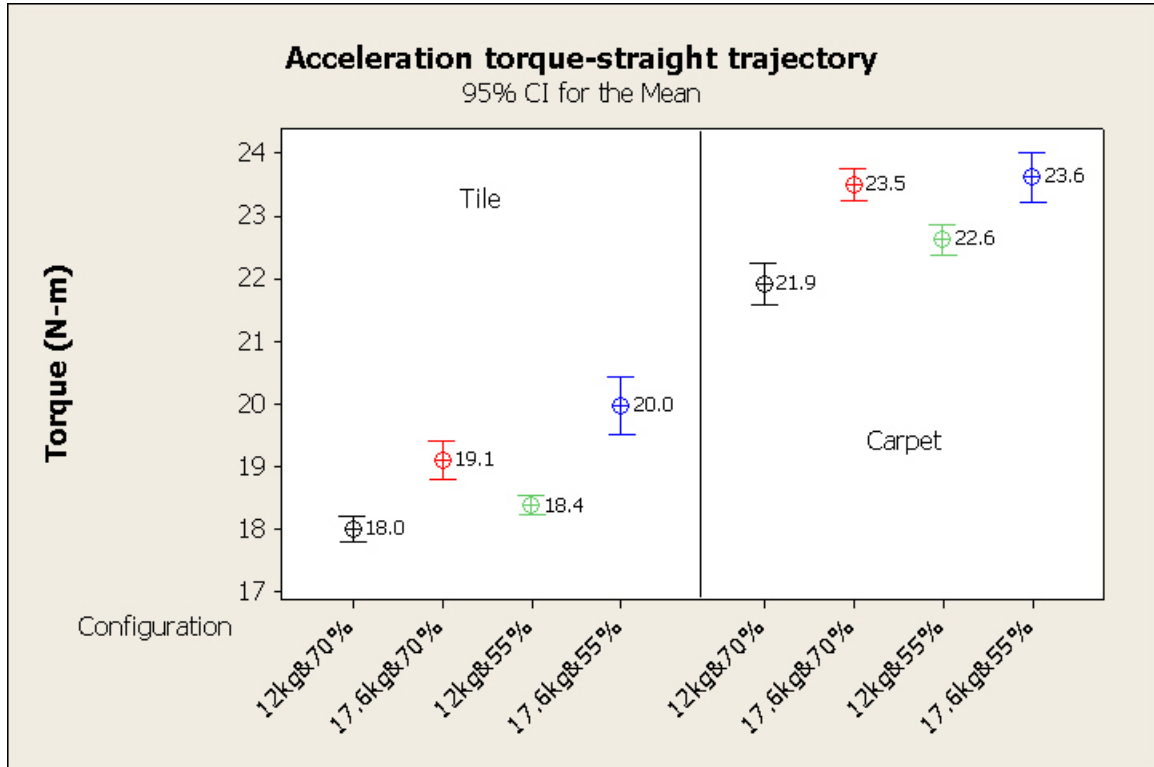


Figure 79. Propulsion torque across configurations for acceleration phase of straight maneuver

The relative influences of mass and weight distribution on torque varied between the straight and turning trajectories and whether the wheelchair was accelerating or at a steady-state speed. During straight acceleration (**Figure 79**), the greater mass required, on average, 7.4% greater torque on tile and 5.8% greater torque on carpet. For this maneuver, the configurations with a 55% weight distributions required 3.3% greater torque on tile and 2% greater torque on carpet. During straight steady-state speeds (**Figure 80**), the 17.6 kg configurations required 8.8% more torque on tile and 3.8% more torque on carpet. The 55% weight distribution configurations required 13.5% greater torque on tile and 11.8% more torque on carpet.

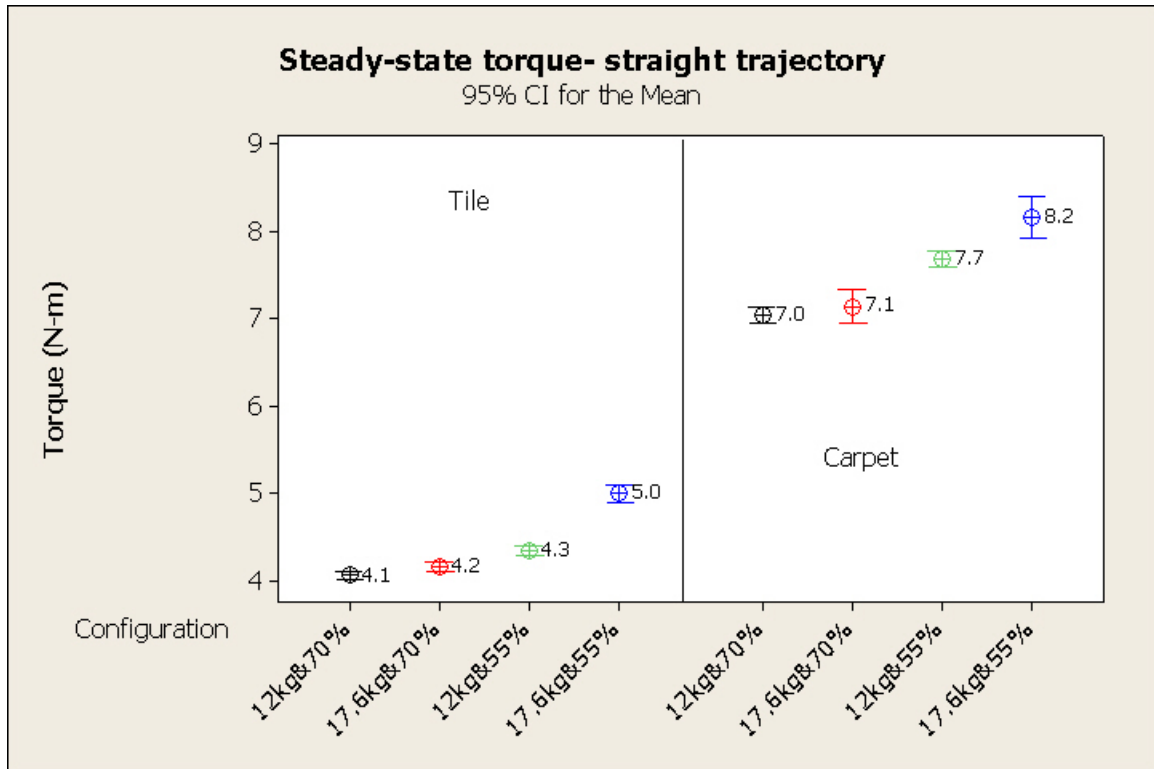


Figure 80. Propulsion torque across configurations for steady-state phase of straight maneuver

Turning torques indicated a greater influence of weight distribution. For the acceleration phase (**Figure 81**), the increased mass required 6.4% and 3.9% more torque on tile and carpet, respectively, while the change in weight distribution increased torque by 16.5% on tile and 4.1% on carpet. During steady-state turning (**Figure 82**), the additional mass increased torque by 10.6% on tile and 4.8% on carpet whereas the 55% weight distribution increased torque by 73% on tile and 5.1% on carpet.

The standard deviations of the means reflect the high repeatability of the AMPS system in measuring propulsion torque, with the forward axle and high mass configuration exhibiting a slightly higher variability. This underscores its value for comparing different configurations of manual wheelchairs. Both the percent changes and effect sizes serve as

useful comparisons against the base configuration of the ULW wheelchair and are reported in **Table 20** and **Table 21**. An effect size of 1.0 indicates that the mean torque of the tested wheelchair is at the 84th percentile of the 12kg&70% wheelchair. An effect size of 2.0 indicates that the tested wheelchair is at the 97.7th percentile of the base ULW wheelchair configuration. The very large effect sizes, therefore, show a distinction between the torques measured across configurations, trajectories, and surfaces.

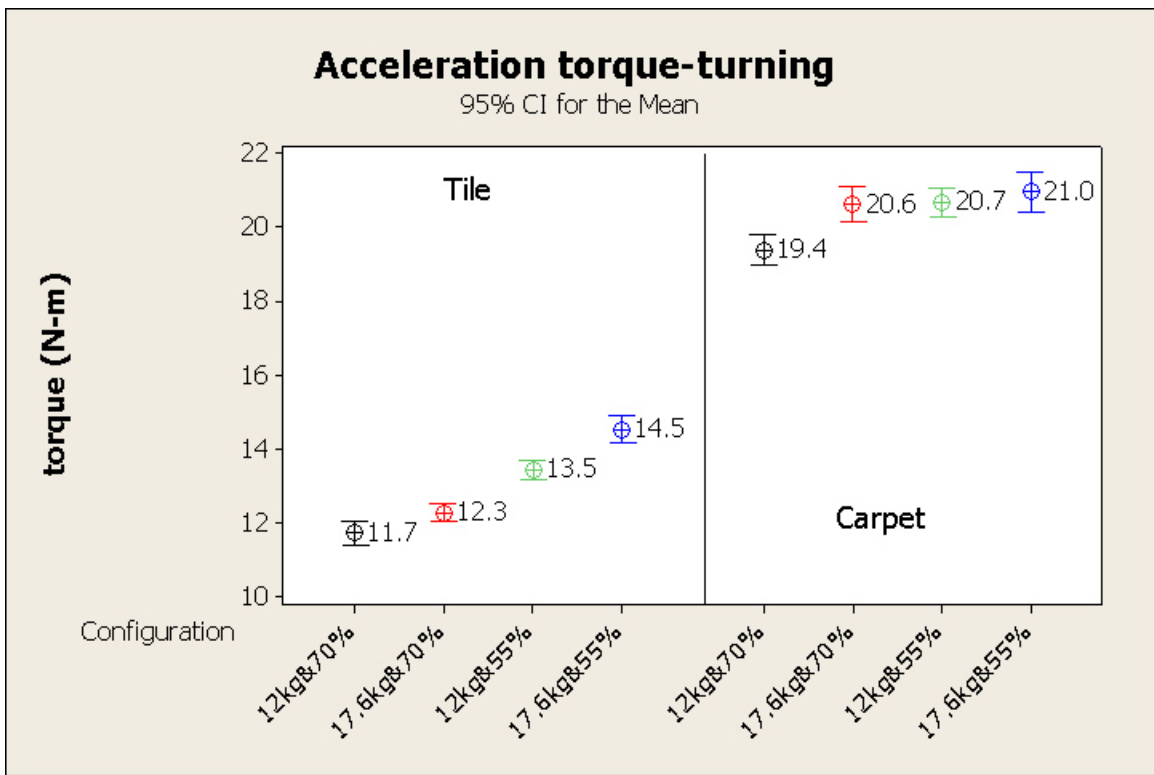


Figure 81. Propulsion torque across configurations for acceleration phase of turning maneuver

Percentage differences, on the other hand, offer a relative comparison that can be used to apply clinical relevancy. Torques measured during acceleration and steady-state speed phases are considered to be stable, meaning that a single torque is required to impart the acceleration or speed during the respective phase of the maneuver. The work performed

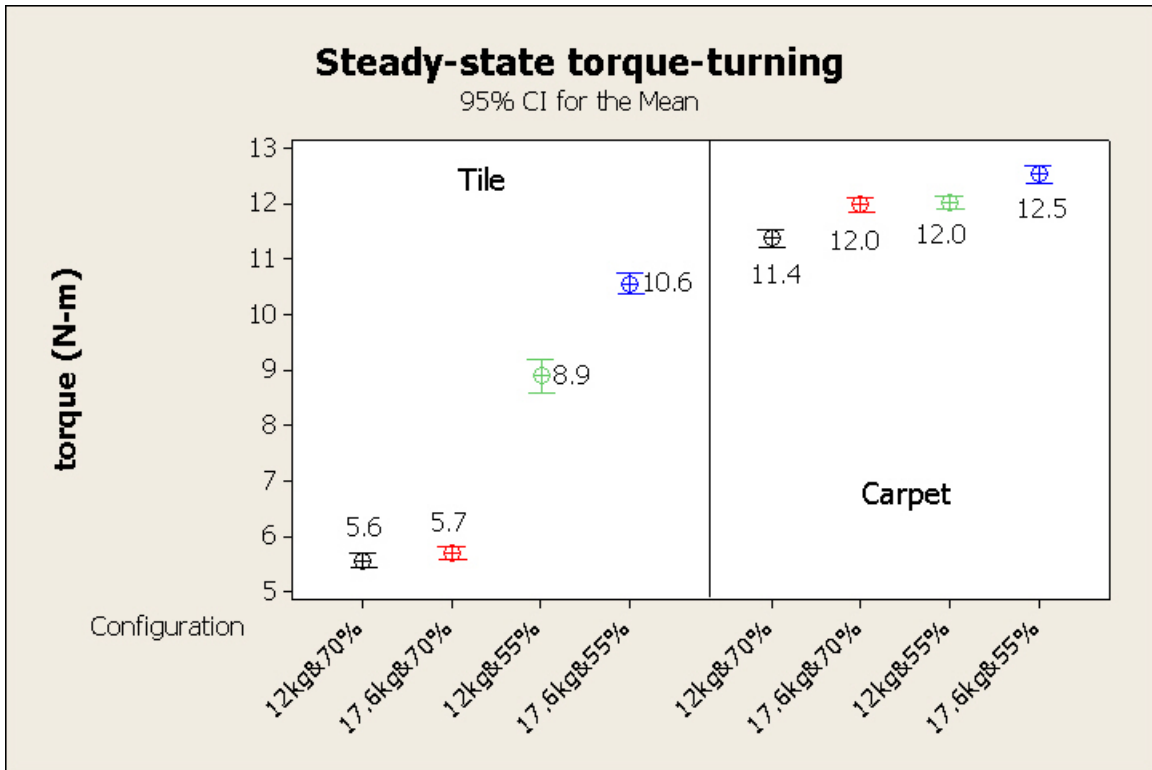


Figure 82. Propulsion torque across configurations for steady-state phase of turning maneuver

over that phase is directly related to the torque as well as the distance over which the torque is applied. Differences in work, therefore, can be used to assess the propulsion effort that a user must impart to complete the maneuver. In this study, the distances traveled in each phase were the same for each test so the torque can be used to evaluate differences in propulsion effort of a user. As an example, consider the straight trajectory on tile. Adding 5.5 kg to the 12.1kg&70% wheelchair increases torque by 6% during acceleration but only by 2.5% when propelling at steady-state. However, if 5.5 kg is added *in combination* to shifting weight to the casters (17.6kg&55% configuration), 11% greater torque is needed to accelerate and 23% greater torque is required to propel at a constant speed. This comparison must be made with the knowledge that the acceleration phase was 2.5 s long and the steady-state speed phase was 5 s long. If a user propels a longer distance, he or she

would be applying this extra propulsion torque for longer durations, so percent difference in torque is a more meaningful comparison compared to the magnitude difference.

The torque required to maneuver a wheelchair is directly related to the inertial and frictional influences of the wheelchair system. Torque during acceleration must be applied to overcome both inertia and friction. In distinction, the torque required to maintain steady-state velocity is influenced by the need to overcome friction. Therefore, torques are naturally greater during acceleration than during steady-state velocity because work is required to accelerate all components with mass.

For the configurations tested, the torque required to accelerate the chair in a straight direction was over twice that required to keep the chair moving. In turning, the acceleration torques were 80% greater than the steady-state torques, a lower but still appreciable increase. From a human perspective, this large difference in torque translates to a heightened instantaneous torque required for a user to accelerate a wheelchair compared to that required to maintain speed. This instantaneous torque imparted by the user can be lowered by accelerating more slowly.

Friction is directly related to tire design and the surface the wheels are rolling on. The influence of friction is very apparent by the large torque differences on carpet versus tile. Carpet required, on average, 55% greater torque than that during maneuvers on tile.

The torque differences between straight and turning are not as straightforward to discuss since different velocities were targeted and a fixed-radius turn requires torque to be applied to only one wheel. However, a statement can be made towards how these two trajectories differ with respect to the types of kinetic energy imparted onto the wheelchair

during a maneuver. A straight trajectory involves a lot of translational KE because the center of mass is moving over a distance; this requires work to be imparted into the system. Turning also involves translational KE as well as turning KE, but the maneuver requires less energy. However, the resistive losses in turning are greater than during straight movement. A straight trajectory involves frictional losses dominated by rolling resistance on the wheels and casters. Turning includes rolling resistance plus tire scrub. The energy losses in turning are much greater as evidenced by the fact that one slows down quicker while turning compared to moving straight (Lin & Sprigle, 2014).

Assessing the torque differences across mass and weight distribution are more complex, but still highlight the influences of inertia and friction. Mass directly impacts inertia and thus would be expected to have greater influence while accelerating. The change in weight distribution affects yaw inertia and the relative friction that exists on the casters and drive wheels. In general, added mass had a greater impact on torque while accelerating a wheelchair in the straight direction on both surfaces. Weight distribution had a greater influence on torque during straight steady-state speeds on both surfaces and during both acceleration and steady-state phases while turning on tile. Mass and weight distribution had nearly equal influences while turning on carpet during both the acceleration and steady-state phases.

During acceleration in a straight trajectory, the respective influences of mass and weight distribution were similar on both surfaces (**Figure 79**). While mass had a greater influence during acceleration, acceleration torque also increased when more weight was placed upon the casters (55% configuration). This latter result can be explained by the greater rolling resistance of the smaller diameter casters relative to the drive wheels (J. J.

Kauzlarich & J. G. Thacker, 1985; Thacker, Sprigle, & Morris, 1994). During steady-state speeds, weight distribution had the greater impact. **Figure 82** illustrates this by the larger torques of the 55% weight distribution configurations regardless of wheelchair mass.

In turning, the relationship between mass and weight distribution changes because of two factors, a change in yaw inertia and an enhanced influence of friction at the drive wheels due to tire scrub. **Table 19** shows that shifting weight to the casters impacts yaw inertia much more than adding 5.5 kg of mass. This corroborates previously reported results on the impact of axle position and configurations on inertia (Caspall, Seligsohn, Dao, & Sprigle, 2013). Because friction is directly related to the normal forces between the surfaces in contact, drive wheel scrub during turning is greater when 70% of weight is placed upon the drive wheels (Lin & Sprigle, 2014). So, while accelerating into a turn, inertia and friction exert opposite influences on propulsion torque. During acceleration on tile, the increased yaw inertia of the 55% configurations leads to greater torques despite the lower scrub torque (**Figure 81**). This inertial influence becomes muted on carpet when friction becomes more pronounced, resulting in nearly identical torques except for the lower torque for the 12kg&70% configuration. During steady state turning, the torque influences are more complex to partition, but AMPS empirically measures system torque. Propulsion torque in steady-state follows the same relationship as during acceleration. Weight distribution has a greater impact on turning torque compared to mass while on tile, but these influences become much smaller when turning on carpet (**Figure 82**).

4.5.2 Impact of Casters and Drive Wheels on Propulsion Cost

Table 22. AMPS Weight-Distribution Configurations and System Yaw Inertia

| Configuration | Yaw Inertia [kg-m ²] | % weight on drive wheels |
|----------------------------------|----------------------------------|--------------------------|
| 60% | 8.89 | 59.3% |
| 60% with 6 x 1" Pneumatic caster | 9.46 | 62.6% |
| 70% | 7.33 | 69.7% |
| 70% with 6 x 1" Pneumatic caster | 7.75 | 73.4% |
| 80% | 6.37 | 79.2% |
| 80% with 6 x 1" Pneumatic caster | 6.72 | 82.6% |

The yaw inertias and weight distributions of each weight-distribution configuration are shown in **Table 22**. Separate rows for configurations using the 6 x 1" Pneumatic caster were added, as the use of this caster resulted in a 2" increase in the front wheel elevation, effectively shifting more load onto the drive wheels and changing the wheelbase relative to other casters. However, as this reflects how a single user (as simulated by the constant 113 kg AMPS mass) would configure their wheelchair, the weight distributions with the 6 x 1" Pneumatic caster will be considered categorically equivalent to the other weight-distributions. Yaw inertia increased by 15% and 40% when mass was redistributed from 80% to 70% and 80% to 60% on drive wheels, respectively.

Table 23 – Table 28 summarize the propulsion cost - collapsed by casters and collapsed by drive wheels - for each canonical maneuver on both tile and carpet.

Table 23. AMPS Propulsion Cost for Straight Maneuvers on Tile

| Drive Wheels | Average [J/m] | | | Standard Deviation [J/m] | | |
|-----------------|---------------|------|------|--------------------------|-----|-----|
| | 60% | 70% | 80% | 60% | 70% | 80% |
| Solid Mag | 31.1 | 31.6 | 32.5 | 2.7 | 2.3 | 2.1 |
| Spinergy | 24.5 | 23.0 | 22.2 | 2.0 | 1.8 | 1.9 |
| Stock Pneumatic | 21.9 | 20.3 | 19.6 | 1.9 | 1.7 | 1.6 |

| Casters | Average [J/m] | | | Standard Deviation [J/m] | | |
|-----------------|---------------|------|------|--------------------------|-----|-----|
| | 60% | 70% | 80% | 60% | 70% | 80% |
| 4x1.5" FLSR | 24.0 | 23.7 | 23.9 | 4.0 | 5.0 | 5.8 |
| 5x1.5" Primo SR | 26.1 | 25.3 | 24.8 | 4.4 | 5.5 | 6.3 |
| 5x1" Primo | 25.1 | 24.6 | 24.6 | 3.9 | 4.9 | 5.7 |
| 6x1" Pneumatic | 27.9 | 26.3 | 25.7 | 4.8 | 5.3 | 6.1 |

Table 24. AMPS Propulsion Cost for Straight Maneuvers on Carpet

| Drive Wheels | Average [J/m] | | | Standard Deviation [J/m] | | |
|-----------------|---------------|------|------|--------------------------|-----|-----|
| | 60% | 70% | 80% | 60% | 70% | 80% |
| Solid Mag | 44.1 | 43.7 | 43.2 | 1.5 | 1.4 | 1.4 |
| Spinergy | 37.6 | 35.4 | 33.0 | 1.2 | 1.4 | 1.3 |
| Stock Pneumatic | 38.4 | 35.6 | 33.1 | 1.5 | 1.5 | 1.3 |

| Casters | Average [J/m] | | | Standard Deviation [J/m] | | |
|-----------------|---------------|------|------|--------------------------|-----|-----|
| | 60% | 70% | 80% | 60% | 70% | 80% |
| 4x1.5" FLSR | 39.8 | 38.5 | 36.9 | 3.1 | 4.1 | 5.0 |
| 5x1.5" Primo SR | 40.8 | 38.8 | 36.9 | 3.1 | 4.0 | 4.9 |
| 5x1" Primo | 40.4 | 38.6 | 36.6 | 3.3 | 4.1 | 5.0 |
| 6x1" Pneumatic | 39.2 | 37.0 | 35.4 | 3.1 | 4.3 | 5.2 |

Table 25. AMPS Propulsion Cost for Fixed Wheel Turn Maneuvers on Tile

| Drive Wheels | Average [J/rad] | | | Standard Deviation [J/rad] | | |
|-----------------|-----------------|------|------|----------------------------|-----|-----|
| | 60% | 70% | 80% | 60% | 70% | 80% |
| Solid Mag | 14.3 | 13.9 | 14.1 | 1.0 | 0.5 | 0.4 |
| Spinergy | 13.3 | 13.1 | 13.3 | 0.9 | 0.8 | 0.7 |
| Stock Pneumatic | 13.4 | 13.3 | 13.5 | 1.0 | 0.8 | 0.7 |

| Casters | Average [J/rad] | | | Standard Deviation [J/rad] | | |
|-----------------|-----------------|------|------|----------------------------|-----|-----|
| | 60% | 70% | 80% | 60% | 70% | 80% |
| 4x1.5" FLSR | 12.5 | 12.8 | 13.3 | 0.5 | 0.6 | 0.7 |
| 5x1.5" Primo SR | 14.0 | 13.5 | 13.6 | 0.7 | 0.8 | 0.7 |
| 5x1" Primo | 13.3 | 13.1 | 13.4 | 0.6 | 0.4 | 0.6 |
| 6x1" Pneumatic | 14.9 | 14.2 | 14.2 | 0.6 | 0.4 | 0.4 |

Table 26. AMPS Propulsion Cost for Fixed Wheel Turn Maneuvers on Carpet

| Drive Wheels | Average [J/rad] | | | Standard Deviation [J/rad] | | |
|-----------------|-----------------|------|------|----------------------------|-----|-----|
| | 60% | 70% | 80% | 60% | 70% | 80% |
| Solid Mag | 22.6 | 21.7 | 21.5 | 0.7 | 0.5 | 0.5 |
| Spinergy | 23.5 | 23.1 | 22.8 | 0.8 | 1.2 | 1.1 |
| Stock Pneumatic | 23.4 | 22.3 | 22.1 | 0.9 | 1.1 | 1.1 |

| Casters | Average [J/rad] | | | Standard Deviation [J/rad] | | |
|-----------------|-----------------|------|------|----------------------------|-----|-----|
| | 60% | 70% | 80% | 60% | 70% | 80% |
| 4x1.5" FLSR | 23.2 | 22.5 | 22.2 | 0.6 | 0.7 | 0.8 |
| 5x1.5" Primo SR | 23.8 | 23.1 | 22.9 | 0.8 | 1.1 | 1.1 |
| 5x1" Primo | 23.5 | 22.8 | 22.2 | 0.7 | 1.0 | 0.8 |
| 6x1" Pneumatic | 22.2 | 21.3 | 21.1 | 0.5 | 0.6 | 0.6 |

Table 27. AMPS Propulsion Cost for Zero Radius Turns Maneuvers on Tile

| Drive Wheels | Average [J/rad] | | | Standard Deviation [J/rad] | | |
|-----------------|-----------------|------|------|----------------------------|-----|-----|
| | 60% | 70% | 80% | 60% | 70% | 80% |
| Solid Mag | 14.1 | 11.9 | 10.8 | 2.1 | 1.0 | 0.5 |
| Spinergy | 11.4 | 9.0 | 7.6 | 1.9 | 0.8 | 0.4 |
| Stock Pneumatic | 11.1 | 9.5 | 8.3 | 1.4 | 1.0 | 1.1 |

| Casters | Average [J/rad] | | | Standard Deviation [J/rad] | | |
|-----------------|-----------------|------|-----|----------------------------|-----|-----|
| | 60% | 70% | 80% | 60% | 70% | 80% |
| 4x1.5" FLSR | 10.5 | 9.3 | 8.4 | 1.1 | 1.3 | 1.7 |
| 5x1.5" Primo SR | 13.0 | 10.7 | 9.8 | 1.2 | 1.5 | 1.5 |
| 5x1" Primo | 10.8 | 9.2 | 8.3 | 1.4 | 1.1 | 1.2 |
| 6x1" Pneumatic | 14.6 | 11.2 | 9.0 | 2.2 | 1.4 | 1.3 |

Table 28. AMPS Propulsion Cost for Zero Radius Turns Maneuvers on Carpet

| Drive Wheels | Average [J/rad] | | | Standard Deviation [J/rad] | | |
|-----------------|-----------------|------|------|----------------------------|-----|-----|
| | 60% | 70% | 80% | 60% | 70% | 80% |
| Solid Mag | 16.6 | 15.0 | 13.9 | 1.0 | 0.6 | 0.6 |
| Spinergy | 14.7 | 12.8 | 11.0 | 0.9 | 0.5 | 0.3 |
| Stock Pneumatic | 16.3 | 14.4 | 12.7 | 0.8 | 0.4 | 0.5 |

| Casters | Average [J/rad] | | | Standard Deviation [J/rad] | | |
|-----------------|-----------------|------|------|----------------------------|-----|-----|
| | 60% | 70% | 80% | 60% | 70% | 80% |
| 4x1.5" FLSR | 14.8 | 13.7 | 12.4 | 0.7 | 1.0 | 1.3 |
| 5x1.5" Primo SR | 16.5 | 14.5 | 13.2 | 1.1 | 0.9 | 1.4 |
| 5x1" Primo | 15.3 | 13.7 | 12.3 | 1.1 | 1.0 | 1.1 |
| 6x1" Pneumatic | 16.8 | 14.4 | 12.2 | 0.7 | 1.1 | 1.0 |

The propulsion cost for all three canonical maneuver increased between tile and carpet surfaces. On average, straight propulsion cost increased by 52%, fixed-wheel turn propulsion cost increased by 66%, and zero-radius turns propulsion cost increased by 36%. This suggests straight and fixed-wheel turn maneuvers are the most sensitive to rough surface conditions. On tile, fixed-wheel turn maneuvers had on average a 30% greater propulsion cost than zero-radius turns maneuvers. On carpet, this percent difference increased to 59%. Both of these maneuvers have a kinematic outcome based on heading change. However, the fixed wheel turn is impacted by its larger translational kinetic energy as well as the scrub torque of its fixed drive wheel. The sole resistive loss that is present in zero-radius turns but absent in fixed-wheel turn maneuvers is caster scrub due to swivel, which appears to be too small to offset the differences between these two maneuvers.

ANOVA Analysis

Normality of the dependent measures were assessed using Kolmogorov-Smirnov analysis. Propulsion cost during the straight trajectories was found to violate the assumption of normality. ANOVA was run using a Box-Cox transformation of this data.

Table 29. ANOVA of Straight Maneuvers on Tile

| Source | DF | Adj SS | Adj MS | F-Value | P-Value |
|-----------------------|----|---------|----------|---------|---------|
| DRIVE WHEEL | 2 | 1.20037 | 0.600186 | 882.85 | 0 |
| CASTER | 3 | 0.05607 | 0.018691 | 27.49 | 0 |
| WD CONFIG | 2 | 0.01867 | 0.009333 | 13.73 | 0 |
| DRIVE WHEEL*WD CONFIG | 4 | 0.0309 | 0.007724 | 11.36 | 0 |
| CASTER*WD CONFIG | 6 | 0.00533 | 0.000888 | 1.31 | 0.304 |
| Error | 18 | 0.01224 | 0.00068 | | |
| Total | 35 | 1.32358 | | | |

Table 30. ANOVA of Straight Maneuvers on Carpet

| Source | DF | Adj SS | Adj MS | F-Value | P-Value |
|-----------------------|----|----------|----------|---------|---------|
| DRIVE WHEEL | 2 | 0.347627 | 0.173813 | 1573.83 | 0 |
| CASTER | 3 | 0.010059 | 0.003353 | 30.36 | 0 |
| WD CONFIG | 2 | 0.060054 | 0.030027 | 271.89 | 0 |
| DRIVE WHEEL*WD CONFIG | 4 | 0.020189 | 0.005047 | 45.7 | 0 |
| CASTER*WD CONFIG | 6 | 0.000778 | 0.00013 | 1.17 | 0.363 |
| Error | 18 | 0.001988 | 0.00011 | | |
| Total | 35 | 0.440695 | | | |

For the straight trajectory, the mean propulsion cost values within all three factors were significantly different on both tile and carpet. This result means that the levels within each factor were not equal. The interaction between drive wheel and %WD was also significant on both surfaces, meaning that the response for the type of drive wheel depended on the %WD value.

Table 31. ANOVA of Fixed Wheel Turn Maneuvers on Tile

| Source | DF | Adj SS | Adj MS | F-Value | P-Value |
|-----------------------|----|---------|---------|---------|---------|
| DRIVE WHEEL | 2 | 5.1288 | 2.56442 | 28.07 | 0 |
| CASTER | 3 | 12.4056 | 4.13521 | 45.27 | 0 |
| WD CONFIG | 2 | 0.4508 | 0.22541 | 2.47 | 0.113 |
| DRIVE WHEEL*WD CONFIG | 4 | 0.1635 | 0.04087 | 0.45 | 0.773 |
| CASTER*WD CONFIG | 6 | 2.242 | 0.37367 | 4.09 | 0.009 |
| Error | 18 | 1.6444 | 0.09135 | | |
| Total | 35 | 22.0351 | | | |

Table 32. ANOVA of Fixed Wheel Turn Maneuvers on Carpet

| Source | DF | Adj SS | Adj MS | F-Value | P-Value |
|-----------------------|----|---------|---------|---------|---------|
| DRIVE WHEEL | 2 | 8.548 | 4.27402 | 29.72 | 0 |
| CASTER | 3 | 14.6265 | 4.87551 | 33.9 | 0 |
| WD CONFIG | 2 | 7.2156 | 3.60778 | 25.09 | 0 |
| DRIVE WHEEL*WD CONFIG | 4 | 0.7178 | 0.17945 | 1.25 | 0.326 |
| CASTER*WD CONFIG | 6 | 0.2156 | 0.03593 | 0.25 | 0.953 |
| Error | 18 | 2.5884 | 0.1438 | | |
| Total | 35 | 33.9119 | | | |

For fixed wheel turns, propulsion cost significantly differed across both drive wheel and caster type on both tile and carpet with %WD being significantly different only on carpet. Because the %WD main effect was not significant on tile, its interactions were not assessed. On carpet, because neither interaction was significant, one can infer that the propulsion cost of the components are independent of %WD during fixed wheel turns.

Table 33. ANOVA of Zero Radius Turns Maneuvers on Tile

| Source | DF | Adj SS | Adj MS | F-Value | P-Value |
|-----------------------|----|--------|---------|---------|---------|
| DRIVE WHEEL | 2 | 61.956 | 30.9781 | 78.82 | 0 |
| CASTER | 3 | 35.946 | 11.9821 | 30.49 | 0 |
| WD CONFIG | 2 | 68.334 | 34.1669 | 86.94 | 0 |
| DRIVE WHEEL*WD CONFIG | 4 | 1.21 | 0.3026 | 0.77 | 0.559 |
| CASTER*WD CONFIG | 6 | 10.939 | 1.8231 | 4.64 | 0.005 |
| Error | 18 | 7.074 | 0.393 | | |
| Total | 35 | 185.46 | | | |

Table 34. ANOVA of Zero Radius Turns Maneuvers on Carpet

| Source | DF | Adj SS | Adj MS | F-Value | P-Value |
|-----------------------|----|---------|---------|---------|---------|
| DRIVE WHEEL | 2 | 34.018 | 17.009 | 134.38 | 0 |
| CASTER | 3 | 7.574 | 2.5248 | 19.95 | 0 |
| WD CONFIG | 2 | 66.991 | 33.4957 | 264.64 | 0 |
| DRIVE WHEEL*WD CONFIG | 4 | 1.164 | 0.2909 | 2.3 | 0.099 |
| CASTER*WD CONFIG | 6 | 4.261 | 0.7102 | 5.61 | 0.002 |
| Error | 18 | 2.278 | 0.1266 | | |
| Total | 35 | 116.287 | | | |

For zero radius turns, the mean propulsion cost values within all three factors were significantly different on both tile and carpet. The interactions between casters and %WD was also significant on both surfaces at the $p < 0.05$ level while the interactions between drive wheel and %WD on carpet was significant at the $p < 0.1$ level. The propulsion cost of drive wheel type did not depend on %WD when traveling on tile based upon the non-significant interaction.

The cost of propulsion differed significantly across drive wheel and caster types during all three canonical maneuvers and on both surfaces. This result can be inferred to mean that the selection of drive wheels and casters influences the propulsion of manual wheelchairs on both high and low friction surfaces for both straight and turning trajectories. Different configurations of %WD impacted propulsion cost during two maneuvers, straight and zero radius turns, suggesting that adjustments of fore-aft axle position on a wheelchair strongly influence user effort during these two maneuvers. The 60%-80% span of weight distributions influenced propulsion cost during fixed wheel turns on the higher friction carpeted surface but not on tile.

The interactions with Drive Wheel and Caster types provide insight into the combined influences of %WD, drive wheels and casters on the cost of propulsion. During a straight trajectory, the performance of drive wheels - as measured by propulsion cost - is dependent on the %WD of the wheelchair system. Caster performance is not dependent on the %WD during a straight trajectory. Together, this illustrates the significant impact that drive wheel load has on system rolling resistance, while the load-based variance in caster rolling resistance contribution to the system is not significant. During fixed wheel turns, neither drive wheel or caster performance depends on the %WD of the wheelchair, demonstrating the components' insensitivity to load in this maneuver. Finally, during zero radius turns, caster performance was dependent on %WD levels on both surfaces but drive wheel performance is only dependent on %WD when traveling on carpet. This can be rationalized by the presence of the high-resistance swiveling of the casters in this maneuver, where added front load would amplify this resistive force greatly. Drive wheels, on the other hand, only seem to experience significant load sensitivity on carpet.

Effect Sizes and Percent Differences

Keying off of the ANOVA analysis, both the effect sizes and percent changes were leveraged as useful comparisons against a stock MWC configuration with 80%WD, 5 x 1” Primo casters, and Stock Pneumatic drive wheels. An effect size of 1.0 or 2.0 indicates that propulsion cost of the tested wheelchair is at the 84th percentile or 97.7th percentile of the base wheelchair configuration, respectively. The very large effect sizes, therefore, show a distinction between the propulsion cost measured across configurations, trajectories, and surfaces. Percentage differences, on the other hand, offer a relative comparison that can be used to apply clinical relevancy. These differences in work can be used to quantify the relative propulsion effort that a user must impart to complete the maneuver with different components. In the follow section, the percent changes and effect sizes for different component and weight-distribution configurations are tabulated, each table separated by maneuver and surface type. Green and red highlighting are used to denote increase and decrease with respect to the stock component/configuration, respectively. Effect sizes > 1 are bolded. Corresponding plots of average caster and drive wheel propulsion cost are also included for each maneuver and surface type. These plots will serve to better illustrate the differences between components and configurations summarized by the tables.

Table 35. Straight (Tile) Propulsion Cost % Differences and Effect Sizes

| Drive Wheels | % Change | | | Cohen's d | | |
|-----------------|----------|-------|-------|-------------|-------------|-------------|
| | 60% | 70% | 80% | 60% | 70% | 80% |
| Solid Mag | 42.2% | 55.2% | 66.3% | 3.94 | 5.54 | 6.93 |
| Spinergy | 12.1% | 13.1% | 13.4% | 1.35 | 1.51 | 1.47 |
| Stock Pneumatic | 0.0% | 0.0% | 0.0% | 0.00 | 0.00 | 0.00 |

| %WD | % Change | | | Cohen's d | | |
|------------|-----------|----------|-----------------|-----------|-------------|-----------------|
| | Solid Mag | Spinergy | Stock Pneumatic | Solid Mag | Spinergy | Stock Pneumatic |
| 60% | -4.4% | 10.5% | 11.8% | -0.60 | 1.19 | 1.29 |
| 70% | -2.8% | 3.8% | 4.1% | -0.42 | 0.45 | 0.48 |
| 80% | 0.0% | 0.0% | 0.0% | 0.00 | 0.00 | 0.00 |

| Casters | % Change | | | Cohen's d | | |
|-------------------|----------|-------|-------|-----------|-------|-------|
| | 60% | 70% | 80% | 60% | 70% | 80% |
| 4x1.5" FLSR | -4.3% | -3.5% | -3.0% | -0.28 | -0.18 | -0.13 |
| 5x1.5" Primo SR | 3.9% | 2.7% | 1.0% | 0.24 | 0.13 | 0.04 |
| 5x1" Primo | 0.0% | 0.0% | 0.0% | 0.00 | 0.00 | 0.00 |
| 6x1" Pneumatic | 11.2% | 6.9% | 4.4% | 0.65 | 0.33 | 0.18 |

| %WD | % Change | | | | Cohen's d | | | |
|------------|-------------|-----------------|------------|----------------|-------------|-----------------|------------|----------------|
| | 4x1.5" FLSR | 5x1.5" Primo SR | 5x1" Primo | 6x1" Pneumatic | 4x1.5" FLSR | 5x1.5" Primo SR | 5x1" Primo | 6x1" Pneumatic |
| 60% | 0.7% | 5.1% | 2.2% | 8.9% | 0.03 | 0.23 | 0.11 | 0.42 |
| 70% | -0.5% | 1.7% | 0.1% | 2.5% | -0.02 | 0.07 | 0.00 | 0.11 |
| 80% | 0.0% | 0.0% | 0.0% | 0.0% | 0.00 | 0.00 | 0.00 | 0.00 |

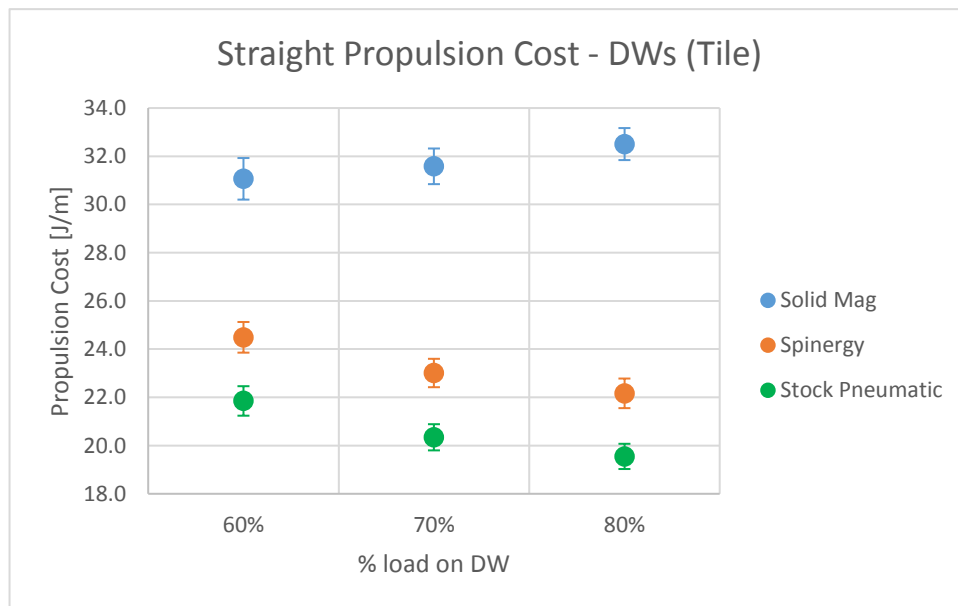


Figure 83. Propulsion Cost of Drive Wheel Configurations for Straight Maneuvers on Tile

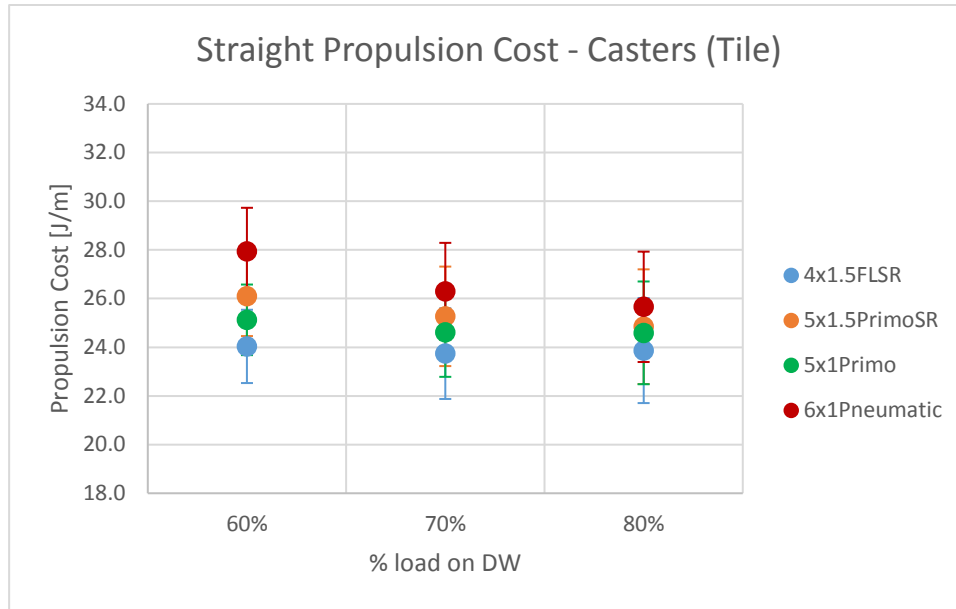


Figure 84. Propulsion Cost of Caster Configurations for Straight Maneuvers on Tile

For propulsion cost of straight maneuvers on tile, MWCs configured with the Solid Mag exhibit the largest positive and increasing effect size (3.94 – 6.93) with respect to configurations with the Stock Pneumatic, which is lowest in propulsion cost. Percent differences between these two drive wheels range from 42.2% to 66.3% across 60% WD to 80% WD. The Spinergy configurations also have large positive effect sizes with respect to the Stock Pneumatic configurations (1.35 – 1.51), with percent differences across weight-distributions ranging from 12.1% to 13.4%. Both Spinergy and Stock Pneumatic configurations experience an increase in propulsion cost with decreased load on drive wheels, with significant effect sizes at 60%WD with respect to their 80%WD configurations (1.19 and 1.29). This translates to a 10.5% and 11.8% increase in propulsion cost, respectively. The Solid Mag configurations, however, decrease in propulsion cost with less load on drive wheels, which translates to the Solid Mag being, on average, less efficient in rolling than the casters within these weight-distributions. Differences between

casters for straight maneuver propulsion cost on tile are smaller, with the 6x1” Pneumatic having the greatest effect size of 0.65 (11.2% greater) at 60%WD when compared to the 5x1” Primo. The 6x1” Pneumatic configurations are also the most sensitive to load, with an effect size of 0.42 (8.9% greater) between its 80%WD and 60%WD configurations. The only caster configurations to register a reduction in propulsion cost relative to the 5x1” Primo is the 4x1.5” FLSR (-4.3%).

Table 36. Straight (Carpet) Propulsion Cost % Differences and Effect Sizes

| Drive Wheels | % Change | | | Cohen's d | | |
|------------------------|----------|-------|-------|-------------|-------------|-------------|
| | 60% | 70% | 80% | 60% | 70% | 80% |
| Solid Mag | 14.7% | 22.8% | 30.8% | 3.79 | 5.59 | 7.47 |
| Spinergy | -2.1% | -0.5% | -0.2% | -0.59 | -0.12 | -0.04 |
| Stock Pneumatic | 0.0% | 0.0% | 0.0% | 0.00 | 0.00 | 0.00 |

| %WD | % Change | | | Cohen's d | | |
|------------|-----------|----------|-----------------|-----------|-------------|-----------------|
| | Solid Mag | Spinergy | Stock Pneumatic | Solid Mag | Spinergy | Stock Pneumatic |
| 60% | 1.9% | 14.0% | 16.2% | 0.58 | 3.72 | 3.75 |
| 70% | 1.0% | 7.2% | 7.5% | 0.31 | 1.78 | 1.75 |
| 80% | 0.0% | 0.0% | 0.0% | 0.00 | 0.00 | 0.00 |

| Casters | % Change | | | Cohen's d | | |
|-------------------|----------|-------|-------|-----------|-------|-------|
| | 60% | 70% | 80% | 60% | 70% | 80% |
| 4x1.5" FLSR | -1.4% | 0.0% | 0.7% | -0.17 | 0.00 | 0.05 |
| 5x1.5" Primo SR | 1.0% | 0.5% | 0.8% | 0.13 | 0.05 | 0.06 |
| 5x1" Primo | 0.0% | 0.0% | 0.0% | 0.00 | 0.00 | 0.00 |
| 6x1" Pneumatic | -2.9% | -4.0% | -3.3% | -0.36 | -0.36 | -0.24 |

| %WD | % Change | | | | Cohen's d | | | |
|------------|-------------|-----------------|------------|----------------|-------------|-----------------|------------|----------------|
| | 4x1.5" FLSR | 5x1.5" Primo SR | 5x1" Primo | 6x1" Pneumatic | 4x1.5" FLSR | 5x1.5" Primo SR | 5x1" Primo | 6x1" Pneumatic |
| 60% | 8.0% | 10.5% | 10.3% | 10.7% | 0.71 | 0.95 | 0.88 | 0.88 |
| 70% | 4.5% | 5.0% | 5.3% | 4.6% | 0.37 | 0.41 | 0.42 | 0.34 |
| 80% | 0.0% | 0.0% | 0.0% | 0.0% | 0.00 | 0.00 | 0.00 | 0.00 |

For straight maneuvers on carpet, the Solid Mag maintains its large positive effect sizes but reflects smaller percent differences (3.79 – 7.47, 14.7% – 30.8%) with respect to the Stock Pneumatic configurations across all weight distributions. On carpet, the Spinergy

configuration propulsion costs are no longer greater than that of Stock Pneumatic configurations and slightly lower in certain cases (-2.9%). This suggests that the Stock Pneumatic straight propulsion costs have increased relative to Spinergy and Solid Mag configurations on carpet. All drive wheel configurations on carpet exhibit an increasing benefit of reduced propulsion with more load on the drive wheels (80%WD). The benefit is small for the Solid Mag configurations (1.9%), but the Spinergy and Stock Pneumatic have a 14% and 16.2% propulsion cost difference between 80%WD and 60%WD. This suggests that increased percent loading on drive wheels is more advantageous on carpet than on tile.

Propulsion cost differences between caster configurations are smaller on carpet compared to on tile. On tile, the caster configurations differed from the 5x1" Primo configurations by an average of 4.5%, while on carpet, they only differed by an average of 1.6%. Furthermore, configurations with the 6x1" Pneumatic were the only caster configuration to have an absolute effect size greater than 0.2, or at greater than the 58th percentile of the 5x1" Primo's propulsion costs. ANOVA results presented a significant difference between the propulsion costs of different caster configurations, but it would appear only MWCs configured with 6x1" Pneumatic casters were distinct from the others. The 6x1" Pneumatic configurations are also different in their propulsion costs on carpet when compared to tile. On carpet, instead of having an increased propulsion cost, this caster's configurations now registered a 2.9% - 4% reduction in propulsion cost relative to the base caster's configurations. This suggests the 6x1" Pneumatic may be an effective caster to use on carpet when traveling in straight maneuvers. Casters configurations were also more sensitive to weight-distribution differences for straight maneuvers on carpet,

with an average 7.4% propulsion cost difference (0.62 effect size) from the base 60% WD, compared to the 2.7% propulsion cost difference (0.12 effect size) on tile.

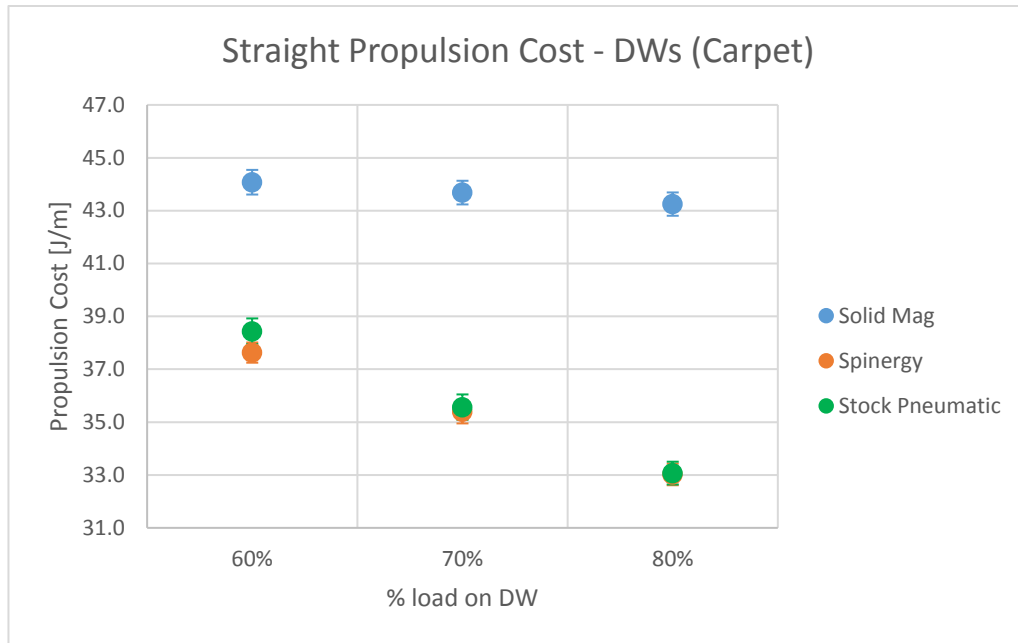


Figure 85. Propulsion Cost of Drive Wheel Configurations for Straight Maneuvers on Carpet

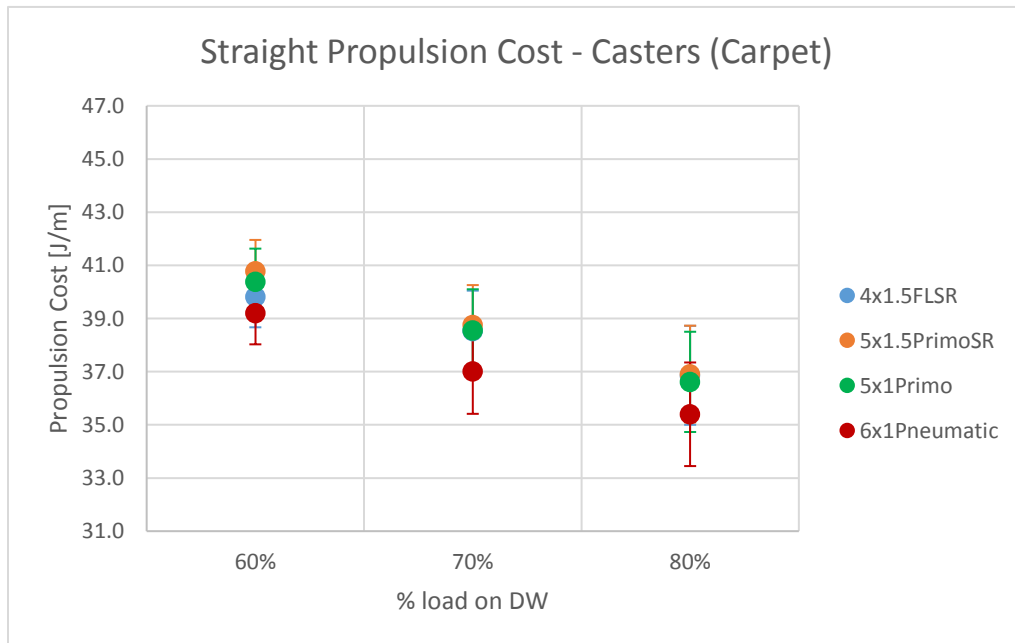


Figure 86. Propulsion Cost of Caster Configurations for Straight Maneuvers on Carpet

Table 37. Fixed Wheel Turn (Tile) Propulsion Cost % Differences and Effect Sizes

| Drive Wheels | % Change | | | Cohen's d | | |
|-----------------|----------|-------|-------|-----------|-------|-------------|
| | 60% | 70% | 80% | 60% | 70% | 80% |
| Solid Mag | 6.9% | 4.3% | 4.6% | 0.91 | 0.89 | 1.05 |
| Spinergy | -0.7% | -1.8% | -1.2% | -0.10 | -0.30 | -0.22 |
| Stock Pneumatic | 0.0% | 0.0% | 0.0% | 0.00 | 0.00 | 0.00 |

| %WD | % Change | | | Cohen's d | | |
|------------|-----------|----------|-----------------|-----------|----------|-----------------|
| | Solid Mag | Spinergy | Stock Pneumatic | Solid Mag | Spinergy | Stock Pneumatic |
| 60% | 1.8% | 0.0% | -0.4% | 0.33 | 0.00 | -0.06 |
| 70% | -1.4% | -1.8% | -1.2% | -0.42 | -0.31 | -0.21 |
| 80% | 0.0% | 0.0% | 0.0% | 0.00 | 0.00 | 0.00 |

| Casters | % Change | | | Cohen's d | | |
|-------------------|----------|-------|-------|--------------|-------------|-------------|
| | 60% | 70% | 80% | 60% | 70% | 80% |
| 4x1.5" FLSR | -6.4% | -2.4% | -0.3% | -1.54 | -0.59 | -0.06 |
| 5x1.5" Primo SR | 5.3% | 2.8% | 1.6% | 1.11 | 0.57 | 0.34 |
| 5x1" Primo | 0.0% | 0.0% | 0.0% | 0.00 | 0.00 | 0.00 |
| 6x1" Pneumatic | 12.1% | 8.3% | 6.3% | 2.76 | 2.49 | 1.69 |

| %WD | % Change | | | | Cohen's d | | | |
|------------|-------------|-----------------|------------|----------------|--------------|-----------------|------------|----------------|
| | 4x1.5" FLSR | 5x1.5" Primo SR | 5x1" Primo | 6x1" Pneumatic | 4x1.5" FLSR | 5x1.5" Primo SR | 5x1" Primo | 6x1" Pneumatic |
| 60% | -6.4% | 3.3% | -0.3% | 5.1% | -1.35 | 0.63 | -0.07 | 1.41 |
| 70% | -3.8% | -0.5% | -1.7% | 0.1% | -0.75 | -0.10 | -0.45 | 0.05 |
| 80% | 0.0% | 0.0% | 0.0% | 0.0% | 0.00 | 0.00 | 0.00 | 0.00 |

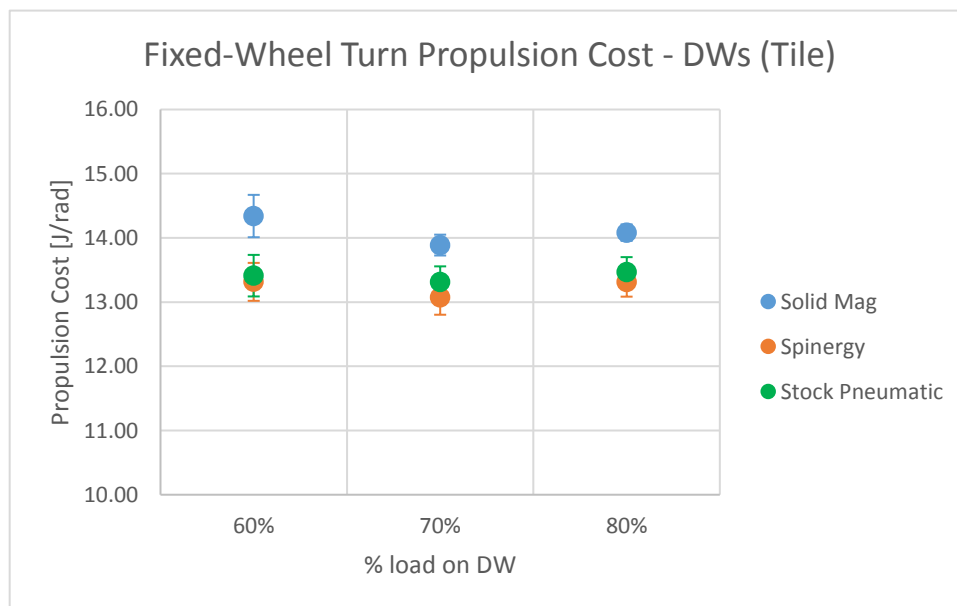


Figure 87. Propulsion Cost of Drive Wheel Configurations for Fixed Wheel Turn Maneuvers on Tile

For fixed-wheel maneuvers on tile, the propulsion cost differences amongst MWCs configured with different casters was greater than that of MWCs configured with different drive wheels. On average, the caster-influenced propulsion cost percent difference was more than 3%, while the drive wheel-influenced difference was 2%. Only the Solid Mag configurations had a significant effect size in their propulsion costs with respect to the Stock Pneumatic configurations, ranging from 0.89 to 1.05 with percent differences from 4.3% to 6.9%. Furthermore, as seen in **Figure 87**, the propulsion cost of each drive wheel configuration appears to reach their minimums at 70%WD. Recalling that the system yaw inertia differences between weight distribution configurations 60%WD and 70%WD (decrease of 1.56 kg-m²), and 70%WD and 80%WD (decrease of 0.96 kg-m²) are different, one might speculate that the balanced between inertial and resistive effects are being altered by the inconsistent system yaw inertias between weight-distribution configurations.

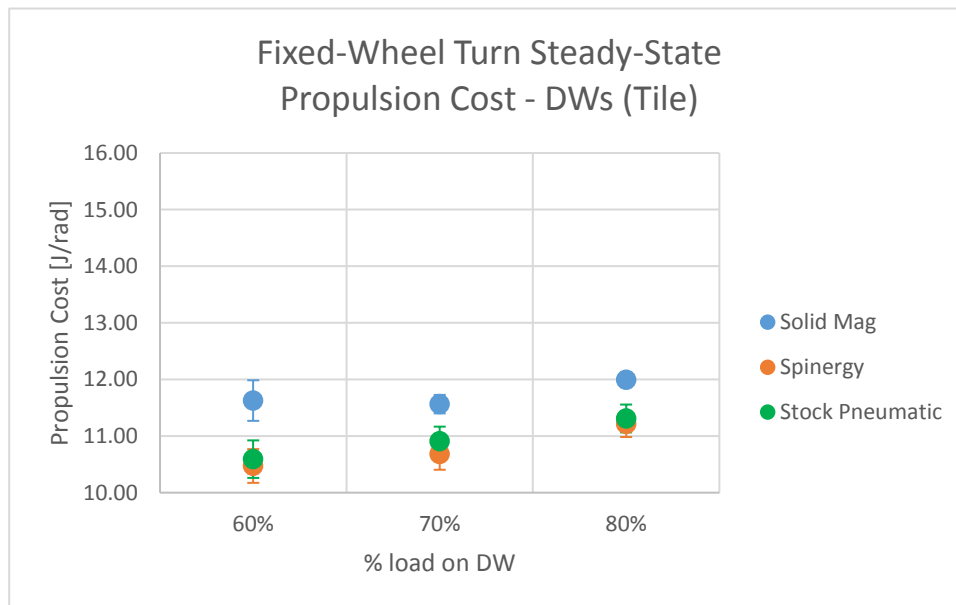


Figure 88. Propulsion Cost of Drive Wheel Configurations for Fixed Wheel Turn Maneuvers on Tile (Steady-State Phase)

To test this theory, we determined the propulsion cost of the steady-state phase for fixed-wheel turn maneuvers to remove the impact of system yaw inertia. Plotting this data in **Figure 88**, we see that while the propulsion costs are reduced across all configurations due to no changes in system kinetic energy, the relative relationship between the different propulsion torques across the three weight-distributions does not change. This implies that the “minimum” propulsion cost occurring at 70% WD is a result of the interactions between the different load sensitivities of their component resistive losses.

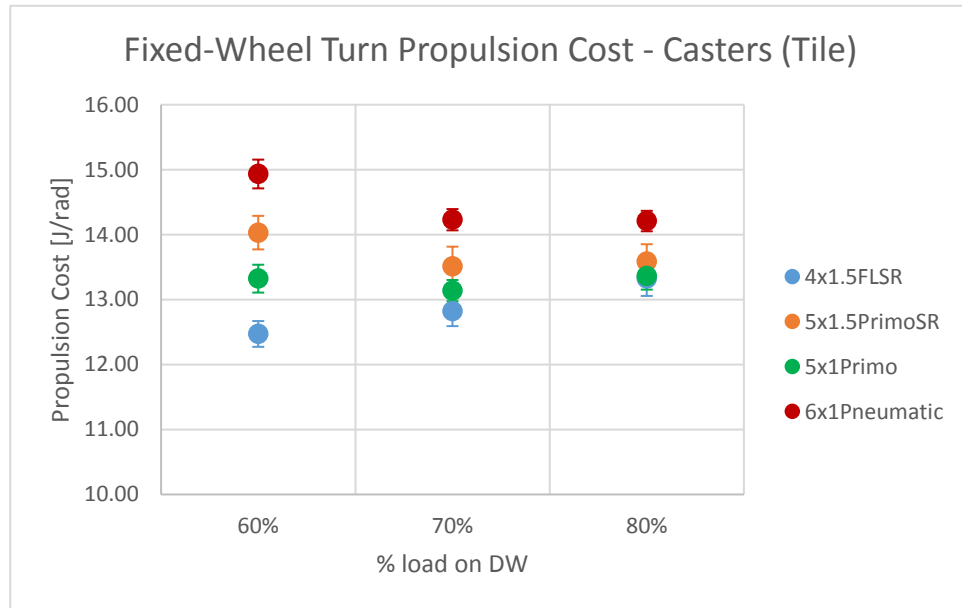


Figure 89. Propulsion Cost of Caster Configurations for Fixed Wheel Turn Maneuvers on Tile

The “minimum” propulsion cost feature can also be seen with the 5x1.5” Primo SR and 5x1” Primo casters. Again, examination of the steady-state propulsion cost yielded no relational changes. In spite of the ANOVA results that indicate a lack of weight-distribution impact on propulsion cost for fixed-wheel turning, the 4x1.5” FLSR and 6x1” Pneumatic configurations exhibited considerable sensitivity to load, with percent differences of -6.4% and 5.1% (effect sizes -1.35 and 1.41) at 60% WD, respectively. This

load sensitivity causes the caster-grouped propulsion costs to become more distinct from each other as you move from 80%WD to 60%WD, as seen in **Figure 89**. At 60%WD, the 4x1.5" FLSR propulsion cost is the smallest, 6.3% (effect size -1.54) less than 5x1" Primo configurations, whereas the 6x1" FLSR propulsion cost is the largest, 12.1% (effect size 2.76) greater than 5x1" Primo configurations. This demonstrates the significant impact casters have on fixed-wheel turning on tile when the MWC is configured at low %WDs.

Table 38. Fixed Wheel Turn (Carpet) Propulsion Cost % Difference and Effect Size

| Drive Wheels | % Change | | | Cohen's d | | |
|------------------------|----------|-------|-------|-----------|-------|-------|
| | 60% | 70% | 80% | 60% | 70% | 80% |
| Solid Mag | -3.4% | -2.8% | -2.7% | -0.98 | -0.75 | -0.71 |
| Spinergy | 0.2% | 3.6% | 3.2% | 0.06 | 0.71 | 0.66 |
| Stock Pneumatic | 0.0% | 0.0% | 0.0% | 0.00 | 0.00 | 0.00 |

| %WD | % Change | | | Cohen's d | | |
|------------|-----------|----------|-----------------|-------------|----------|-----------------|
| | Solid Mag | Spinergy | Stock Pneumatic | Solid Mag | Spinergy | Stock Pneumatic |
| 60% | 5.4% | 3.0% | 6.1% | 1.93 | 0.74 | 1.35 |
| 70% | 1.2% | 1.6% | 1.3% | 0.50 | 0.34 | 0.27 |
| 80% | 0.0% | 0.0% | 0.0% | 0.00 | 0.00 | 0.00 |

| Casters | % Change | | | Cohen's d | | |
|-------------------|----------|-------|-------|--------------|--------------|--------------|
| | 60% | 70% | 80% | 60% | 70% | 80% |
| 4x1.5" FLSR | -1.2% | -1.2% | -0.1% | -0.43 | -0.30 | -0.03 |
| 5x1.5" Primo SR | 1.4% | 1.2% | 2.8% | 0.42 | 0.27 | 0.64 |
| 5x1" Primo | 0.0% | 0.0% | 0.0% | 0.00 | 0.00 | 0.00 |
| 6x1" Pneumatic | -5.2% | -6.7% | -5.4% | -1.95 | -1.80 | -1.71 |

| %WD | % Change | | | | Cohen's d | | | |
|------------|-------------|-----------------|------------|----------------|-------------|-----------------|-------------|----------------|
| | 4x1.5" FLSR | 5x1.5" Primo SR | 5x1" Primo | 6x1" Pneumatic | 4x1.5" FLSR | 5x1.5" Primo SR | 5x1" Primo | 6x1" Pneumatic |
| 60% | 4.2% | 4.0% | 5.5% | 5.6% | 1.34 | 0.94 | 1.58 | 2.23 |
| 70% | 1.3% | 0.9% | 2.4% | 1.0% | 0.37 | 0.18 | 0.57 | 0.36 |
| 80% | 0.0% | 0.0% | 0.0% | 0.0% | 0.00 | 0.00 | 0.00 | 0.00 |

For fixed-wheel turn maneuvers on carpet, the average propulsion cost percent differences amongst casters and drive wheels are quite similar, both at ~2.7%. This is reduced relative to the differences observed amongst components on tile. From tile to

carpet, configurations with Solid Mag go from having the greatest propulsion cost to the least, with an average of 3% less propulsion cost than the base Stock Pneumatic configurations. The opposite is true for the Spinerge configurations, which is an average of 2.3% greater in propulsion cost than the Stock Pneumatic configurations. In contrast to ANOVA results, Solid Mag and Stock Pneumatic have moderate sensitivity to weight distribution, with 5.4% and 6.1% (effect sizes 1.93 and 1.35) greater propulsion cost at 60% WD than 80% WD.

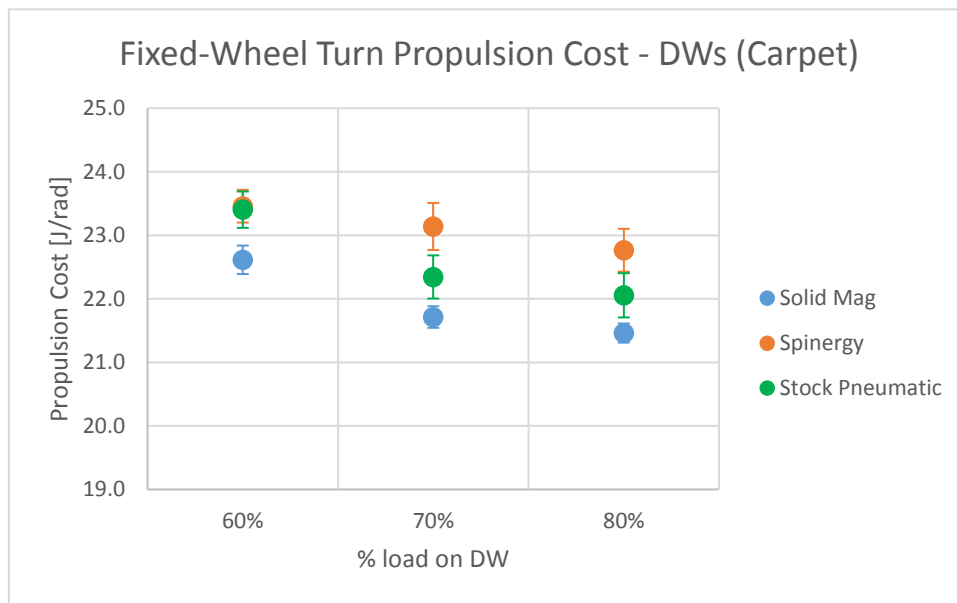


Figure 90. Propulsion Cost of Drive Wheel Configurations for Fixed Wheel Turn Maneuvers on Carpet

The benefit of the configurations with 4x1.5” FLSR caster is diminished on carpet, only 1% less in propulsion cost than the 5x1” Primo configurations. Configurations with the 6x1” Pneumatic and 5x1.5” Primo SR take on the opposite behavior, with the 6x1” Pneumatic configurations going from greatest in propulsion cost on tile to least propulsion cost on carpet, with an average of 5.8% (effect size -1.82) less propulsion cost than the 5x1” Primo configurations. All casters exhibit some sensitivity to load, with 4% to 5.6% increase in propulsion cost between the 80% WD and 60% WD configurations. This result

corroborates the Bascou's 2015 study of wheelchair turning resistance, where increased COM distance from the rear axle corresponded to increased turning deceleration (Bascou et al., 2015).

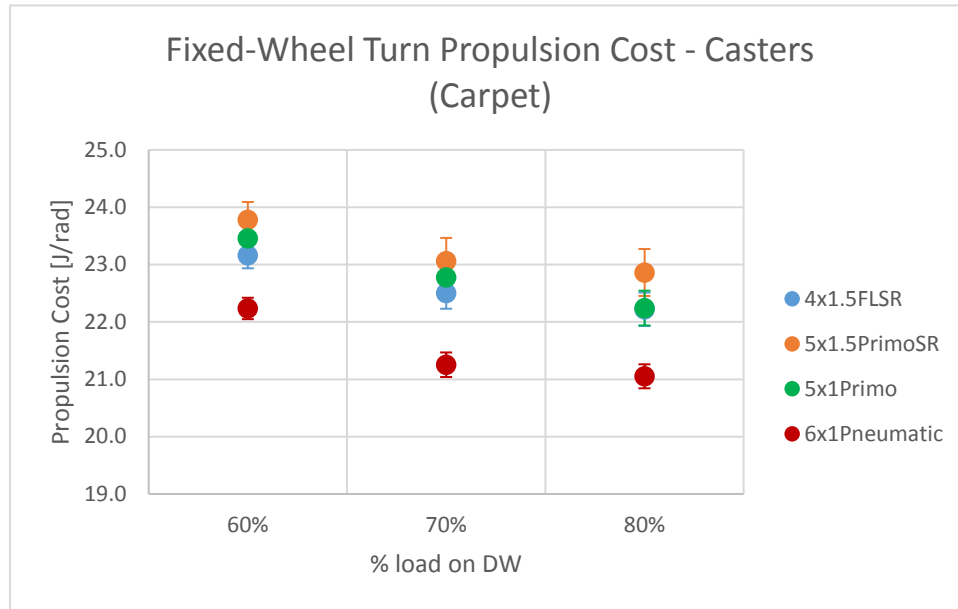


Figure 91. Propulsion Cost of Caster Configurations for Fixed Wheel Turn Maneuvers on Carpet

Table 39. Zero Radius Turns (Tile) Propulsion Cost % Differences and Effect Sizes

| Drive Wheels | % Change | | | Cohen's d | | |
|------------------------|----------|-------|-------|-------------|-------------|-------------|
| | 60% | 70% | 80% | 60% | 70% | 80% |
| Solid Mag | 26.8% | 24.7% | 29.4% | 1.66 | 2.34 | 2.75 |
| Spinergy | 2.4% | -6.0% | -8.7% | 0.16 | -0.61 | -0.86 |
| Stock Pneumatic | 0.0% | 0.0% | 0.0% | 0.00 | 0.00 | 0.00 |

| %WD | % Change | | | Cohen's d | | |
|------------|-----------|----------|-----------------|-------------|-------------|-----------------|
| | Solid Mag | Spinergy | Stock Pneumatic | Solid Mag | Spinergy | Stock Pneumatic |
| 60% | 31.3% | 50.4% | 34.0% | 2.16 | 2.77 | 2.23 |
| 70% | 10.5% | 18.1% | 14.6% | 1.43 | 2.12 | 1.12 |
| 80% | 0.0% | 0.0% | 0.0% | 0.00 | 0.00 | 0.00 |

| Casters | % Change | | | Cohen's d | | |
|-------------------|----------|-------|-------|-------------|-------------|-------------|
| | 60% | 70% | 80% | 60% | 70% | 80% |
| 4x1.5" FLSR | -2.6% | 1.8% | 1.1% | -0.22 | 0.14 | 0.06 |
| 5x1.5" Primo SR | 20.8% | 17.0% | 18.0% | 1.68 | 1.18 | 1.08 |
| 5x1" Primo | 0.0% | 0.0% | 0.0% | 0.00 | 0.00 | 0.00 |
| 6x1" Pneumatic | 35.0% | 22.2% | 8.8% | 2.01 | 1.62 | 0.58 |

| %WD | % Change | | | | Cohen's d | | | |
|------------|-------------|-----------------|------------|----------------|-------------|-----------------|-------------|----------------|
| | 4x1.5" FLSR | 5x1.5" Primo SR | 5x1" Primo | 6x1" Pneumatic | 4x1.5" FLSR | 5x1.5" Primo SR | 5x1" Primo | 6x1" Pneumatic |
| 60% | 25.2% | 33.0% | 29.9% | 61.2% | 1.46 | 2.35 | 1.85 | 3.05 |
| 70% | 11.4% | 9.6% | 10.5% | 24.1% | 0.62 | 0.63 | 0.74 | 1.65 |
| 80% | 0.0% | 0.0% | 0.0% | 0.0% | 0.00 | 0.00 | 0.00 | 0.00 |

For zero-radius turns maneuvers on tile, large differences were present amongst both drive wheels and casters. Solid Mag configurations presented the greatest percent increase in propulsion cost with respect to the Stock Pneumatic configurations, ranging from 24.7% to 29.4% (effect sizes 1.66 to 2.75). Spinergy configurations were lowest in propulsion cost for 70%WD and 80%WD, with 6% and 8.7% percent reductions with respect to the Stock Pneumatic configurations. Drive wheels as a whole were very sensitive to weight distribution changes, with effect sizes > 1 for all comparisons of 70%WD and 60%WD to the base 80%WD. The percent increases in propulsion cost ranged from 10.5% - 18.1% and 31.3% - 50.4%, respectively.

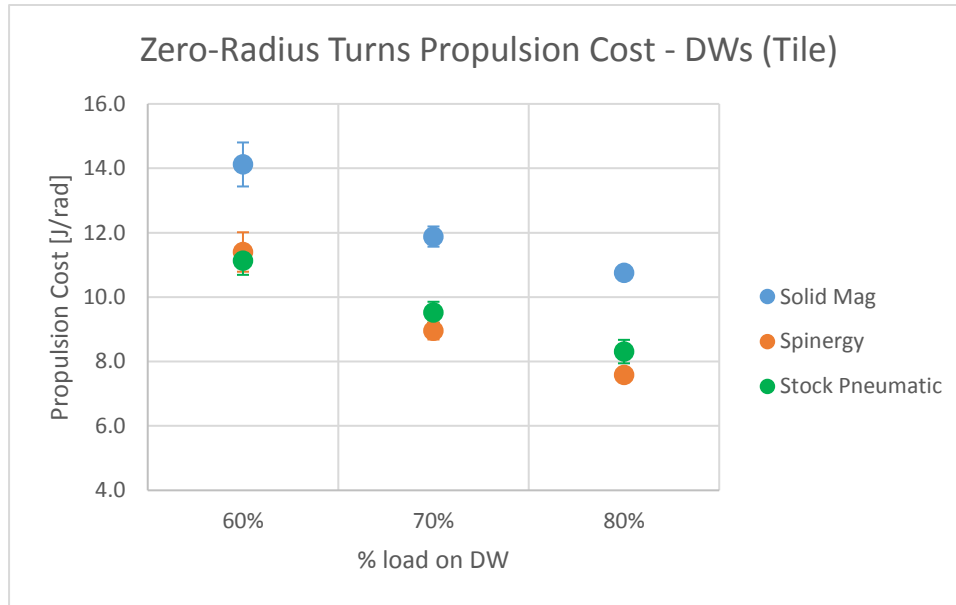


Figure 93. Propulsion Cost of Drive Wheel Configurations for Zero Radius Turns Maneuvers on Tile

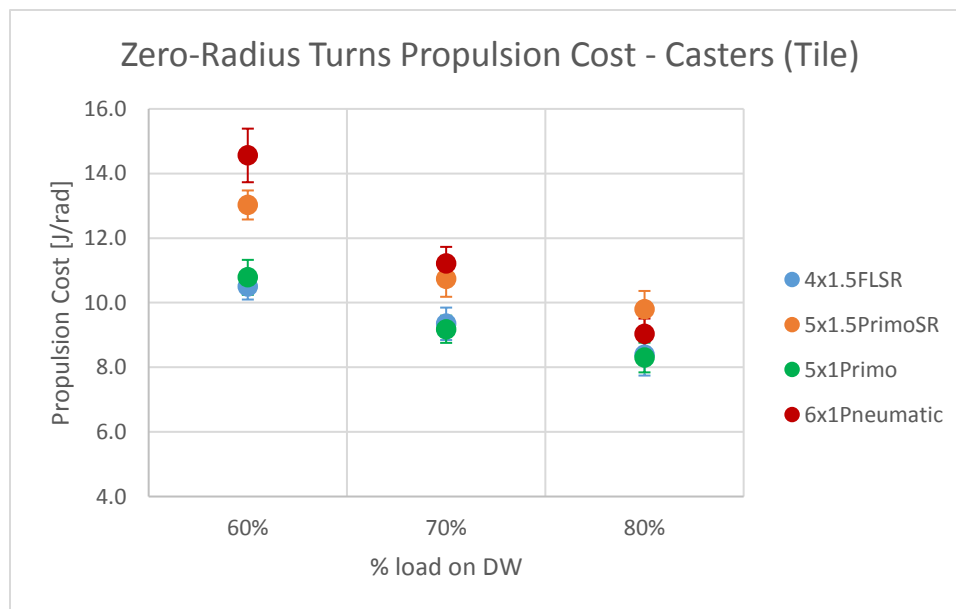


Figure 92. Propulsion Cost of Caster Configurations for Zero Radius Turns Maneuvers on Tile

Amongst casters, the 4x1.5" FLSR was similar to the 5x1" Primo in propulsion cost across weight distributions. The 5x1.5" Primo SR and 6x1" Pneumatic configurations, in contrast, were significantly greater in propulsion cost, with percent differences ranging

from 18% - 20.8% (effect sizes 1.08 – 1.68) and 8.8% to 35% (effect sizes 0.58 – 2.01), respectively. As seen from the ranges, the propulsion cost of the 6x1” Pneumatic configurations did not differ much from the 5x1” Primo configurations during larger loads on the drive wheels, but presented a significant difference as more load was shifted from drive wheels to casters. The 5x1.5” Primo SR configurations maintained a more constant difference from the base caster configurations across weight distributions. Based on the larger propulsion cost percent differences between %WDs compared to drive wheels, it may be hypothesized that the caster rolling resistance and swivel scrub torque play a larger part in zero-radius turns on tile than drive wheels.

Table 40. Zero Radius Turns (Carpet) Propulsion Cost % Difference and Effect Size

| Drive Wheels | % Change | | | Cohen's d | | |
|------------------------|----------|--------|--------|--------------|--------------|--------------|
| | 60% | 70% | 80% | 60% | 70% | 80% |
| Solid Mag | 1.9% | 4.6% | 8.8% | 0.33 | 1.39 | 2.04 |
| Spinergy | -9.4% | -11.1% | -13.7% | -1.85 | -3.52 | -4.25 |
| Stock Pneumatic | 0.0% | 0.0% | 0.0% | 0.00 | 0.00 | 0.00 |

| %WD | % Change | | | Cohen's d | | |
|------------|-----------|----------|-----------------|-------------|-------------|-----------------|
| | Solid Mag | Spinergy | Stock Pneumatic | Solid Mag | Spinergy | Stock Pneumatic |
| 60% | 19.7% | 34.0% | 27.8% | 3.18 | 5.55 | 5.55 |
| 70% | 8.4% | 16.0% | 12.7% | 1.98 | 4.01 | 3.83 |
| 80% | 0.0% | 0.0% | 0.0% | 0.00 | 0.00 | 0.00 |

| Casters | % Change | | | Cohen's d | | |
|-------------------|----------|-------|-------|-------------|-------|-------|
| | 60% | 70% | 80% | 60% | 70% | 80% |
| 4x1.5" FLSR | -3.3% | -0.2% | 0.8% | -0.55 | -0.02 | 0.08 |
| 5x1.5" Primo SR | 7.3% | 6.0% | 7.6% | 1.02 | 0.86 | 0.73 |
| 5x1" Primo | 0.0% | 0.0% | 0.0% | 0.00 | 0.00 | 0.00 |
| 6x1" Pneumatic | 9.8% | 5.0% | -1.3% | 1.63 | 0.64 | -0.14 |

| %WD | % Change | | | | Cohen's d | | | |
|------------|-------------|-----------------|------------|----------------|-------------|-----------------|-------------|----------------|
| | 4x1.5" FLSR | 5x1.5" Primo SR | 5x1" Primo | 6x1" Pneumatic | 4x1.5" FLSR | 5x1.5" Primo SR | 5x1" Primo | 6x1" Pneumatic |
| 60% | 19.6% | 24.3% | 24.6% | 38.5% | 2.41 | 2.57 | 2.68 | 5.31 |
| 70% | 10.0% | 9.5% | 11.1% | 18.1% | 1.09 | 1.08 | 1.25 | 2.04 |
| 80% | 0.0% | 0.0% | 0.0% | 0.0% | 0.00 | 0.00 | 0.00 | 0.00 |

For zero-radius turns maneuvers on carpet, the order of component configuration propulsion costs were preserved relative to the results found on tile. Component sensitivity to load was also preserved (effect size magnitudes almost all greater than 1 across all components), with caster configurations' propulsion cost percent differences ranging 19.6% - 38.5% between 80%WD and 60%WD, and drive wheel configurations' propulsion cost percent differences ranging 19.7% - 34% between 80%WD and 60%WD. However the magnitude of the propulsion cost differences between most components was reduced. The Solid Mag configurations were only 1.9% - 8.8% (effect sizes 0.33 – 2.04) greater in propulsion cost, compared to 26.8% - 29.4% greater on tile. However, the Spinergy configurations did undergo a relative increased reduction in propulsion cost, 9.4% - 13.7% less than Stock Pneumatic configurations on carpet.

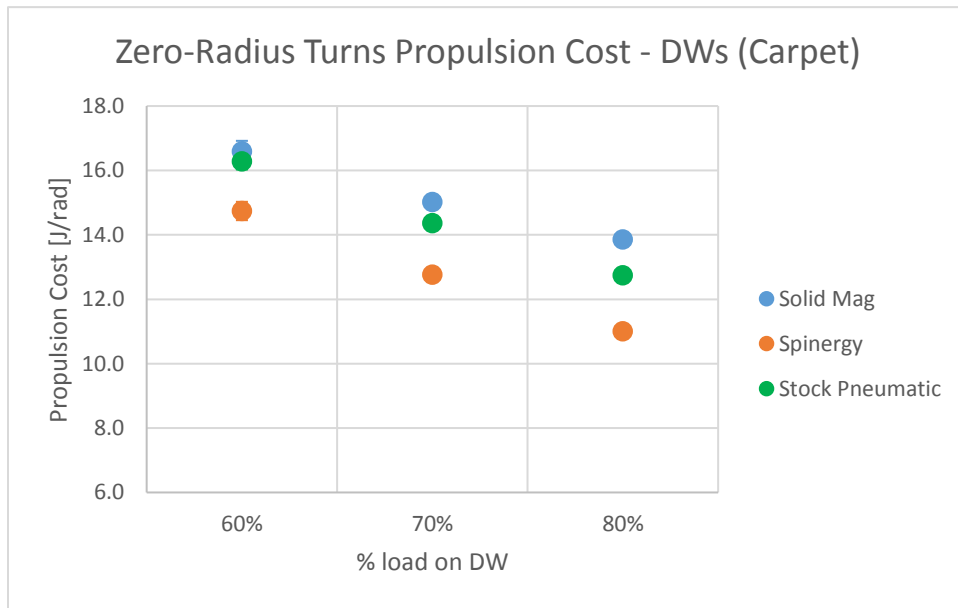


Figure 94. Propulsion Cost of Caster Configurations for Zero Radius Turns Maneuvers on Carpet

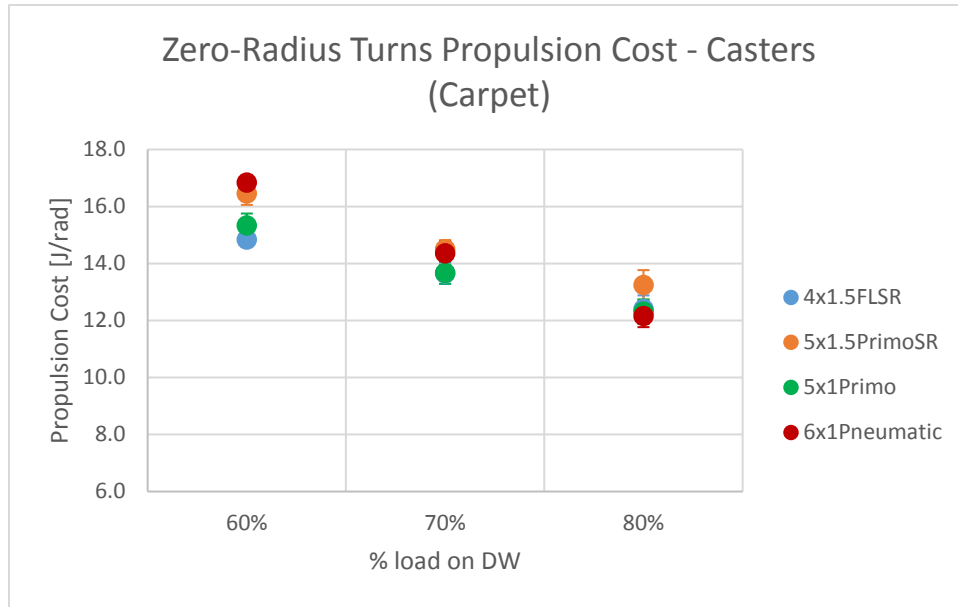


Figure 95. Propulsion Cost of Drive Wheel Configurations for Zero Radius Turns Maneuvers on Carpet

Propulsion cost differences amongst casters were greatest at the 60% WD, with the 4x1.5 FLSR 3.3% (effect size -0.55) less than the 5x1” Primo, and the 5x1.5” Primo SR and 6x1” Pneumatic 7.3% and 9.8% (effect sizes 1.02 and 1.63) greater in propulsion cost, respectively. On carpet, the relative propulsion cost differences between drive wheel configurations (average of 8.2%) was greater than that of caster configurations (average of 4.6%), implying that drive wheel impact for zero-radius turns on carpet is greater.

Visualized Component Performance Across Maneuvers and Surfaces

To illustrate the performance of each component and its tradeoffs between straight and turning maneuvers, the straight and turning propulsion costs for each component - separated by drive wheels and casters - were plotted against each other for tile and carpet surfaces (**Figure 96 – Figure 99**). Turning propulsion cost of fixed-wheel turning was used for the drive wheel plots, while zero-radius turns was used for caster plots. The rationale for these plot combinations stems from pairing the caster and drive wheels with the turning canonical maneuver where they each theoretically present the largest contribution to system turning resistance.

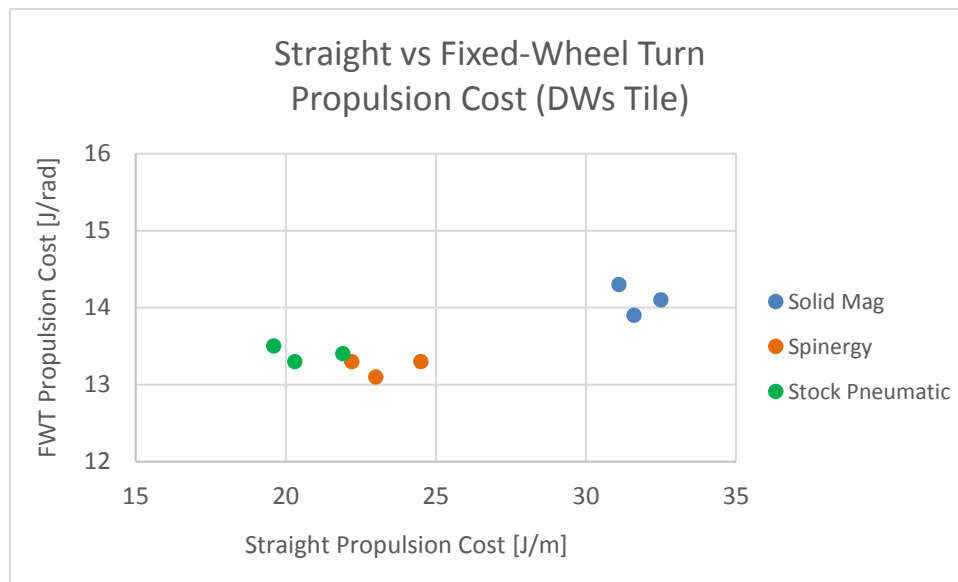


Figure 96. Straight versus Turning Propulsion Cost for DW Configurations on Tile

Figure 96 and **Figure 97** plots of drive wheel data are on the same scale, as are **Figure 98** and **Figure 99** plots of caster data. This allows for the change in differences between components when moving between a tile and carpeted surface to be perceived.

Configurations with the Stock Pneumatic drive wheel outperformed the other drive wheels on tile, with only slightly more turning propulsion cost than the Spinerger across the different %WDs. On carpet, the Spinerger exhibited a similar straight propulsion cost to that of the Stock Pneumatic and a substantially reduced turning propulsion cost, making it the best performer amongst the pneumatic drive wheels on this surface. The Solid Mag performed poorly for both straight and turning propulsion cost on tile, but presented the lowest in turning propulsion cost on carpet.

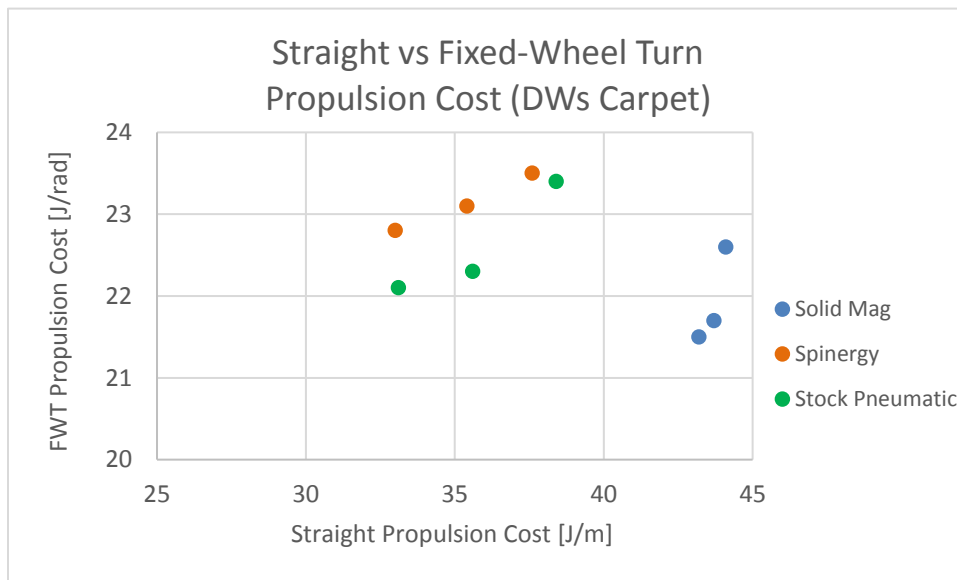


Figure 97. Straight versus Turning Propulsion Cost for DW Configurations on Carpet

Based on these results, the advantage a Stock Pneumatic has over the Solid Mag is significant in straight maneuvers on tile and carpet, as well as turning maneuvers on tile. Both of these drive wheels often come as standard accessories to MWCs, so selecting the Stock Pneumatic would offer the best performance at the same financial expense. The Solid Mag, however, may be a more suitable choice for instances of indoor wheelchair use on rough surfaces given its reduced turning propulsion cost in these settings. The Spinerger

drive wheels also largely outperform the Solid Mag on both surfaces, corroborating human study findings comparing high pressure pneumatics and solid drive wheels (de Groot, Vegter, & van der Woude, 2013). The Spinerge drive wheels, however, typically price in at \$600+ for a set. Its difference in performance from the Stock Pneumatic is only better in turning propulsion cost on carpet, and in fact worse in straight propulsion cost on hard (tile) surfaces. This lack of difference in performance was also found in human subject studies comparing stock pneumatic and Spinerge drive wheels (Hughes, Sawatzky, & Hol, 2005; Mason, Lemstra, van der Woude, Vegter, & Goosey-Tolfrey, 2015). Thus, the performance “difference” may not justify the cost of these particular drive wheels.

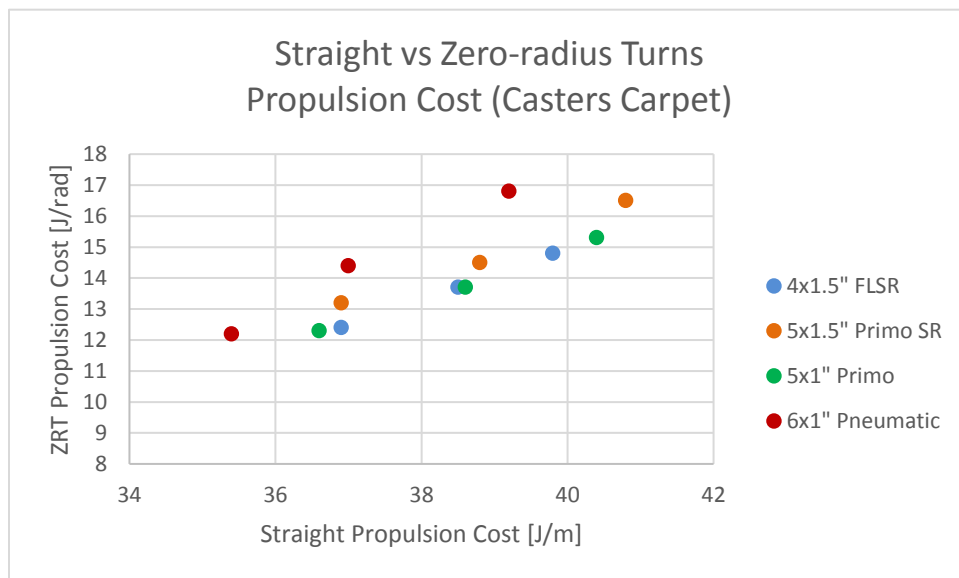


Figure 98. Straight versus Turning Propulsion Cost for Caster Configurations on Tile

Use of different casters, as a whole, did not demonstrate as large a separation in propulsion costs as the drive wheels. Straight propulsion cost on both carpet and tile appeared to be more impacted by %WD than differences amongst casters. A notable difference, however, was the 6x1” Pneumatic’s change from having the greatest straight

propulsion cost on tile to having the least on carpet. The 6x1” Pneumatic is also greatest in turning propulsion cost on tile, but is relatively close to the other caster configurations in turning propulsion cost on carpet. This implies that the 6x1” Pneumatic may be an advantageous caster to use on carpet surfaces. Another caster that stands out is the 4x1.5” FLSR, which is least in both straight turning propulsion cost on tile. However, its straight propulsion torque on carpet is the greatest at 80%WD. Thus, the 4x1.5” FLSR may be the more optimal caster to use on a hard (tile) surface.

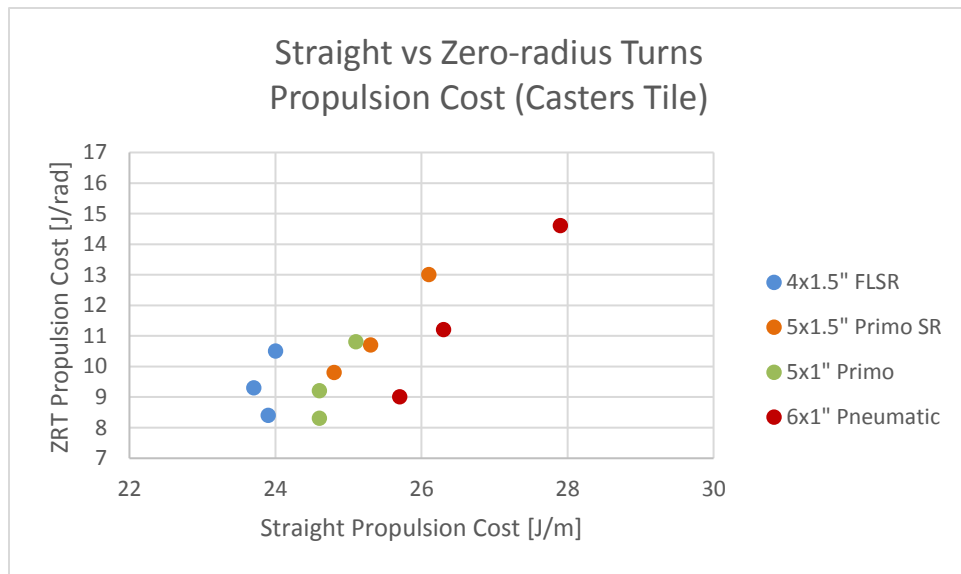


Figure 99. Straight versus Turning Propulsion Cost for Caster Configurations on Carpet

CHAPTER 5. EMPIRICAL MODELING

This chapter highlights the use of competent-level measurements of resistive loss (Chapter 2) to develop predictive models of system-level MWC propulsion cost, as measured by AMPS (Chapter 4). Three linear regression models were developed, one for each AMPS canonical maneuver. Linking the component-level test results to system-level MWC propulsion cost enables third parties to predict MWC performance based on comparatively simple component-testing methodologies.

5.1 Model Definitions

The outcome variable for each model was propulsion cost, as defined for each corresponding maneuver. The predictor variables included both inertial and resistive parameters, either measured on a system-level or calculated from component-level measurements. Ultimately, system weight-distribution, system yaw inertia, and system resistance were selected as the potential predictors in each model, with the system yaw inertia omitted from the straight maneuver model due to the absence of turning. The selection basis for these model predictors stemmed from the underlying mechanics of each maneuver, as well as the predicate findings in the component-level and system-level testing, specifically those pertaining to the AMPS study of caster and drive wheels.

Within inertial predictors, system yaw inertia was fed into the models for the fixed-wheel turn and zero-radius turns. Mass was omitted due to its invariance across system-level tests (within the AMPS caster and drive wheels study). Component inertial

measurement were also omitted due to their previously assessed insignificant contribution to system propulsion work across all canonical maneuvers.

Within resistive predictors, weight-distribution was selected for its load-based impact on resistance and system resistance was defined as a weighted combination of caster and drive wheel rolling resistance and scrub torque. All three models' system resistances were defined differently, framed off of the resistive loss models defined in Chapter 3 for each canonical maneuver. By using system resistance instead of the individual measured component resistances, we offer a theoretical model-motivated predictor of each maneuver's resistive loss, as well as verify the accuracy of the resistive loss models.

In defining the system resistance for each model (maneuver), the equations followed the forces and torques in of the resistive loss models of Chapter 4, except for two distinctions. First was how the resistance of combined rolling and turning were defined. In the resistive loss models, the equations of motion for fixed-wheel turning and zero-radius turns both incorporated a two-force term to describe each instance of rolling and turning of drive wheels. The first term was linear rolling resistance, and the second term a scrub torque with rolling. However, component testing only measured pure scrub of the drive wheels without rolling. Therefore, two definitions of combined drive wheel rolling and turning were devised: 1) only linear rolling resistance, and 2) a combination of linear rolling resistance and pure scrub torque. It is understood that the true resistance of combined drive wheel rolling and turning falls somewhere in between these two definitions, as this resistance should be greater than that of linear rolling resistance, but also much less pronounced than that of pure scrub torque. The implementation of two

different definitions resulted in two corresponding types of system resistance definitions for both fixed-wheel turning and zero-radius turns: “type 1” and “type 2”.

The second distinction between the Chapter 4 equations of motion are in the zero-radius turns model’s definitions of system resistance. Previously, the caster scrub torque contribution to system turning resistance was a separate undefined function, as the instances of scrub torque from caster swivel were transient, not continuous like the other resistive terms in the definition. However, while transient, the swiveling of casters had been observed in AMPS trials to slow the system momentarily as a whole, indicating the resistive scrub torque is brief but large in magnitude. This notion, combined with starting with simplicity, motivated us to simply add the two caster scrub torques directly to the system resistance definitions for the zero-radius turns model.

The system resistance definition(s) for each model are listed below. To clarify terminology, “DW” refers to drive wheel, “RR” refers to rolling resistance force, and “scrub” refers to scrub torque.

Straight [N]

1) System Resistance = $2*(DW\ RR) + 2*(Caster\ RR)$

Fixed Wheel Turn [Nm]

1) System Resistance = (DW torque) + (DW RR)*(DW – DW distance) + (Caster RR)*(left caster – fixed DW distance) + (Caster RR)*(right caster – fixed DW distance)

2) System Resistance = $2*(DW\ torque) + (DW\ RR)*(DW - DW\ distance) + (Caster\ RR)*(left\ caster - fixed\ DW\ distance) + (Caster\ RR)*(right\ caster - fixed\ DW\ distance)$

Zero Radius Turns [Nm]

- 1) System Resistance = $2 * (\text{Caster torque}) + 2 * (\text{DW RR}) * (\text{DW} - \text{DW distance}) / 2 + (\text{Caster RR}) * (\text{left caster} - \text{axle center distance}) + (\text{Caster RR}) * (\text{right caster} - \text{axle center distance})$
- 2) System Resistance = $2 * (\text{DW torque}) + 2 * (\text{Caster torque}) + 2 * (\text{DW RR}) * (\text{DW} - \text{DW distance}) / 2 + (\text{Caster RR}) * (\text{left caster} - \text{axle center distance}) + (\text{Caster RR}) * (\text{right caster} - \text{axle center distance})$

5.2 Modeling Methods

Outcome variable values of propulsion cost were taken from the AMPS systems-level study of different casters and drive wheels. Within this study, four casters (4x1.5” FLSR, 5x1.5” Primo SR, 5x1” Primo, 6x1” Pneumatic), three drive wheels (Solid Mag, Spinergy, Stock Pneumatic), and three weight-distribution configurations (60%WD, 70%WD, 80%WD) were combined to measure propulsion cost across the three canonical maneuvers on tile and carpet. One representative average of 10 repeated trials (5 per direction) was used for each configuration combination, resulting in 72 propulsion cost values per maneuver, 36 on tile and 36 on carpet. These 72 values were used as the outcome values for their corresponding models. The zero-radius turns maneuver’s velocity profile differed between tile and carpet surfaces. However, as the propulsion and braking phases of the maneuver were both used to calculate propulsion cost, there was no impact on ΔKE work due to different velocities since starting and ending velocities were always zero. Furthermore, maneuvers on carpet and tile were programmed to travel the same yaw angles, and the use of propulsion cost over propulsion work normalizes any velocity profile differences. Thus, it was justified to also combine the zero-radius turns maneuver’s carpet and tile propulsion costs in the model.

Predictor variable values were assigned based on the corresponding components and weight-distribution a propulsion cost represented. System yaw inertia was taken from previous iMachine data and the caster and drive wheel rolling resistances and scrub torques were taken from the results of the component-level testing in Chapter 2. The resistive loss terms were combined in accordance to each model’s definition to yield the system resistance predictors.

Linear regression modeling was conducted via SPSS (IBM) following the forward method, where predictors were entered into the model based on an $F \leq 0.05$ criterion. Multicollinearity amongst predictors was assessed using variable inflation factors (VIF). Model R^2 values were recorded, as were unstandardized predictor coefficients and standardized beta coefficients.

5.3 Model Results

Table 41. Linear Regression Modeling Results

| Model | Adjusted R^2 | Std. Error of the Estimate | Predictors Entered | Unstd. Coeff. (B) | Std. Coeff. (Beta) | Significance (p-value) |
|-----------------------------------|----------------------------------|-----------------------------------|---------------------------|--------------------------|---------------------------|-------------------------------|
| <i>Straight</i> | 0.973 | 1.32 | System Resistance | 1.234 | 0.987 | 0 |
| | | | Constant | 14.602 | | 0 |
| <i>Fixed Wheel Turn 1</i> | 0.891 | 1.52 | System Resistance 1 | 1.457 | 0.945 | 0 |
| | | | Constant | 1.464 | | 0.043 |
| Fixed Wheel Turn 2 | 0.752 | 2.29 | System Resistance 2 | 1.056 | 0.884 | 0 |
| | | | System Yaw Inertia | 0.9 | 0.213 | 0.001 |
| | | | Constant | -6.986 | | 0.007 |
| <i>Zero Radius Turns 1</i> | 0.876 | 0.98 | System Resistance 1 | 0.875 | 0.937 | 0 |
| | | | Constant | 5.36 | | 0 |
| Zero Radius Turns 2 | 0.503 | 1.97 | System Resistance 2 | 0.375 | 0.513 | 0 |
| | | | System Yaw Inertia | 1.245 | 0.486 | 0 |
| | | | Constant | -4.554 | | 0.026 |

Overall, at least one model per maneuver type registered a strong fit to the data, all with adjusted $R^2 > 0.87$. These models all had their maneuver's System Resistance as their sole predictors, indicating that the resistive loss models coupled with component testing are good predictors of system propulsion cost. Weight distribution was not entered into any of the regression models, likely because the load configuration differences were already captured and represented in the different system resistance predictors. System yaw inertia and System Resistance (type 2) was entered into the second models for both fixed-wheel turn and zero-radius turns, with no signs of collinearity between the entered predictors ($VIF < 1.01$). These multi-variable regression models expressed a poorer predictive power, with adjusted $R^2 \leq 0.752$. Furthermore, the SEE for the type 2 models (2.29, 1.97) were substantially greater than that of type 1 models (1.52, 0.98). The selection of the type 1 system resistances as better fitting models indicate that the type 2 models are indeed over-estimating the resistances associated with combined rolling and turning of drive wheels. Based on these results, we can say that the combined rolling and turning resistance is better represented by linear rolling resistance force (type 1) than by a direct summation of linear rolling resistance force and non-rolling scrub torque (type 2).

While the adjusted R^2 value informs the closeness of the data to our model projection, the distribution of data along the regression line should be assessed visually. In doing so, we observed that while the fixed-wheel turn model demonstrated a higher adjusted R^2 of 0.891 compared to the zero-radius turns model's adjusted R^2 of 0.876, the distribution of the fixed-wheel turn model's data was very clustered (**Figure 102**). In contrast, the straight model and zero-radius turns models both displayed a very high

variance in the modeled data, with even distributions along the regression model lines as seen in **Figure 100** and **Figure 101**. Data is colored categorically by surface type.

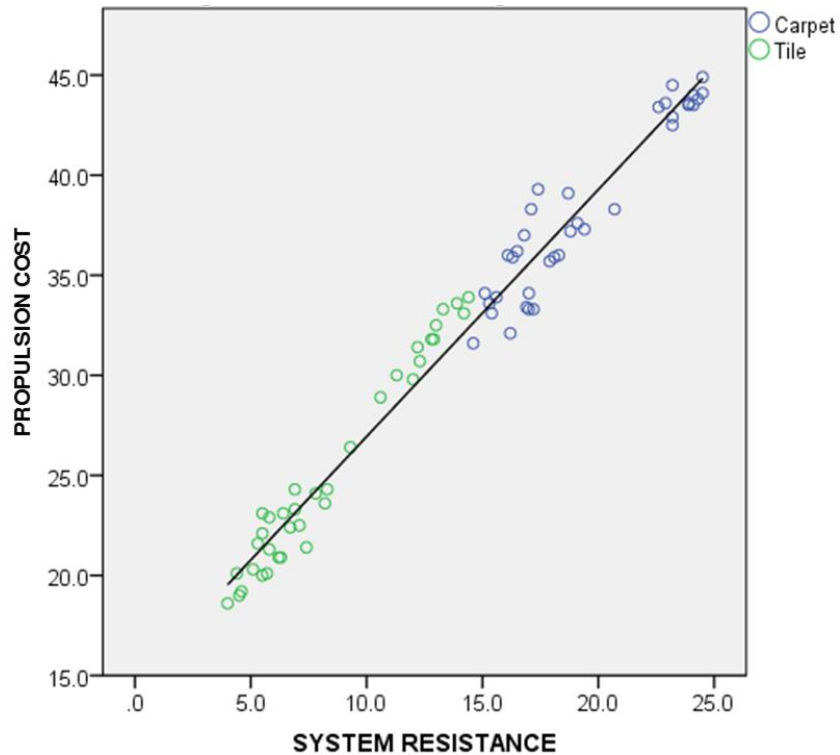


Figure 100. Straight Maneuver Linear Regression Model

Comparing **Figure 100** and **Figure 101**, the straight model displays a tighter fit to the data, reflecting its higher adjusted R^2 of 0.973 compared to the zero-radius turns model's adjusted R^2 of 0.876. In the straight model, the regions for tile and carpet are quite distinct, with minimal overlap. In the zero-radius turns model, the regions of tile and carpet demonstrate more overlap, indicating that this maneuver is more sensitive to surface conditions than the straight maneuver.

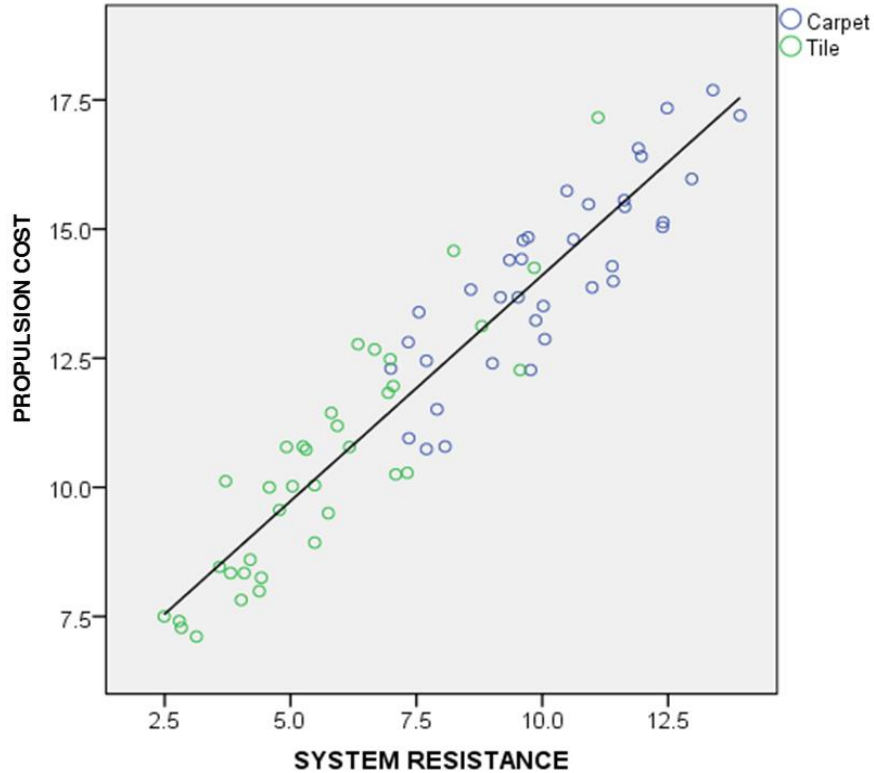


Figure 101. Zero Radius Turns Maneuver Linear Regression Model

In **Figure 102**, we can observe the aforementioned clustering of data for the fixed-wheel model. Tile data is grouped entirely at the lower range of the model while carpet data is grouped entirely at the higher range of the model. Within each surface type, the data does not appear to take on a strong linear relationship. Furthermore, this “model” presents the largest SEE at 1.52, relative to

To assess why this clustering is present in the fixed-wheel model, we compared the propulsion cost variation for all three maneuvers. On tile, both straight and zero-radius turns maneuvers’ propulsion costs had CV (coefficient of variation) $> 20\%$, while fixed wheel turn maneuvers’ propulsion cost had CV = 5.8%. On carpet, both straight and zero-radius turns maneuvers’ propulsion costs had CV (coefficient of variation) $> 11\%$, while

fixed wheel turn maneuvers' propulsion cost had $CV = 4.4\%$. Based on these statistics, it can be said that the fixed-wheel turn model's outcome variable values are too low variance. This indicates one of two things: 1) the fixed-wheel turn maneuver requires more propulsion cost variance, such as by testing an intermediate surface between tile and carpet, or 2) the fixed-wheel turn canonical maneuver needs to be adjusted such that it stresses the system more greatly, either by adjusting maneuver accelerations or the proportion between acceleration and steady-state phase.

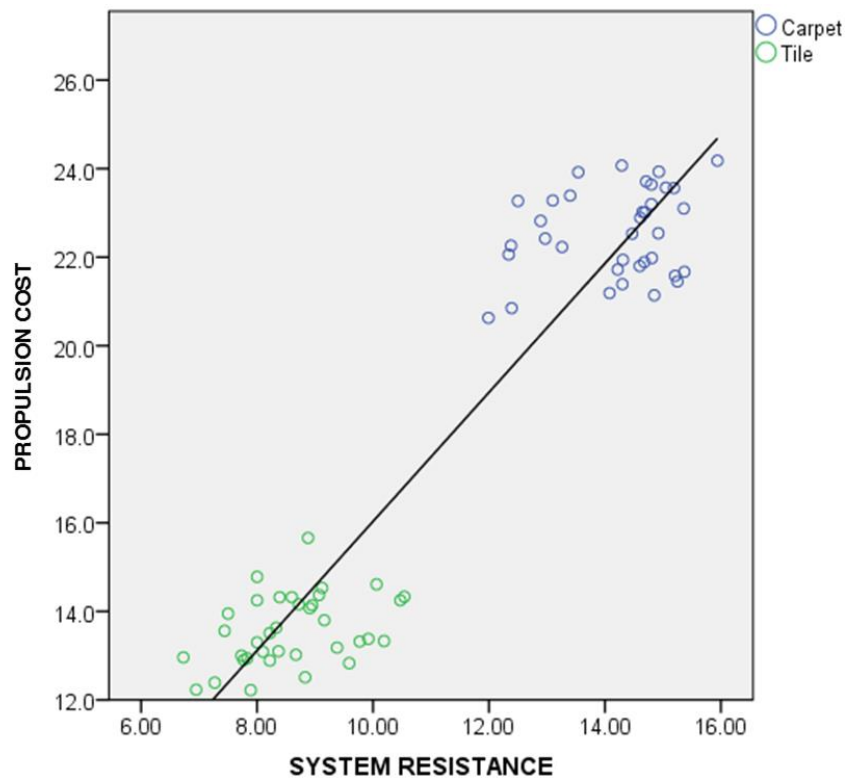


Figure 102. Fixed Wheel Turn Maneuver Linear Regression Model

In **Figure 103**, we color the fixed-wheel turn data by drive wheel type. In both tile and carpet, each drive wheel's data forms a distinct cluster. On tile, the model over-predicts Solid Mag propulsion cost and under-predicts the Stock Pneumatic propulsion cost. On carpet, the model under-predicts Solid Mag propulsion cost and over-predicts the Stock Pneumatic propulsion cost. From the plot, the Spinergy data lines up well with the existing model slope, while the Stock Pneumatic data appears to fit better to a model with greater regression slope and the Solid Mag data fits better to a model with a smaller regression slope. Since drive wheel scrub torque is only present in the system resistance of the fixed-wheel turn model, this particular component test may be impacting the system resistance predictor to cause these separations.

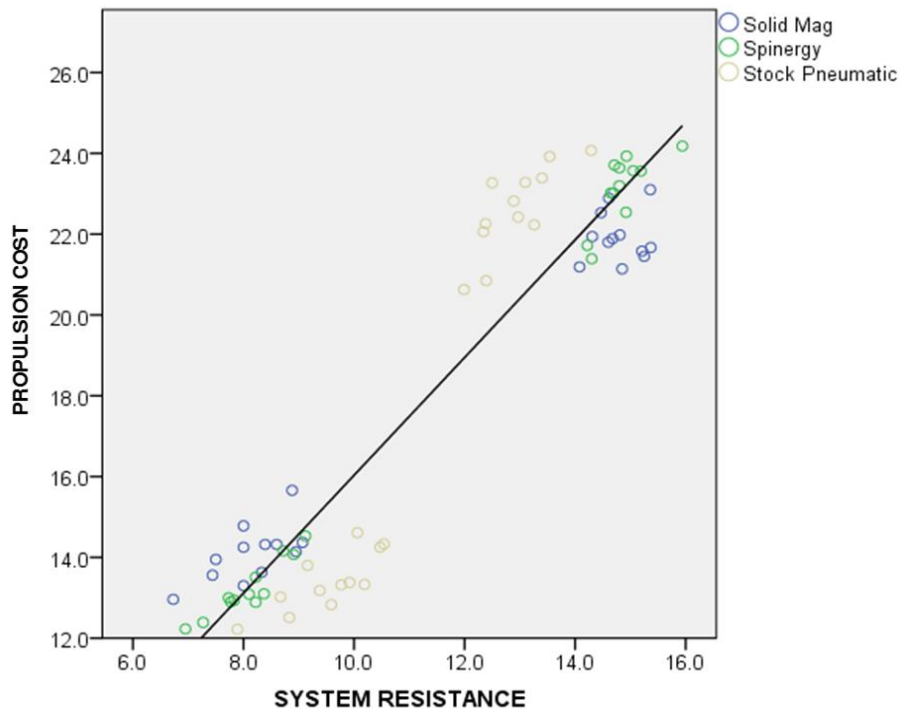


Figure 103. Fixed Wheel Turn Maneuver Linear Regression Model (Colored by Drive Wheels)

In **Figure 104**, we plot the system resistance with the drive wheel scrub torque removed from the system resistance predictor. The relative system resistance of the drive wheels seem to change, but the horizontal spread of the data doesn't appear to improve, suggesting the drive wheel scrub torque measurements may not be responsible for the system resistance variance. This reinforces that the component resistive differences are real, and that it is likely the lack of the current fixed-wheel turn's sensitivity to distinguish propulsion cost across components that is causing the data clustering.

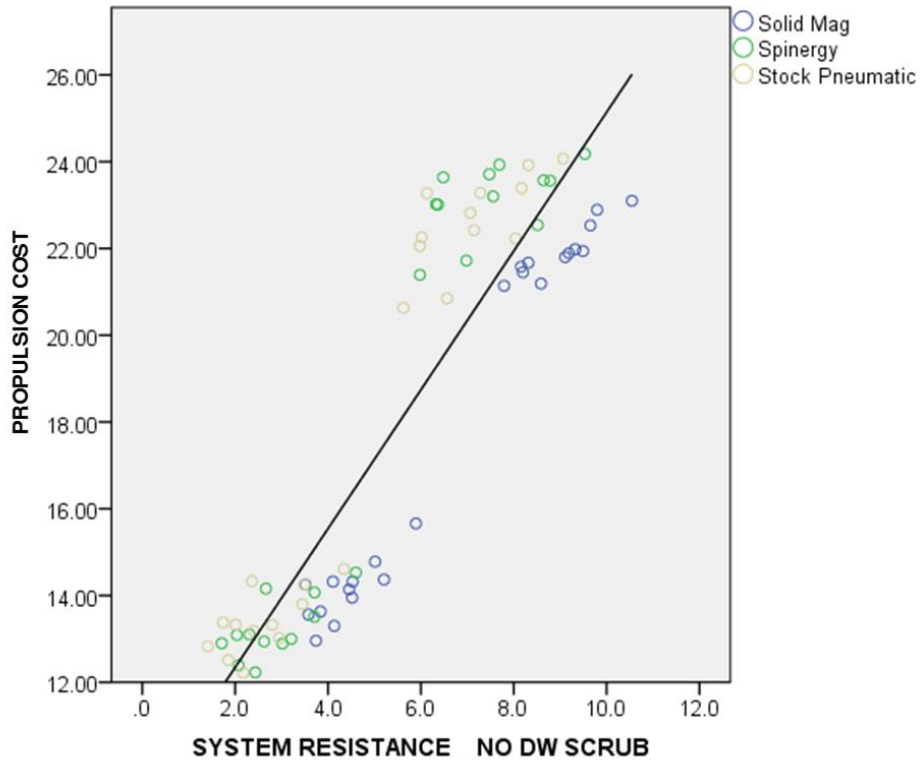


Figure 104. Fixed Wheel Turn Maneuver Linear Regression Model (System Resistance Minus Drive Wheel Scrub)

In applying each model towards predicting MWC performance, the standard error of the estimate (SEE) listed in **Table 41** quantifies the uncertainty of the predicted propulsion cost. To put this in perspective, we can compare these uncertainties to measured propulsion cost differences. The straight model SEE = 1.32 J/m, while straight propulsion cost differences between the more similar Spinergy and Stock Pneumatic are at 2.6 J/m, which at the worst case uncertainty of 2.64 J/m (opposite but equal max SEE) would make these two wheels indistinguishable. Applying a more conservative combined uncertainty of 1.32 J/m, however, the model would only be unable to distinguish the propulsion costs of the 5 x 1" Primo from the 4 x 1.5" FLSR and 5 x 1.5" SR configurations. Using this same rationale, the drive wheel propulsion costs for fixed-wheel turning on tile would be indistinguishable if predicted by the model (SEE = 1.52), and only the 4 x 1.5" FLSR and 6 x 1" Pneumatic would be predicted to be different in propulsion cost. In the zero-radius turns model (SEE = 0.98), differences between every component for zero-radius turning on tile could be predicted, except for very similar components like the Spinergy and Stock Pneumatic, as well as the 4 x 1.5" FLSR and 5 x 1" Primo caster, each differing only by a propulsion cost of 0.3 J/rad.

CHAPTER 6. CONCLUSIONS AND FUTURE WORK

6.1 Conclusions

Within the breadth of the work conducted for this dissertation, the research objective of developing capabilities to characterize and predict manual wheelchair performance were met.

The research aim of measuring MWC component inertial and resistive properties was accomplished through designed methodologies that characterized the rotational inertia, rolling resistance, and scrub torque of caster and drive wheels. Three new measurement devices were fabricated to this end: the coast-down cart, the caster scrub test rig, and the drive wheel scrub test rig. A diverse set of 4 drive wheels and 8 casters were evaluated for tile and carpet surfaces with these instruments. These tests yielded several interesting observations, including:

- Differences in component inertial properties have a negligible impact relative to combined system mass of the MWC and user ($< 1\%$ change in system kinetic for a 100 kg user)
- Drive wheel differences in rolling resistance and scrub torque are much more pronounced than casters, implying the greater impact in their proper selection.
- The solid mag experiences rolling resistance several times greater than the three pneumatic drive wheels, indicating it is ill-suited for long-distance use.

- The stock pneumatic out-performs the high-priced Spinergy except for in scrub torque on tile, suggesting the limited performance benefits of the Spinergy may not justify its financial cost.
- Soft and pneumatic casters have the greatest rolling resistance on tile, but the lowest on carpet.
- The 4 x 1.5” Frog Leg Soft Roll and 5 x 1” Primo caster demonstrated the best balance of minimal rolling resistance and scrub torque on tile and carpet surfaces, respectively.
- The three pneumatic drive wheels are the least sensitive to load compared all other components (casters included) in terms of rolling resistance, but are also the most load-sensitive in terms of scrub torque.

The research aim of characterizing system-level MWC performance was accomplished by methodologies that quantified the propulsion torque and propulsion cost of various MWC configurations on tile and carpet. To this end, a wheelchair-propelling robot, AMPS, was developed. Three canonical maneuvers for AMPS were defined, based on their external validity and balanced collective representation of different kinetic energies and resistive losses. These maneuvers were applied towards investigating the impact of mass and weight-distribution on propulsion torque, as well as the impact of 4 casters and 3 drive wheels on propulsion cost. The two studies yielded the following important observations:

- Mass has a more dominant effect on straight propulsion torque during acceleration, while weight-distribution exerts a greater influence than mass during steady-state velocities.

- Weight distribution has a greater impact on turning propulsion torque compared to mass while on tile, but these influences become much smaller when turning on carpet.
- The Spinerger configurations out-performed the stock pneumatic configurations on carpet, primarily in turning maneuvers, but under-performed on tile, primarily in the straight maneuver. Does this justify the financial investment it requires?
- Consistent with the component test results, the solid mag was by far the greatest in rolling resistance. In contrast with the component test results, it performed better on carpet than tile for turning maneuvers. This indicates a more advantageous use of this ubiquitous drive wheel in indoor spaces requiring ample turning and on high friction surfaces like carpet.
- Straight maneuvers on tile are more insensitive to caster type than on carpet.
- Best performing casters were the 4 x 1.5" Frog Leg Soft Roll and 5 x 1" Primo, only greater in propulsion cost for straight maneuvers on tile.
- Consistent with component test results, the Primo 6 x 1" caster had the greatest straight propulsion cost on tile and least on carpet.

The research aim of predicting system-level MWC performance was accomplished by applying linear regression modeling. System-level propulsion costs from the second aim were used as outcome variables, and component measures of resistive loss from the first aim were used to calculate system resistance predictor variables. The system resistance definitions were based on the resistive loss models developed as part of the second aim. System yaw inertia and weight-distribution were also entered as predictor variables. The regression results were as follow:

- System yaw inertia and weight-distribution were not entered into the accepted (strongest) regression models, partially due to collinearity as both system yaw inertia and system resistance are indirect functions of weight-distribution.
- Accepted fixed-wheel turn and zero-radius turns models had system resistance values (type 1) without scrub torque from combined drive wheel rolling and turning, indicating linear rolling resistance is a better and reasonable approximation of combined rolling and turning within our canonical maneuvers.
- All accepted models had $R^2 > 0.87$. However, based on visual assessment and comparison of model SEE to measured component differences, it was found the straight and zero-radius turns models were able to make much more distinguishing propulsion cost predictions than the fixed-wheel turn model.

As a whole, the work of this dissertation has developed a scientifically-motivated MWC performance metric and measurement method, the results of which will empower wheelchair users and clinicians to make more informed choices on selecting MWC components and setting MWC configurations. Furthermore, the modeling efforts have demonstrated the capacity for using simple MWC component tests to predict system-level performance, creating a series of tools for manufacturers to assess and optimize their MWC designs.

6.2 Future Work

Further research can be done using the tools and findings of this dissertation work. The first next steps would involve improving the existing methodologies and shoring up certain weaknesses. These include:

- Assessing the fixed-wheel turn maneuver at different surface types to add variance to the model.
- Modifying the specific kinematics of the fixed-wheel turn to increase sensitivity between different components, if those differences exist.
- Developing component-level test methods to characterize the resistive losses of combined rolling and turning of wheels.
- Adding variance to all models by test several different system masses. This is also very likely to introduce inertial predictors in the models, which current are only represented by system resistance predictors.
- Incorporating cyclic propulsion to the AMPS system to better reflect the kinetics and kinematics of human propulsion of MWCs.

Beyond these next steps that can be framed as short-term goals, there exists an opportunity for collaborative work with more far-reaching impacts. These include:

- Engaging more representatives of the wheelchair industry to promote assimilation of AMPS propulsion cost as a standard, representative performance metric for grading manual wheelchairs.
- Packaging the models and component-test methods for easy adaptation by wheelchair industry manufacturers to optimize their designs in-house.
- Using AMPS to inform the variables for human-subject wheelchair studies, as the system's higher sensitivity can better detect mechanical performance differences amongst MWCs and configurations. Being cognizant of the relative mechanical performance differences will also help isolate the impact of human-wheelchair

interaction biomechanics, as the propulsion effort measured by the human-subject studies are a function of both factors.

- Applying system-level test methods to validate the existing wheelchair models in literature, as most are not empirically validated or are based purely on component-level test methods that can overlook the impact of system-level propulsion properties, such as shift in weight-distribution.

REFERENCES

- Bascou, J, Pillet, H, Kollia, K, Sauret, C, Thoreux, P, & Lavaste, F. (2014). Turning resistance of a manual wheelchair: a theoretical study. *Computer methods in biomechanics and biomedical engineering*, 17(sup1), 94-95.
- Bascou, J, Sauret, C, Villa, C, Lavaste, F, & Pillet, H. (2015). Measurement of wheelchair adjustment effects on turning deceleration. *Computer methods in biomechanics and biomedical engineering*, 18(sup1), 1882-1883.
- Bohannon, R. W. (2007). Number of pedometer-assessed steps taken per day by adults: a descriptive meta-analysis. *Phys Ther*, 87(12), 1642-1650. doi: 10.2522/ptj.20060037
- Boninger, M. L., Dicianno, B. E., Cooper, R. A., Towers, J. D., Koontz, A. M., & Souza, A. L. (2003). Shoulder magnetic resonance imaging abnormalities, wheelchair propulsion, and gender. *Arch Phys Med Rehabil*, 84(11), 1615-1620.
- Brubaker, CE. (1986). Wheelchair prescription: an analysis of factors that affect mobility and performance. *J Rehabil Res Dev*, 23(4), 19-26.
- Caspall, J. J., Seligsohn, E., Dao, P. V., & Sprigle, S. . (2013). Changes in inertia and effect on turning effort across different wheelchair configurations. *J Rehabil Res Dev*, 50(10). doi: <http://dx.doi.org/10.1682/JRRD.2012.12.0219>
- Caspall, Jayme J, Seligsohn, Erin, Dao, Phuc V, & Stephen Sprigle PhD, PT. (2013). Changes in inertia and effect on turning effort across different wheelchair configurations. *Journal of rehabilitation research and development*, 50(10), 1353.
- Chénier, Félix, Bigras, Pascal, & Aissaoui, Rachid. (2011). *A new dynamic model of the manual wheelchair for straight and curvilinear propulsion*. Paper presented at the Rehabilitation Robotics (ICORR), 2011 IEEE International Conference on.
- Cohen, J. (1988). *Statistical power analysis for the behavioral sciences* (2nd ed.). Hillsdale, NJ: Lawrence Earlbaum Associates.
- Cooper, Rory A. (1990). A systems approach to the modeling of racing wheelchair propulsion. *J Rehabil Res Dev*, 27(2), 151-162.
- Cowan, Rachel E, Boninger, Michael L, Sawatzky, Bonita J, Mazoyer, Brian D, & Cooper, Rory A. (2008). Preliminary outcomes of the SmartWheel Users' Group database: a proposed framework for clinicians to objectively evaluate manual wheelchair propulsion. *Archives of Physical Medicine and Rehabilitation*, 89(2), 260-268.
- D1349-14, ASTM. (2014). Standard Practice for Rubber - Standard Conditions for Testing: ASTM International.

- de Groot, Sonja, Vegter, Riemer JK, & van der Woude, Lucas HV. (2013). Effect of wheelchair mass, tire type and tire pressure on physical strain and wheelchair propulsion technique. *Medical engineering & physics*, 35(10), 1476-1482.
- Du Bois JL, Lieven NA, & Adhikari S. (2009). Error analysis in trifilar inertia measurements. . *Exper Mech.*, 49(4), 533-540.
- E1337-90, ASTM. (2012). Standard Test Method for Determining Longitudinal Peak Braking Coefficient of Paved Surfaces Using Standard Reference Test Tire: ASTM International.
- Eicholtz, M. R., Caspall, J. J., Dao, P. V., Sprigle, S., & Ferri, A. (2012). Test method for empirically determining inertial properties of manual wheelchairs. *J Rehabil Res Dev*, 49(1), 51-62.
- Ellis, John Ronaine. (1969). *Vehicle dynamics*: Random House Business.
- Foster J, Kortge J, & Wolanin M. (1977). "Hybrid III-A Biomechanically-Based Crash Test Dummy, *SAE Technical Paper 770938*.
- Frank, T. G., & Abel, E. W. (1989). Measurement of the turning, rolling and obstacle resistance of wheelchair castor wheels. *J Biomed Eng*, 11(6), 462-466.
- Franke, G, Suhr, W, & Rieß, F. (1990). An advanced model of bicycle dynamics. *European Journal of Physics*, 11(2), 116.
- Gordon, John, Kauzlarich, JJ, & Thacker, John G. (1989). Tests of two new polyurethane foam wheelchair tires. *J Rehabil Res Dev*, 26(1), 33-46.
- Hoffman, Martin D, Millet, Guillaume Y, Hoch, Anne Z, & Candau, Robin B. (2003). Assessment of wheelchair drag resistance using a coasting deceleration technique. *American journal of physical medicine & rehabilitation*, 82(11), 880-889.
- Hofstad, M., & Patterson, P. E. (1994). Modelling the propulsion characteristics of a standard wheelchair. *Journal of Rehabilitation Research and Development*, 31(2), 129-137.
- Hou ZC, Lu Y, Lao Y, & Liu D. (2009). A new trifilar pendulum approach to identify all inertia parameters of a rigid body or assembly. . *Mechanism Machine Theory.*, 44(6), 1270-1280.
- Hughes, Barbara, Sawatzky, Bonita J, & Hol, Adrienne T. (2005). A comparison of spinergy versus standard steel-spoke wheelchair wheels. *Archives of physical medicine and rehabilitation*, 86(3), 596-601.
- Hurd, Wendy J, Morrow, Melissa MB, Kaufman, Kenton R, & An, Kai-Nan. (2009). Wheelchair propulsion demands during outdoor community ambulation. *Journal of Electromyography and Kinesiology*, 19(5), 942-947.

- International Standards Organization. (2008). ISO 7176 Wheelchair Standards- Section 11: Test Dummies: International Standards Organization,.
- Johnson, Barry W, & Aylor, James H. (1985). Dynamic modeling of an electric wheelchair. *Industry Applications, IEEE Transactions on*(5), 1284-1293.
- Kauzlarich, J. J., & Thacker, J. (1985). Wheelchair tire rolling resistance and fatigue. *Journal of Rehabilitation Research and Development*, 22, 25-41.
- Kauzlarich, J. J., & Thacker, J. G. (1985). Wheelchair tire rolling resistance and fatigue. *J Rehabil Res Dev*, 22(3), 25-41.
- Kaye, H Stephen, Kang, Taewoon, & LaPlante, Michell P. (2000). Mobility Device Use in the United States. Disability Statistics Report 14.
- Kwarciak AM, Yarossi M, Ramanujam A, Dyson-Hudson TA, & Sisto SA. (2009). Evaluation of wheelchair tire rolling resistance using dynamometer-based coast-down tests. *Journal of Rehabilitation Research and Development*, 46(7), 931-938.
- Levy, C. E., Buman, M. P., Chow, J. W., Tillman, M. D., Fournier, K. A., & Giacobbi, P., Jr. (2010). Use of power assist wheels results in increased distance traveled compared with conventional manual wheeling. *Am J Phys Med Rehabil*, 89(8), 625-634. doi: 10.1097/PHM.0b013e3181e72286
- Liles, Howard, Huang, Morris, Caspall, Jayme, & Sprigle, Stephen. (2014). Design of a Robotic System to Measure Propulsion Work of Freewheeling Wheelchair Maneuvers.
- Lin, J., & Sprigle, S. (2014). *Evaluation of total wheelchair resistance in straight and curvilinear coast-down test*. Paper presented at the annual RESNA conference, Indianapolis, IN.
- Lin, Jui-Te, Huang, Morris, & Sprigle, Stephen. (2015). Evaluation of wheelchair resistive forces during straight and turning trajectories across different wheelchair configurations using free-wheeling coast-down test. *Journal of rehabilitation research and development*, 52(7), 763.
- Mason, Barry S, Lemstra, M, van der Woude, Lucas HV, Vegter, R, & Goosey-Tolfrey, Victoria L. (2015). Influence of wheel configuration on wheelchair basketball performance: Wheel stiffness, tyre type and tyre orientation. *Medical engineering & physics*, 37(4), 392-399.
- Medola, F., Dao, P., Caspall, J., & Sprigle, S. (2013). Partitioning Kinetic Energy during Freewheeling Wheelchair Maneuvers. *IEEE Trans Neural Syst Rehabil Eng*. doi: 10.1109/tnsre.2013.2289378
- Oyster, M. L., Karmarkar, A. M., Patrick, M., Read, M. S., Nicolini, L., & Boninger, M. L. (2011). Investigation of factors associated with manual wheelchair mobility in

persons with spinal cord injury. *Arch Phys Med Rehabil*, 92(3), 484-490. doi: 10.1016/j.apmr.2010.09.025

Pacejka, Hans. (2005). *Tire and vehicle dynamics*: Elsevier.

Ringegni, P. L., Actis, M. D., & Patanella, A. J. (2001). An experimental technique for determining mass inertial properties of irregular shape bodies and mechanical assemblies. *Measurement*, 29(1), 63-75. doi: [http://dx.doi.org/10.1016/S0263-2241\(00\)00028-2](http://dx.doi.org/10.1016/S0263-2241(00)00028-2)

Robertson, R. N., Boninger, M. L., Cooper, R. A., & Shimada, S. D. (1996). Pushrim forces and joint kinetics during wheelchair propulsion. *Arch Phys Med Rehabil*, 77(9), 856-864.

Rozendaal LA, Veeger HE, & van der Woude LH. (2003). The push force pattern in manual wheelchair propulsion as a balance between cost and effect. *J Biomech.*, 36(2), 239-247.

Sauret, Christophe, Bascou, Joseph, de Saint Rémy, Nicolas, Pillet, Hélène, Vaslin, Philippe, & Lavaste, François. (2012). Assessment of field rolling resistance of manual wheelchairs. *J Rehabil Res Dev*, 49(1), 63-74.

Sawatzky, B. J., Denison, I., & Kim, W. O. (2002). Rolling, rolling, rolling. *Rehab Management*, 9, 36-39.

Silva, LCA, Corrêa, FC, Eckert, JJ, Santiciolli, FM, & Dedini, FG. (2017). A lateral dynamics of a wheelchair: identification and analysis of tire parameters. *Computer methods in biomechanics and biomedical engineering*, 20(3), 332-341.

Sonenblum SE, Sprigle S, & Lopez RA. (2012a). Manual Wheelchair Use: Bouts of Mobility in Everyday Life. *Rehabilitation Research and Practice*, 7. doi: 10.1155/2012/753165

Sonenblum SE, Sprigle S, & Lopez RA. (2012b). Manual Wheelchair Use: Bouts of Mobility in Everyday Life,” *Rehabilitation Research and Practice*. *Rehabilitation Research and Practice*, 7. doi: 10.1155/2012/753165

Thacker, J, & Foraiati, K. (1991). Ride Comfort *Wheelchair Mobility* (pp. 27-33): University of Virginia Rehabilitation Engineering Center Annual Report.

Thacker, J. G., Sprigle, S., & Morris, B. (1994). *Understanding the technology when selecting wheelchairs*: RESNA Press.

van der Linden, Mariëtta L. , Valent, Linda, Veeger, H.E.G., & van der Woude, Luc H.V. (1996). The effect of wheelchair handrim tube diameter on propulsion efficiency and force application (tube diameter and efficiency in wheelchairs). *IEEE Transactions on Rehabilitation Engineering*, 4(3), 123-132.

- van der Woude, L. H., Geurts, C., Winkelman, H., & Veeger, H. E. (2003). Measurement of wheelchair rolling resistance with a handle bar push technique. *J Med Eng Technol*, 27(6), 249-258. doi: 10.1080/0309190031000096630
- van der Woude LHV, Dallmeijer AJ, Janssen TWJ, & Veeger D. (2001). Alternative modes of manual wheelchair ambulation: An overview. *Am J Phys Med Rehabil* 80, 765-777.
- van der Woude LHV, Veeger HEJ, Rozendal RH, & et al. (1988). Wheelchair racing: effect of rim diameter and speed on physiology and technique. *Med Sci Sports Exerc*, 20, 492-500.
- van der Woude LHV, Veeger HEJ, Hendrich KE, et al. . (1988). Manual wheelchair propulsion: effects of power output on physiology and technique. *Med Sci Sports Exerc*, 20, 70-78.